Measuring CP-Violation by Tagging Soft Muons in $t\bar{t}$ Events Using the ATLAS Detector at the Large Hadron Collider

James David Shinner

Department of Physics
Royal Holloway, University of London

A thesis submitted to the University of London
for the degree of Doctor of Philosophy

Declaration

I hereby declare that the work presented in this thesis is my own. Where the work of others has been consulted, this has been indicated in the text.

The measurement that forms the core of the thesis was carried out as part of the ATLAS experiment, and makes full use of techniques and software developed by this collaboration. The results are undergoing approval for public release, and are intended for publication in a journal. I am analysis lead for this publication effort, and I have carried out the majority of the work that has produced the measurement, which constitutes the work written up for this thesis. Feedback, discussion, and support have been provided by other members of the analysis team from Royal Holloway, University of London and Università degli Studi di Roma Tor Vergata. The remaining work that remains to be completed before the analysis can be unblinded and final measurements can be extracted is detailed where relevant, and will be completed by other members of the analysis team.

In addition to this measurement, I made a significant contribution to the trigger configuration system (see Section 5.2.5). This involved conducting various performance studies in relation to the redesign of the trigger configuration database, as well as the development of a new suite of software to provide a command-line interface for interacting with this database. These studies are not discussed in detail in this thesis.

James David Shinner
24th April 2023

Abstract

A measurement of CP-violation is presented, making use of an event selection whereby soft muons from the semileptonic decays of b-hadrons and c-hadrons are tagged in lepton+jets $t\bar{t}$ events originating from proton-proton collisions in the ATLAS detector at the Large Hadron Collider. Four methods are considered for the process of same-top/different-top assignment, with the kinematic likelihood fitting method found to marginally perform best when assessed in terms of the total uncertainty on the final results. The feasibility of extending the measurement by complementing the existing time-integrated asymmetries with a time-dependent asymmetry is explored and is found to be promising. The combined charge count distribution $N^{\ell\mu}$ of the soft muon and prompt lepton is presented for Monte Carlo simulation and for data corresponding to an integrated luminosity of $139\,\text{fb}^{-1}$ and a centre-of-mass energy of $\sqrt{s} = 13\,\text{TeV}$. In addition, the Monte Carlo distribution is unfolded to a fiducial volume and combined with a set of measured decay chain fractions to extract observable charge asymmetries and a set of underlying CP-violation asymmetries, which are presented along with their associated statistical and systematic uncertainties. These asymmetries and their uncertainties are discussed, along with the ramifications for the measurement of these asymmetries in the experimental data and the impact of such a measurement on searches for sources of CP-violation not described by the Standard Model.

Acknowledgements

I would like to begin by thanking my PhD supervisor Professor Véronique Boisvert for guiding me along the often exciting, often arduous journey that has been the last four years. Your insight and friendship have been invaluable throughout.

Secondly, I would like to thank Glen, Pedro, Tracey, and the rest of the staff and students in the Royal Holloway Particle Physics Group for many an interesting discussion in group meetings, and for help and support with all things physics, statistics, computing, and beyond. An additional 'grazie mille' to Marco, Francesco, Lucio, and the rest of the group at Tor Vergata for help in understanding all the finer details and quirks of ATLAS software and top physics.

To Callum, Pim, and Sean, thank you for the many days of help, companionship, and evenings at the pub, and the much needed breaks from physics. To Emily, thank you for agreeing to take up the mantle of the CP-violation analysis, I have every faith in you to see it through. Good luck!

To my whole family, and especially to Mum and Dad, you have my endless gratitude and love for supporting me in everything and always pushing me to strive to be the best I can, in academics and in life. I promise not to make you call me 'Dr. Shinner' quite as often as I may have joked about.

And finally, to the person who deserves thanks more than any other, Erin Janey. For standing by me through thick and thin, putting up with my often antisocial working hours, listening to me rave, rant, laugh, and cry about physics in equal measure, and for being proofreader and editor extraordinaire. Love you.

Contents

Figures

Tables

Acronyms

AdaBoost Adaptive Boosting

ALICE A Large Ion Collider Experiment

ATLAS A Toroidal LHC Apparatus

AUC Area Under Curve

BDT Boosted Decision Tree

BSM Beyond the Standard Model

CART Classification and Regression Trees

CERN The European Organisation for Nuclear Research

CKM Cabbibo-Kobayashi-Maskawa

CMB Cosmic Microwave Background

CMS Compact Muon Solenoid

CSC Cathode Strip Chamber

DAQ Data Acquisition System

FASER Forward Search Experiment

FSR Final-state Radiation

HLT High Level Trigger

ID3 Iterative Dichotomiser 3

IP Interaction Point

ISR Initial-state Radiation

JER Jet Energy Resolution

JES Jet Energy Scale

JVT Jet Vertex Tagger

L1 Level 1

LAr Liquid Argon

LHC Large Hadron Collider

LHCb Large Hadron Collider Beauty

LHCf Large Hadron Collider Forward

LINAC2 Linear Accelerator 2

LINAC4 Linear Accelerator 4

MC Monte Carlo

MDT Monitored Drift Tube

MoEDAL Monopole and Exotics Detector At the LHC

NLO Next-to-leading Order

NN Neural Network

PDF Parton Distribution Function

PDG Particle Data Group

PS Proton Synchrotron

PSB Proton Synchrotron Booster

QCD Quantum Chromodynamics

QED Quantum Electrodynamics

QFT Quantum Field Theory

ROC Receiver Operating Characteristic

RoI Region-of-interest

RPC Resistive Plate Chamber

SCT Semiconductor Tracker

SLC Semileptonic Correction

SMT Soft Muon Tagging

SPS Super Proton Synchrotron

ST/DT Same-top/different-top

TGC Thin Gap Chamber

TOTEM Total, Elastic, and Diffractive Cross-Section Measurement

TRT Transition Radiation Tracker

In memory of Anne P. K. Shinner - Grandma, I hope this would make you proud.

Jimbo

Chapter 1

Introduction

Developed from the unification of several prior theories in the 20th Century, the Standard Model of particle physics provides humanity's best understanding of the fundamental sub-atomic particles which make up everything, and the forces by which they interact. Since its conception, the theory has proved to have remarkable predictive power, leading to important experimental discoveries. However, the theory fails to provide a full description of observed phenomena [1]. For example, it lacks a description of gravitation, does not account for the observation of dark matter or neutrino oscillations, and does not explain the domination of matter over antimatter in the observable universe.

The Large Hadron Collider (LHC), located at the European Organisation for Nuclear Research (CERN) in Geneva, Switzerland, is the largest particle accelerator ever built, colliding high-energy beams of protons accelerated to almost the speed of light. These collisions produce fundamental particles, in greater quantities and at higher energies than has ever been achieved elsewhere, inside detector experiments located around the particle accelerator ring. A Toroidal LHC Apparatus (ATLAS) is one such general-purpose detector experiment, designed to be sensitive to a broad array of physics processes. It provides an ideal laboratory for examining the disparities between Standard Model predictions and observations of nature, and is the source of the experimental data used in this thesis.

This thesis concentrates on the asymmetry between matter and antimatter. When matter and antimatter interact, they annihilate, releasing large quantities of energy. From the absence of evidence of such annihilations in astronomical observations and studies of the cosmic microwave background (CMB), it can be deduced that no antimatter-dominated regions exist in the observable universe, nor did they in the past [2]. The universe is dominated by matter. The theoretical predictions of the Standard Model give rise to some asymmetries in the laws of physics between matter and antimatter, known as CP-violation (see Chapter 4 for full definition), but not enough to explain the disparity that is observed. Furthermore, there is tension in current experimental results, with some agreeing with the Standard Model predictions, and some suggesting much higher levels of CP-violation may be present. By making use of a technique known as soft muon tagging (SMT), this thesis presents a measurement of the levels of CP-violation in the decays of bottom quarks coming from top-antitop pairs in proton-proton collision events recorded by the ATLAS detector at the LHC. Making use of novel techniques, and attempting to reduce uncertainties when compared to previous results, this measurement aims to establish whether or not the level of CP-violation is in line with Standard Model predictions. If it is higher, this would pave the way towards new theories of physics beyond the Standard Model, potentially containing the level of CP-violation required to answer the fundamental cosmological question of why the universe is made of matter and not antimatter.

The structure of the thesis is as follows. Chapter 2 provides an overview of the theoretical foundations, recounting the development of the Standard Model, its mathematical structure, and how particles interact with one another. It is followed by Chapter 3, detailing the phenomenology of the top quark and bottom quark. The phenomenon of CP-violation is explored in Chapter 4, including how the phenomenon was discovered, along with a review of the current state of experimental evidence in this area and how this motivates the work in this thesis. Chapter 5 introduces the LHC and the ATLAS experiment, and Chapter 6 gives details of ATLAS simulation and reconstruction methods. In Chapter 7, the general analysis strategy for the CP-violation measurement is laid out, along with the details of object and event selection requirements. Chapter 8 then explores the composition and estimation of the background processes that contribute to the measurement, and Chapter 9 details the various sources of uncertainty that need to be considered. Chapters 10 and 11 detail the processes of same-top/different-top (ST/DT)-assignment and unfolding, two of the key techniques used in the analysis. The feasibility of complementing the existing time-integrated measurement with a future time-dependent measurement is explored in Chapter 12. At the time of writing this thesis, a small amount of work remains to be done in order to fully complete the measurement, unblind the analysis and extract the final results. However, various intermediate results have been produced to date, namely the plots of kinematic and combined charge-count distributions as measured in experimental data, the extracted charge and CP-violation asymmetries as measured in simulation, and the tables of uncertainties. These results are presented and discussed in Chapter 13, and this is followed by final conclusions in Chapter 14, including an explanation of what work remains to be completed.

Chapter 2

The Standard Model

The Standard Model of particle physics, an example of a quantum field theory (QFT), provides descriptions of the elementary particles and the fundamental forces that govern their interactions. As such, it provides humanity's most complete picture of the laws of the universe at the smallest scales. This chapter begins with descriptions of the fundamental forces and particles of the Standard Model (Sections 2.1 and 2.2), and then sets the development of the theory in its historical context (Section 2.3). Explanations of the Standard Model Lagrangian and interactions are provided (Sections 2.4 and 2.5), which are intended to be sufficient to motivate the experimental work that is detailed thereafter. The scope of this thesis will not extend to a more in-depth dive into the technicalities of QFT than that which is considered necessary. References [1, 3–5] have been consulted throughout the writing of this chapter.

2.1 Fundamental Forces

There are four fundamental forces, or interactions, that occur between particles: electromagnetism, the weak interaction, the strong interaction, and gravitation.

The electromagnetic interaction affects particles possessing an electric charge, and is responsible for phenomena such as light, the formation of atoms from nuclei and electrons, and the formation of chemical bonds between atoms.

The weak interaction affects particles possessing weak isospin (the analogue of electric charge for the electromagnetic interaction). It is responsible for all flavour-changing interactions, such as radioactive beta decay.

The strong interaction affects particles possessing a colour charge and is responsible for the binding of protons and neutrons into atomic nuclei and the binding of quarks (see Section 2.2) into protons, neutrons, and other composite particles.

Gravitation affects all massive particles. The most accurate description of gravitation is provided by the theory of general relativity, which is not consistent with the Standard Model in its present form.

2.2 Fundamental Particles

The Standard Model comprises several categories of fundamental particles, which are detailed below, and summarised in Fig. 2.1. All of the fundamental particles have a corresponding antiparticle, with equal mass and opposite electric charge. Everything described below should be taken to apply to both particles and antiparticles, other than where differences are explicitly highlighted.

The particles can be divided based on their intrinsic angular momentum, known as spin. Particles with half-integer spin are called fermions, and particles with integer spin are called bosons.

The fundamental fermions are all spin-$\frac{1}{2}$ particles, and are subdivided into particles that participate in strong interactions, and those that only participate in electroweak interactions.

The fermions that participate in strong interactions are called quarks. There are three generations of quarks (antiquarks), with two quarks (antiquarks) per generation, an up-type quark (antiquark) characterised by a $+\frac{2}{3}$ $(-\frac{2}{3})$ electric charge, and a down-type quark (antiquark) characterised by a $-\frac{1}{3}$ $(+\frac{1}{3})$ electric charge. The three generations of up-type quarks in ascending order by mass are the up (antiup) quark, u $(\bar{u})$, the charm (anticharm) quark, c $(\bar{c})$, and the

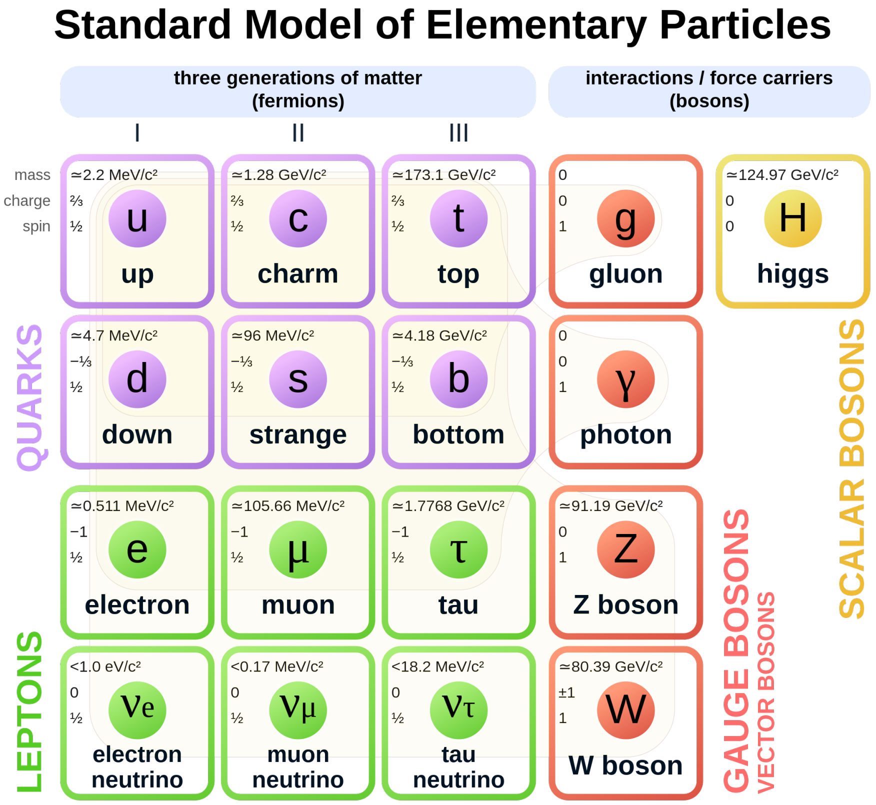

Figure 2.1 An overview of the fundamental particles of the Standard Model, detailing their groupings, generations, masses, electric charges, and spins [6].

top (antitop) quark, t ($\bar{t}$). The three generations of down-type quarks in ascending order by mass are the down (antidown) quark, d ($\bar{d}$), the strange (antistrange) quark, s ($\bar{s}$), and the bottom (antibottom) quark, b ($\bar{b}$). In addition to their electric charge, quarks (antiquarks) possess a colour (anticolour) charge which can take one of three values, known as red (antired), green (antigreen), and blue (antiblue). Only the up and down quarks are stable, and make up the protons and neutrons in the nuclei of atoms. The top, bottom, charm, and strange quarks are produced in high-energy collisions, and are unstable, forming lower mass states.

Due to the asymptotic freedom property of the strong interaction, quarks do not propagate as free particles (with the exception of the top quark, which is so unstable as to decay before hadronisation can occur). They are instead confined within composite particles called hadrons, which have an overall neutral colour charge. These composite hadrons can be separated into two classes. Baryons (antibaryons) are made up of three quarks (antiquarks), carrying one red (antired), one green (antigreen), and one blue (antiblue) colour charge. Protons and neutrons, with quark content uud and ddu respectively, are the most well-known examples of baryons, but more than 100 different types of baryon have been observed [7]. The other class of hadrons, mesons, are made up of a quark-antiquark pair, carrying a colour charge and the corresponding anticolour charge. Similarly to baryons, many such mesons have been observed, with the most commonly formed being the pions, π^+, π^-, and π^0, with quark content $u\bar{d}$, $d\bar{u}$, and $u\bar{u}/d\bar{d}$ respectively [8]. The collection of hadrons precipitating from the hadronisation of a single quark is known as a jet.

The fermions that only participate in electroweak interactions are called leptons. There are three generations of leptons (antileptons), with each generation consisting of a negatively (positively) charged lepton (antilepton) and a neutral lepton (antilepton), also known as a neutrino (antineutrino). The three generations of charged leptons (antileptons) in ascending order by mass are the electron (antielectron, or positron), e^- (e^+), muon (antimuon), μ^- (μ^+), and tau (antitau), τ^- (τ^+). The three generations of neutrinos (antineutrinos) are correspondingly the electron neutrino (antielectron neutrino), ν_e ($\bar{\nu_e}$), muon neutrino (antimuon neutrino), ν_μ ($\bar{\nu_\mu}$), and tau neutrino (antitau neutrino), ν_τ ($\bar{\nu_\tau}$). The Standard Model predicts that neutrinos have zero mass, however the experimental observation of neutrino oscillations suggests that they in fact have a small but non-zero mass [9].

All fermions possess an additional intrinsic property known as chirality, a Lorentz-invariant measure of the direction of spin in relation to the direction of momentum. Individual fermions can be either left-handed or right-handed. Only left-handed (right-handed) fermions (antifermions) participate in the weak interaction. Particles of both left-handed and right-handed chirality have been observed for all flavours of fermion, with the exception of neutrinos. Right-handed neutrinos, also known as sterile neutrinos, would only interact via gravitation if they do exist, making them extremely hard to observe.

The fundamental bosons are subdivided into gauge bosons, spin-1 particles that mediate the fundamental interactions, and scalar bosons, spin-0 particles.

For each of the fundamental interactions, there are as many gauge bosons as there are generators of the symmetry group governing the interaction. The $U(1)$ symmetry governing electromagnetism has one generator, and thus electromagnetism has one massless gauge boson, the photon, γ. The weak interaction is governed by an $SU(2)$ symmetry with three generators, and has three massive gauge bosons, the W^-, W^+, and Z, with $m_{W^\pm} = 80.379 \pm 0.012\,\text{GeV}$ and $m_Z = 91.1876 \pm 0.0021\,\text{GeV}$ [10]. The strong interaction is governed by an $SU(3)$ symmetry with eight generators, and has eight massless gauge bosons, known as gluons, g, which propagate in eight independent colour-anticolour states and are subject to the same asymptotic freedom property as quarks, meaning they cannot be observed directly, but hadronise to form jets. For the gauge bosons, the W^- and W^+ are antiparticles of each other, while the photon, Z-boson, and gluon are themselves their own antiparticles.

The sole scalar boson is the Higgs boson, H, with $m_H = 125.10 \pm 0.14\,\text{GeV}$.

2.3 Development of the Standard Model

The forerunner to QFT began at the turn of the 20th century. In order to explain the frequency distribution of black-body radiation in 1900, German physicist Max Planck postulated that energy is quantised, comprising discrete quanta rather than a continuous spectrum [11]. In 1905, Albert Einstein furthered this hypothesis by proposing energy quanta as particles of light (it was later that these would become known as photons), in order to explain the photoelectric effect [12]. Over the following years, this idea was expanded and developed into a theory of quantum mechanics. By 1926, equivalent formulations were developed by Erwin Schrödinger and Heisenberg, Born, and Jordan to describe simple quantum mechanical systems such as the hydrogen atom [13, 14].

In 1928, British physicist Paul Dirac reconciled the theories of quantum mechanics and special relativity with a description of the electromagnetic interactions between electrons and photons [15]. This can be encapsulated by the Dirac equation,

$$(i\partial\!\!\!/ - m)\psi = 0, \tag{2.1}$$

where $i = \sqrt{-1}$ is the imaginary unit, m is the mass, ψ is the waveform of the electron, and $\partial\!\!\!/$ is the 4-dimensional partial derivative expressed in Feynman slash notation (the convention of natural units is also used here and from now on, where the reduced Planck constant, $\hbar$, and speed of light, c, are set to $\hbar = c = 1$).

Dirac originally interpreted this as a single-particle equation, but this was later reinterpreted as a full field theory, suggesting the existence of antiparticles through the negative energy solutions to the Dirac equation. The antiparticle counterpart of the electron, the positron, was experimentally confirmed in 1932 [16]. Early attempts to extend the Dirac equation to multi-particle systems failed, as a variety of perturbative calculations in the theory resulted in infinite quantities. In the 1940s, a procedure called renormalisation was introduced to rectify this problem of infinities and develop a fully consistent QFT for the electromagnetic interaction, known as quantum electrodynamics (QED) [17].

In the 1950s, Yang and Mills generalised QFTs to more complex symmetries than the $U(1)$ symmetry underpinning QED, giving rise to a family of theories known as non-Abelian gauge theories [18]. The weak interaction, proposed originally by Fermi to explain radioactive beta decay, was unified with QED by Glashow, Weinberg, and Salam in the 1960s, as a non-Abelian gauge theory based on a combined $U(1) \times SU(2)$ symmetry [19–22]. This electroweak theory also incorporated the Higgs mechanism, by which the gauge bosons acquire mass [23–25]. The W and Z gauge bosons of the electroweak theory were confirmed in 1983 by the Underground Area 1 and Underground Area 2 experiments at CERN [26–29]. The Higgs boson was confirmed experimentally in 2012 by the ATLAS and Compact Muon Solenoid (CMS) collaborations, again at CERN [30, 31]. The unified electroweak theory has also been experimentally verified for the second and third generation leptons, the muon and tau, which were confirmed by experiment in 1936 and 1975 respectively [32, 33].

At a similar time to the unification of the electroweak interaction, the particles that participate in the strong interaction, called quarks, were first proposed by Gell-Mann and Zweig [34, 35]. The gauge theory for this interaction, based on an $SU(3)$ symmetry, was finalised in 1973 with the addition of the principle of asymptotic freedom to give the theory known as quantum chromodynamics (QCD) [36, 37]. The gauge boson of QCD, the gluon, was experimentally confirmed in 1978 [38]. At the time of QCD's inception, quark models involved only three flavours. The non-observation of flavour changing neutral currents meant that by 1970 the discovery of a fourth quark was anticipated [39]. In 1973, Kobayashi and Maskawa noted that the experimental observation of CP-violation could be explained by the existence of six quark flavours [40]. The charm quark was experimentally confirmed in 1974 by teams at the Stanford Linear Accelerator Complex and Brookhaven National Laboratory [41, 42]. Teams at Fermilab then confirmed the observation of the bottom quark in 1977, and announced the discovery of the top quark at the Tevatron collider in 1995 [43–45].

2.4 The Standard Model Lagrangian

Mathematically, the Standard Model is a QFT with gauge symmetry $U(1) \times SU(2) \times SU(3)$. According to Noether's Theorem, symmetries are intrinsically linked to conserved quantities [46]. The global symmetries of spacetime under translation in time, translation in space, and rotation give rise to conservation of energy, momentum, and angular momentum respectively. Similarly, the gauge (local, e.g. not necessarily applied simultaneously at all points in spacetime) symmetry of the Standard Model gives rise to conserved quantities: the colour charge of QCD, and the weak isospin and hypercharge of the unified electroweak interaction (which gives rise to the conservation of electric charge, the conservation law of classical electromagnetism).

The fundamental objects called particles are understood in the Standard Model to be excitations of quantum fields. The behaviour of the fields can be summarised by writing down the Lagrangian density, $\mathcal{L}$ (referred to simply as the Lagrangian from now on), respecting the gauge symmetry described above. The Lagrangian determines the dynamics of the system according to the principle of least action. The full Lagrangian for the Standard Model can be summarised as

$$\mathcal{L} = \mathcal{L}_{\text{Gauge}} + \mathcal{L}_{\text{Fermion}} + \mathcal{L}_{\text{Higgs}} + \mathcal{L}_{\text{Yukawa}}, \tag{2.2}$$

where the first two terms, $\mathcal{L}_{\text{Gauge}}$ and $\mathcal{L}_{\text{Fermion}}$ describe the propagation and interaction of the gauge bosons and fermions. The latter two terms, $\mathcal{L}_{\text{Higgs}}$ and $\mathcal{L}_{\text{Yukawa}}$, describe the Higgs field and Yukawa couplings, both of which are involved in the mechanism by which the particles of the Standard Model acquire masses.

The gauge term,

$$\mathcal{L}_{\text{Gauge}} = -\frac{1}{4}B_{\mu\nu}B^{\mu\nu} - \frac{1}{4}W^a_{\mu\nu}W^{\mu\nu}_a - \frac{1}{4}G^a_{\mu\nu}G^{\mu\nu}_a, \tag{2.3}$$

describes the free propagation (and self-interaction) of the gauge boson, where the fields B_μ and W^a_μ, $a = 1, \ldots, 3$ correspond respectively to the gauge symmetries $U(1)$ and $SU(2)$, while the fields G^a_μ, $a = 1, \ldots, 8$ correspond to $SU(3)$. The fields G^a_μ therefore correspond with the eight gluon fields, while the photon and electroweak gauge boson fields are linear combinations of B_μ and W^a_μ.

The individual fermion terms (with f running over the six quark fields and six lepton fields, giving 12 terms in total) take the form

$$\mathcal{L}^f_{\text{Fermion}} = i\bar{\psi}_f \not{D} \psi_f, \tag{2.4}$$

where $\not{D}$ is the covariant derivative. The covariant derivative describes not only the free propagation of the fermion, but also how the fermion field is coupled to the gauge fields in interaction terms. The derivative therefore takes a different form for the quark fields, which participate in QCD interactions, and the lepton fields, which do not. It also differs between the charged and neutral lepton fields.

A consequence of the gauge symmetry of $\mathcal{L}_{\text{Gauge}}$ and $\mathcal{L}_{\text{Fermion}}$ is that it requires them to be massless. None of the fields include a mass term such as that seen in the Dirac equation of the free electron (Eq. 2.1). The solution to how the particles acquire masses lies in their interaction with the Higgs field.

The Higgs term in the Lagrangian introduces the scalar Higgs field, ϕ, as

$$\mathcal{L}_{\text{Higgs}} = (D_\mu \phi)^\dagger (D^\mu \phi) - V(\phi), \tag{2.5}$$

where $V(\phi)$ is the Higgs potential,

$$V(\phi) = \mu^2 \phi^\dagger \phi + \lambda(\phi^\dagger \phi)^2, \tag{2.6}$$

for μ and λ constants under the restriction $\lambda > 0$, $\mu^2 < 0$. A visualisation of the Higgs potential is shown in Fig. 2.2. The vacuum (lowest energy) state of the field occurs at $\phi = v = \sqrt{-\frac{\mu^2}{\lambda}}$, a non-zero value. The symmetry of the Lagrangian is said to be spontaneously broken. For a global symmetry, this spontaneous symmetry breaking would produce new massless particles called Goldstone bosons [47]. However, in the case of the gauge symmetry of the Standard Model, via the Higgs mechanism, mass terms appear instead for the W, Z, and the Higgs boson itself, all proportional to the Higgs field vacuum expectation value, v, along with additional interaction terms between the gauge bosons and the Higgs field.

The spontaneous symmetry breaking of the Higgs mechanism also gives rise to fermion masses through the coupling of the Higgs field to the fermion fields. The individual terms that make up $\mathcal{L}_{\text{Yukawa}}$ (with f again running over the flavours of fermion) are of the form

$$\mathcal{L}^f_{\text{Yukawa}} = y_f(\bar{L}_f \phi R_f + \bar{R}_f \phi^\dagger L_f), \tag{2.7}$$

where L_f and R_f are the left-handed doublet and right-handed singlets pertaining to each fermion field and y_f is a parameter known as a Yukawa coupling, named for the Japanese physicist who originally proposed interactions of this form [49]. After spontaneous symmetry breaking, these terms can be resolved into Higgs-fermion interactions and fermion mass terms. These mass terms are dependent on the Higgs field vacuum expectation value, v, and the Yukawa coupling,

$$m_f = \frac{y_f}{\sqrt{2}} v. \tag{2.8}$$

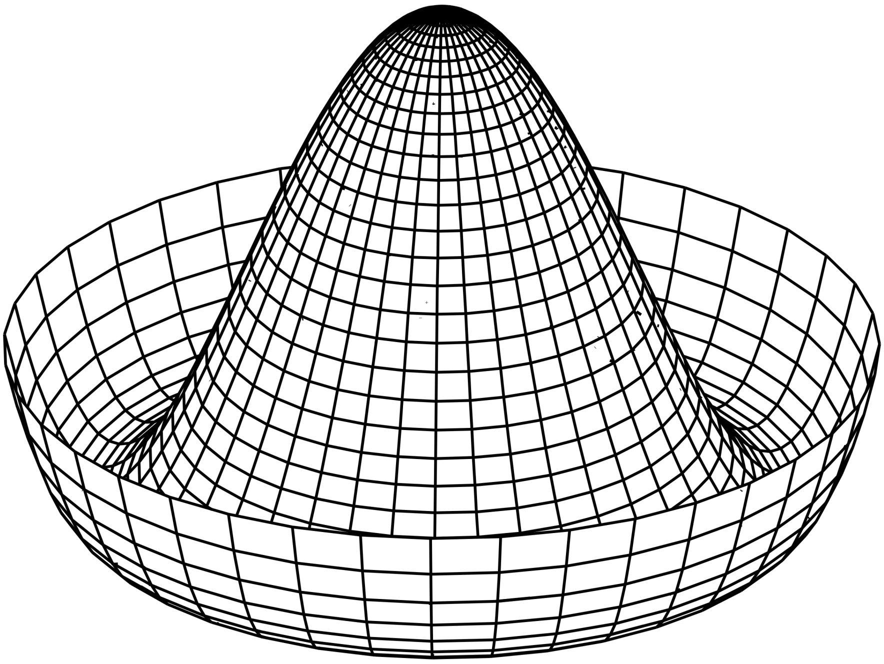

Figure 2.2 A visualisation of the Higgs potential, showing the ring of local minima that corresponds to the non-zero expectation value of the vacuum state [48].

2.5 Standard Model Interaction Vertices

The Standard Model Lagrangian described in Section 2.4 contains terms that dictate the interactions that are observed between particles. These interaction terms can be expressed in a concise form by making use of a pictorial representation known as a Feynman diagram rather than writing out the terms explicitly [50]. In these diagrams, lines represent the propagation of particles, vertices represent their interactions, and time and momentum flow from left to right. The representations of the different particles are shown in Fig. 2.3.

The different interaction vertices that are permitted in the Standard Model are summarised in Fig. 2.4, and are detailed below.

Three different vertices exist for the strong interaction (Fig. 2.4(a)), mediated by gluons. There is a 3-point interaction vertex between quarks and gluons, as well as 3-point and 4-point self-interaction vertices between gluons.

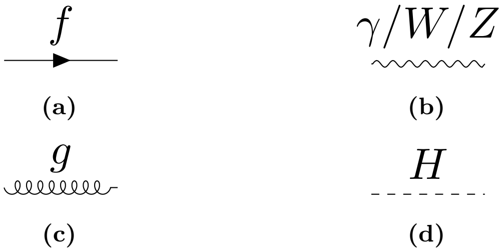

Figure 2.3 The Feynman diagram representations of the different particles of the standard model, showing: **(a)** the propagator for a fermion, with the arrow on the propagator pointing in (against) the time direction to indicate a particle (antiparticle); **(b)** the propagator for an electroweak gauge boson; **(c)** the propagator for a gluon; **(d)** the propagator for a Higgs boson.

The vertices for the electroweak interaction are shown in Fig. 2.4(b). The photon interacts with any electrically charged fermion, while the Z-boson interacts with any fermion in the flavour-preserving neutral current interaction. The W-boson mediates the flavour-changing charged current interaction. In the case of leptons, the interaction occurs strictly within generations. For example, a vertex could involve an incoming electron and outgoing electron neutrino, but not an incoming electron and outgoing muon neutrino. In the case of quarks, the interaction occurs between an up-type quark and a down-type quark only. However, unlike leptons, which have equal coupling strengths for all generations, not all flavour-changing current interactions involving quarks are equally likely. The mass eigenstates of the quarks that propagate freely are linear combinations of the weak eigenstates that are involved in the interaction. They are related by the Cabbibo-Kobayashi-Maskawa (CKM) matrix as

$$V_{CKM} = \begin{vmatrix} V_{ud} & V_{us} & V_{ub} \\ V_{cd} & V_{cs} & V_{cb} \\ V_{td} & V_{ts} & V_{tb} \end{vmatrix} = \begin{vmatrix} 0.974 & 0.225 & 0.004 \\ 0.225 & 0.973 & 0.041 \\ 0.009 & 0.040 & 0.999 \end{vmatrix}, \tag{2.9}$$

where the magnitudes of the different elements are proportional to the coupling strength for that interaction [40, 51, 52]. As a consequence of this, interactions involving quarks of the same generation are heavily favoured over those that mix generations. In addition to the vertices between electroweak gauge bosons and fermions, there are 3-point and 4-point self-interaction vertices between the electroweak gauge bosons.

The vertices for the Higgs field can be seen in Fig. 2.4(c). The Higgs boson interacts with all massive fermions. The strength of the interaction is proportional to the mass of the fermion, so the interactions with the heavy quarks dominate. A similar 3-point interaction vertex exists for the Higgs boson and the massive electroweak gauge bosons, accompanied by a 4-point interaction for the same particles. There are also 3-point and 4-point Higgs self-interaction vertices.

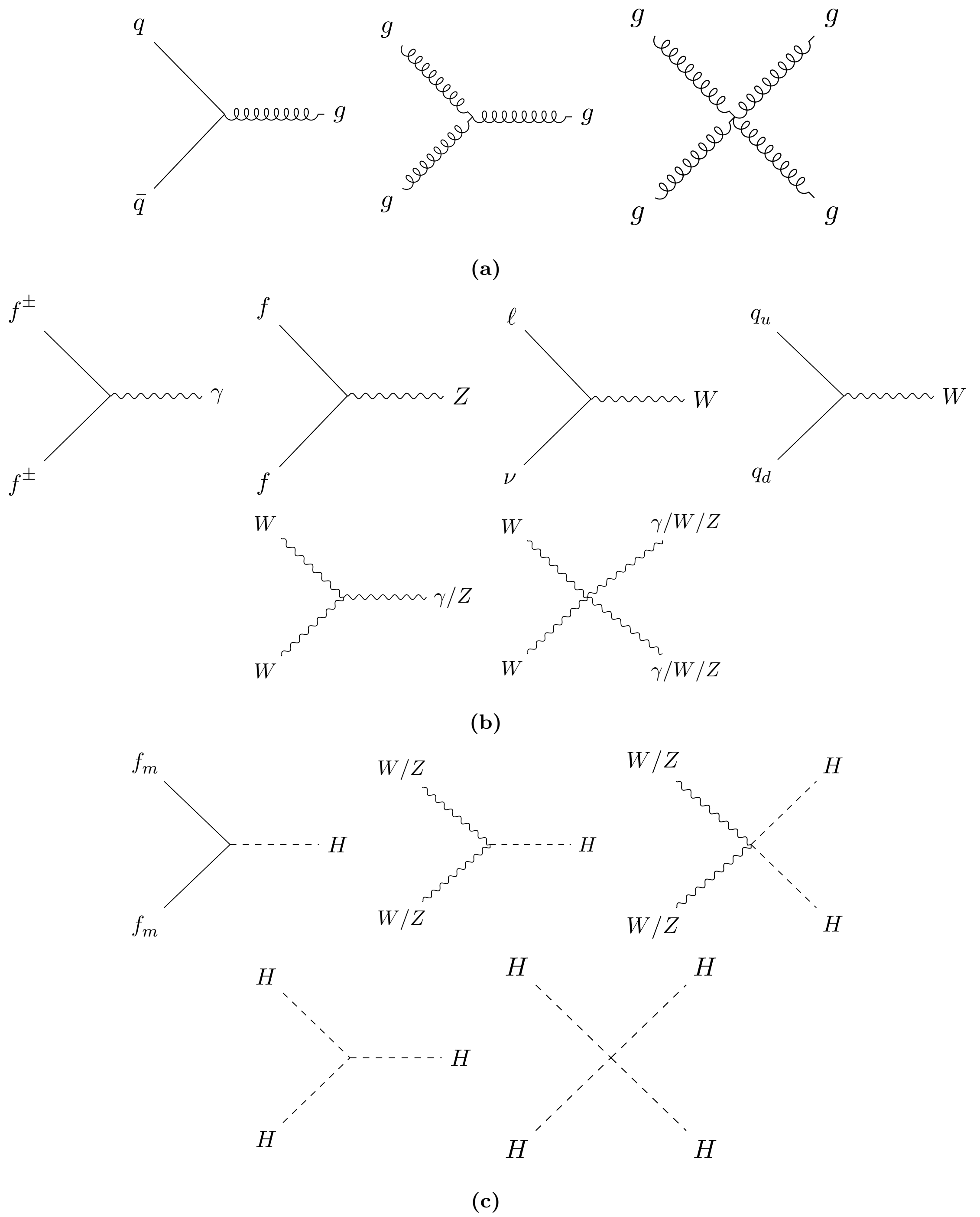

Figure 2.4 The Feynman diagram representations of the interaction vertices of the Standard Model, comprising: **(a)** the strong interactions - the quark (q)-gluon (g) vertex, and the 3-point and 4-point gluon self-interaction vertices; **(b)** the electroweak interactions - the photon (γ) vertex with a charged fermion ($f^\pm$), the Z-boson vertex with any fermion (f), the W-boson vertices with a charged lepton (ℓ) and neutrino (ν) of the same generation or an up-type (q_u) and down-type (q_d) quark, and the 3-point and 4-point gauge boson self-interaction vertices; **(c)** the Higgs interactions - the Higgs vertex with a massive fermion (f_m), and the 3-point and 4-point Higgs-electroweak boson and Higgs self-interaction vertices.

Chapter 3

Phenomenology

Phenomenology is the science of using the mathematical predictions of a theory, such as the Standard Model, in order to predict the behaviour of particles when they are observed in an experimental setting. In this chapter, Sections 3.1 and 3.2 are dedicated to the phenomenological predictions for the top quark and bottom quark, the two particles of central importance to the work in this thesis. They cover the modes by which these particles are produced and decay, and discuss their individual peculiarities and properties.

3.1 The Top Quark

The top quark is the heaviest of all the Standard Model particles, and is orders of magnitude heavier than the other five flavours of quark. As a consequence, it has a much shorter lifetime than the other flavours of quark. While the other quarks undergo hadronisation to form baryons or mesons, the top quark decays via the weak interaction before the hadronisation process can occur. It thus provides a unique opportunity to study a bare quark, without the state of the particle being impacted by hadronisation, and is thus a topic of interest for experimental study.

3.1.1 Top Quark Properties

While the Standard Model theorises that all of the fermion masses are proportional to the Higgs vacuum expectation value, v, the Yukawa couplings that act as constants of proportionality, or equivalently the masses themselves, are considered to be free parameters. This means they are not explicitly predicted by the theory and must be determined experimentally. The global average value of the top quark mass, m_t, as computed by the Particle Data Group (PDG) using data from direct measurements made at the LHC and Tevatron, is $m_t = 172.76 \pm 0.30\,\text{GeV}$ [53]. The results of direct measurements of m_t by the ATLAS and CMS collaborations at the LHC are shown in Fig. 3.1.

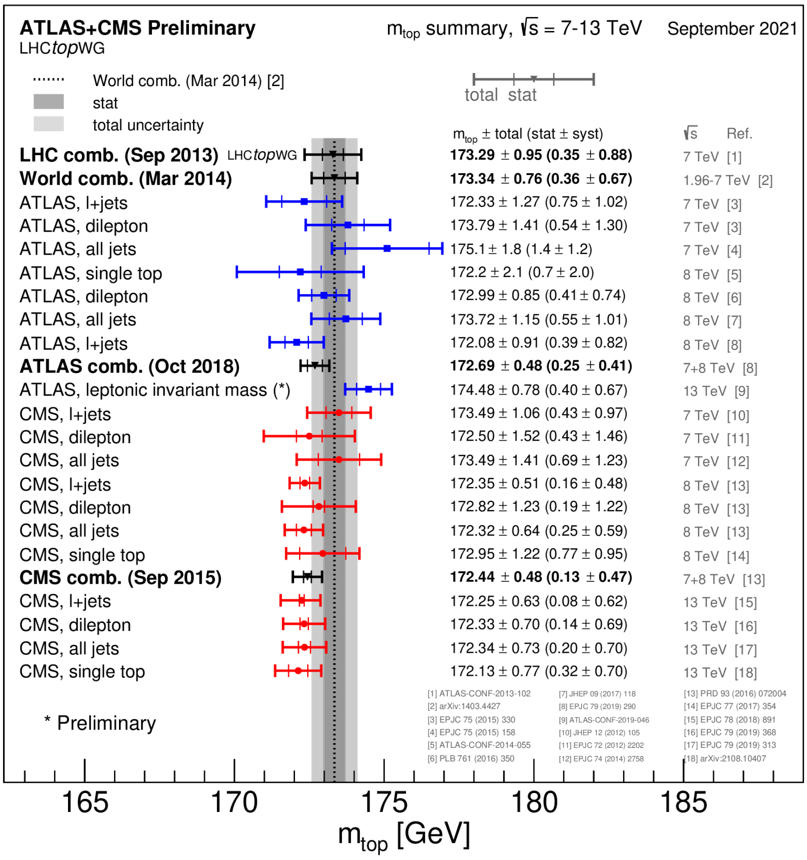

Figure 3.1 The results of direct measurements of the top quark mass, m_t, by the ATLAS and CMS collaborations [54].

The PDG average for the total decay width of the top quark mass is $\Gamma_t = 1.42^{+0.19}_{-0.15}$ GeV, which corresponds to a lifetime of $\tau_t \approx 10^{-25}$ s [53]. Comparison with the timescale of hadronisation, $\tau_{hadronisation} \approx 10^{-24}$ s, shows why the top quark decays before hadronisation can occur [55].

3.1.2 Top Quark Production

The top quark can be produced through a variety of processes, with the dominant production mode being the production of a top-antitop pair, $t\bar{t}$, as shown in Fig. 3.2. At proton-antiproton colliders such as the Tevatron, the majority ($\sim 85\%$) of $t\bar{t}$ production proceeds via quark-antiquark annihilation (Fig. 3.2(a)). However, at proton-proton colliders such as the LHC, the majority ($\sim 90\%$) of $t\bar{t}$ production proceeds via gluon-gluon fusion (Fig. 3.2(b)). This difference is due to the presence of valence antiquarks in a proton-antiproton collision, plus the fact that the LHC operates at a higher centre-of-mass energy than the Tevatron, at which a larger fraction of the proton momentum is carried by gluons [56].

After $t\bar{t}$ production, the most common production modes are the electroweak single-top processes, as shown in Fig. 3.3, which can be divided into three channels: the t-channel (Fig. 3.3(a)), the s-channel (Fig. 3.3(b)), and the tW-channel (Fig. 3.3(c)).

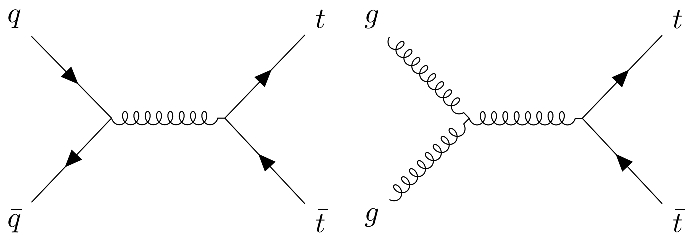

(a) **(b)**

Figure 3.2 The Feynman diagram representations of the modes of production for a top-antitop pair, $t\bar{t}$, broken down into: **(a)** quark-antiquark annihilation; **(b)** gluon-gluon fusion.

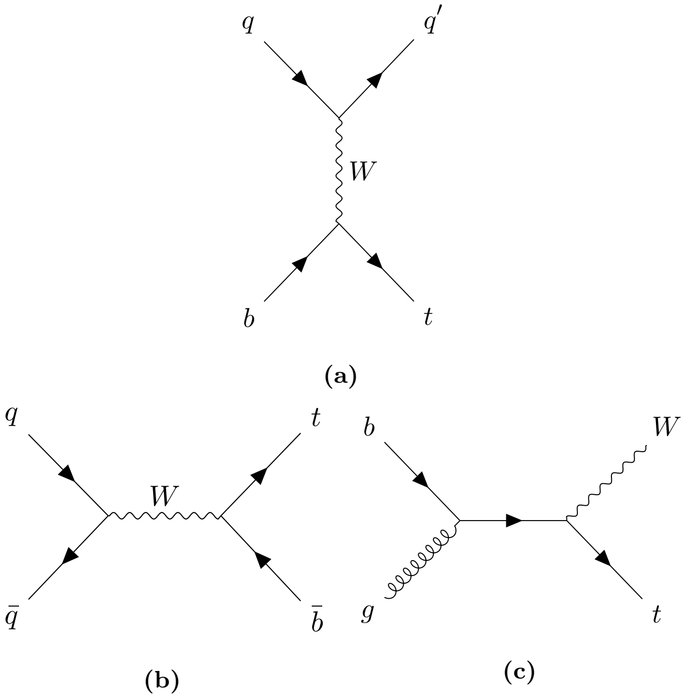

Figure 3.3 The Feynman diagram representations of single-top production: **(a)** the t-channel; **(b)** the s-channel; **(c)** the tW-channel.

In addition, there are additional less common production modes where a $t\bar{t}$ pair is produced in association with a boson, a single top quark is produced in association with a boson, or four top quarks are produced together.

The theoretical and measured cross sections for all of the top quark production modes at the LHC are shown in Fig. 3.4.

3.1.3 Top Quark Decay

The decay of the top (antitop) quark is dominated by the decay to a W^+ (W^-) and a bottom (antibottom) quark. All other possible decays are heavily suppressed ($< 0.1\%$) [58]. The W^+ (W^-) decays into an up-type quark (antiquark) and down-type antiquark (quark) or a neutrino (antineutrino) and a charged antilepton (lepton). Ignoring mass effects, the leptonic branching ratios are expected to sum to $\frac{1}{3}$, with equal contribution from each generation, while the hadronic branching ratios are expected to sum to $\frac{2}{3}$, with contributions proportional to

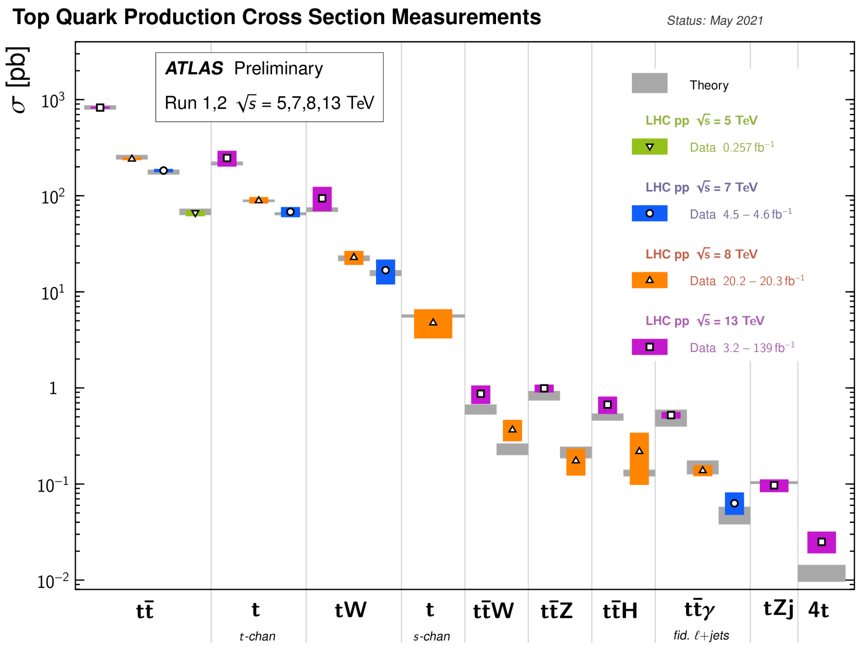

Figure 3.4 The theoretical and measured cross sections, σ, for the different top quark production modes at the LHC, at a range of centre-of-mass energies, $\sqrt{s}$ [57].

the relevant elements of the CKM matrix. The sum of the hadronic branching ratios has been measured to be $67.41 \pm 0.27\%$, while the individual leptonic fractions have been measured to be $10.86 \pm 0.09\%$ [10].

The decay of the $t\bar{t}$ system is categorised into channels according to the decay mode of the two W-bosons.

The all-hadronic channel (45.7%) involves both W-bosons decaying to hadrons. This is the most prevalent channel, but the final state contains a large number of jets, making it difficult to reconstruct and separate from background processes with a similar final state signature.

The dilepton channel (10.5%) involves both W-bosons decaying to leptons. This results in a clean final state signature, but occurs far less frequently than the all-hadronic channel.

The lepton + jets channel (43.8%) involves one of the W-boson decaying to hadrons and the other decaying to leptons. The channel provides a balance of a relatively clean final state (with a lepton making the process easy to identify) and a reasonably high branching ratio.

3.2 The Bottom Quark

As discussed in Section 3.1.3, a $t\bar{t}$ pair decays to produce a b and a $\bar{b}$. Unlike the top quark, these b-quarks propagate long enough to undergo hadronisation, resulting in a b-hadron inside a jet of other hadronic particles. Such a jet leaves a distinct signature in a particle detector, allowing them to be distinguished from jets of light hadrons through a process known as b-tagging.

The b-hadrons most commonly formed from the b-quark ($\bar{b}$-quark) are, in order of prevalence, the B^+ (B^-) meson, the B^0 ($\bar{B}^0$) meson, the B_s^0 ($\bar{B}_s^0$) meson, and then a variety of b-baryons. The production fractions and masses for each of these particles have been well measured experimentally [59, 60].

Between the production and decay of a B^0 or B_s^0, a process called mixing can occur. This involves the particles B^0 and B_s^0 oscillating into their antiparticle counterparts $\bar{B}^0$ and $\bar{B}_s^0$ via box processes, as shown in Fig. 3.5. The time-dependence of the oscillation can be modelled as a cosine function, with oscillation frequency Δm_q. Experimental measurements have shown that Δm_s is an order of magnitude larger than Δm_d, and thus B_s^0 oscillations take place on a shorter timescale than B^0 oscillations [61, 62].

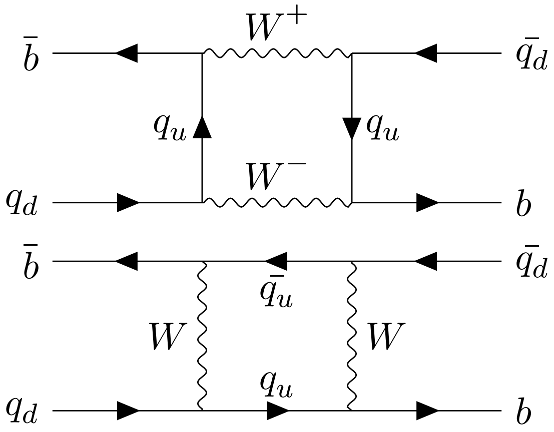

Figure 3.5 The box diagram processes responsible for neutral B-meson mixing, where $q_d = d, s$ is a down-type quark and $q_u = u, c, t$ is an up-type quark.

A full summary of the b-hadrons is given in Table 3.1, showing their particle content, mass, production fraction, and oscillation frequency.

There are a large number of decay modes for the b-hadrons (over 600 in one case), but overall fractions (also known as branching ratios) can be given for the final states produced from an initial b-quark. Of particular interest to this thesis is the final state containing a muon and muon neutrino, arising from the semileptonic decay of a b-hadron (or of a c-hadron further down the decay chain). The branching ratio for this final state is $BR(b \to \mu^- \nu_\mu X) = (10.95^{+0.29}_{-0.25})\%$, where X denotes any collection of particles [63]. The energy and momentum distributions of such muons are skewed towards lower values than the comparable distributions for leptons coming from the initial decay of a top quark (see Section 3.1.3). As such, a lepton from the initial decay of a top quark is referred to as a prompt lepton, while a muon originating from the decay of a b-quark is known as a soft muon.

Hadron	Particle Content	Mass (MeV)	f_q (%)	Δm_q (ps^{-1})
B^+ (B^-)	$\bar{b}u$ ($b\bar{u}$)	5279.34 ± 0.12	40.8 ± 0.7	0
B^0 ($\bar{B}^0$)	$\bar{b}d$ ($b\bar{d}$)	5279.65 ± 0.12	40.8 ± 0.7	0.5065 ± 0.0019
B^0_s ($\bar{B}^0_s$)	$\bar{b}s$ ($b\bar{s}$)	5366.88 ± 0.14	10.0 ± 0.8	17.749 ± 0.020
b-baryon ($\bar{b}$-baryon)	$\bar{b}q_1q_2$ ($b\bar{q}_1\bar{q}_2$)	> 5600	8.4 ± 1.1	0

Table 3.1 A summary of the b-hadrons formed in the hadronisation of a $\bar{b}$ (b) quark and their properties, where f_q is the production fraction and Δm_q is the mixing oscillation frequency [63–66].

Chapter 4

CP-Violation

This chapter is devoted to the concept of CP-violation, starting with an introduction of the symmetries of charge conjugation and parity in Sections 4.1 and 4.2, before introducing the combined CP-symmetry and the discovery of its violation in Section 4.3. Sections 4.4 to 4.7 explore the measurements of CP-violation asymmetries and related quantities, and the implications for CP-violation for the matter-antimatter asymmetry of the universe. The chapter concludes in Section 4.8 by summarising the consequences of measurements of CP-violation up to this point and how the work in this thesis is motivated by, and fits into, the wider scientific picture.

4.1 Charge Conjugation

The charge conjugation operator, C, replaces a particle with its antiparticle. As such, applying C to a positively charged particle will result in a negatively charged particle, and vice-versa, hence the name.

The classical theory of electrodynamics is invariant under C-symmetry (replacing all particles with their antiparticles), as changing the sign of all electric charges results in the same forces between them. QED and QCD give similar results. However, the weak interaction of the Standard Model does not respect this.

Only left-handed fermions and right-handed antifermions are seen to participate in the weak interaction. Therefore, taking as an example a left-handed neutrino, and exchanging it with its antiparticle, a left-handed antineutrino, does not lead to the same physics being observed. Thus C-symmetry is violated.

4.2 Parity

The parity operator, P, involves a reflection in space, such as that observed when looking in a mirror. It was long assumed that P-symmetry was a symmetry respected by all theories, but like with C-symmetry it is seen experimentally that it is respected by QCD and QED but broken in the weak interaction.

This was first postulated in 1954 by Lee and Yang, who noticed a lack of evidence for parity conservation in weak processes [67]. They proposed potential experimental methods by which this could be determined. One such experiment was carried out and published in 1957 by a team at Columbia University led by Wu, with the results confirmed in a separate experiment shortly after by another team from the same university [68, 69]. The Wu experiment involved recording the direction of emitted electrons from the radioactive beta decay of Cobalt-60 nuclei with their spins aligned to a magnetic field. If parity were conserved, electrons would be expected to be observed in equal quantities in the directions parallel and opposite to the nuclear spin. However, electron emissions were observed to mostly be emitted in the direction opposite to the nuclear spin, and parity was thus observed to be violated. This experiment, along with the confirmation that neutrinos were exclusively left-handed, helped confirm the chiral structure of the weak interaction [70].

Returning to the example of a left-handed neutrino, a reflection in space would result in a right-handed neutrino, which would not participate in the weak interaction and therefore would not result in the same physics being observed. Thus P-symmetry is violated.

4.3 Discovery of CP-Violation

Following the discovery of parity violation, Landau proposed the combined CP-operator as the basis for the symmetry that was truly conserved [71]. This appears to solve the problem of the left-handed neutrino example. Exchanging the particle for its antiparticle and mirroring space results in a right-handed antineutrino, which participates in the weak interaction in the same way as the original particle.

However, CP-symmetry was discovered to be violated in 1964 [72]. Whereas C-symmetry and P-symmetry are said to be maximally violated, meaning that the mirror image of a parity-violating process never occurs, CP-violation effects are small, and the symmetry is close to exact, but broken.

CP-violation has been confirmed for multiple neutral mesons. The first discoveries were for the K^0 meson [72–74]. Subsequent results from experiments known as B-factories confirmed CP-violation for the B^0 meson [75–77]. In more recent years, the Large Hadron Collider beauty (LHCb) collaboration discovered CP-violation for the B_s^0 meson [78]. Most recently, CP-violation was confirmed for the D^0 meson, again by LHCb [79].

4.4 CP-Violation and the Unitarity of the CKM Matrix

The CKM matrix, as shown in Eq. 2.9, is pivotal in describing the weak interaction of quarks. In the Wolfenstein parametrisation, the elements of the matrix are written in terms of four parameters, A, λ, ρ, and η [80]. This gives

$$V_{CKM} = \begin{vmatrix} V_{ud} & V_{us} & V_{ub} \\ V_{cd} & V_{cs} & V_{cb} \\ V_{td} & V_{ts} & V_{tb} \end{vmatrix} = \begin{vmatrix} 1-\frac{\lambda^2}{2} & \lambda & A\lambda^3(\rho - i\eta) \\ -\lambda & 1-\frac{\lambda^2}{2} & A\lambda^2 \\ A\lambda^3(1-\rho-i\eta) & -A\lambda^2 & 1 \end{vmatrix} + \mathcal{O}(\lambda^4). \tag{4.1}$$

CP-violation requires an irreducible complex phase to be present in the CKM matrix, which corresponds in the Wolfenstein parametrisation to a value of $\eta \neq 0$. Furthermore, the Standard Model requires that the CKM matrix be unitary, i.e. $V_{CKM}^{\dagger} V_{CKM} = I$, where I is the identity matrix. This imposes a restriction on the elements of the matrix,

$$V_{ud}V_{ub}^{*} + V_{cd}V_{cb}^{*} + V_{td}V_{tb}^{*} = 0. \tag{4.2}$$

In terms of the parameters of the Wolfenstein parametrisation, this reduces to a vector equation constraining a triangle in the $\rho - \eta$ plane with vertices at (0,0), (1,0), and (ρ, η). Measurements of CP-violation and neutral meson mixing properties can be related to parameters of this triangle, such as the lengths of its sides and the angles. If any such measurements suggest that a closed triangle is not formed, this would point to physics beyond the Standard Model (BSM). The latest compilation of such measurements performed by the CKMfitter group is shown in Fig. 4.1, and is in line with Standard Model expectations [81].

4.5 CP-Violation Asymmetries

The CP-violating effects observed in processes involving neutral mesons can be broken down into multiple types. These are:

- Direct CP-Violation: CP-violating effects occur directly in the decay of a neutral meson. The equivalent processes for the meson and its antiparticle do not occur at equal rates. $\Gamma(M^0 \to X) \neq \Gamma(\bar{M}^0 \to \bar{X})$.
- Indirect CP-Violation: CP-violating effects occur indirectly, through the mixing process. The equivalent processes involving mixing for the meson and its antiparticle do not occur at equal rates. $\Gamma(M^0 \to \bar{M}^0 \to X) \neq \Gamma(\bar{M}^0 \to M^0 \to \bar{X})$.

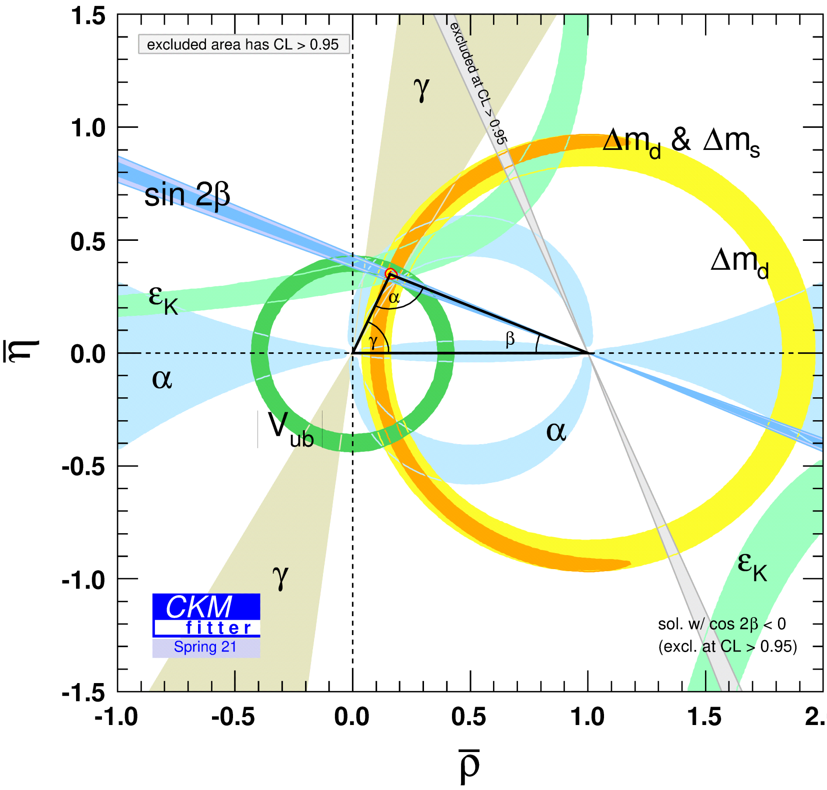

Figure 4.1 The current constraints on the unitarity triangle for the CKM matrix from a global fit of experimental results [82]. For full explanation of the various constraints, please see reference [81].

- CP-Violation in Interference: CP-violating effects occur through interference of decays that can proceed with or without mixing. The processes with and without mixing do not occur at equal rates. $\Gamma(M^0 \to X) \neq \Gamma(M^0 \to \bar{M}^0 \to X)$.

In all of the above equations, Γ denotes a decay width, M^0 denotes a general neutral meson for which CP-violation occurs, and X denotes a collection of final state particles.

Asymmetries can then be formed to quantify the level of these CP-violating effects. For example, the time-integrated asymmetry for direct CP-violation would be

$$A_{\text{dir}} = \frac{\Gamma(M^0 \to X) - \Gamma(\bar{M}^0 \to \bar{X})}{\Gamma(M^0 \to X) + \Gamma(\bar{M}^0 \to \bar{X})}. \tag{4.3}$$

A similar time-integrated asymmetry can be constructed for indirect CP-violation, and CP-violation in interference is only expected to be accessible through construction of a time-dependent asymmetry. Such asymmetries provide a quantification of the level of CP-violation in a process.

4.6 Measurements of CP-Violation Asymmetries in B-Mesons

In 2010, the D∅ collaboration at Fermilab reported that they had observed an anomalous like-sign dimuon asymmetry by measuring production of two muons with the same charge from a sample of b-hadrons [83]. The result,

$$A^b_{sl} = -0.00957 \pm 0.00251(\text{Stat.}) \pm 0.00146(\text{Syst.}), \tag{4.4}$$

differs by 3.2σ from the Standard Model prediction.

When interpreted to be a result wholly of indirect CP-violation (from mixing effects), the asymmetry A^b_{sl} receives contributions from B^0 and B^0_s mixing as

$$A^b_{sl} = f_d^{D\varnothing} a^d_{sl} + f_s^{D\varnothing} a^s_{sl}, \tag{4.5}$$

where $f_d^{D\varnothing}$, $f_s^{D\varnothing}$ are respectively the fractions of B^0 and B^0_s that contribute to the asymmetry (depending on the production fractions as listed in Table 3.1, and also on the experimental setup of D∅. They are both ~ 0.5). Both a^d_{sl} and a^s_{sl} are asymmetries of the form described in Section 4.5, for indirect CP-violation in the mixing of B^0 and B^0_s mesons respectively. Explicitly,

$$a^d_{sl} = \frac{\Gamma(B^0 \to \bar{B}^0 \to \mu^+ X) - \Gamma(\bar{B}^0 \to B^0 \to \mu^- X)}{\Gamma(B^0 \to \bar{B}^0 \to \mu^+ X) + \Gamma(\bar{B}^0 \to B^0 \to \mu^- X)}, \tag{4.6}$$

$$a^s_{sl} = \frac{\Gamma(B^0_s \to \bar{B}^0_s \to \mu^+ X) - \Gamma(\bar{B}^0_s \to B^0_s \to \mu^- X)}{\Gamma(B^0_s \to \bar{B}^0_s \to \mu^+ X) + \Gamma(\bar{B}^0_s \to B^0_s \to \mu^- X)}. \tag{4.7}$$

Both of these mixing asymmetries have since been measured independently by LHCb [84, 85]. The results were

$$a^d_{sl} = -0.0002 \pm 0.0019(\text{Stat.}) \pm 0.0030(\text{Syst.}), \tag{4.8}$$

$$a^s_{sl} = -0.0039 \pm 0.0026(\text{Stat.}) \pm 0.0020(\text{Syst.}). \tag{4.9}$$

Both of these results are found to be in agreement with the Standard Model and only marginally compatible with the D∅ result. A comparison of these results is shown in Fig. 4.2.

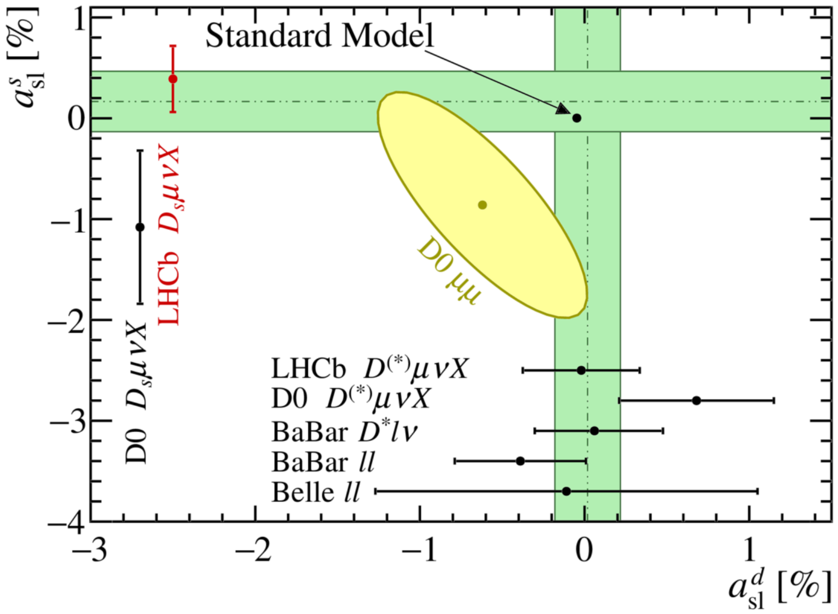

Figure 4.2 A summary of the most recent measurements of the indirect CP-violation asymmetries a^d_{sl} and a^s_{sl}, for the mixing of B^0 and B^0_s mesons respectively, and how they compare to the Standard Model prediction and the D∅ anomalous like-sign dimuon asymmetry [86].

While the LHCb results suggest that an interpretation of the D∅ anomalous like-sign dimuon asymmetry as evidence of indirect CP-violation beyond the level predicted by the Standard Model is invalid, it has also been shown that the asymmetry can be interpreted in terms of direct CP-violation in the decays of b-hadrons and c-hadrons [87, 88]. While these are often assumed to be zero as the Standard Model predictions are orders of magnitude smaller than the predictions for indirect CP-violation, this is not necessarily the case if the direct CP-violation comes from a BSM source [89]. Inclusive (i.e. with contributions from all possible intermediate hadrons) direct CP-violation asymmetries of the form described in Section 4.5 are defined for an initial b-quark and an initial c-quark as

$$A^b_{\text{dir}} = \frac{\Gamma(b \to \mu^- X) - \Gamma(\bar{b} \to \mu^+ X)}{\Gamma(b \to \mu^- X) + \Gamma(\bar{b} \to \mu^+ X)}, \tag{4.10}$$

$$A^c_{\text{dir}} = \frac{\Gamma(\bar{c} \to \mu^- X) - \Gamma(c \to \mu^+ X)}{\Gamma(\bar{c} \to \mu^- X) + \Gamma(c \to \mu^+ X)}. \tag{4.11}$$

In isolation (i.e. considering all other sources of CP-violation to be 0), a value of $|A^b_{\text{dir}}| \approx 0.003$ or $|A^c_{\text{dir}}| \approx 0.01$ would explain the D∅ results, neither of which have yet been ruled out by experiment. A combination of direct CP-violation effects in b-hadron and c-hadron decays can also be considered, and the compatibility of a range of values of A^b_{dir} and A^c_{dir} with the D∅ results is shown in Fig. 4.3.

A prescription has been developed for measuring CP-violation asymmetries using top quarks at the general-purpose detector experiments of the LHC, ATLAS and CMS [90]. This prescription defines three direct CP-violation asymmetries, $A^{b\ell}_{\text{dir}}$, $A^{c\ell}_{\text{dir}}$, and A^{bc}_{dir}.

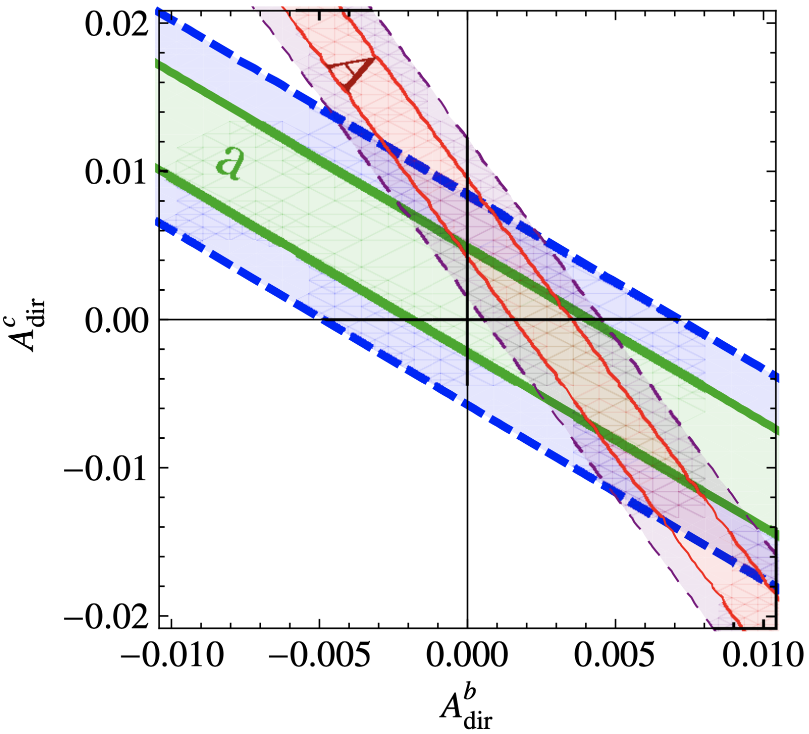

Figure 4.3 The compatibility of a range of values for the direct CP-violation asymmetries A^b_{dir} and A^c_{dir}, for b-hadron and c-hadron decays respectively, with the anomalous asymmetries a and A observed by the D∅ collaboration [87].

$A^{b\ell}_{\text{dir}}$ and $A^{c\ell}_{\text{dir}}$ are identical to the asymmetries A^{b}_{dir} and A^{c}_{dir} previously defined in Eqs. 4.10 and 4.11. The third asymmetry, A^{bc}_{dir}, quantifies the asymmetry in decays of b-hadrons to c-hadrons as

$$A^{bc}_{\text{dir}} = \frac{\Gamma(b \to cX) - \Gamma(\bar{b} \to \bar{c}X)}{\Gamma(b \to cX) + \Gamma(\bar{b} \to \bar{c}X)}. \tag{4.12}$$

The prescription also defines inclusive indirect CP-violation asymmetries related to b-hadron mixing as

$$A^{b\ell}_{\text{mix}} = \frac{\Gamma(b \to \bar{b} \to \mu^{+}X) - \Gamma(\bar{b} \to b \to \mu^{-}X)}{\Gamma(b \to \bar{b} \to \mu^{+}X) + \Gamma(\bar{b} \to b \to \mu^{-}X)}, \tag{4.13}$$

$$A^{bc}_{\text{mix}} = \frac{\Gamma(b \to \bar{b} \to \bar{c}X) - \Gamma(\bar{b} \to b \to cX)}{\Gamma(b \to \bar{b} \to \bar{c}X) + \Gamma(\bar{b} \to b \to cX)}. \tag{4.14}$$

Under the assumption that direct CP-violation can be neglected, these asymmetries become equivalent, and the B-meson mixing asymmetry is denoted A^{b}_{mix} ($A^{b}_{\text{mix}} = A^{b\ell}_{\text{mix}} = A^{bc}_{\text{mix}}$) [91, 92].

By being inclusive, the asymmetries of this prescription are potentially open to new sources of BSM CP-violation that are missed by exclusive measurements such as those measured by LHCb in Eqs. 4.8 and 4.9.

The ATLAS collaboration published the results of a measurement following this prescription in 2017 (the predecessor to the measurement described in this thesis) [93]. Constraints are placed on each of the inclusive asymmetries by considering it to be the sole source of CP-violation (i.e. each asymmetry is derived with all others set to zero).

The results of this measurement are shown in Table 4.1, along with comparisons to previous experimental limits, the Standard Model prediction, and the required asymmetry to explain the D∅ anomalous like-sign dimuon asymmetry solely as a consequence of direct CP-violation.

While the indirect CP-violation asymmetry A^{b}_{mix} is not competitive with existing limits, the constrained values for $A^{b\ell}_{\text{dir}}$ and $A^{c\ell}_{\text{dir}}$ are improvements over existing limits. The constrained value of A^{bc}_{dir} is the first limit of its kind. Within the uncertainties, all asymmetries are compatible with the Standard Model predictions. The direct CP-violation asymmetries are also at a level that is compatible with the hypothesis that the anomalous like-sign dimuon asymmetry can be explained as a consequence of BSM direct CP-violation. Reducing the uncertainties on the measurement should therefore lead to a result that can either confirm or refute this hypothesis. Such a reduction of uncertainties is an aim of the updated measurement described in this thesis. The statistical uncertainties are expected to be significantly reduced due to the larger $139\,\text{fb}^{-1}$ dataset, and a reduction in the systematic uncertainties is a key motivator for re-examining the strategy for performing the ST/DT-assignment as detailed in Chapter 10. In addition to the reduction in uncertainties, the $139\,\text{fb}^{-1}$ dataset opens up the prospect of extending the measurement by incorporating time-dependent asymmetries, as explored in Chapter 12.

4.7 Baryogenesis and Implications for CP-Violation

Matter and antimatter coming into contact will annihilate to produce high-energy photon radiation. Therefore, the existence of antimatter-dominated regions in the current universe can be ruled out, as any such regions would produce a large amount of observable photon radiation at the boundary with matter-dominated regions (the homogeneity of the CMB excludes them from being sufficiently far apart to avoid leaving an observable signature) [2]. Furthermore, observations of the CMB and the abundances of light elements in the intergalactic medium can be used to quantify the baryon-photon ratio, giving

$$\eta_{B/\gamma} = \frac{N_B - N_{\bar{B}}}{N_\gamma} \approx \frac{N_B - N_{\bar{B}}}{N_B + N_{\bar{B}}} \approx 10^{-10}, \tag{4.15}$$

A	Measured, A	Existing Limit, $\|A\|$	SM Pred., $\|A\|$	Compatibility with D∅, $\|A\|$
$A^{b\ell}_{\text{dir}}$	0.5 ± 0.5	< 1.2 [87]	$< 10^{-5}$ [87, 90]	≥ 0.3
$A^{c\ell}_{\text{dir}}$	1.0 ± 1.0	< 6.0 [87]	$< 10^{-9}$ [87, 90]	≥ 1.0
A^{bc}_{dir}	-1.0 ± 1.1	-	$< 10^{-7}$ [94]	-
A^{b}_{mix}	-2.5 ± 2.8	< 0.1 [95]	$< 10^{-3}$ [95–97]	-

Table 4.1 A summary of the results of the ATLAS measurement of inclusive CP-violation asymmetries in semileptonic b-hadron decays [93]. All asymmetry numbers are $\times 10^{-2}$. Also included for comparison are existing experimental limits on the magnitude of the asymmetry prior to the ATLAS measurement (at the 2σ level), Standard Model predictions for the magnitude of the asymmetry, and the asymmetry required to explain the D∅ anomalous like-sign dimuon asymmetry solely as a consequence of direct CP-violation.

where N_B and $N_{\bar{B}}$ are the number of baryons and antibaryons present in the early universe, and N_γ is the number of photons arising from their annihilation [98, 99]. This result implies that there were $10^{10} + 1$ baryons in the early universe for every 10^{10} antibaryons.

It can be seen that there is an observable matter-antimatter asymmetry, with the current universe dominated by matter. An explanation is required for why this is the case.

One such explanation is that such an asymmetry may have simply been an initial condition of the universe. However, it is widely considered that there was an inflationary epoch in the very early universe (from $\sim 10^{-36}$ s to $\sim 10^{-32}$ s after the Big Bang singularity) [100–102]. Such an inflationary epoch would disperse any initial asymmetry by an exponential amount, so an observed post-inflation baryon-photon ratio of 10^{-10} as per Eq. 4.15 would require a pre-inflation asymmetry many, many orders of magnitude higher, at a level thought to be unfeasible.

Without an initial imbalance, the current asymmetry must have been generated through a post-inflation mechanism, which is given the name of baryogenesis. Baryogenesis was shown by Sakharov to be reliant on a set of three necessary conditions [103]. These conditions, named after him, are known as the Sakharov conditions:

1. Baryon number violation.

2. C-violation and CP-violation.

3. Departure from thermal equilibrium.

CP-violation can thus be seen to be a necessary ingredient in explaining the observed matter-antimatter asymmetry. However, predicted levels of CP-violation within Standard Model processes are not enough to produce an asymmetry in agreement with Eq. 4.15, suggesting that additional sources of CP-violation must exist, beyond the scope of those found in Standard Model interactions in the quark sector.

4.8 The Way Forward

Since the discovery of CP-violation in 1964, the phenomenon has been extensively probed experimentally. However, it remains a subject that requires further experimental investigation in order to resolve the tension between results reported from different sources. On the one hand, results from tests of the unitarity of the CKM-matrix (see Section 4.4) and results from the B-factories and LHCb (see Section 4.6) suggest that levels of observed CP-violation are consistent with the small values predicted by the Standard Model. On the other hand, the anomalous like-sign dimuon asymmetry observed by the $D\varnothing$ collaboration (see Section 4.6) and the cosmological baryon-photon ratio (see Section 4.7) suggest that additional BSM sources of CP-violation must exist.

One option for additional sources of CP-violation would be confirmation of previously undiscovered CP-violating processes in sectors of the Standard Model other than neutral mesons. Such processes have been theorised to occur in the neutrino sector, and results from the latest generation of neutrino experiments indicate early evidence of CP-violation, although this is below the level of statistical significance required to confirm a discovery [104]. In principle, CP-violation could also occur in strong interaction processes, but a lack of any observable electric dipole moment of the neutron strongly suggests that this is not the case [105]. An explanation of why the parameters of QCD appear to be so delicately fine-tuned to preserve CP-symmetry is considered an open theoretical question.

Another option for additional sources of CP-violation would be contributions to neutral meson processes from BSM physics such as a BSM source of additional direct CP-violation, as discussed in Section 4.6. Building on a previous measurement of CP-violation asymmetries in b-hadrons while employing new techniques and attempting to increase the precision, the measurement described in this thesis aims to elucidate whether any such BSM contribution is present, by determining whether the level of direct CP-violation is in agreement or in conflict with Standard Model predictions.

Chapter 5

Experimental Setup

The data used for the work in this thesis was collected using state-of-the-art particle physics machinery, which this chapter is dedicated to explaining. Section 5.1 introduces the CERN accelerator complex and the LHC, while Section 5.2 introduces the ATLAS experiment and its various subsystems.

5.1 The LHC

Since commencement of operations in 2008, the LHC has been the flagship particle collider of the international research organisation CERN, and is the largest machine of its kind ever built [106]. Located in the vicinity of Geneva, Switzerland on the Swiss-French border, the LHC accelerates and collides high-energy beams of protons inside an underground tunnel with a circumference of 27 km. These proton-proton collisions produce copious amounts of fundamental particles, providing large quantities of experimental data that can be used to confirm or refute theoretical descriptions of the behaviour of such particles. A full schematic diagram of the CERN accelerator complex, of which the LHC is a part, is shown in Fig. 5.1.

The initial source for the collider's protons is a bottle of hydrogen gas. For Run 1 and Run 2 of the LHC (2008-2018), the hydrogen gas was passed through an electric field in order to ionise it and separate the protons from the electrons, and these protons are accelerated

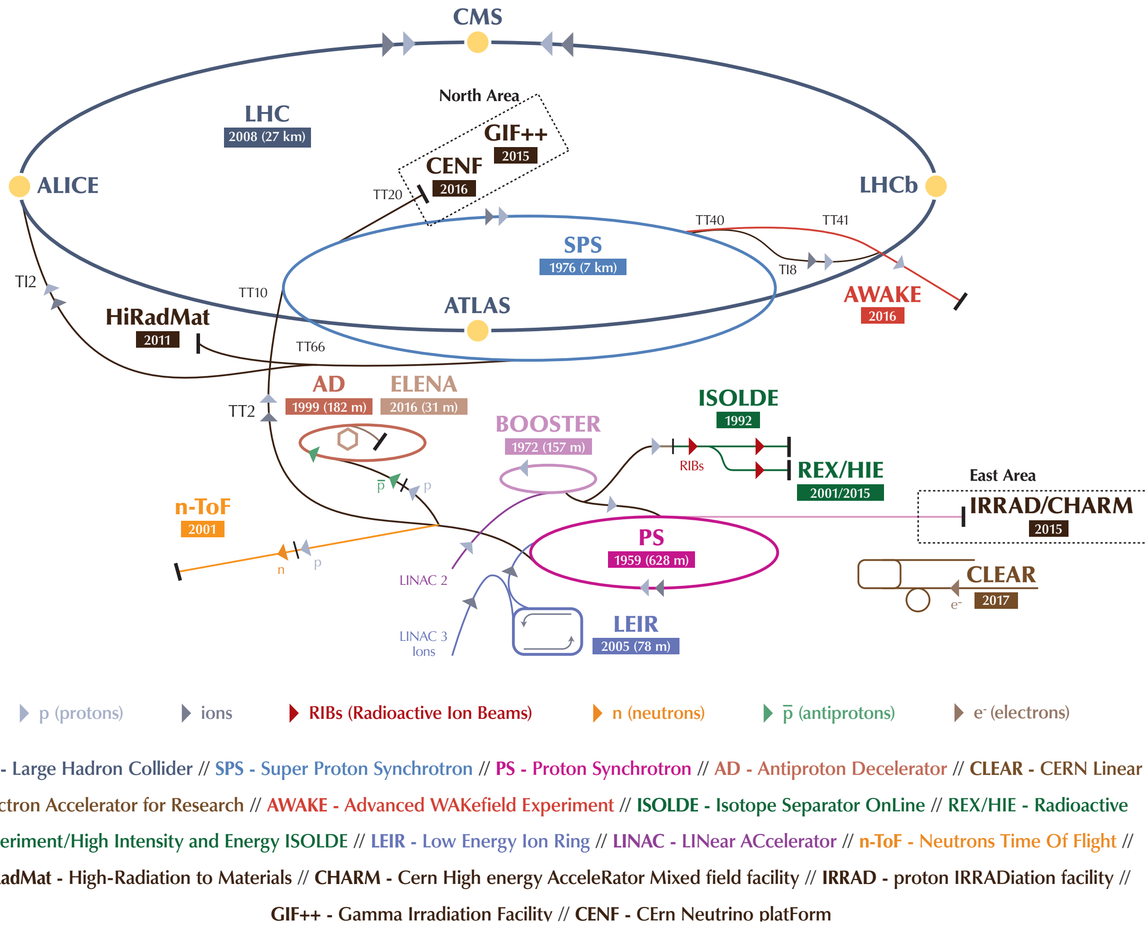

LHC - Large Hadron Collider // **SPS** - Super Proton Synchrotron // **PS** - Proton Synchrotron // **AD** - Antiproton Decelerator // **CLEAR** - CERN Linear Electron Accelerator for Research // **AWAKE** - Advanced WAKefield Experiment // **ISOLDE** - Isotope Separator OnLine // **REX/HIE** - Radioactive EXperiment/High Intensity and Energy ISOLDE // **LEIR** - Low Energy Ion Ring // **LINAC** - LINear ACcelerator // **n-ToF** - Neutrons Time Of Flight // **HiRadMat** - High-Radiation to Materials // **CHARM** - Cern High energy AcceleRator Mixed field facility // **IRRAD** - proton IRRADiation facility // **GIF++** - Gamma Irradiation Facility // **CENF** - CErn Neutrino platForm

Figure 5.1 A schematic diagram of the CERN accelerator complex, which includes the LHC and its various pre-accelerators and detector experiments. The year that operations commenced and the diameters of accelerator rings are also shown where applicable [107].

through Linear Accelerator 2 (LINAC2) to obtain a proton beam [108]. From Run 3 onwards (beginning in 2022), a new, more efficient system will be utilised, which first provides a source of negatively charged hydrogen ions (hydrogen atoms with an additional electron). After being passed through Linear Accelerator 4 (LINAC4), the additional electrons are stripped away to leave a proton beam [109].

The proton beam is made up of many bunches, each containing approximately 10^{11} protons and separated by 25 ns [110]. After the initial pass through LINAC2 or LINAC4, the proton beam is passed through a series of further pre-accelerators, beginning with the Proton Synchrotron Booster (PSB). From the PSB, they pass to the Proton Synchrotron (PS), then from the PS to the Super Proton Synchrotron (SPS), and finally from the SPS to the main LHC ring [111].

Within the LHC ring, proton beams are bent around the circular tunnel in opposite directions inside two parallel beam-pipes, steered and accelerated by 9593 superconducting magnets [110]. When each beam reaches its maximum energy of 6.5 TeV (giving a total centre-of-mass energy, labelled $\sqrt{s}$, of $\sqrt{s} = 13\,\text{TeV}$), they perform 11,245 turns of the LHC per second, travelling at 99.9999991% of the speed of light [110].

The beams are steered together at four locations known as Interaction Point (IP)s around the LHC ring, where bunches of protons from each of the beams collide, producing up to one billion collisions per second [110]. These four IPs are where the eight detector experiments of the LHC are located [112]. IP1 is home to ATLAS, Large Hadron Collider forward (LHCf), and Forward Search Experiment (FASER) [113–115]. A Large Ion Collider Experiment (ALICE) is situated at IP2 [116]. CMS and Total, Elastic, and Diffractive Cross-Section Measurement (TOTEM) are situated at IP5 [117, 118]. Last but not least is IP8, the location of LHCb and Monopole and Exotics Detector at the LHC (MoEDAL) [119, 120]. The ATLAS and CMS experiments are multi-purpose and designed to investigate a broad physics programme. LHCb concentrates on measurements of phenomena in b-quark processes. FASER, LHCf, and TOTEM are designed to measure proton collisions that occur at small angles, known as forward-physics, in order respectively to search for low-mass weakly interacting particles, to simulate cosmic rays under laboratory conditions, and to make precise determinations of proton properties.

The ALICE detector is used to measure heavy-ion collisions (a smaller physics programme run alongside the main programme of proton-proton collisions), while MoEDAL is used to search for the production of magnetic monopoles across both proton-proton and heavy-ion collisions.

The amount of collisions recorded at particle physics experiments, such as those described above, is measured in terms of a quantity called luminosity. The particle flux per unit area and unit time is called the instantaneous luminosity (with dimensions of inverse area × inverse time). For the head-on collision of two identical Gaussian beams, an expression can be derived for the instantaneous luminosity, $\mathcal{L}$, in terms of the beam parameters, giving

$$\mathcal{L} = \frac{N_p^2 f N_b}{4\pi \Sigma_x \Sigma_y}, \tag{5.1}$$

where N_p is the number of particles per bunch, f is the revolution frequency, N_b is the number of bunches per beam, and Σ_x and Σ_y are the beam widths in the x and y directions respectively [121]. According to this formula, the LHC is capable of delivering an instantaneous luminosity of $\sim 10^{34}\,\mathrm{cm}^{-2}\mathrm{s}^{-1}$, and the maximum instantaneous luminosity recorded during Run 2 was $2.1 \times 10^{34}\,\mathrm{cm}^{-2}\mathrm{s}^{-1}$ [122, 123].

A measure of how many collisions occurred over a period of time is given by the integrated luminosity, which can be related to the total number of collisions, N, by

$$N = \sigma \int \mathcal{L}\, dt, \tag{5.2}$$

where σ is the total cross section, which is a measure of the probability that a process will occur, with dimensions of area [124].

The integrated luminosity delivered to the ATLAS experiment for each year of data-taking in Run 1 and Run 2 is shown in Fig. 5.2, while the total integrated luminosity at ATLAS during

Run 2 is shown in Fig. 5.3. By the end of Run 2, 139 fb^{-1} of collisions were recorded and deemed to be good for physics analysis (expressed in units of barns, with $1\,\text{b} = 10^{-28}\,\text{m}^2$) [123].

5.2 The ATLAS Experiment

The ATLAS experiment is a general purpose particle detector, and the most voluminous particle detector ever constructed. The detector apparatus is cylindrical and is 44 m long with a diameter of 25 m [127]. It sits 100 m below ground at IP1, and weighs 7,000 tonnes.

The detector comprises several components, each dedicated to a different aspect of reconstructing particle collision events, as well as a system of solenoidal and toroidal magnets. A full schematic diagram of the detector is shown in Fig. 5.4.

5.2.1 Magnet System

A charged particle passing through the magnetic field created by the detector's magnet system will experience a Lorentz force,

$$\mathbf{F} = q\mathbf{v} \times \mathbf{B}, \tag{5.3}$$

where q is the particle's electric charge, $\mathbf{v}$ is the particle's velocity, and $\mathbf{B}$ is the magnetic field. Consequently, the particle's trajectory will bend. Measuring the direction of curvature allows the particle's charge to be inferred, while measuring the degree of curvature allows the particle's velocity, and thus momentum, to be inferred.

The ATLAS magnet system consists of four separate arrays of superconducting magnets [129]. A central solenoid surrounds the Inner Detector, providing a 2 T magnetic field [130]. The rest of the detector is surrounded by toroid magnets, with one central barrel toroid and two smaller

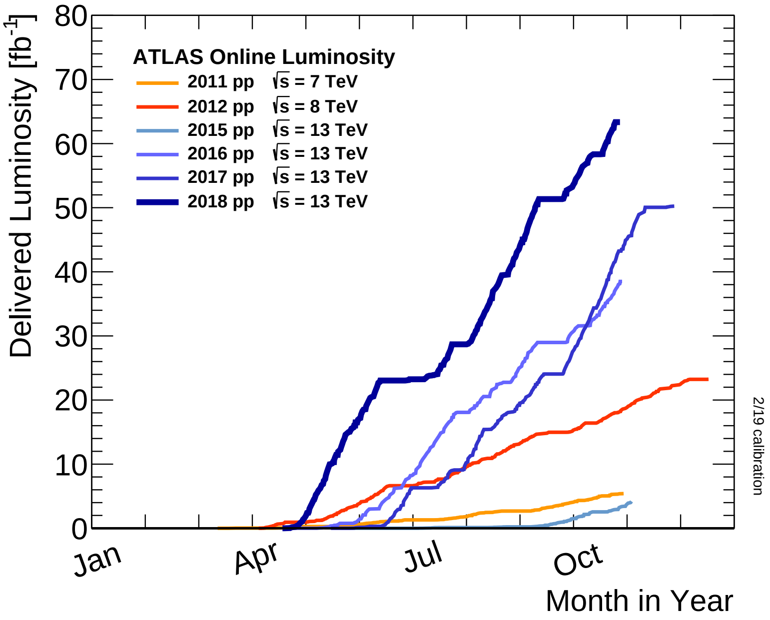

Figure 5.2 The integrated luminosity delivered to the ATLAS experiment for each year of data-taking in Run 1 and Run 2 of the LHC [125].

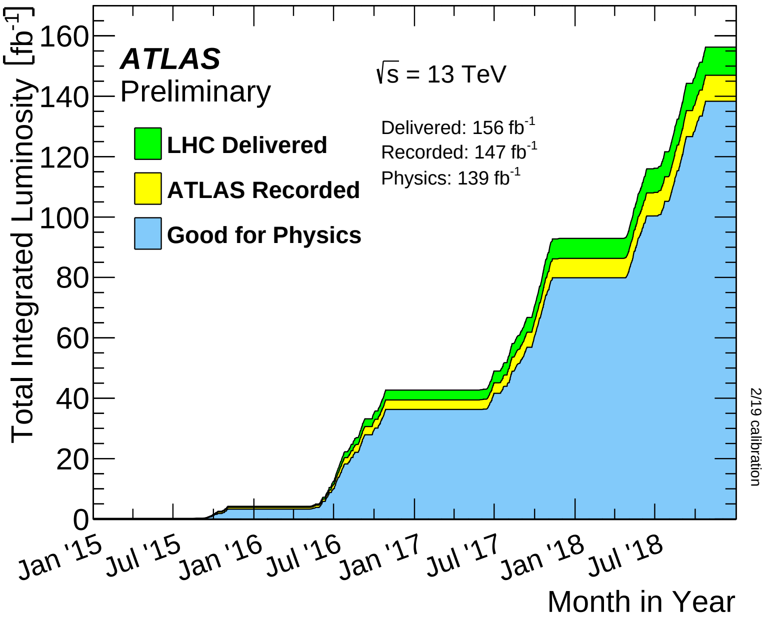

Figure 5.3 The integrated luminosity delivered to the ATLAS experiment by the LHC (green), recorded by ATLAS (yellow), and deemed to be good for physics analysis (blue), during Run 2 of the LHC [126].

end-cap toroids [131, 132]. These provide a non-uniform magnetic field of between 2 T and 8 T. A diagram of the magnet system is shown in Fig. 5.5.

5.2.2 Inner Detector

The Inner Detector, as shown in Fig. 5.6, is the component of the detector closest to the beamline and collision point [133]. It has three subsystems, which are (from innermost to outermost) the Pixel Detector, Semiconductor Tracker (SCT), and Transition Radiation Tracker (TRT).

The Pixel Detector is made up of 92 million silicon pixels in four layers immediately around the beamline. Particles passing through leave behind energy deposits in these pixels, which are denoted as hits and measured with a location precision of 10 µm. These hits are then used to reconstruct the track of the particle.

The SCT is designed similarly to the Pixel Detector but on a larger scale. It makes use of four layers of silicon micro-strip sensors, allowing particle tracks to be measured with a precision of 25 µm.

The TRT sits outside the Pixel Detector and SCT, and makes use of 300,000 drift tubes. These tubes are 4 mm in diameter and contain a gold-plated tungsten wire surrounded by a gas mixture (predominantly Xenon gas). Charged particles passing through the tube will ionise the gas and in turn produce a current in the wire, which allows for particle tracks to be measured with a precision of 170 µm. Combining measurements from multiple tubes improves this to a precision of 50 µm. Between the drift tubes, materials of varying dielectric constants are used to detect photons produced as transition radiation, allowing electrons to be identified and distinguished from other charged particles such as pions.

5.2.3 Calorimeters

After passing through the Inner Detector and the solenoid magnet, particles reach the ATLAS detector's calorimeter systems. These are designed to absorb particles, measuring the energy

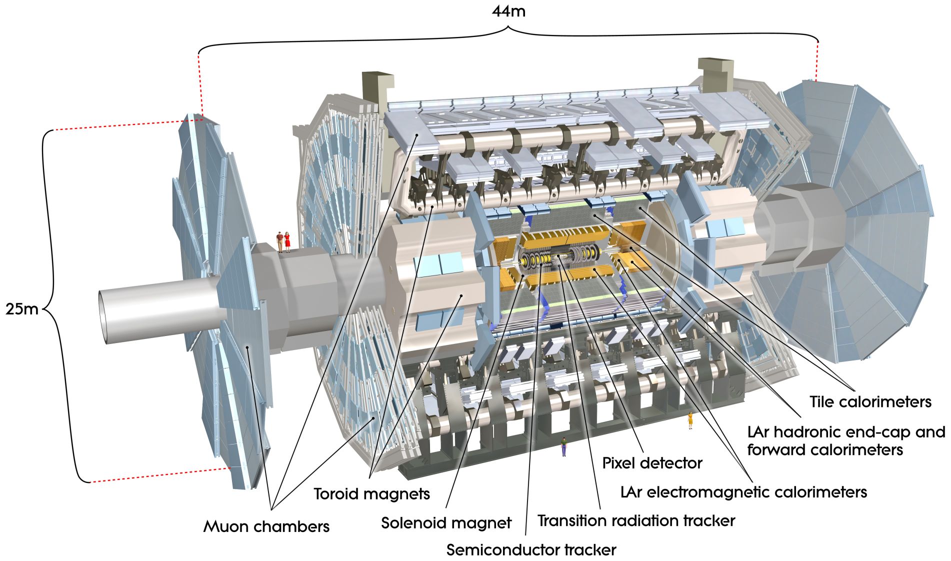

Figure 5.4 A schematic diagram of the ATLAS detector, with the different detector components and the magnet system labelled [128].

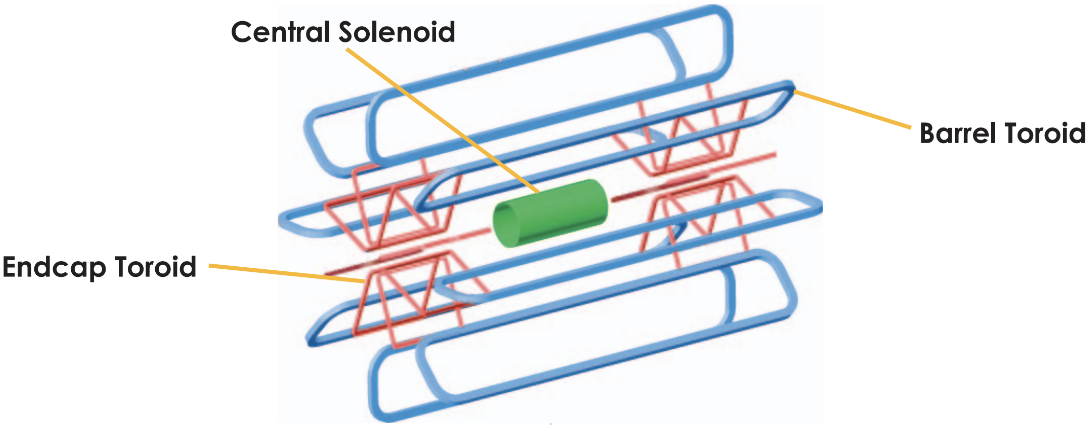

Figure 5.5 The geometry of the ATLAS magnet system, which comprises the central solenoid, barrel toroid, and two end-cap toroids [127].

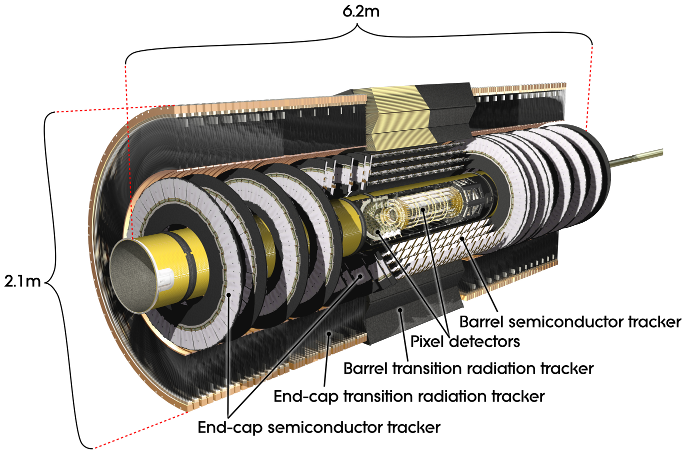

(a)

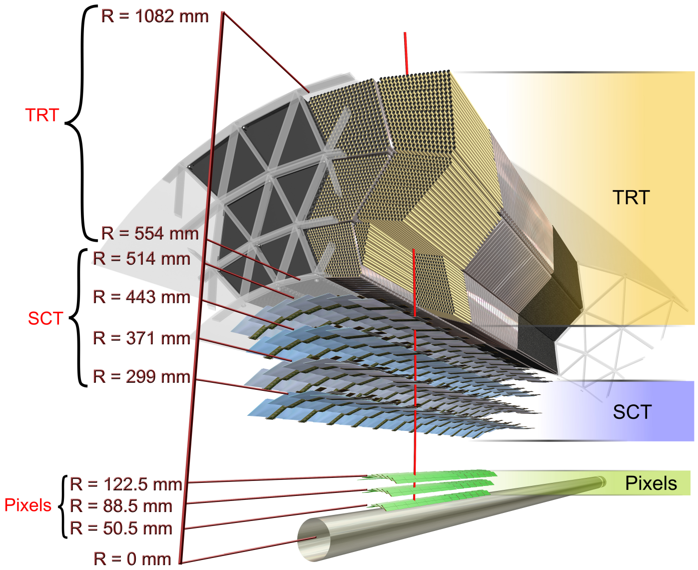

(b)

Figure 5.6 A view of the ATLAS Inner Detector, showing: **(a)** a side-on view; **(b)** a cross-sectional view [134].

that is deposited. They are therefore made up of alternating layers of an absorbing high-density metal and an active material which measures the energy.

ATLAS has multiple calorimeter systems, as shown in Fig. 5.7. The Electromagnetic Calorimeters are designed to measure particles which interact electromagnetically, such as electrons and photon. The Hadronic Calorimeters are designed to measure particles which interact via the strong force, namely hadrons. An additional Forward Calorimeter is used to provide coverage of the forward region of the detector.

The barrel and end-cap Electromagnetic Calorimeters make use of layers of lead as the absorber, and liquid Argon (LAr) as the active material [135]. When a particle is absorbed, a shower of lower-energy particles is produced, which ionises the LAr and produces a measurable current that can be used to determine the energy of the original particle.

The end-cap Hadronic Calorimeters operate in a similar way to the Electromagnetic Calorimeters, using layers of copper alongside LAr. However, the barrel Hadronic Calorimeter uses steel as an absorber and active layers that are made up of plastic scintillating tiles [136]. A particle shower passing through this scintillating material produces photons within the material, which are converted into an electric current.

The Forward Calorimeter is used to measure the particles produced at the smallest angle from the original proton beam. It is a LAr calorimeter, operating on the same principle as the LAr calorimeters described above, but making use of copper and tungsten tubes as an absorbing material instead of sheets of metal.

5.2.4 Muon Spectrometer

The calorimeter systems described above are sufficient to absorb the majority of particles produced in collision events. However, this is not the case for muons. They have a much higher mass than electrons, which makes them much less likely to deposit energy in the Electromagnetic Calorimeter, as the bremsstrahlung process that dominates electron energy-loss is heavily suppressed for higher masses. Unlike taus, which are heavier still, muons are also

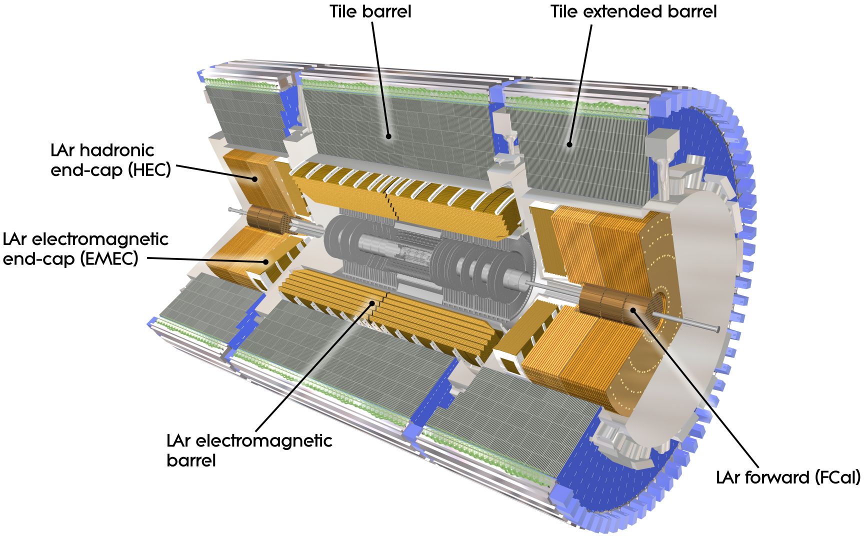

Figure 5.7 The arrangement of the ATLAS Electromagnetic, Hadronic, and Forward Calorimeter systems [137].

relatively stable and are likely to pass through the Inner Detector and calorimeter systems before decaying to lighter particles, while taus will only travel short distances before decaying.

The outermost system of the ATLAS detector is the Muon Spectrometer, which is dedicated to tracking muons after they pass out of the calorimeters [138]. It extends outwards from a radius of 4.25 m from the beamline to a radius of 11 m and thus makes up a majority of the detector by volume.

The Muon Spectrometer comprises 4,000 individual muon chambers, which can be subdivided into four types of chamber: Monitored Drift Tube (MDT), Cathode Strip Chamber (CSC), Thin Gap Chamber (TGC), and Resistive Plate Chamber (RPC). Fig. 5.8 highlights the location of these components of the Muon Spectrometer within the ATLAS detector.

MDTs operate on a similar principle to the TRT of the Inner Detector, using tubes containing a tungsten wire surrounded by gas in order to make precise measurements of muon momentum.

CSCs are an example of a multi-wire proportional chamber, using arrays of cathodes to detect ionisation. The arrays of cathodes are segmented in a particular pattern in order to allow precise coordinate determination and construct the track of passing muons.

The final two types of chamber, TGCs and RPCs, operate on a similar ionisation principle, but sacrifice precision in favour of fast read-out speeds. This is essential for triggering on muons (see Section 5.2.5), and TGCs and RPCs are therefore used for this purpose, in the end-cap and barrel region respectively. In addition, they are used to supplement the precision measurements made by the MDTs and CSCs.

5.2.5 Trigger and Data Acquisition

Collectively, the detector subsystems described in Sections 5.2.2 to 5.2.4 provide up to 100 million signal channels to be read out for each particle physics collision event, and the peak rate of such events during an LHC run is 40 MHz. Capturing and recording all this data would be unfeasible, requiring a data bandwidth of approximately 60 TB/s. To solve this, ATLAS employs a trigger system, which works in conjunction with the Data Acquisition System (DAQ) to make quick decisions on which events contain signatures of interesting physics that should be retained for further study, and which events are likely to be well-understood processes such as elastic proton collisions that can therefore be discarded. A diagram of the full trigger and data acquisition system is shown in Fig. 5.9

The first component of the trigger system is the Level 1 (L1) trigger, which utilises custom-built hardware to make rapid decisions in under 2.5 µs [140]. The L1 hardware algorithms use the lower-precision signals from the calorimeters and the Muon Spectrometer to identify likely candidates for interesting physics objects such as electrons, muons, and jets, as well as where in the detector such an object was registered, which is deemed a region-of-interest (RoI).

The RoIs are passed from the L1 trigger to the High Level Trigger (HLT), a software-based system which runs on a high-performance computing cluster [141]. This reconstructs RoIs using precise information from all detector components, providing a final decision on events in a time of 200 µs.

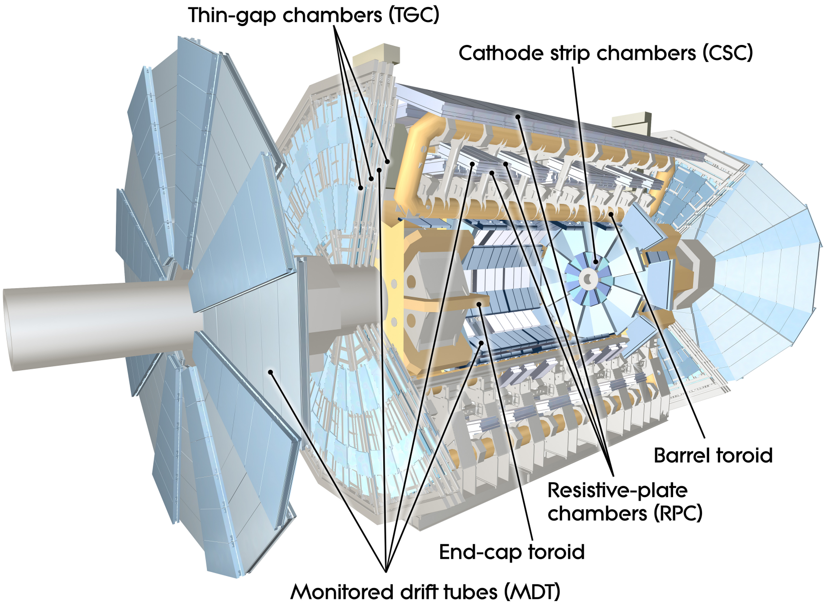

Figure 5.8 A diagram of the ATLAS detector, highlighting the components that collectively make up the Muon Spectrometer system [139].

There are many possible combinations of individual L1 and HLT triggers that can result in an overall decision to keep or discard an event. Such combinations are referred to as trigger chains. The management of trigger chains, settings for HLT algorithms, and all other information required for the successful operation of the trigger system is facilitated by a trigger configuration database, which is used as part of a software system to dynamically control the setup of the trigger system throughout a data-taking run [142].

In the time it takes for the L1 and HLT decisions to be made, the DAQ manages whether data needs to be buffered, discarded, or saved to permanent storage. The event rate is reduced from the initial value of 40 MHz to approximately 100 kHz after the L1 decision, and to a final rate of approximately 1.5 kHz after the HLT decision. This corresponds to a data bandwidth reduction from an initial value of 60 TB/s to approximately 160 GB/s after the L1 decision, and to a final rate of approximately 1.5 GB/s after the HLT decision. This reduction by several orders-of-magnitude results in a feasible volume of data to be saved to permanent storage, although this still provides a logistical challenge, with more than 10 PB of data from the ATLAS experiment being saved to permanent storage every year.

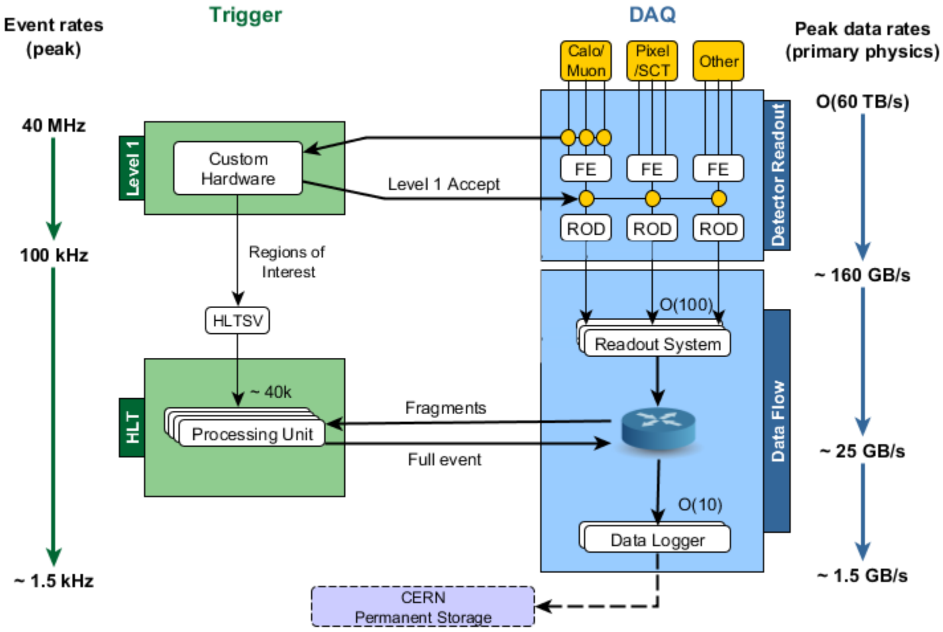

Figure 5.9 A diagram of the ATLAS trigger and data acquisition system, showing how the L1, HLT, and DAQ systems interact, and how the event rate and data bandwidth are reduced at each step of the triggering process [143]. The system components include the frontend (FE) system, readout driver (ROD), and the HLT supervisor (HLTSV).

Chapter 6

Simulation and Object Reconstruction

In order to test theoretical frameworks such as the Standard Model, the data collected by the ATLAS experiment is compared with the results of simulations performed according to such a theory. This chapter begins with Section 6.1, an introduction to how these simulations are performed. Section 6.2 then describes the object reconstruction procedures that are used to turn signals (or simulated signals) from the ATLAS experiment into physics objects such as reconstructed leptons and jets.

6.1 Monte Carlo Simulations

Theories such as the Standard Model are QFTs, and thus inherently probabilistic. These simulations are performed using Monte Carlo (MC) methods, which use pseudorandom sampling to model this probabilistic behaviour [144].

MC event generators are used to model the different stages of a particle physics event. The first stage is to model the hard collision of protons, where the fraction of the proton momentum transferred to a constituent quark or gluon, collectively referred to as a parton, is modelled using a parton distribution function (PDF) [145, 146]. Matrix element calculations, to fixed-order in perturbation theory, are then used to simulate the hard interaction between initial-state partons and to determine the final-state particles that these interactions produce. Above an energy scale of approximately 1 GeV, the initial-state radiation (ISR) and final-state radiation (FSR) of gluons is modelled according to the Dokshitzer-Gribov-Lipatov-Altarelli-Parisi equations [147–149]. Below this energy scale, hadronisation is modelled using non-perturbative calculations according to either a string or a cluster model [150, 151]. The result of each parton collision receives corrections to account for the effect of additional interactions from the original proton collision and the effect of other nearby proton-proton collisions within the beam, known as pileup.

The resulting objects of such simulations before the modelling of hadronisation is a collection of free quarks, gluons, and leptons, and is referred to as the parton-level truth of the simulation. The resulting objects after the modelling of hadronisation is a collection of stable hadrons and leptons, and is referred to as the particle-level truth of the simulation.

The final step of the simulation process is to model how the particle-level objects are expected to interact with the detector. A piece of software called GEANT4 is used to provide a detailed simulation of the ATLAS detector and account for measurement resolutions, detector geometry, and defects and malfunctions that may affect how components operate [152–154]. This level of simulation also applies the same object reconstruction algorithms described in Section 6.2.

The collection of objects obtained after the modelling of the detector is referred to as the reconstruction-level or reco-level of the simulation, and is directly comparable with data obtained from the ATLAS experiment.

6.2 Object Reconstruction

The raw electronic (or simulated) signals collected by the different detector components provide details of the tracks and energy deposits left by particles passing through the ATLAS detector. This information is then used to reconstruct physics objects, such as leptons and jets, which can be used for analysis.

6.2.1 Physical Quantities

Before introducing the different physics objects that are reconstructed, it is necessary to introduce the physical quantities that are assigned based on the spatial and energy information recorded by the detector.

The geometry of the ATLAS detector can be parametrised by a system of Euclidean coordinates, x, y, and z, with the origin at the interaction point in the centre of the detector. The positive z-direction is defined to be along the beamline in the anticlockwise direction. The positive x-direction is defined to be towards the centre of the LHC ring, and the positive y-direction is defined to be upwards towards the Earth's surface.

The geometry of the ATLAS detector can also be parametrised by an angular coordinate system, where r and ϕ represent the radial distance and azimuthal angle from the beamline in the transverse plane (perpendicular to the beamline), with the $\phi = 0$ direction defined similarly to the x-direction and $-\pi < \phi \leq \pi$. The third coordinate is the polar angle θ, with the $\theta = 0$ direction defined similarly to the positive z-direction and $0 < \theta \leq \pi$. However, θ is not a Lorentz-invariant quantity under boosts along the z-direction, making it unsuitable for description of relativistic particles. Instead, the pseudorapidity, η, is used, defined as $\eta = -\ln\tan\frac{\theta}{2}$, as differences in pseudorapidity, $\Delta\eta$, are Lorentz-invariant.

The plane in which an object's track has been recorded is then parametrised by the spatial coordinates η and ϕ. Angular separation between two objects is measured as $\Delta R = \sqrt{(\Delta\eta)^2 + (\Delta\phi)^2}$, where $\Delta\eta$ and $\Delta\phi$ are respectively the difference in η and ϕ between the two particles. Impact parameters d_0 and $z_0 \sin\theta$ are also defined, which are the distances from the point of a track's closest approach to the origin in the $x - y$ and $r - z$ planes respectively.

The energy and momentum of objects is inferred from the curvature of tracks due to the Lorentz force as described by Eq. 5.3. The total momentum vector, $\mathbf{p}$, can be broken down into its Cartesian scalar components, p_x, p_y, and p_z, but more commonly, the physical scalar quantities used are the transverse momentum (the component of the momentum in the plane perpendicular to the beamline), p_{T}, the energy, E, and the invariant mass, m, defined as

$m = E^2 - \mathbf{p}^2$. In addition to the energy and momentum, the electric charge, q, can also be inferred from the direction of curvature of a track.

A summary of the physical quantities assigned to reconstructed physics objects is given in Table 6.1.

6.2.2 Electron Reconstruction

Electrons are expected to leave a track in the Inner Detector and an energy deposit in the Electromagnetic Calorimeter.

Due to the processes of bremsstrahlung and pair-production by which an electron forms a shower of electrons and photons, a cluster of individual tracks and energy deposits is observed in practice. Electron reconstruction proceeds in three stage: seed-cluster reconstruction, track reconstruction, and electron-candidate reconstruction [155]. In the first stage, the Electromagnetic Calorimeter is divided into 200×256 towers in $\eta \times \phi$ space, and a sliding-window algorithm of 3×5 towers is used to search for localised energy deposits of greater than 2.5 GeV, called seed-clusters. For overlapping clusters, only the highest energy cluster is retained. In the second stage, Inner Detector tracks are formed from hits (individual signals) in the Pixel Detector and SCT. These are then extended to match the signals from the TRT, and criteria are applied to remove ambiguous tracks. In the third stage, the seed-clusters are algorithmically matched to these reconstructed tracks, and the cluster size-window is increased to fully account for all the energy deposited by the original electron.

Reconstructed electrons are categorised according to two sets of criteria, the first of which is a likelihood-based identification to distinguish real electrons from so-called fakes, where light hadrons such as charged pions mimic the electron signature and pass the electron reconstruction requirements [155, 156]. The likelihood-based identification provides three working points: loose, medium, and tight. The loose working point provides the best electron efficiency (meaning the highest proportion of real electrons is reconstructed), but at the cost of the worst levels of fake

Physical Quantity	Definition
$x/y/z$	Cartesian coordinates
r	Radial distance from beamline
ϕ	Azimuthal angle
θ	Polar angle ($\Delta\theta$ non-Lorentz-invariant)
η	Pseudorapidity ($\Delta\eta$ Lorentz-invariant)
$\Delta R(A, B)$	Angular separation between particles A, B
d_0	Impact parameter in $x - y$ plane
$z_0 \sin\theta$	Impact parameter in $r - z$ plane
$\mathbf{p}$	Momentum vector
$p_x/p_y/p_z$	Cartesian components of momentum
p_{T}	Transverse momentum
E	Energy
q	Electric charge

Table 6.1 A summary of the physical quantities assigned to reconstructed physics objects.

rejection. Conversely, the tight working point provides high levels of fake rejection, but at a cost of the lowest electron efficiency. The medium working point balances the two.

The second is an isolation requirement to distinguish prompt electrons (coming from the initial hard interaction) from electrons arising from other sources, such as semileptonic decays or photon conversion within hadronic jets [156]. This can be done by requiring electron signatures to be well-separated from other nearby signatures, using either track-based or calorimeter information. A variety of working points are defined, based on how strict the isolation is required to be.

6.2.3 Muon Reconstruction

As muons pass through the detector, they will leave a track in the Inner Detector, little to no signature in the calorimeters, and a track in the chambers of the Muon Spectrometer.

Muon reconstruction proceeds by performing track reconstruction separately in both the Inner Detector and Muon Spectrometer, and then combining the resultant tracks [157]. Track reconstruction in the Inner Detector proceeds as described for electrons in Section 6.2.2. In the Muon Spectrometer, track segments in individual muon chambers are identified with a computer vision technique known as a Hough transform [158], and a fit method is used to combine identified track segments into tracks. Inner Detector and Muon Spectrometer tracks can be combined by performing a combined track fit, using an inside-out or segment tagging algorithm that extrapolates the Inner Detector track and attempts to match it to Muon Spectrometer track segments, extrapolating a Muon Spectrometer track to a region not covered by the Inner Detector, or by matching an Inner Detector track to a muon-compatible calorimeter deposit.

As with electrons, reconstructed muons are categorised with identification criteria, to distinguish real prompt muons from non-prompt muons caused by hadron decays-in-flight or fake muons caused by punchthrough of jets to the Muon Spectrometer, with non-prompt muons being much more prevalent than fakes [157]. Loose, medium, and tight working points are defined to balance muon efficiency and non-prompt/fake rejection.

Isolation criteria are also used similarly to those for electrons to distinguish muons from nearby hadronic activity [157]. These make use of track-based, calorimeter-based, or combined information to search for tracks and/or energy deposits in conical regions of ΔR around the muon, which are used to define a variety of isolation working points.

6.2.4 Tau Reconstruction

Taus are not directly reconstructed, as their short lifetime means they will decay very rapidly, either to lighter leptons, which are reconstructed as described in Sections 6.2.2 and 6.2.3, or to hadrons, which are reconstructed as jets as described below in Section 6.2.6. A variety of techniques are then employed to distinguish jets originating from taus from jets originating from QCD processes [159].

6.2.5 Neutrino Reconstruction

Neutrinos only interact with other matter via the weak interaction, meaning that any neutrinos created during collisions in the ATLAS detector will pass out of the detector without leaving a detectable signature in any of the detector components. However, their presence can be inferred through the laws of conservation of energy and momentum. If all particles are absorbed by the detector, the sum of momentum in the transverse plane should be zero. Therefore, by summing the transverse momentum of all reconstructed objects and accounting for an additional soft radiation term, the total missing transverse momentum, $E_{\mathrm{T}}^{\mathrm{miss}}$, can be constructed, as well as the azimuthal angle ϕ of this missing momentum [160]. This can be taken to correspond to the total transverse momentum carried away by neutrinos that did not interact with the detector (assuming no contributions from BSM particles).

For events where the neutrino is expected to come from the decay of a W-boson, and the accompanying lepton has been reconstructed, an additional quantity is defined. This is the transverse mass of the W-boson, $m_{\mathrm{T}}(W)$, and is given by

$$m_{\mathrm{T}}(W) = \sqrt{2{p_{\mathrm{T}}}^{l} E_{\mathrm{T}}^{\mathrm{miss}}(1 - \cos \Delta\phi)}, \tag{6.1}$$

where ${p_{\mathrm{T}}}^{l}$ is the transverse momentum of the lepton, and $\Delta\phi$ is the difference in the azimuthal angle between the lepton and the missing transverse momentum.

6.2.6 Jet Reconstruction

As introduced in Section 2.2, quarks and gluons produced in proton-proton collisions do not propagate freely, but hadronise to form collimated jets of stable hadrons. The experimental signature left in the ATLAS detector by a jet is a large number of tracks in the Inner Detector, and a large number of energy deposits in the Electromagnetic Calorimeter and Hadronic Calorimeter.

Jet reconstruction begins by identifying topological cell clusters, which are three-dimensional regions of the calorimeters with a large energy deposit [161]. The anti-k_t algorithm is used to identify such clusters, building roughly conical clusters around the most significant energy deposits using a distance measure between particles based on an inverse power of k_t (with k_t equivalent to p_{T}) [162]. Recent developments have introduced particle flow algorithms, where the information from these topological clusters is combined with track information from the Inner Detector, and spatial information and the momentum inferred from the curvature of a track is used to identify tracks and topological clusters with individual particles produced in the hadronisation process [163]. By subtracting these tracks and topological clusters associated with hadronisation, the remaining tracks and topological clusters can be related to the hard interactions occurring before hadronisation. Previous to the introduction of particle flow jets, jets were reconstructed solely from the topological clusters. In comparison to this, particle flow jets provide increased precision for measurements of jet energy and angular quantities, especially for low-p_{T} jets.

Pileup interactions contribute a significant level of background interactions to jet reconstruction efforts. As well as the advantages described above, particle flow jets provide better suppression of pileup interactions compared to purely topological jets. Additional pileup suppression is provided by placing a requirement on the output of a multivariate algorithm called the jet vertex tagger (JVT), which makes use of track-based variables and profile likelihood fitting to identify pileup events [164].

In addition to reconstructing jets, it is important to be able to distinguish jets originating from a heavy-flavour hadron such as a b-quark or c-quark from those originating from light-flavour hadrons and gluons. This is achieved by a family of algorithms collectively known as flavour tagging algorithms, with the primary exemplar being b-tagging.

Low-level b-tagging algorithms exploit the fact that b-hadrons (see Section 3.2) have a relatively long lifetime, which means tracks originating from the b-hadron decay will point back to a secondary vertex, as opposed to the primary vertex to which tracks from the original hard interaction will point [165]. Two impact parameter b-tagging algorithms, `IP2D` and `IP3D`, look for tracks from secondary vertices, characterised by large values of the transverse and longitudinal impact parameters, d_0 and $z_0 \sin\theta$. The secondary vertex tagging algorithm `SV1` searches through potential two-track vertices in order to reconstruct a secondary vertex from a b-hadron decay. The `JetFitter` algorithm attempts to identify the vertices of the full b-hadron decay chain: the primary vertex from the original hard interaction, the secondary vertex from the b-hadron decay, and a tertiary vertex from the decay of a c-hadron that was produced at the secondary vertex.

High-level b-tagging algorithms combine the outputs of these low-level b-tagging algorithms with kinematic variables (jet p_{T} and η), and use these variables as the inputs to machine learning algorithms in order to make a final decision. The first of these is the `MV2c10` algorithm, which makes use of a boosted decision tree (BDT) [165]. This was improved upon with the introduction of the `DL1r` algorithm, which utilises a deep feed-forward neural network (NN), and additionally has a recurrent NN component which improves on the impact parameter based methods described above [166]. These high-level algorithms are calibrated to provide different working points, which balance the b-tagging efficiency with the levels of light-jet and c-jet rejection.

Chapter 7

Analysis Strategy

This chapter details the strategy by which the analysis is performed and measurements of CP-violation asymmetries are extracted. This builds on the theoretical prescription and prior ATLAS measurement, as previously described in Section 4.6 [90, 93]. The analysis makes use of the lepton+jets $t\bar{t}$ channel, as introduced in Section 3.1.3, plus a requirement that the event contains a soft muon, as introduced in Section 3.2. To identify events in this channel, selection requirements are placed on the physical quantities of reconstructed physics objects (Section 7.1). Additional selection requirements specify which objects must be present in an event (Section 7.2). The leading-order Feynman diagram for the events passing these selection requirements is shown in Fig. 7.1. The central idea of the analysis is that due to charge conservation, the charge of the soft muon can be used to infer the charge of the final hadronic particle that decayed to produce it. Similarly, the charge of the prompt lepton can be used to infer the flavour of the initial b-quark at the time of its production from the decay of the top quark. By measuring the charges of the soft muon and the prompt lepton, observable charge asymmetries are constructed, and this is detailed in Section 7.3. It is then possible to disentangle the contributions of the various mixing and decay processes that occur between the production of the original b-quark and the decay of the final hadronic particle, in order to derive CP-violation asymmetries. This is detailed in Section 7.4. These CP-violation asymmetries are of the form described in Section 4.5, and can be compared to other experimental limits and Standard Model predictions, such as the values previously presented in Table 4.1. The charge and CP-violation asymmetries are assessed both in Standard Model simulations and in data from the ATLAS experiment. The data samples for both simulation and experimental data are discussed in Section 7.5.

7.1 Object Selection

Physics objects are reconstructed according to the standard ATLAS procedures as described in Section 6.2. The object selection requirements follow the various recommendations of the ATLAS Combined Performance groups, and are designed to provide a good level of reconstruction

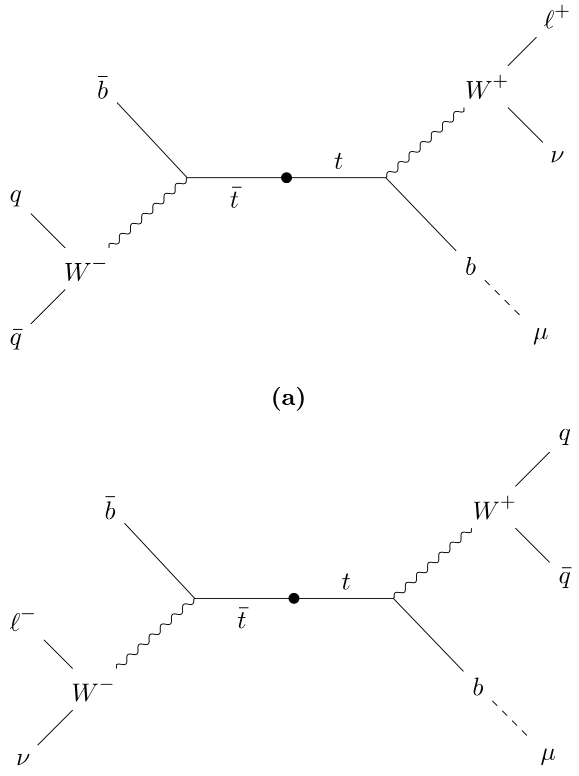

(a)

(b)

Figure 7.1 The Feynman diagram of the semileptonic $t\bar{t}$ events with a soft muon used in this analysis, for the case of: **(a)** a same-top event, with the prompt lepton and soft muon originating from the same side of the $t\bar{t}$ system; **(b)** a different-top event, with the prompt lepton and soft muon originating from different sides of the $t\bar{t}$ system.

efficiency balanced with a good level of rejection for fakes and objects from areas of the detector such as the calorimeter transition regions where there is poor detection coverage.

7.1.1 Jet Selection

Jet objects are reconstructed using the particle flow algorithm, as introduced in Section 6.2.6. Reconstructed objects are then required to have $p_{\mathrm{T}} > 25\,\mathrm{GeV}$ and $|\eta| < 2.5$. Quality criteria are applied to remove fake jets from sources such as detector noise, and a cut of JVT> 0.59 is used to suppress pileup for low-p_{T} ($p_{\mathrm{T}} < 60\,\mathrm{GeV}$), central ($|\eta| < 2.4$) jets [167]. An overlap removal procedure is applied to avoid erroneous double-counting of electrons as jets.

For flavour-tagging, as introduced in Section 6.2.6, a b-tagged status is assigned to jets passing the above selection criteria by making use of the `DL1r` algorithm at the 77% efficiency working point [168].

7.1.2 Electron Selection

Electron objects are reconstructed as described in Section 6.2.2, and are required to have $|\eta| < 2.47$. Objects in the aforementioned calorimeter transition region, $1.37 < |\eta| < 1.52$, are rejected. They are required to pass the criteria for the 'tight' working point of the likelihood-based identification, and the criteria for the 'gradient' working point for the isolation [169]. Three additional selection requirements are imposed on the transverse and longitudinal impact parameters and the transverse momentum: $|z_0 \sin\theta| < 0.5\,\mathrm{mm}$, $|\frac{d_0}{\sigma(d_0)}| < 5$, and $p_{\mathrm{T}} > 25\,\mathrm{GeV}$.

7.1.3 Muon Selection

Muon objects are reconstructed as described in Section 6.2.3, and are required to have $|\eta| < 2.5$ and $p_{\mathrm{T}} > 4\,\mathrm{GeV}$. They can then be considered for selection alongside electrons as prompt leptons (from the W-boson), or they can be tagged as soft muons (from the decay chain of the b-quark).

To be selected as prompt leptons, muons must have $|z_0 \sin\theta| < 0.5\,\mathrm{mm}$, $|\frac{d_0}{\sigma(d_0)}| < 3$, and $p_\mathrm{T} > 25\,\mathrm{GeV}$. They must also pass the criteria for the 'medium' identification working point and the 'gradient' isolation working point [170]. They are also required to be separated by $\Delta R > 0.4$ from the nearest reconstructed jet.

Muons that do not pass the above prompt lepton selection are then additionally considered to be tagged as soft muons. To pass this selection, muons are required to pass the criteria for the 'tight' identification working point, to pass loose impact parameter requirements of $|z_0 \sin\theta| < 3\,\mathrm{mm}$ and $|d_0| < 3\,\mathrm{mm}$. They must be within $\Delta R < 0.4$ of the nearest reconstructed jet. This nearest jet is then considered to be SMT-tagged. If more than one muon is tagged for a single SMT-tagged jet, only the highest p_T soft muon is kept.

Due to a bug in the implementation of the particle flow jet reconstruction algorithm, fake jets can be erroneously reconstructed from the tracks of an isolated muon. Additional cuts are required to ensure soft muon candidates are actually non-isolated, i.e. associated with a real jet and not a fake jet due to the particle flow bug. The first of these additional cuts requires at least 25% of the candidate jet p_T to come from a combination of additional tracks associated to the same vertex as the muon track and the neutral-particle calorimeter deposits in a cone around the muon track. The second cut requires that either the fraction of the candidate jet's energy coming from the electromagnetic calorimeter must be < 0.8, or the number of tracks in the candidate jet with $p_\mathrm{T} > 500\,\mathrm{MeV}$ must be > 2.

7.2 Event Selection

Event selection is applied after the object selection procedure described above, and specifies the criteria that must be met for an event to be kept for analysis.

The criteria are that the event:

- Must pass the lowest un-prescaled single-electron or single-muon trigger (see Section 5.2.5).
- Must contain exactly one reconstructed prompt lepton (electron or muon).

- Must contain at least one reconstructed soft muon.
- Must contain at least four reconstructed jets
- The top four jets when ordered by p_{T} must have $p_{\mathrm{T}} > 30\,\mathrm{GeV}$ (any SMT-tagged jets in the top four are excepted from this requirement, so e.g. an event with three light jets with $p_{\mathrm{T}} > 30\,\mathrm{GeV}$ and one SMT-tagged jet with $p_{\mathrm{T}} < 30\,\mathrm{GeV}$ will pass).
- Must contain at least one jet that is b-tagged by the `DL1r` algorithm (which does not necessarily have to be the same jet that is SMT-tagged).
- Must have $E_{\mathrm{T}}^{\mathrm{miss}} > 30\,\mathrm{GeV}$ and $E_{\mathrm{T}}^{\mathrm{miss}} + m_{\mathrm{T}}(W) > 60\,\mathrm{GeV}$ (see Section 6.2.5).

7.3 Constructing Charge Asymmetries

The inference of the flavour of the initial b-quark and final hadron in the decay chain of the soft muon is quantified through the construction of observable charge asymmetries. The first step in this process is to stratify events into four bins, according to the combination of the charge of the prompt lepton, ℓ, and soft muon, μ. This combined charge is denoted $q^{\ell\mu}$, with $q^{\ell\mu} \in \{--, ++, -+, +-\}$. The first and last charge in $q^{\ell\mu}$ corresponds to the charge of the prompt lepton and soft muon respectively.

Before continuing to the construction of observable charge asymmetries, it is necessary to apply the procedure of ST/DT-assignment to establish whether the prompt lepton and soft muon came from the same side or different sides of the $t\bar{t}$ system. The necessity of this can be seen by examining Fig. 7.1. The object of using the prompt lepton charge is to infer the flavour of the initial b-quark that eventually produces the soft muon. In the same-top case of Fig. 7.1(a), where the soft muon and prompt lepton come from the same side of the $t\bar{t}$ system, the prompt lepton correctly correlates to the b-quark associated with the soft muon (explicitly: ℓ^+ implies W^+, which implies t, which implies the initial quark was a b). However, in the different-top case of Fig. 7.1(b), where the soft muon and prompt lepton come from opposite sides of the $t\bar{t}$ system, the prompt lepton correlates with the opposite-side b-quark and must therefore be corrected (explicitly: ℓ^- implies W^-, which implies $\bar{t}$, which implies the opposite-side b-quark was a $\bar{b}$, which implies the initial quark was a b). In practice, this correction is made by flipping the sign of the prompt lepton charge for different-top events (so a same-top event with a positively charged prompt lepton and positively charged soft muon has $q^{\ell\mu} = ++$, but a different-top event with a positively charged prompt lepton and positively charged soft muon has $q^{\ell\mu} = -+$). ST/DT-assignment is the process of determining which events are same-top and which are different-top, in order to apply this correction. It will be discussed in detail in Chapter 10.

After the ST/DT-assignment correction has been applied, the number of events in each bin of $q^{\ell\mu}$ is counted, and these counts are denoted $N^{\ell\mu}$. Detector and reconstruction effects are removed from $N^{\ell\mu}$ using a process called unfolding, discussed in Chapter 11. After unfolding, the same-sign and opposite-sign charge asymmetries, denoted A^{SS} and A^{OS} respectively, are constructed as

$$A^{\mathrm{SS}} \equiv \frac{P(b \to \ell^+) - P(\bar{b} \to \ell^-)}{P(b \to \ell^+) + P(\bar{b} \to \ell^-)} = \frac{\frac{N^{++}}{N^+} - \frac{N^{--}}{N^-}}{\frac{N^{++}}{N^+} + \frac{N^{--}}{N^-}}, \tag{7.1}$$

$$A^{\mathrm{OS}} \equiv \frac{P(b \to \ell^-) - P(\bar{b} \to \ell^+)}{P(b \to \ell^-) + P(\bar{b} \to \ell^+)} = \frac{\frac{N^{+-}}{N^+} - \frac{N^{-+}}{N^-}}{\frac{N^{+-}}{N^+} + \frac{N^{-+}}{N^-}}, \tag{7.2}$$

where $N^+ = N^{++} + N^{+-}$ and $N^- = N^{-+} + N^{--}$ are respectively the total number of events with a positively and negatively charged prompt lepton, and $P(X)$ denotes the probability of process X occurring. The above Eqs. 7.1 and 7.2 are expressed in terms of these ratios of ratios in order to be independent of any asymmetry in the charges of the prompt leptons (i.e. $N^+ \neq N^-$). Such an asymmetry might arise from the reconstruction process, or from the underlying $t\bar{t}$ production charge asymmetry at the LHC, which results in slightly higher quantities of t than $\bar{t}$ at central values of η [171]. While such effects are small, they would affect the observable charge asymmetries and mask the contribution of the CP-violating effects that the analysis is designed to study if Eqs. 7.1 and 7.2 were expressed without these additional ratios.

Following the construction of these observable charge asymmetries, the next step is to link them to the underlying CP-violation asymmetries.

7.4 Deriving CP-Violation Asymmetries

Deriving the link between the observable charge asymmetries and the underlying CP-violation asymmetries of the form described in Section 4.5 requires knowledge of the physics processes that contribute to each of the observable charge asymmetries introduced in Eqs. 7.1 and 7.2. There are three decay chains that contribute to A^{SS}, and three decay chains that contribute to A^{OS}.

The decay chains (for the case of an initial t, with the case of an initial $\bar{t}$ being implied) that contribute to A^{SS} are

$$t \to \ell^+ \nu (b \to \bar{b}) \to \ell^+ \mu^+ X, \tag{7.3}$$

$$t \to \ell^+ \nu (b \to c) \to \ell^+ \mu^+ X, \tag{7.4}$$

$$t \to \ell^+ \nu (b \to \bar{b} \to c\bar{c}) \to \ell^+ \mu^+ X, \tag{7.5}$$

where X denotes any hadronic final state. Diagrams for the decay chains are shown in Fig. 7.2, and the number of events in each of these decay chains is respectively denoted by the count N_{r_b} (Eq. 7.3), N_{r_c} (Eq. 7.4), and $N_{r_{c\bar{c}}}$ (Eq. 7.5).

Similarly, the decay chains that contribute to A^{OS} are

$$t \to \ell^+ \nu b \to \ell^+ \mu^- X, \tag{7.6}$$

$$t \to \ell^+ \nu (b \to \bar{b} \to \bar{c}) \to \ell^+ \mu^- X, \tag{7.7}$$

$$t \to \ell^+ \nu (b \to c\bar{c}) \to \ell^+ \mu^- X. \tag{7.8}$$

Diagrams for the decay chains are shown in Fig. 7.3, and the number of events in each of these decay chains is respectively denoted by the count $N_{\tilde{r}_b}$ (Eq. 7.6), $N_{\tilde{r}_c}$ (Eq. 7.7), and $N_{\tilde{r}_{c\bar{c}}}$ (Eq. 7.8).

These counts are measured in MC simulations, and used to derive the decay chain fractions as

$$r_b \equiv \frac{N_{r_b}}{N_{r_b} + N_{r_c} + N_{r_{c\bar{c}}}}, \tag{7.9}$$

$$r_c \equiv \frac{N_{r_c}}{N_{r_b} + N_{r_c} + N_{r_{c\bar{c}}}}, \tag{7.10}$$

$$r_{c\bar{c}} \equiv \frac{N_{r_{c\bar{c}}}}{N_{r_b} + N_{r_c} + N_{r_{c\bar{c}}}}, \tag{7.11}$$

$$\tilde{r}_b \equiv \frac{N_{\tilde{r}_b}}{N_{\tilde{r}_b} + N_{\tilde{r}_c} + N_{\tilde{r}_{c\bar{c}}}}, \tag{7.12}$$

$$\tilde{r}_c \equiv \frac{N_{\tilde{r}_c}}{N_{\tilde{r}_b} + N_{\tilde{r}_c} + N_{\tilde{r}_{c\bar{c}}}}, \tag{7.13}$$

$$\tilde{r}_{c\bar{c}} \equiv \frac{N_{\tilde{r}_{c\bar{c}}}}{N_{\tilde{r}_b} + N_{\tilde{r}_c} + N_{\tilde{r}_{c\bar{c}}}}. \tag{7.14}$$

These decay chain fractions are then used to derive the relations between the observable charge asymmetries, A^{SS} and A^{OS}, and the underlying CP-violation asymmetries, $A^{b\ell}_{\mathrm{dir}}$, $A^{c\ell}_{\mathrm{dir}}$, A^{bc}_{dir}, $A^{b\ell}_{\mathrm{mix}}$, and A^{bc}_{mix} (as defined in Section 4.5), giving

$$A^{\mathrm{SS}} = r_b A^{b\ell}_{\mathrm{mix}} + r_c(A^{bc}_{\mathrm{dir}} - A^{c\ell}_{\mathrm{dir}}) + r_{c\bar{c}}(A^{bc}_{\mathrm{mix}} - A^{c\ell}_{\mathrm{dir}}), \tag{7.15}$$

$$A^{\mathrm{OS}} = \tilde{r}_b A^{b\ell}_{\mathrm{dir}} + \tilde{r}_c(A^{bc}_{\mathrm{mix}} + A^{c\ell}_{\mathrm{dir}}) + \tilde{r}_{c\bar{c}}(A^{c\ell}_{\mathrm{dir}}), \tag{7.16}$$

where the negative sign for $A^{c\ell}_{\text{dir}}$ arises from the definition of $A^{c\ell}_{\text{dir}}$ (Eq. 4.11) with the opposite sign-convention to the decay chain contributing to A^{SS} (Eq. 7.4). For example, an excess of $c \to \ell^+$ over $\bar{c} \to \ell^-$ would give a negative $A^{c\ell}_{\text{dir}}$, but should contribute positively to A^{SS}.

While both the observable charge asymmetries and the decay chain fractions depend on the fiducial phase-space volume defined by the full list of selection cuts from Sections 7.1 and 7.2, this dependence cancels out in combination. This leaves the unfolded CP-violation asymmetries independent of the ATLAS experiment and the fiducial volume, and therefore comparable with theoretical predictions and results from other experiments.

Examining Eqs. 7.15 and 7.16 reveals a heavily underconstrained system of equations, with five CP-violation asymmetries to be extracted from two measured charge asymmetries. Additional constraints must be added. Following the prescription of [90], each CP-violation is considered in turn as if it is solely responsible for the observed value of the charge asymmetries.

In the case of all three direct CP-violation asymmetries being set to zero, $A^{b\ell}_{\text{mix}} = A^{bc}_{\text{mix}} = A^{b}_{\text{mix}}$, and this can be extracted as

$$A^{b}_{\text{mix}} = \frac{A^{\text{SS}}}{r_b + r_{c\bar{c}}}. \tag{7.17}$$

Similarly, considering each direct CP-violation asymmetry as the sole responsible asymmetry yields

$$A^{b\ell}_{\text{dir}} = \frac{A^{\text{OS}}}{\tilde{r}_b}, \tag{7.18}$$

$$A^{c\ell}_{\text{dir}} = -\frac{A^{\text{SS}}}{r_c + r_{c\bar{c}}}, \tag{7.19}$$

$$A_{\mathrm{dir}}^{bc} = \frac{A^{\mathrm{SS}}}{r_c}. \tag{7.20}$$

Extracting the CP-violation asymmetries in this way is essentially a conservative limit-setting exercise yielding an upper bound, i.e. they are the maximum values of each CP-violation asymmetry allowed by the observed charge asymmetries values. A combination of less extreme values across several of the CP-violation asymmetries could also explain the observed charge asymmetry values.

7.5 Simulation and Experimental Data Samples

The analysis described in this thesis makes use of two primary datasets: a Standard Model MC simulation data sample, and an ATLAS experimental data sample.

For the MC simulation sample (see Section 6.1), a non-all-hadronic $t\bar{t}$ (containing both lepton + jets and dilepton $t\bar{t}$ events) sample (ATLAS dataset ID 410470, derivation TOPQ1) is used [172]. Event generation is performed at next-to-leading order (NLO) using the `POWHEG BOX` computing framework [173–176]. Parton showering and hadronisation is modelled using `Pythia` 8.3 [177]. Detector simulation is performed using GEANT4 [152–154]. The integrated luminosity of this MC dataset is normalised to the integrated luminosity of the data sample described below, so that the samples can be directly compared.

Additional MC samples are used to derive systematic uncertainties, and will be described in the discussion of those uncertainties in Chapter 9.

The experimental data sample is the ATLAS Full Run 2 dataset, comprising 139 fb^{-1} of collision data collected by the ATLAS collaboration between 2015 and 2018.

All of the data samples used in the analysis are listed in Table 7.1.

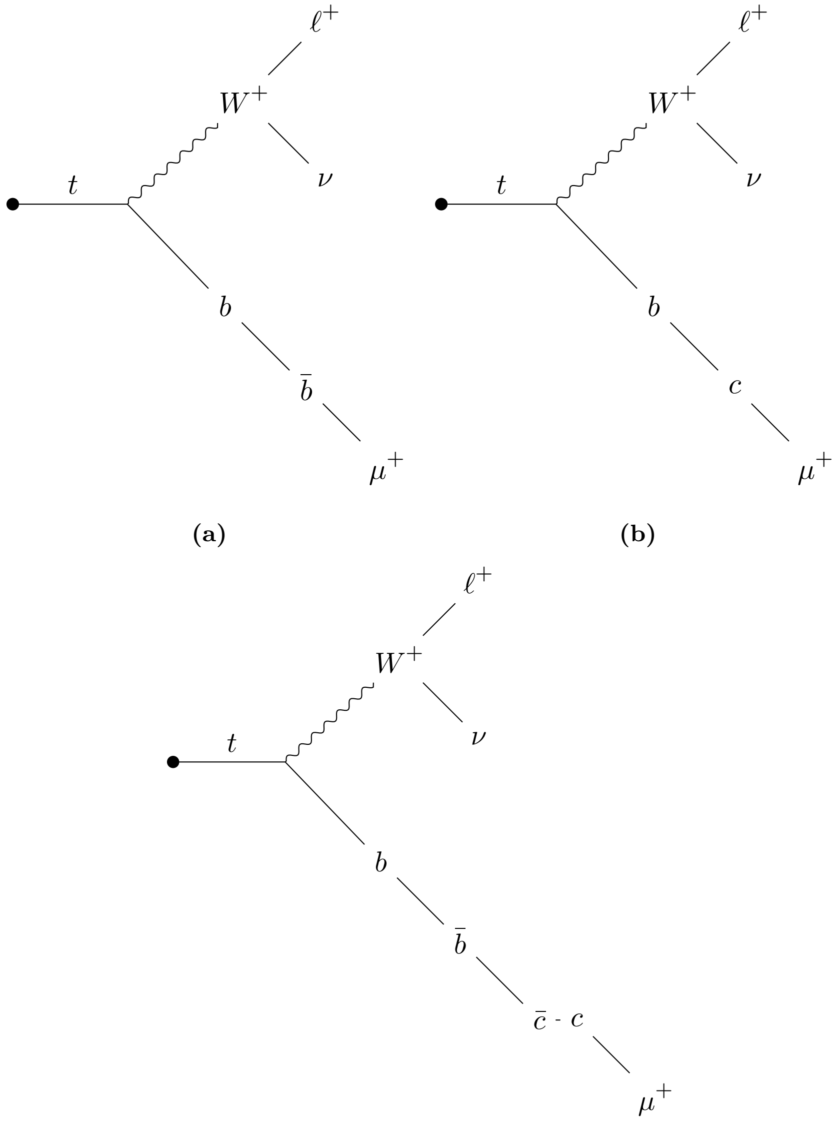

(a) **(b)**

(c)

Figure 7.2 Diagrams of the soft muon decay chains that contribute to the same-sign asymmetry A^{SS}, showing the chains that correspond to the counts: **(a)** N_{r_b}; **(b)** N_{r_c}; **(c)** $N_{r_{c\bar{c}}}$. Each diagram should be taken as also implying the conjugate diagrams, with all particles swapped with their antiparticles.

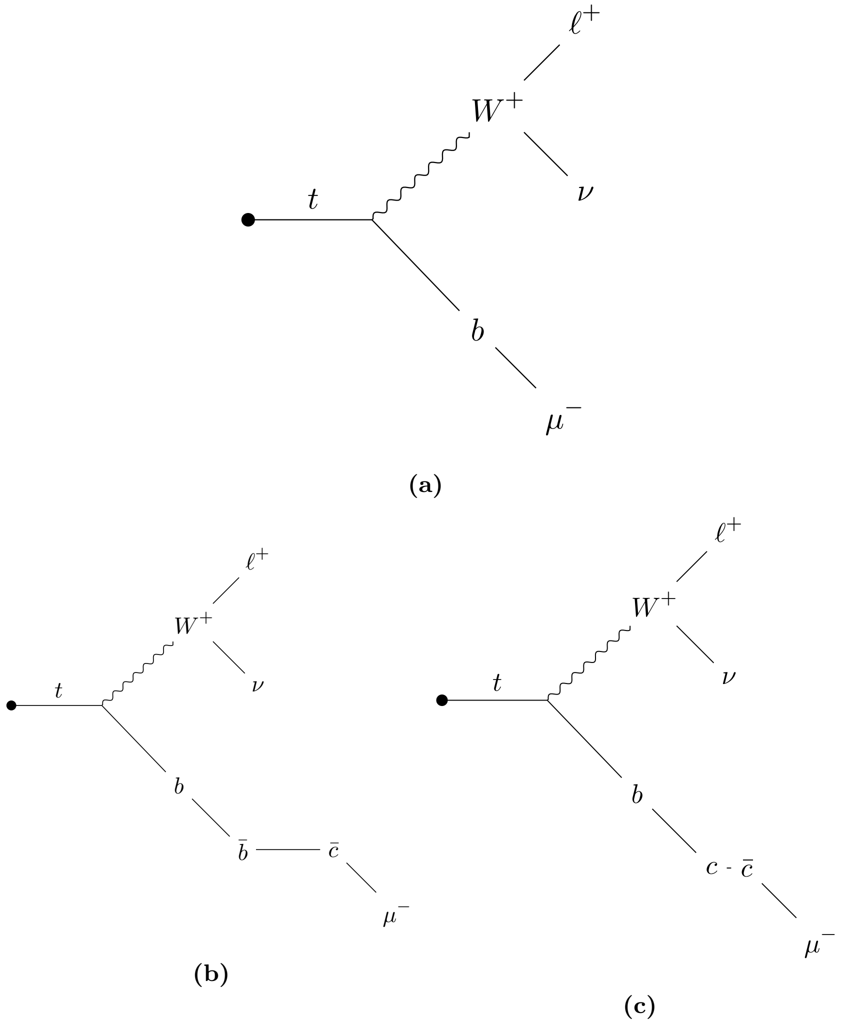

(a)

(b)

(c)

Figure 7.3 Diagrams of the soft muon decay chains that contribute to the opposite-sign asymmetry A^{OS}, showing the chains that correspond to the counts: **(a)** $N_{\tilde{r}_b}$; **(b)** $N_{\tilde{r}_c}$; **(c)** $N_{\tilde{r}_{c\bar{c}}}$. Each diagram should be taken as also implying the conjugate diagrams, with all particles swapped with their antiparticles.

Sample	DSID	NLO Event Generator	Parton Shower Algorithm
ATLAS Full Run 2 ($139\,\mathrm{fb}^{-1}$) Dataset	n/a	n/a	n/a
Primary MC - Non-All-Hadronic $t\bar{t}$	410470	`POWHEG`	`Pythia` 8.3
NLO Event Generator Uncertainty - Lepton+Jets $t\bar{t}$	410464	`MadGraph5_aMC@NLO`	`Pythia` 8.3
NLO Event Generator Uncertainty - Dilepton $t\bar{t}$	410465	`MadGraph5_aMC@NLO`	`Pythia` 8.3
Parton Shower Uncertainty - Lepton+Jets $t\bar{t}$	410557	`POWHEG`	`Herwig` 7.2.3
Parton Shower Uncertainty - Dilepton $t\bar{t}$	410558	`POWHEG`	`Herwig` 7.2.3
h_{damp} Variation Uncertainty - Lepton+Jets $t\bar{t}$	410480	`POWHEG`	`Pythia` 8.3
h_{damp} Variation Uncertainty - Dilepton $t\bar{t}$	410482	`POWHEG`	`Pythia` 8.3

Table 7.1 A list of the data samples that are used in the analysis described in this thesis, showing: samples, (in the case of MC) ATLAS dataset ID (DSID), and (in the case of MC) which event generators and parton shower algorithms were used when generating the samples.

Chapter 8

Background Estimation

While the selection cuts described in Sections 7.1 and 7.2 are partially designed to suppress the effect on the measured quantities of processes other than the signal process, it is impossible to completely eliminate all sources of background. There are various reducible and irreducible contributions that mimic the signal process final state. However, by estimating the level of the different background contributions to each bin of the observed $N^{\ell\mu}$ distribution through a mixture of different techniques, it is possible to subtract these backgrounds from the distribution, isolating the contributions coming from the signal process and ensuring the final measurement is unaffected by these backgrounds.

The backgrounds can be separated into two categories, which are considered separately. The first category, explored in Section 8.1, is the set of background processes coming from within $t\bar{t}$ events, which mimic the signature of a true soft muon when there is no true soft muon present. The second category, explored in Section 8.2, is the set of background processes coming from non-$t\bar{t}$ events, which mimic the final state of a lepton + jets $t\bar{t}$ event in its entirety and also contain one of: a true soft muon from the semileptonic decay of a b-hadron or c-hadron in a heavy-flavour jet, a muon coming from the decay-in-flight of a charged pion or kaon in a light-flavour jet, or a so-called fake soft muon. This fake soft muon is actually a jet containing charged hadrons that has punched through to the muon systems of the detector and is erroneously reconstructed as a muon.

For both $t\bar{t}$ and non-$t\bar{t}$ background processes, it is important to consider how they contribute to the event counts $N^{\ell\mu}$. Some background processes contain a prompt lepton and soft muon that are produced in a correlated manner, so the charges are correlated as in the signal process, while for some processes the lepton and soft muon production are completely unrelated. Additionally, some background processes are expected to produce equal numbers of positively-charged and negatively-charged prompt leptons and thus contribute a flat shape evenly across all four bins of the $N^{\ell\mu}$ distribution, while other background processes are expected to produce more prompt leptons of one particular charge and will therefore contribute more prominently to certain bins, resulting in a non-flat shape being added to the distribution.

The contributions of the different $t\bar{t}$ background processes as measured in MC simulation are presented in Table 8.1. At the time of writing this thesis, the estimation of the various non-$t\bar{t}$ background processes has not yet been carried out for the analysis, and this work remains to be done before the analysis can be unblinded and proceed to publication. To illustrate the expected levels of contribution for each source of background, Table 8.2 has been included, presenting the contribution of each source in the previous ATLAS measurement [93], and these contributions are expected to remain broadly similar for the current measurement.

8.1 $t\bar{t}$ Backgrounds

The backgrounds from within $t\bar{t}$ events pass every aspect of the selection in a genuine manner, with the exception of the soft muon selection. This means that these background processes will be identical to the signal process in containing a real prompt lepton and missing transverse momentum from the decay of a W, the same number of jets, and the same number of b-tagged jets. However, these background events do not contain a genuine soft muon. Instead, the soft muon selection may be erroneously satisfied for a variety of reasons, which are detailed in turn below. All of the $t\bar{t}$ backgrounds can be estimated from MC simulation, and are incorporated into the acceptance terms that are applied as part of the unfolding process (see Section 11.2).

If one of the W-leptons from a dilepton $t\bar{t}$ event is a muon and is produced close to a jet, it may be removed in the jet overlap removal process, and then in turn pass the soft muon selection. As this muon will always be a different-top muon, it is expected to contribute more significantly to the same-sign bins of the $N^{\ell\mu}$ distribution.

In genuine lepton + jets $t\bar{t}$ events, the hadronically-decaying W-boson can decay to a c-hadron, and this can decay semileptonically to produce a muon that may pass the soft muon selection. As with the muons coming from dilepton events, this will always be a different-top muon and is therefore expected to contribute more significantly to the same-sign bins of the $N^{\ell\mu}$ distribution.

Muons coming from pileup interactions, semileptonic decays of heavy-flavour quarks from additional ISR or FSR, or decays-in-flight of pions and kaons, can all fake the soft muon selection criteria. All of these sources are expected to contribute equally across all bins of the $N^{\ell\mu}$ distribution.

The contributions of the different $t\bar{t}$ background sources, as measured in MC simulation scaled to an integrated luminosity of 139 fb^{-1}, are presented in Table 8.1.

Source	Fraction of $t\bar{t}$ Sample	Relative Fraction of Signal Process
Signal	80.4%	100.0%
W-leptons	1.0%	1.2%
$W \to c \to \mu$	7.0%	8.7%
Pileup, IFSR, Decays-in-Flight	11.6%	14.4%

Table 8.1 The contributions of the various sources of background within $t\bar{t}$ processes, as measured in MC simulation scaled to an integrated luminosity of 139 fb^{-1}, detailing the source, what fraction of the total sample is made up by this source, and the relative fraction of each source to the signal process. The signal contribution is also included for comparison, listed in italics.

8.2 Non-$t\bar{t}$ Backgrounds

The non-$t\bar{t}$ background processes that contribute to the measurement are, in order of expected contribution from highest to lowest: the W+jets process, the single-top process, the multijet (or QCD) process, the Z+jets process, and the diboson process. Each of these processes is considered in turn below. The contributions of the different non-$t\bar{t}$ background sources to the previous ATLAS measurement are provided in Table 8.2 [93].

8.2.1 W+Jets

W+jets events are produced at the LHC in various ways, and have a large overall production cross section. They can mimic the signature of a lepton+jets $t\bar{t}$ event in the case that the W-boson, decaying to produce a charged lepton and neutrino, is accompanied by multiple light- and heavy-flavour jets. Proton-antiproton colliders such as the Tevatron saw production of equal quantities of W^{+}+jets and W^{-}+jets events, but at a proton-proton collider such as the LHC, approximately 30% more W^{+}+jets events are produced than W^{-}+jets events, as there are more valence up quarks than down quarks and the PDFs of the proton show that up quarks receive more of the initial proton momentum than down quarks [178]. This means that the background contribution of W+jets events will contain more positively-charged than negatively-charged leptons. Two possible Feynman diagrams for the W+jets background are shown in Fig. 8.1. W-bosons produced in association with a charm quark, as shown in Fig. 8.1(a), can produce a soft muon from a semileptonic charm quark decay, and this charge will be correlated with the charge of the prompt lepton. Contributions where a soft muon is produced from an unrelated heavy-flavour jet, as shown in Fig. 8.1(b), will result in no correlation between the soft muon and prompt lepton charges.

The W+jets contribution to the total background is estimated using a combination of MC simulation and data-driven techniques.

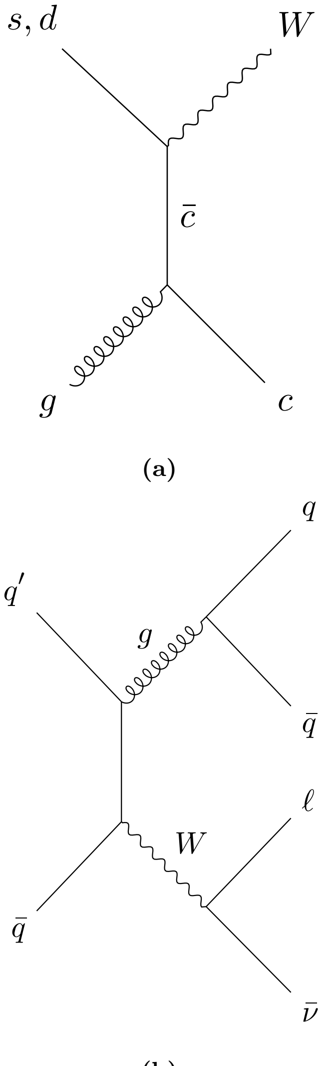

(a)

(b)

Figure 8.1 The Feynman diagram representations of W+jets production for the case of: **(a)** correlated W-boson production with a charm quark; **(b)** the general case.

8.2.2 Single-Top

Single-top events can fulfil most of the selection criteria of a lepton + jets $t\bar{t}$ event when the top decays to produce a W-boson, which can produce a prompt lepton, and a b-quark, which can produce a soft muon. The charge of this soft muon and prompt lepton will be correlated. With the addition of multiple jets, single-top events can then pass all the selection requirements of the $t\bar{t}$ signal process. Single-top production proceeds via the three Feynman diagrams introduced in the discussion of top quark phenomenology in Section 3.1, and are shown in Fig. 3.3. For the t-channel (Fig. 3.3(a)) and s-channel (Fig. 3.3(b)) processes, the top quark is produced from a W-boson, and so the background contribution from these channels will contain more positively-charged than negatively-charged prompt leptons in the same manner as described for the W+jets background above. In addition to the production of a correlated prompt lepton and soft muon, both the t-channel and the s-channel allow the possibility of the soft muon and prompt lepton charges not being correlated. The soft muon can come from the $\bar{b}$-quark in the s-channel, and in the case of the t-channel process, a significant fraction of the initial b-quarks will have been produced as part of a $b\bar{b}$ pair, meaning the soft muon can be produced from the other side of this pair. The tW-channel (Fig. 3.3(c)) results in correlated prompt lepton and soft muon charges only, and will contribute equal quantities of positively-charged and negatively-charged prompt leptons.

The single-top contribution to the total background is estimated from MC simulation.

8.2.3 Multijet

The multijet background comes from events containing multiple jets, both light-flavour and heavy-flavour, produced from the valence quarks of the collided protons and from gluon radiation. These jets can produce real prompt leptons and soft muons through photon conversions and semileptonic decays, which will have uncorrelated charges and contribute equal numbers of positively-charged and negatively-charged prompt leptons. Additionally, hadronic particles can fake prompt electrons, and both prompt and soft muons. The signature of an electron is charged tracks and energy deposits in the Electromagnetic Calorimeter, which can be mimicked by the combination of a π^+/π^- (leaving tracks due to being charged) and a π^0 (which decays to photons that register as energy deposits). Muons can be faked in two ways, via decays-in-flight or punchthrough. Despite the probabilities for fakes being low, the cross section for the multijet background is extremely high, and it therefore still contributes a significant number of events to the total background.

The difficulty of performing MC simulations for non-perturbative QCD interactions means that a data-driven method must be utilised to estimate the multijet contribution to the total background. This measurement utilises the technique known as the ABCD method, where background-rich control regions (labelled B, C, and D) are defined by inverting the requirements imposed by two of the selection cuts that can be considered independent. The correlations between the multijet contributions in these three control regions are then used to infer the multijet contribution in the signal region (labelled A).

8.2.4 Z+Jets

In Z+jets events, produced as shown in Fig. 8.2, the prompt lepton can be produced by the decay of the Z-boson to produce two charged leptons, as shown in Fig. 8.2(a). One of these may be reconstructed as the prompt lepton, while the other escapes the detector undetected or does not pass the lepton selection cuts and therefore provides the missing transverse momentum that is required alongside the prompt lepton for the signal process. Alternatively, the Z-boson can mimic the missing transverse momentum by decaying to two neutrinos, as shown in Fig. 8.2(b), while a jet provides a fake prompt lepton candidate. In both cases, the soft muon will have to be produced from a heavy-flavour jet or faked as previously discussed, and the charge is therefore not correlated with the charge of the prompt lepton. There is also no reason for Z+jets events to contribute more positively-charged than negatively-charged prompt leptons, or vice versa.

Similarly to single-top, the Z+jets contribution to the total background is estimated from MC simulation.

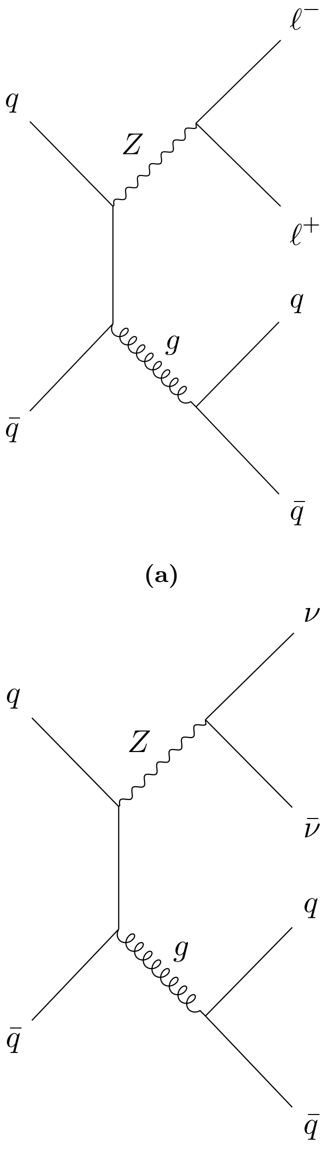

(a)

(b)

Figure 8.2 The Feynman diagram representations of Z+jets production, for the case of: **(a)** the Z-boson decaying to a charged lepton and antilepton; **(b)** the Z-boson decaying to a charged neutrino and antineutrino.

8.2.5 Diboson

Diboson production proceeds via the Feynman diagrams shown in Fig. 8.3. The W-bosons and Z-bosons that are produced lead to the lepton + jets $t\bar{t}$ signature being mimicked according to the same principles as described for the W+jets and Z+jets processes. Both WW-production (Fig. 8.3(a)) and ZZ-production (Fig. 8.3(b)) will contribute equal quantities of positively-charged and negatively-charged prompt leptons, but WZ-production (Fig. 8.3(c)) will contribute an excess of positively charged prompt leptons in the same manner as W+jets, t-channel single-top, and s-channel single-top.

As with Z+jets and single-top, the diboson contribution to the total background is estimated from MC simulation.

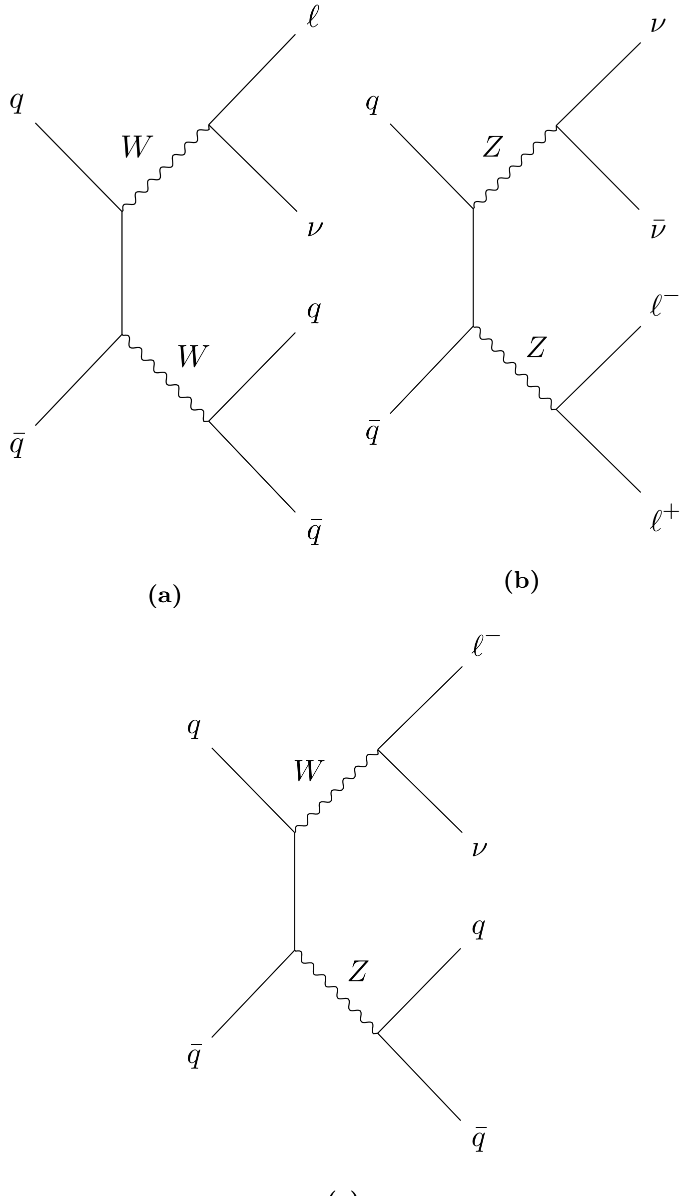

(a) **(b)**

(c)

Figure 8.3 The Feynman diagram representations of diboson production, for the case of: **(a)** WW production; **(b)** ZZ production; **(c)** WZ production.

Source	Fraction of Total Events	Relative Fraction of $t\bar{t}$ MC
$t\bar{t}$ MC	82.4%	100.0%
W+Jets	6.7%	8.1%
Single-Top	4.9%	5.9%
Multijet	4.2%	5.1%
Z+Jets	1.6%	2.0%
Diboson	0.1%	0.1%

Table 8.2 The contributions of the various sources of background from non-$t\bar{t}$ processes as measured in the previous ATLAS analysis at 8 TeV, detailing the source, what fraction of the total event count is made up by this source, and the relative fraction of each source to the $t\bar{t}$ MC [93]. The $t\bar{t}$ MC contribution is also included for comparison, listed in italics.

Chapter 9

Uncertainties

When presenting particle physics measurements, it is important to quantify the uncertainty on the measured quantity, as well as the central value. This chapter discusses the various sources of uncertainty that are considered for the measurement in this thesis. It begins in Section 9.1 with a discussion of the statistical uncertainty, a consequence of the number of observations made. The measurement is also subject to systematic uncertainties, which can be subdivided into two categories. The first of these are detector systematics, discussed in Section 9.2, which arise from the physical measurement process, and modelling systematics, discussed in Section 9.3, which arise from the way the theory predictions are modelled in simulations. This chapter focuses on how these uncertainties arise and how they are assessed. The impact of the statistical and systematic uncertainties are presented alongside the results in Chapter 13.

At the time of writing this thesis, a small handful of the systematic uncertainties that need to be assessed still need to be implemented before the analysis can be unblinded and proceed to publication. All the uncertainties are covered in this chapter, with those still to be assessed noted in the text and where they are presented in Tables 9.1, 9.2, and 13.1 to 13.3.

9.1 Statistical Uncertainty

The core of a particle physics measurement involves defining a region, or regions, of fiducial phase-space (by defining a list of selection cuts), and then counting the number of events that fall into this phase-space (pass the selection cuts). For the measurement in this thesis, four regions are defined, with corresponding $N^{\ell\mu}$ counts N^{--}, N^{++}, N^{-+}, and N^{+-} of the total number of events in each region in the data sample (see Chapter 7).

Such a count of total number of events, generally denoted n, can be treated as a Poisson-distributed variable, such that

$$n \sim P(\nu_s + \nu_b), \tag{9.1}$$

$$f(n; \nu_s, \nu_b) = \frac{(\nu_s + \nu_b)^n}{n!} \exp -(\nu_s + \nu_b), \tag{9.2}$$

with contributions from signal and background processes with expected number of events ν_s and ν_b respectively [179]. An observed count n_{obs} then gives an estimate of $\nu = \nu_s + \nu_b$, and as the standard deviation of a Poisson-distributed variable is equal to the square root of the mean, the observed count with its statistical uncertainty is $n_{\mathrm{obs}} \pm \sqrt{n_{\mathrm{obs}}}$.

For the measurement in this thesis, the quantities of interest are not the counts themselves but the observable charge and underlying CP-violation asymmetries defined in Sections 7.3 and 7.4 which comprise combinations of these counts after the procedure of unfolding. The statistical uncertainty on the four data $N^{\ell\mu}$counts is taken to be the square root as explained above, and propagated to the unfolded asymmetries by performing statistical pseudoexperiments, as described in Section 11.4.1. This is done to ensure correlations between the different $N^{\ell\mu}$ are accounted for. Basic error propagation would neglect these correlations, resulting in an overestimation of the statistical uncertainty on the unfolded asymmetries.

For all MC simulation samples, the total number of events is normalised to the same integrated luminosity as the data sample to ensure that the statistical uncertainties are comparable.

9.2 Detector Systematics

Detector systematics arise from uncertainties in the various object reconstruction techniques described in Section 6.2. For the assessment of most of the detector systematics, the MC simulation is re-performed with the quantity of interest varied up/down by one standard deviation, and these up/down-variations are compared to the nominal MC to assess the uncertainty. For the remainder of the detector systematics, known as two-point systematics, only one re-performed MC sample is compared to the nominal MC. This variation is symmetrised to get the final uncertainty.

The various detector systematics are described in the remainder of this section. A summary of all the detector systematics is presented in Table 9.1.

9.2.1 Leptons

Lepton uncertainties arise in the reconstruction of both electrons and muons (as described in Sections 6.2.2 and 6.2.3. Efficiency scale factors are applied to simulation samples, to ensure that the reconstruction process is fully consistent with the experimental data samples. These are centrally derived by the ATLAS collaboration using a method known as tag-and-probe in samples of $Z \to \ell^+\ell^-(\ell = e, \mu)$ events in data and simulation [155, 157]. Each scale factor is provided with associated up/down-variations that are propagated to the final measurement. The total uncertainty for electrons varies with p_T, from $< 0.5\%$ when $p_\mathrm{T} > 30\,\mathrm{GeV}$ to $> 1\%$ for low-p_T electrons. The total uncertainty for muons is $< 0.5\%$.

Additional lepton uncertainties arise from correction factors applied to simulation samples to ensure that lepton momentum scale and resolution are consistent with experimental data.

These correction factors are derived from reconstructed dilepton masses in $Z \to \ell^+\ell^-(\ell = e, \mu)$ and $J/\psi \to \ell^+\ell^-(\ell = e, \mu)$ events [157, 180].

Soft muons are calibrated with the same scale factors as are used for prompt muons, with an additional step performed to verify that these scale factors are not found to be dependent on the charge of the soft muons, as this would potentially introduce a bias to the measured asymmetries.

Both prompt electrons and muons can be faked by hadronic particles, and an additional uncertainty is applied pertaining to the data-driven estimate of the contributions from such fakes.

An additional uncertainty arises for electrons, coming from the correction to ensure that charge-misidentification (where a positron is incorrectly reconstructed as an electron, or vice-versa) rates are consistent between data and simulation.

At the time of writing this thesis, the setup of the tools required to fully assess the fake lepton and electron charge-misidentification uncertainties is ongoing, so all results in Chapter 13 are quoted with estimated values taken from the previous ATLAS measurement [93].

9.2.2 Jets

Jet uncertainties arise from the usage of the JVT to suppress pileup in the reconstruction process, from the correction factors associated with the jet energy scale (JES) and the jet energy resolution (JER), and from flavour-tagging.

The efficiency scale factor for the JVT pileup-suppression cut is derived from $Z \to \mu^+\mu^-$ events in data and simulation, and the uncertainty associated with this scale factor is assessed by varying this scale factor [164]. An additional pileup-related uncertainty is considered, which relates to the data-simulation correction of the number of pileup events.

The JES and JER corrections are derived from a combination of test-beam data, collision data, and simulation across a variety of different event types [181]. The uncertainties are obtained in accordance with ATLAS recommendations, considering 23 nuisance parameters for the JES and eight nuisance parameters for the JER [182].

Dedicated flavour-tagging scale factors are derived from data and simulation to ensure that the levels of b-jet, c-jet, and light-jet events are correct. The b-jet and c-jet scale factors are p_{T}-dependent, while the light-jet scale factor depends on both p_{T} and η. Uncertainties are assessed in association with each of these scale factors using an eigen-variation model that reduces the total number of variations by combining small variations together. This results in six b-jet eigen-variations, three c-jet eigen-variations, and 13 light-jet eigen-variations, along with two additional uncertainties arising from the extrapolation of these scale factors to jets beyond the calibrated p_{T}-spectrum [168].

In addition to these flavour-tagging scale factors, an uncertainty arises from the correction factor applied to account for the SMT mistag rate, i.e. the fraction of true light jets that are erroneously labelled as SMT-tagged jets by the procedure described in Section 7.1.3. As with the electron charge-misidentification uncertainty, the assessment of this uncertainty is yet to be fully implemented, so the results presented in Chapter 13 make use of estimated values taken from the previous ATLAS measurement [93].

9.2.3 $E_{\mathrm{T}}^{\mathrm{miss}}$

The overall reconstructed missing transverse momentum, $E_{\mathrm{T}}^{\mathrm{miss}}$ comprises a hard term, matched to reconstructed leptons and jets, and a soft term, coming from calorimeter deposits not matched to any of the aforementioned objects. The uncertainties assessed on reconstructed leptons and jets, as described above in Sections 9.2.1 and 9.2.2 include the effect they have on the hard $E_{\mathrm{T}}^{\mathrm{miss}}$ term, while momentum scale and resolution uncertainties on the soft term are assessed separately [160]. The soft term momentum scale is assessed with an up/down-variation, while the soft term momentum resolution is assessed with two-point uncertainties that represent the resolution in the directions parallel and perpendicular to the hard term.

Detector Systematic	Components (Up/Down vs. Two-Point)
Electron Momentum Scale and Resolution	2 (Up/Down)
Muon Momentum Scale and Resolution	4 (Up/Down)
Prompt Lepton Isolation, Reconstruction, & Trigger	17 (Up/Down)
Soft Muon Isolation & Reconstruction	4 (Up/Down)
JES	23 (Up/Down)
JER	8 (Up/Down)
JVT	1 (Up/Down)
Pileup	1 (Up/Down)
Flavour-Tagging	19 (Up/Down)
$E_{\mathrm{T}}^{\mathrm{miss}}$ Momentum Scale	1 (Up/Down)
$E_{\mathrm{T}}^{\mathrm{miss}}$ Momentum Resolution	2 (Two-Point)
Electron Charge-Misidentification	Unfinalised
SMT Mistag Rate	Unfinalised
Fake Lepton Estimation	Unfinalised
Background Estimation	Unfinalised

Table 9.1 A summary of the detector systematics included in the measurement presented in this thesis, along with how many components are considered for each source of uncertainty. The unfinalised uncertainties are those for which the implementation is ongoing at the time of writing this thesis, and therefore the number of components is not known.

9.2.4 Backgrounds

Uncertainties arise from estimating the contributions of the various background components, as described in Chapter 8. These include an uncertainty on the total cross section for the single-top components, and normalisation uncertainties on the W+jets, Z+jets, diboson, and multijet components. As the final yields for each background component are yet to be obtained, the results in Chapter 13 are presented with an estimate from the previous ATLAS measurement [93].

9.3 Modelling Systematics

Modelling systematics arise from the way the MC simulation is performed, as described in Section 6.1. For some aspects of the modelling, an alternative MC sample is used and compared to the nominal MC, with the variation symmetrised to get the final uncertainty. For other aspects of the modelling, the nominal MC is reweighted to reflect the desired systematic variation, and this reweighted sample is compared with the original one to assess the uncertainty.

The various modelling systematics are described in the remainder of this section. A summary of all the modelling systematics is presented in Table 9.2.

9.3.1 PDF

There is an uncertainty associated with the choice of PDF set used to determine the momentum of initial-state partons in the first step of the MC simulation process. The choice of the nominal PDF set, and the assessment of this modelling systematic are carried out in accordance with the `PDF4LHC` recommended prescription [183]. The nominal MC sample uses the baseline `NNPDF` 3.0 set, and this is compared to 30 `PDF4LHC` error sets, each defined by a reweighting scheme. Therefore, 30 reweighted samples are produced and the variations are summed in quadrature and symmetrised to obtain the final uncertainty.

9.3.2 NLO Generator

The second step in the MC simulation process is to use NLO event generators to simulate the final-state particles produced in the original hard collision (see Section 6.1). As discussed in Section 7.5, the `POWHEG BOX` framework is used for the nominal MC [173–176]. To assess the modelling systematic associated with this choice of NLO generator, an alternative sample is created using the `MadGraph5_aMC@NLO` framework [184–186]. The rest of the simulation process is kept the same and the variation between the two samples is symmetrised and taken as the final uncertainty.

9.3.3 Parton Shower

The third step in the MC simulation process is the modelling of the parton shower and hadronisation. As discussed in Section 7.5, the nominal MC uses `Pythia` 8.3 to do this [177]. An alternative sample is created using `Herwig` 7.2.3 [187, 188]. The rest of the simulation process is kept the same and the variation between the two samples is symmetrised and taken as the final uncertainty.

9.3.4 ISR/FSR

The results of the measurement may be affected by the level of ISR and FSR, as higher or lower levels of gluon radiation will change the number of jets in an event and the jet p_{T} distribution, affecting the likelihood of events passing the selection cuts and the ability to distinguish b-tagged or SMT-tagged jets from others. The uncertainties associated with the level of radiation are assessed as described below, in accordance with the latest ATLAS recommendations [189].

For the ISR, up/down-variations are produced by varying the renormalisation and factorisation scales, along with the value of the coupling constant for the strong interaction in the initial-state, α_s^{ISR}. For the FSR uncertainty, up/down-variations are produced by varying the coupling constant for the strong interaction in the final-state, α_s^{FSR}.

In addition to these up/down-variations, an alternative sample is generated with a higher value of the resummation damping factor, h_{damp}, which is a `POWHEG` parameter proportional to the mass of the top quark, m_t, that controls the matching between the NLO generator and the parton shower. It effectively controls the amount of high-p_{T} radiation that is produced. The variation between the original sample and the alternative sample is symmetrised and taken as the final uncertainty.

9.3.5 b/c-Hadron Production Fraction and Hadron-to-Muon Branching Ratio

The production fractions for b-hadrons and c-hadrons are well-measured by the PDG (see, for example, the PDG values for the production fractions for b-hadrons listed in Table 3.1). The same is true for the branching ratios of these hadrons for the semileptonic decay that produces a soft muon. The values for these production fractions and branching ratios as measured in MC simulation may differ from the PDG values, and these MC simulation samples must be reweighted to bring the values into line by applying scale factors to each event. Alongside the scale factors used to reweight to the nominal PDG values, additional scale factors are generated to obtain up/down-variations corresponding to the uncertainty on these PDG values. At the time of writing this thesis, the implementation of these uncertainties is still a work-in-progress, so the results in Chapter 13 are presented with an estimate from the previous ATLAS measurement [93].

Modelling Systematic	Components (Up/Down vs. Two-Point)
ISR	3 (Up/Down)
FSR	1 (Up/Down)
h_{damp} Variation	1 (Two-Point)
NLO Generator	1 (Two-Point)
Parton Shower	1 (Two-Point)
PDF	30 (Two-Point)
b/c-Hadron Production Fraction	7^* (Up/Down)
Hadron-to-Muon Branching Ratio	5^* (Up/Down)

Table 9.2 A summary of the modelling systematics included in the measurement presented in this thesis, along with how many up/down and two-point components are considered for each source of uncertainty. The asterisks denote the systematics for which the implementation is ongoing at the time of writing this thesis, and therefore the number of components is not final.

Chapter 10

ST/DT-Assignment

As introduced in Section 7.3 and presented in Fig. 7.1, there are two classes of events that make up the signal process for the analysis presented in this thesis. In the same-top case of Fig. 7.1(a), the prompt lepton (either an electron or a muon) and soft muon originate from the same side of the $t\bar{t}$ system (they either both come from the top quark, or both come from the antitop quark). In the different-top case of Fig. 7.1(b), the prompt lepton and soft muon originate from opposite sides of the $t\bar{t}$ system (with one coming from the top quark, and one coming from the antitop quark). To ensure correct values of the combined charge $q^{\ell\mu}$ are propagated to the observable charge asymmetries and underlying CP-violation asymmetries, it is necessary to figure out which events should be classified as same-top and which should be classified as different-top. ST/DT-assignment is the name given to this process, and this chapter describes the studies performed with MC simulations in order to optimise this process. It begins with Section 10.1, a discussion of the performance metrics by which ST/DT-assignment is to be assessed.

From comparing the leading-order Feynman diagrams, Fig. 7.1(a) and Fig. 7.1(b), the prompt lepton and soft muon appear as if they should be well separated in the detector. A naive solution would thus be to separate same-top and different-top events through the imposition of a cut on the total angular separation between the two particles, $\Delta R(\ell, \mu)$. This is explored in Section 10.2. However, due to NLO contributions from initial- and final-state gluon radiation, the situation is not as clear cut as the leading-order picture would suggest, and there is scope for the development of a more sophisticated method. The method employed by the previous ATLAS measurement was a statistical technique called kinematic likelihood fitting [93]. This method is again implemented, and is discussed in Section 10.3. However, this method was previously found to be highly sensitive to jet-related systematic uncertainties, accounting for a significant proportion of the uncertainty on the final results in the previous ATLAS measurement. A third approach is therefore introduced, with the aim of providing better performance than a simple method such as the $\Delta R(\ell, \mu)$, whilst being less sensitive to key systematic uncertainties than the kinematic likelihood fitting method. This approach is to make use of machine learning methods, also known as multivariate analysis. A BDT algorithm is implemented and trained on two feature sets, and the studies performed for this approach are detailed in Section 10.4.

The comparison of the performance of all of these methods, and the selection of the final method that is used to derive the final results of the measurement, are presented in Section 13.2.

10.1 Performance Metrics

While the ST/DT-assignment may at first glance seem vital in ensuring accurate results are obtained for the observable charge asymmetries and underlying CP-violation asymmetries, the situation needs to be considered in more depth. As the process of ST/DT-assignment (and the entire reconstruction process more generally) are extensively modelled in MC simulations and a process known as unfolding (to be discussed in detail in Chapter 11) is applied to correct for any mistakes such as getting the ST/DT-assignment wrong, any ST/DT-assignment method could, in theory, be used to derive accurate asymmetry results. This would include a hypothetical assignment method that amounted to random guessing, or a method that got the assignment wrong for every single event.

However, this does not mean that the ST/DT-assignment is unimportant or that the choice of method for performing it is irrelevant. Instead of affecting the accuracy of the results, the performance of the ST/DT-assignment will affect the uncertainty on these results. Not only will the performance affect the statistical uncertainty (a perfect correction would lead to a much smaller statistical uncertainty resulting from the unfolding process than a random guess would), but as discussed previously, the sensitivity of the chosen final method to systematic effects is expected to be a key contributor to the systematic uncertainties that apply to the final results. Therefore, the best way to select the final method is to assess all candidate methods on the resulting overall (statistical + systematic) uncertainty on the final asymmetries, and the results of doing this are presented in Section 13.3.

Whilst the overall uncertainty is to be used as the metric to make the final decision, it is useful to define simpler baseline metrics for assessing the standalone performance of ST/DT-assignment methods, in order to give an idea of how well a method can separate same-top and different-top events and act as a proxy for the overall uncertainty when performing method optimisation. Obtaining the overall uncertainty requires the entire analysis chain to be in place, and even then takes a lot more computing power than a simpler metric, making it unfeasible to use for methods such as those described in Section 10.4, where optimisation requires metrics to be computed many thousands of times.

The two key baseline metrics that are introduced are the efficiency and the purity. The efficiency is the fraction of true events for which the reconstructed ST/DT-status matches the true ST/DT-status, while the purity is the fraction of reconstructed events for which the reconstructed ST/DT-status matches the true ST/DT-status.

The full definitions of the same-top efficiency, $\varepsilon_{\mathrm{ST}}$, different-top efficiency, $\varepsilon_{\mathrm{DT}}$, and overall efficiency, ε, are

$$\varepsilon_{\mathrm{ST}} \equiv \frac{n(\text{reco same-top} \cap \text{truth same-top})}{n(\text{truth same-top})}, \tag{10.1}$$

$$\varepsilon_{\mathrm{DT}} \equiv \frac{n(\text{reco different-top} \cap \text{truth different-top})}{n(\text{truth different-top})}, \tag{10.2}$$

$$\varepsilon \equiv \frac{n(\text{reco same-top} \cap \text{truth same-top}) + n(\text{reco different-top} \cap \text{truth different-top})}{n(\text{truth same-top}) + n(\text{truth different-top})}. \quad (10.3)$$

Similarly, the full definitions of the same-top purity, ρ_{ST}, different-top purity, ρ_{DT}, and overall purity, ρ, are

$$\rho_{\mathrm{ST}} \equiv \frac{n(\text{reco same-top} \cap \text{truth same-top})}{n(\text{reco same-top})}, \quad (10.4)$$

$$\rho_{\mathrm{DT}} \equiv \frac{n(\text{reco different-top} \cap \text{truth different-top})}{n(\text{reco different-top})}, \quad (10.5)$$

$$\rho \equiv \frac{n(\text{reco same-top} \cap \text{truth same-top}) + n(\text{reco different-top} \cap \text{truth different-top})}{n(\text{reco same-top}) + n(\text{reco different-top})}. \quad (10.6)$$

In all of the above Eqs. 10.1 to 10.6, $n(C)$ refers to the number of events in a sample that satisfy condition C. It should be noted that for methods that assign ST/DT-status to all events in a sample, the overall efficiency and overall purity will be equal by construction, as $n(\text{truth same-top}) + n(\text{truth different-top}) = n(\text{reco same-top}) + n(\text{reco different-top})$. This is the case for the angular separation and machine learning methods (subject to only one cut being placed on the relevant distributions), but is not the case for the kinematic likelihood fitting method and may not be the case in general.

Additionally to the efficiency and purity, for methods that output a distribution rather than just a simple decision (such as the angular separation and machine learning methods), an additional metric is introduced, based on a plot of the receiver operating characteristic (ROC) curve. Initially introduced for the analysis of radar signals in the Second World War, ROC curves show the diagnostic power of a binary classifier over a range of decision thresholds (cut values below and above which the decision is made). They are traditionally labelled with the false positive rate and true positive rate, but as the aim of ST/DT-assignment is not strictly to discriminate between positives and negatives, it is more correct to label the axes of ROC curves with ε_{ST} and $(1 - \varepsilon_{\text{DT}})$ in this context. ROC curves show how the efficiency for both classes varies as the decision threshold is taken from one extreme at the bottom left corner in ROC space (at which all events are labelled as different-top, so $\varepsilon_{\text{ST}} = 0$ and $\varepsilon_{\text{DT}} = 1$), all the way to the other at the top right corner in ROC space (at which all events are labelled as same-top, so $\varepsilon_{\text{ST}} = 1$ and $\varepsilon_{\text{DT}} = 0$). A perfect classifier that correctly assigned every single event would be represented by a point in the top-left corner of ROC space (with $\varepsilon_{\text{ST}} = 1$ and $\varepsilon_{\text{DT}} = 1$), while a random classifier that guessed the status of each event at random would be represented by a straight line from the bottom left corner to the top right corner in ROC space. Therefore, a more performant classifier will fill more of the area in ROC space between the representation of the random classifier and the representation of the perfect classifier, and this is quantified with the final baseline metric, the ROC area under curve (AUC). The concept of ROC curves, showing all the elements described above, is illustrated in Fig. 10.1.

10.2 Angular Separation Method

The first method implemented for performing the ST/DT-assignment is conceptually simple. The total angular separation between the prompt lepton and soft muon is calculated, and a cut is placed on this distribution, below which events are assigned to be same-top, and above which events are assigned to be different-top. The calculation and distribution of $\Delta R(\ell, \mu)$ is presented in Section 10.2.1, and the performance results are discussed in Section 10.2.2.

10.2.1 Calculating $\Delta R(\ell, \mu)$

The total angular separation provides a combined measure of the difference in the the pseudorapidity, η, and the azimuthal angle, ϕ. The separate η distributions of the prompt lepton

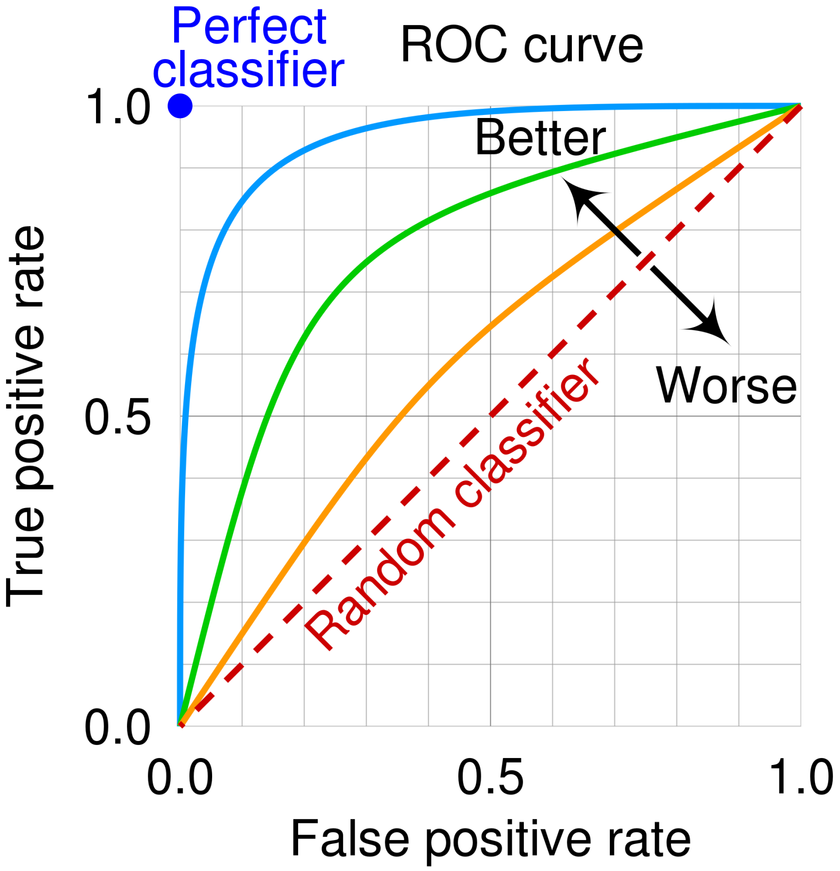

Figure 10.1 An illustration of ROC curves for a binary classifier, showing the curves for three example classifiers (from best performing to worst in blue, green, and orange respectively). Also shown are the representations of a perfect classifier and a random classifier [190].

and the soft muon are shown in Fig. 10.2, and the separate ϕ distributions of the prompt lepton and the soft muon are shown in Fig. 10.3. These show that individually, both the prompt lepton and soft muon pseudorapidity are distributed evenly around a central value of $\eta = 0$, with the troughs in the distribution being consequences of the areas of the detector with limited detection coverage, such as the calorimeter transition regions. Similarly, both the prompt lepton and soft muon azimuthal angle are distributed uniformly.

The differences in the pseudorapidity and azimuthal angle are calculated as

$$\Delta\eta(\ell,\mu) = |\eta(\ell) - \eta(\mu)|, \tag{10.7}$$

$$\Delta\phi(\ell,\mu) = \begin{cases} |\phi(\ell) - \phi(\mu)|, & |\phi(\ell) - \phi(\mu)| \leq \pi \\ 2\pi - |\phi(\ell) - \phi(\mu)|, & |\phi(\ell) - \phi(\mu)| > \pi \end{cases}, \tag{10.8}$$

where the multi-case structure of Eq. 10.8 ensures that values remain within the defined range of $-\pi < \phi \leq \pi$. The distribution of $\Delta\eta(\ell,\mu)$ is shown in Fig. 10.4, and the distribution of $\Delta\phi(\ell,\mu)$ is shown in Fig. 10.5. Breaking down the overall distributions into the same-top and different-top components shows separation between the two cases, with a higher level of separation in $\Delta\phi(\ell,\mu)$ than $\Delta\eta(\ell,\mu)$.

As introduced in Section 6.2.1, the total angular separation combines the two angular separations of Eqs. 10.7 and 10.8 as

$$\Delta R(\ell,\mu) = \sqrt{\Delta\eta(\ell,\mu)^2 + \Delta\phi(\ell,\mu)^2}. \tag{10.9}$$

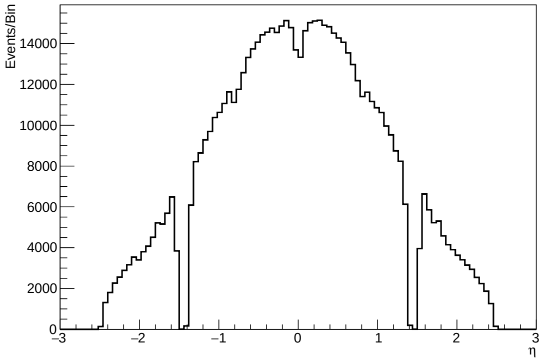

(a)

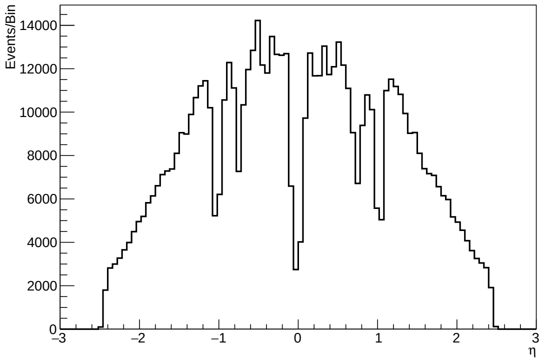

(b)

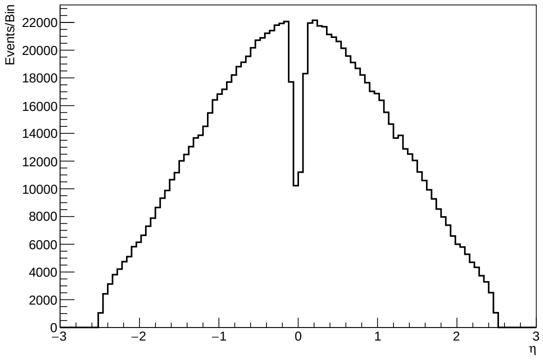

(c)

Figure 10.2 The distributions of the pseudorapidity, η, in MC simulation scaled to an integrated luminosity of $139\,\mathrm{fb}^{-1}$, for: **(a)** the prompt electron; **(b)** the prompt muon; **(c)** the soft muon.

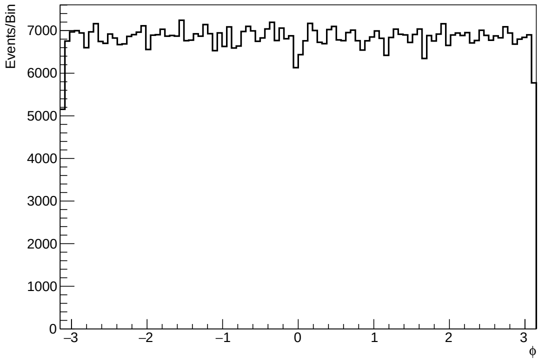

(a)

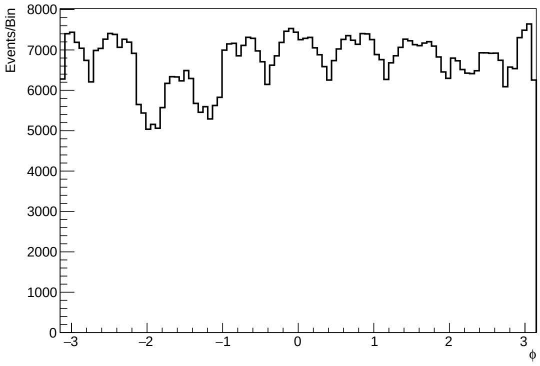

(b)

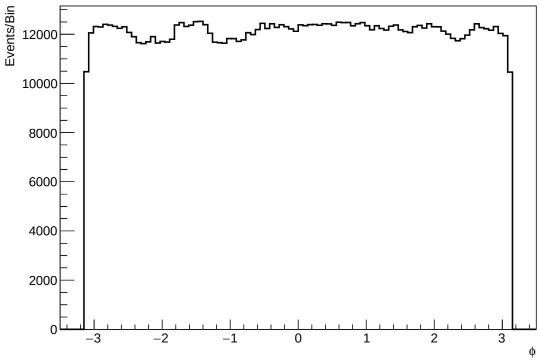

(c)

Figure 10.3 The distributions of the azimuthal angle, ϕ, in MC simulation scaled to an integrated luminosity of $139\,\mathrm{fb}^{-1}$, for: **(a)** the prompt electron; **(b)** the prompt muon; **(c)** the soft muon.

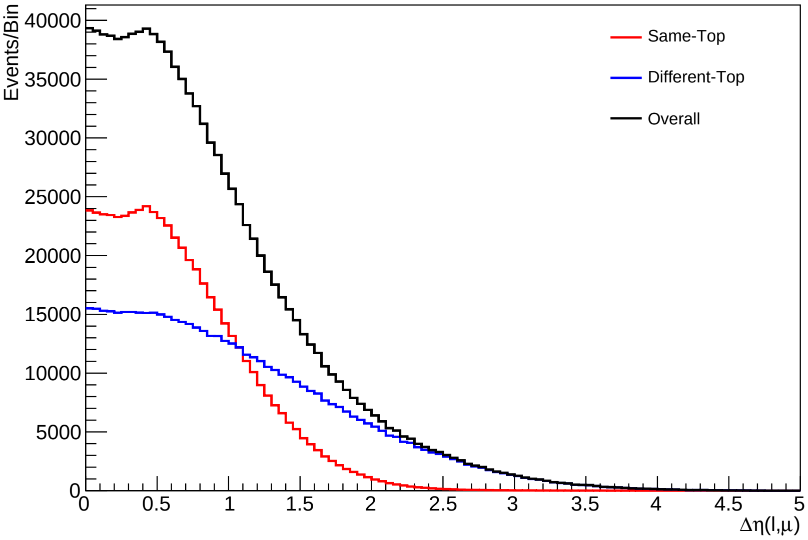

Figure 10.4 The difference in pseudorapidity between the prompt lepton and soft muon, $\Delta\eta(\ell, \mu)$, in MC simulation scaled to an integrated luminosity of 139 fb^{-1}.

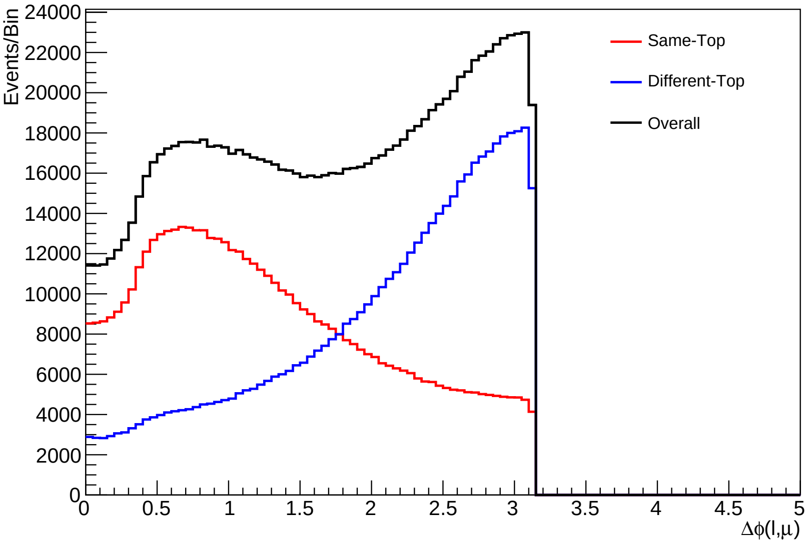

Figure 10.5 The difference in the azimuthal angle between the prompt lepton and soft muon, $\Delta\phi(\ell, \mu)$, in MC simulation scaled to an integrated luminosity of 139 fb^{-1}.

Due to all leptons being constrained by the selection cuts to $|\eta| < 2.5$, and the defined range of the azimuthal angle being $|\phi| \leq \pi$, the effective range for the total angular separation is $0 \leq \Delta R(\ell,\mu) \lesssim 5.905$. The distribution of $\Delta R(\ell,\mu)$ is shown in Fig. 10.6, with the overall distribution and the breakdown into the same-top and different-top components. The separation between the two cases is more significant than the separation that can be seen in Figs. 10.4 and 10.5.

10.2.2 Performance

In order to determine the optimal cut point, a range of $\Delta R(\ell,\mu)$ cuts are tested (from $\min(\Delta R(\ell,\mu)) = 0$ to $\max(\Delta R(\ell,\mu)) = 5.905$ in increments of 0.005), with the efficiency and purity being calculated for each cut. The ROC curve for such a cut is shown in Fig. 10.7, and the ROC AUC is 0.785 ± 0.002. The results for the same-top, different-top, and overall efficiency (purity) can be seen in Fig. 10.8(a) (Fig. 10.8(b)). The optimal cut point is seen to be at $\Delta R(\ell,\mu) = 2.050$, giving an overall efficiency and purity of $\varepsilon = \rho = 73.0 \pm 0.1\%$. All the above performance numbers are quoted with the associated statistical uncertainty.

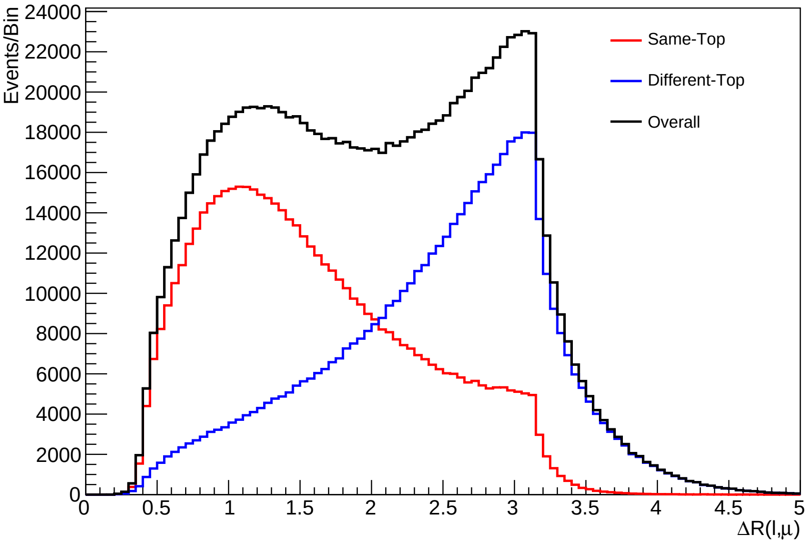

Figure 10.6 The total angular separation between the prompt lepton and soft muon, $\Delta R(l,\mu)$, in MC simulation scaled to an integrated luminosity of $139\,\mathrm{fb}^{-1}$.

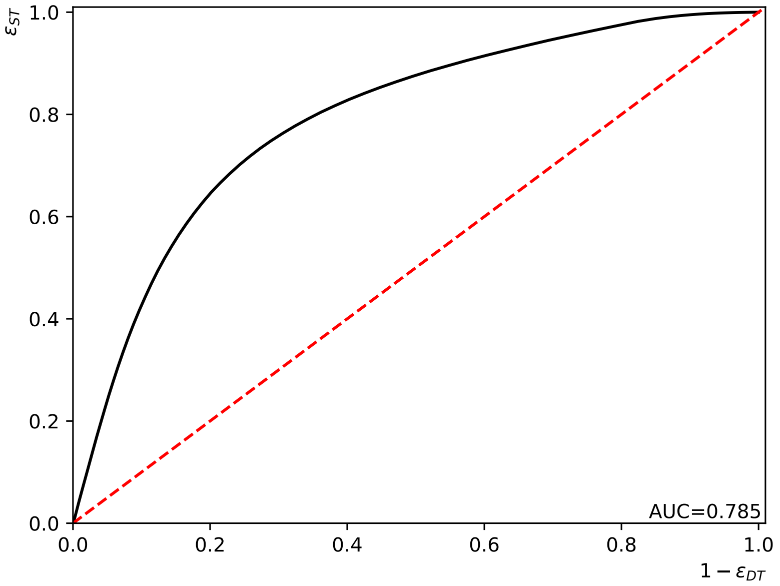

Figure 10.7 The ROC curve showing the effect of placing a cut on the total angular separation between the prompt lepton and soft muon, $\Delta R(\ell, \mu)$, on the same-top and different-top efficiencies, $\varepsilon_{\mathrm{ST}}$ and $\varepsilon_{\mathrm{DT}}$, in MC simulation scaled to an integrated luminosity of $139\,\mathrm{fb}^{-1}$. The plot also shows the value of the ROC AUC metric for this curve, and the dotted red line represents the expected performance of a random classifier.

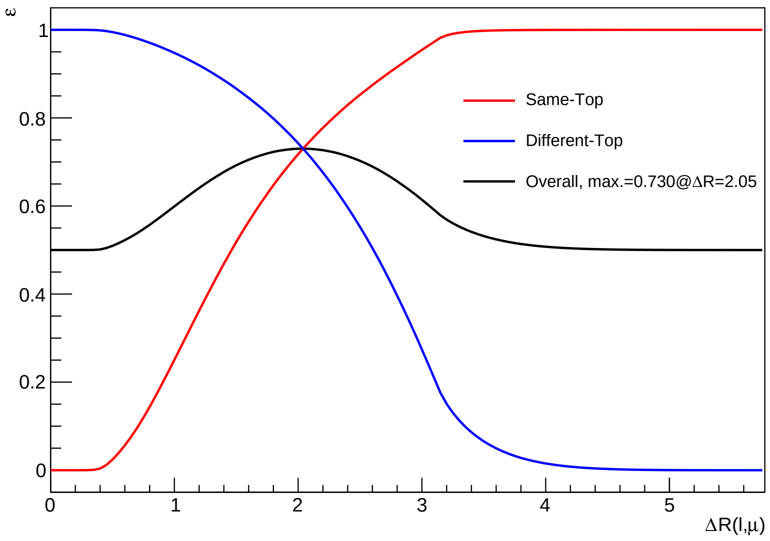

(a)

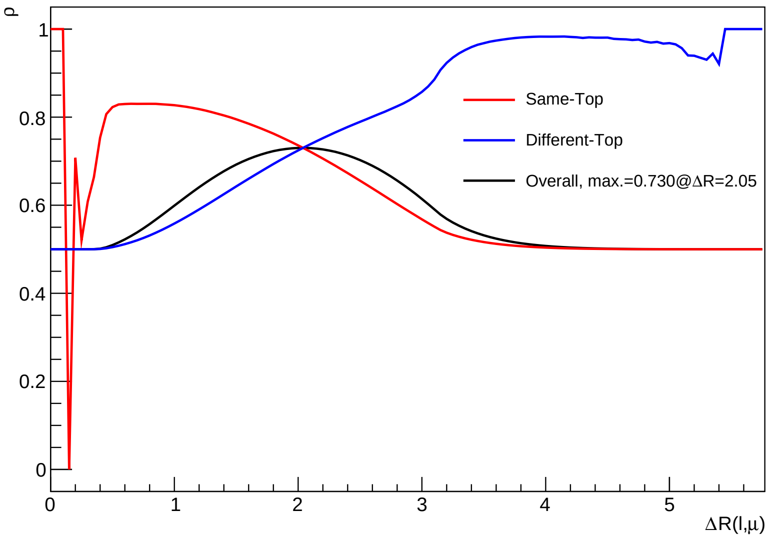

(b)

Figure 10.8 The results of placing a range of cuts on the total angular separation between the prompt lepton and soft muon, $\Delta R(\ell, \mu)$, in MC simulation scaled to an integrated luminosity of $139\,\text{fb}^{-1}$, showing: **(a)** the efficiency, ε; **(b)** the purity, ρ.

10.3 Kinematic Likelihood Fitting Method

The second approach implemented for the ST/DT-assignment is a likelihood-based kinematic fitting method, performed with the `KLFitter` package [191, 192]. The idea is to use this likelihood-based method to establish which is the most likely association of reconstructed objects to the expected truth decay products. One such permutation of associations for four reconstructed jets would be that the first jet is associated with the truth b, the second jet is associated with the truth $\bar{b}$, and the third and fourth jets are associated interchangeably with the truth light quarks from the hadronic W. Another permutation would be to instead associate the first jet with the truth $\bar{b}$, the second jet with the truth b, and the third and fourth jets with the truth light quarks. All such permutations are assessed in turn to determine which is considered most likely. The likelihood function used by the `KLFitter` package is described in Section 10.3.1, with Section 10.3.2 detailing the work that was carried out to optimise the method and apply a correction for the momentum carried away by the neutrino in order to improve performance. The performance results are discussed in Section 10.3.3.

10.3.1 Likelihood Function and Permutation Ranking

The likelihood function for each permutation is defined as

$$\begin{aligned}\mathcal{L} = &\mathcal{B}(m_{q_1q_2q_3}|m_t,\Gamma_t)\cdot\mathcal{B}(m_{q_1q_2}|m_W,\Gamma_W)\cdot\mathcal{B}(m_{q_4\ell\nu}|m_t,\Gamma_t)\cdot\mathcal{B}(m_{\ell\nu}|m_W,\Gamma_W)\\ &\cdot\prod_{i=1}^{4}W_{jet}(E^{meas}_{jet,i}|E^{truth}_{jet,i})\cdot W_\ell(E^{meas}_\ell|E^{truth}_\ell) \qquad ,\\ &\cdot W_{miss}(E^{\mathrm{miss},meas}_{\mathrm{T},x}|p^{truth}_{\nu,x})\cdot W_{miss}(E^{\mathrm{miss},meas}_{\mathrm{T},y}|p^{truth}_{\nu,y})\end{aligned} \tag{10.10}$$

where the parentheses in each term contain reco-level quantities in the first part, and truth-level quantities in the second part. For the reconstructed quantities: $m_{q_1q_2q_3}$, $m_{q_1q_2}$, $m_{q_4\ell\nu}$, and $m_{\ell\nu}$ are invariant masses calculated from the reconstructed particles' four-momenta, $E^{meas}_{jet,i}$ and E^{meas}_ℓ are the measured energies of the reconstructed jets and prompt lepton, and

$E_{\mathrm{T},x}^{\mathrm{miss},meas}$ and $E_{\mathrm{T},y}^{\mathrm{miss},meas}$ are the x- and y-components of the measured missing transverse momentum. For the truth quantities: m_t, Γ_t and m_W, Γ_W are the known (fixed) masses and decay widths of the top quark and W, $E_{jet,i}^{truth}$, E_{ℓ}^{truth} are the energies of the true jets and prompt lepton, and $p_{\nu,x}^{truth}$, $p_{\nu,y}^{truth}$ are the x- and y- components of the true neutrino momentum. The first four terms in the likelihood quantify the agreement between the reconstructed invariant masses with the known values of the true masses and decay widths, by way of Breit-Wigner constraints, $\mathcal{B}$, of the form

$$\mathcal{B}(m_{reco}|m_{true}, \Gamma_{true}) = \frac{1}{(m_{reco}^2 - m_{true}^2)^2 + m_{true}^2 \Gamma_{true}^2}. \tag{10.11}$$

The remaining terms constrain the values of the true energies and momenta (which are the free parameters that are varied to maximise the likelihood) using the measured values, by way of transfer functions, W. These are conditional probability distributions for obtaining a particular reconstructed value given a particular true value, and are highly detector-dependent. For the ATLAS detector they are parametrised by five parameters, q_i with $i \in \{1, \ldots, 5\}$, which are fitted to distributions in MC simulations. For the energy, the functions are modelled as double Gaussian functions of the form

$$W(E^{meas}|E^{truth}) = \frac{1}{\sqrt{2\pi}(q_2 + q_3 q_5)} \left[e^{-\frac{(\Delta E - q_1)^2}{2q_2^2}} + q_3 e^{-\frac{(\Delta E - q_4)^2}{2q_5^2}} \right], \tag{10.12}$$

with $\Delta E = \frac{E^{truth} - E^{meas}}{E^{truth}}$, while a standard Gaussian function is used for the $E_{\mathrm{T}}^{\mathrm{miss}}$ transfer function [193]. This takes the form

$$W(E_{\mathrm{T}}^{\mathrm{miss},meas}|p_{\nu}^{truth}) \propto \left[e^{-\frac{\Delta E_{\mathrm{T}}}{2\sigma^2}} \right], \tag{10.13}$$

with $\Delta E_{\mathrm{T}} = p_{\nu}^{truth} - E_{\mathrm{T}}^{\mathrm{miss},meas}$ and $\sigma = q_1 + \frac{q_2}{1+e^{-q_3(p_{\nu}^{truth}-q_4)}}$.

Once the likelihood of Eq. 10.10 has been maximised for each individual permutation, a probability is defined for each permutation in the event. For the i^{th} permutation, this is

$$p_i = \frac{\mathcal{L}_i}{\sum_k \mathcal{L}_k}, \tag{10.14}$$

where $\mathcal{L}_i$ and $\mathcal{L}_k$ are the maximised likelihoods of the i^{th} and k^{th} permutations respectively, with k running over all the possible permutations in an event. Permutations are then ranked according to this probability to decide which is the most likely association of jets with truth-level objects. Examining which truth-level object the SMT-tagged jet is associated with can then be used to infer whether the event is a same-top or different-top event.

10.3.2 Optimisation

The `KLFitter` likelihood fitting procedure, as described above in Section 10.3.1, can be configured by adjusting several setup options. All such setup options are investigated, and assessed in MC simulation in order to provide an optimised setup with the best performance. The best setup options (as assessed by overall efficiency, see Section 10.1) are found to be:

- Consider all possible permutations of five jets (it is unfeasible to consider all permutations for a large number of jets, as the number of permutations, N, scales with the number of jets, n, as $N = \frac{n!}{2(n-4)!}$ - `KLFitter` allows for a choice between $n = 4$, for which $N = 12$, and $n = 5$, for which $N = 60$).
- These five jets are selected by first selecting any b-tagged jets (see Section 7.1.1), and then selecting jets in descending order of p_{T}.
- Veto any permutations where SMT-tagged jets are assigned to a light jet position (i.e. SMT-tagged jets must be associated to the b or $\bar{b}$ - this is necessary to perform the

ST/DT-assignment, but results in a small drop in overall efficiency due to events where the SMT-tagged jets do not get selected for consideration as described above).

- The top mass parameter, m_t, is fixed to the underlying value used in the MC simulation, similarly to the other mass and decay width parameters (it can instead be considered a free parameter of the fit).

As well as these setup options, it is possible to specify an extension to the likelihood function of Eq. 10.10. This is known as the angular extended likelihood, and adds additional terms to the base likelihood to account for the predicted distribution of helicity in the electroweak W decays [194]. The angular extended likelihood, $\mathcal{L}_{ext}$, is given by

$$\mathcal{L}_{ext} = \mathcal{L} \cdot \frac{1}{\Gamma_W} \frac{d\Gamma_W}{d\cos(\theta^*_{q,b_{had}})} \cdot \frac{1}{\Gamma_W} \frac{d\Gamma_W}{d\cos(\theta^*_{\ell,b_{lep}})}, \tag{10.15}$$

with

$$\frac{1}{\Gamma_W} \frac{d\Gamma_W}{d\cos(\theta^*_{q,b_{had}})} = \frac{3}{4} F_0 (1 - \cos(\theta^*_{q,b_{had}})^2) + \frac{3}{8} (F_L + F_R)(1 + \cos(\theta^*_{q,b_{had}})^2), \tag{10.16}$$

$$\frac{1}{\Gamma_W} \frac{d\Gamma_W}{d\cos(\theta^*_{\ell,b_{lep}})} = \frac{3}{4} F_0 (1 - \cos(\theta^*_{\ell,b_{lep}})^2) + \frac{3}{8} F_L (1 - \cos(\theta^*_{\ell,b_{lep}}))^2 + \frac{3}{8} F_R (1 + \cos(\theta^*_{\ell,b_{lep}}))^2. \tag{10.17}$$

$\theta^*_{q,b_{had}}$ is defined as the angle between the direction of the truth-level light quark and the reverse direction of the b-quark associated to the hadronically-decaying W, and $\theta^*_{\ell,b_{lep}}$ is defined as the angle between the direction of the truth-level prompt lepton and the reverse direction of the b-quark associated to the leptonically-decaying W. $F_0 = 0.687$, $F_L = 0.311$, and $F_R = 0.0017$ are respectively the fractions of W-decays with longitudinal, left-handed, and right-handed helicity [195]. The angular extended likelihood is found to provide a better overall efficiency than the base likelihood, and is therefore selected as the preferred method.

A final option is investigated to further boost the `KLFitter` performance, which is to apply a semileptonic correction (SLC) to the SMT-tagged jets. The soft muon and neutrino which are produced in the semileptonic decay of a b-hadron or c-hadron carry energy and momentum, and therefore the momentum of a jet that is reconstructed after this decay will have a correspondingly lower energy/momentum and slightly displaced direction when compared to the original energy/momentum and direction of the initial b-quark. As terms in the likelihood function are attempting to match this reconstructed jet to the initial b-quark, failure to account for the products of the semileptonic decay will lead to lower performance for SMT-tagged jets for which these decays have taken place. The SLC adjusts the four-momentum of the SMT-tagged jet to account for this effect.

A theoretically perfect SLC would adjust the four-momentum vector of the jet, $p^{\text{jet}} = (p_{\text{T}}^{\text{jet}}, \eta^{\text{jet}}, \phi^{\text{jet}}, E^{\text{jet}})$, by adding the four-momenta of the soft muon, p^{μ}, and the neutrino, p^{ν}, to obtain the post-correction four-momentum, $p_{\text{SLC}}^{\text{jet}}$, as

$$p_{\text{SLC}}^{\text{jet}} = p^{\text{jet},*} + p^{\mu,*} + p^{\nu}, \tag{10.18}$$

where $p^{\text{jet},*}$ and $p^{\mu,*}$ are the four-momenta of the jet and soft muon after correctly accounting for the muon energy loss due to ionisation of the material in the detector. This energy, E_{loss}^{μ}, is reconstructed as part of the jet, despite originating from the soft muon. The level of energy lost is well understood, and so it is possible to correct this by making the adjustments

$$E^{\text{jet},*} = E^{\text{jet}} - E_{\text{loss}}^{\mu}, \tag{10.19}$$

$$E^{\mu,*} = E^{\mu} + E^{\mu}_{\text{loss}}, \tag{10.20}$$

and then using these adjusted energy values to recompute the four-momenta in order to get $p^{\text{jet},*}$ and $p^{\mu,*}$.

A perfect SLC as described by Eq. 10.18 can only be obtained in truth-level MC simulation when the neutrino's four-momentum is known. For reconstruction-level, the neutrino passes out of the detector without interacting. The soft muon four-momentum is well-defined, but the measured E_{T}^{miss} is not sufficient to disentangle the neutrino from the semileptonic decay in the SMT-tagged jet from the neutrino from the W-boson decay. Under the assumption that the energy scale is high enough that the soft muon can be considered massless, the soft muon and neutrino would on average be expected to be produced with equal energy, leading to

$$p^{\text{jet}}_{\text{SLC}} = p^{\text{jet},*} + p^{\mu,*} + p^{\nu} \approx p^{\text{jet},*} + 2p^{\mu,*}. \tag{10.21}$$

In order to avoid relying on this potentially naive assumption, a generalised version of this correction is considered:

$$p^{\text{jet}}_{\text{SLC}} = p^{\text{jet},*} + p^{\mu,*} + p^{\nu} \approx p^{\text{jet},*} + \alpha p^{\mu,*}, \tag{10.22}$$

and a range of values of α are checked, in steps of 0.05 from $\alpha = 1.50$ to $\alpha = 2.1$, and the best performance (in all of overall, same-top, and different-top efficiency and purity) is found to be for $\alpha = 2.0$, in line with the massless limit assumption. The performance is also tested for the truth-based perfect SLC, to see how the performance compares to the level of performance that would be achievable if the neutrino could be reconstructed.

10.3.3 Performance

The performance of various configurations is shown in Table 10.1. The addition of the angular extended likelihood and the best SLC with $\alpha = 2.0$ both provide an increase in performance across all metrics, and both of these options are therefore selected for the final configuration. Comparing this final configuration to the truth-based perfect SLC shows that a further increase in performance would be possible if full neutrino reconstruction could be achieved, but that this further increase in performance is relatively small - the SLC with $\alpha = 2.0$ achieves 94.0% (93.3%) of the increase in overall efficiency (purity) that would be gained by using a perfect SLC.

Configuration	ε	$\varepsilon_{\mathrm{ST}}$	$\varepsilon_{\mathrm{DT}}$	ρ	ρ_{ST}	ρ_{DT}
Optimised Setup, Base LH	$69.4 \pm 0.1\%$	$65.6 \pm 0.1\%$	$73.2 \pm 0.1\%$	$70.8 \pm 0.1\%$	$72.5 \pm 0.1\%$	$69.2 \pm 0.1\%$
Optimised Setup, Angular Ext. LH	$70.1 \pm 0.1\%$	$66.5 \pm 0.1\%$	$73.7 \pm 0.1\%$	$71.5 \pm 0.1\%$	$73.1 \pm 0.1\%$	$69.9 \pm 0.1\%$
Optimised Setup, Angular Ext. LH, SLC ($\boldsymbol{\alpha = 2.0}$)	$\mathbf{78.0 \pm 0.1\%}$	$\mathbf{76.7 \pm 0.1\%}$	$\mathbf{79.3 \pm 0.1\%}$	$\mathbf{78.5 \pm 0.1\%}$	$\mathbf{79.2 \pm 0.1\%}$	$\mathbf{77.8 \pm 0.1\%}$
Optimised Setup, Angular Ext. LH, Perfect SLC	$78.5 \pm 0.1\%$	$77.4 \pm 0.1\%$	$79.6 \pm 0.1\%$	$79.0 \pm 0.1\%$	$79.6 \pm 0.1\%$	$78.4 \pm 0.1\%$

Table 10.1 The performance results for various `KLFitter` configurations, including different likelihoods (LH) and different forms of SLC. The performance is assessed in terms of the efficiency, ε, and purity, ρ, both for the overall sample and separately for same-top and different-top events. The performance for the final setup of the algorithm is highlighted. All numbers are derived from MC simulation scaled to an integrated luminosity of $139\,\mathrm{fb}^{-1}$, and are quoted with their associated statistical uncertainty.

10.4 Machine Learning Method

The third approach for the ST/DT-assignment is to implement a machine learning method, specifically a supervised binary-classification algorithm. Such algorithms are trained using a labelled dataset, comprising events for which the value of a binary target variable, $\mathbf{y}$, is known. The training process then results in a function, f, that maps a set of input features, X, to the value of this binary target variable, such that $f(X) = \mathbf{y}$. This function, also known as a classifier, can then be applied to a separate dataset for which the target variable is not known, in order to make predictions of this variable.

In the case of ST/DT-assignment, the target variable is the ST/DT-status, defined to be 1 for same-top events and -1 for different-top events. The input features are a subset of the measured physical properties of objects such as leptons and jets (see Table 6.1 and Section 6.2.1). The labelled dataset is obtained from MC simulations where the truth-level ST/DT-status is known. This labelled dataset is split into two samples, with 75% (the training dataset) being used for training and optimisation, and the remaining 25% (the testing dataset) being held back as an independent sample to test model performance. Events are split into the training and testing dataset in a stratified manner, meaning one in four same-top events is selected at random to go into the testing dataset, and the rest go into the training dataset. This process is repeated for different-top events. This ensures that the balance of same-top versus different-top events is the same between both datasets.

The feature sets constructed to train the machine learning method are introduced in Section 10.4.1, followed by an explanation of the algorithms and software packages used in Section 10.4.2. Sections 10.4.3 and 10.4.4 then details the work carried out to optimise and assess the performance of the implemented method.

10.4.1 Constructing Input Feature Sets

It is not necessarily the case that all the quantities measured by the ATLAS detector are passed as input features to the machine learning algorithms. Due to the largest systematic uncertainties in the previous round of the analysis being the jet-related systematics, two feature sets are considered [93]. The first of these is a purely leptonic feature set, denoted X_ℓ, where none of the jet-related variables are used as input features. The second is a full feature set, defined as X_f, comprising both leptonic and jet-related variables.

X_ℓ comprises:

- The kinematic and intrinsic properties of the prompt lepton, as shown in Fig. 10.9: p_T^ℓ, E^ℓ, η^ℓ, ϕ^ℓ, q^ℓ, and binary variables (with value 1 if true, 0 if false) for whether the prompt lepton is an electron or a muon.
- The kinematic and intrinsic properties of the soft muon, as shown in Fig. 10.10: p_T^μ, E^μ, η^μ, ϕ^μ, q^μ, d_0^μ, $|\frac{d_0}{\sigma(d_0)}|^\mu$, and $(z_0 \sin\theta)^\mu$.
- The neutrino-related kinematic quantities, as shown in Fig. 10.11: $E_\mathrm{T}^\mathrm{miss}$, $\phi(E_\mathrm{T}^\mathrm{miss})$, and $m_\mathrm{T}(W)$.
- The angular separations between the prompt lepton and soft muon, as shown in Fig. 10.12: $\Delta\eta(\ell,\mu)$, $\Delta\phi(\ell,\mu)$, and $\Delta R(\ell,\mu)$.

Examining Figs. 10.9 to 10.12, it can be seen that most of the constituent features of X_ℓ show little to no separation between same-top and different-top events. There is a small level of separation visible for the prompt lepton transverse momentum (Fig. 10.9(a)), energy (Fig. 10.9(b)), and charge (Fig. 10.9(e)). There is no separation visible in any of the soft muon features, but a small level of separation is visible in the missing transverse momentum (Fig. 10.11(a)) and the transverse W-mass (Fig. 10.11(c)). The largest separation can be seen in the angular separation features (Figs. 10.12(a) to 10.12(c)), which further reinforces the motivations behind choosing $\Delta R(\ell,\mu)$ as the candidate for a single-variable ST/DT-assignment method as explored in Section 10.2.

X_f comprises all the above leptonic features, plus:

- The kinematic and flavour-tag properties of the four highest-p_T jets (with index $i \in \{1,\ldots,4\}$): $p_\mathrm{T}^{\mathrm{jet},i}$, $E^{\mathrm{jet},i}$, $\eta^{\mathrm{jet},i}$, $\phi^{\mathrm{jet},i}$, and binary variables for whether the jets are b-tagged with `DL1r` or SMT-tagged. These features are shown in Fig. 10.13 for the highest-p_T jet, with the distributions for the second-, third-, and fourth-highest looking similar (but with correspondingly lower p_T and E distributions).

- Additional angular separations between the SMT-tagged jet and other physics objects: $\Delta\eta(\mathrm{jet}^{\mathrm{SMT}}, \ell)$, $\Delta\phi(\mathrm{jet}^{\mathrm{SMT}}, \ell)$, and $\Delta R(\mathrm{jet}^{\mathrm{SMT}}, \ell)$, as shown in Fig. 10.14; $\Delta\eta(\mathrm{jet}^{\mathrm{SMT}}, \mu)$, $\Delta\phi(\mathrm{jet}^{\mathrm{SMT}}, \mu)$, and $\Delta R(\mathrm{jet}^{\mathrm{SMT}}, \mu)$, as shown in Fig. 10.15; and $\Delta\eta(\mathrm{jet}^{\mathrm{SMT}}, \mathrm{jet}^{i})$, $\Delta\phi(\mathrm{jet}^{\mathrm{SMT}}, \mathrm{jet}^{i})$, and $\Delta R(\mathrm{jet}^{\mathrm{SMT}}, \mathrm{jet}^{i})$, as shown in Fig. 10.16.

As with X_ℓ, examining Fig. 10.13 (and the equivalent distributions for the second-, third-, and fourth-highest-p_T jets) shows that the majority of the kinematic features of X_f show very little separation, although a small level of separation is visible in the transverse momentum (Fig. 10.13(a)), energy (Fig. 10.13(b)), and flavour-tagging (Figs. 10.13(e) and 10.13(f)) features. The distributions (and level of separation) of the angular separation features for the SMT-tagged jet and prompt lepton (Figs. 10.14(a) to 10.14(c)) mirror the leptonic angular separation features (Figs. 10.12(a) to 10.12(c)), as would be expected from the fact that the soft muon and SMT-tagged jet are intrinsically linked. A small level of separation can also be seen in the angular separation features for the SMT-tagged jet and soft muon (Figs. 10.15(a) to 10.15(c)). Separation can be seen in all of the angular separation features for the SMT-tagged jet and the four highest-p_T jets (Figs. 10.16(a) to 10.16(l)), which makes intuitive sense as the spatial arrangement of jets has proved to have discriminating power in top-reconstruction methods such as `KLFitter`, as introduced in Section 10.3.

It is important to note that a key element of machine learning methods is their multivariate nature, meaning not only can they make use of all the single-feature separations seen here, they excel in utilising the correlations between features to pick up separations that may only be apparent when considering multiple feature dimensions.

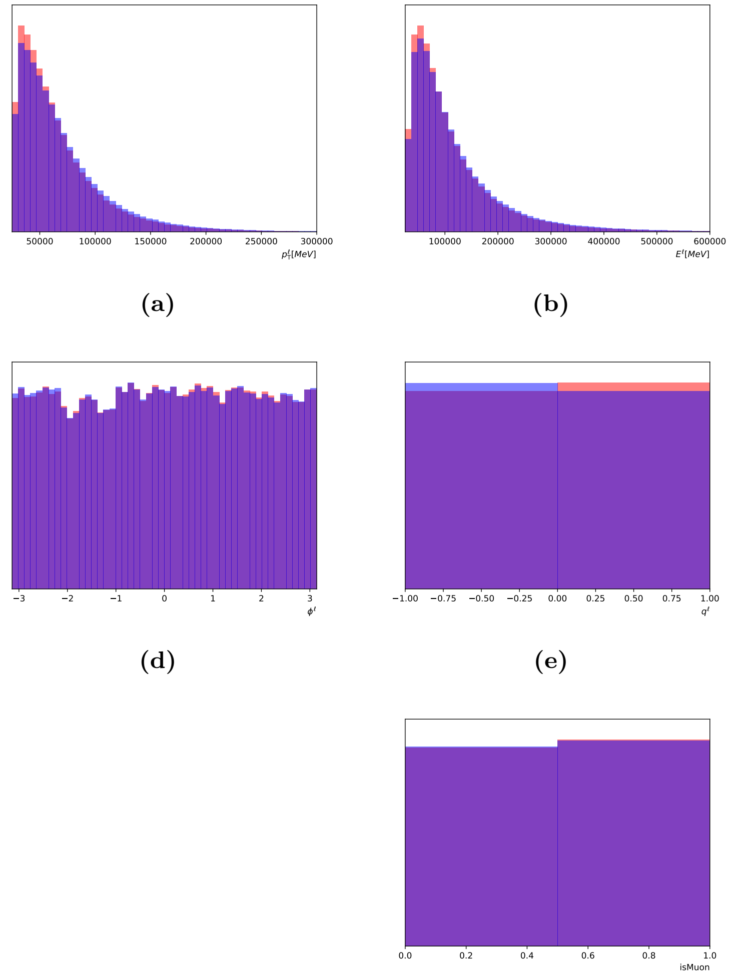

(a) **(b)** **(c)**

(d) **(e)** **(f)**

(g)

Figure 10.9 The normalised distributions of the prompt lepton input features on the training dataset, with the true same-top events shown in red and the true different-top events shown in blue, comprising: **(a)** p_{T}^{ℓ}; **(b)** E^{ℓ}; **(c)** η^{ℓ}; **(d)** ϕ^{ℓ}; **(e)** q^{ℓ}; **(f)** `isElectron`; **(g)** `isMuon`.

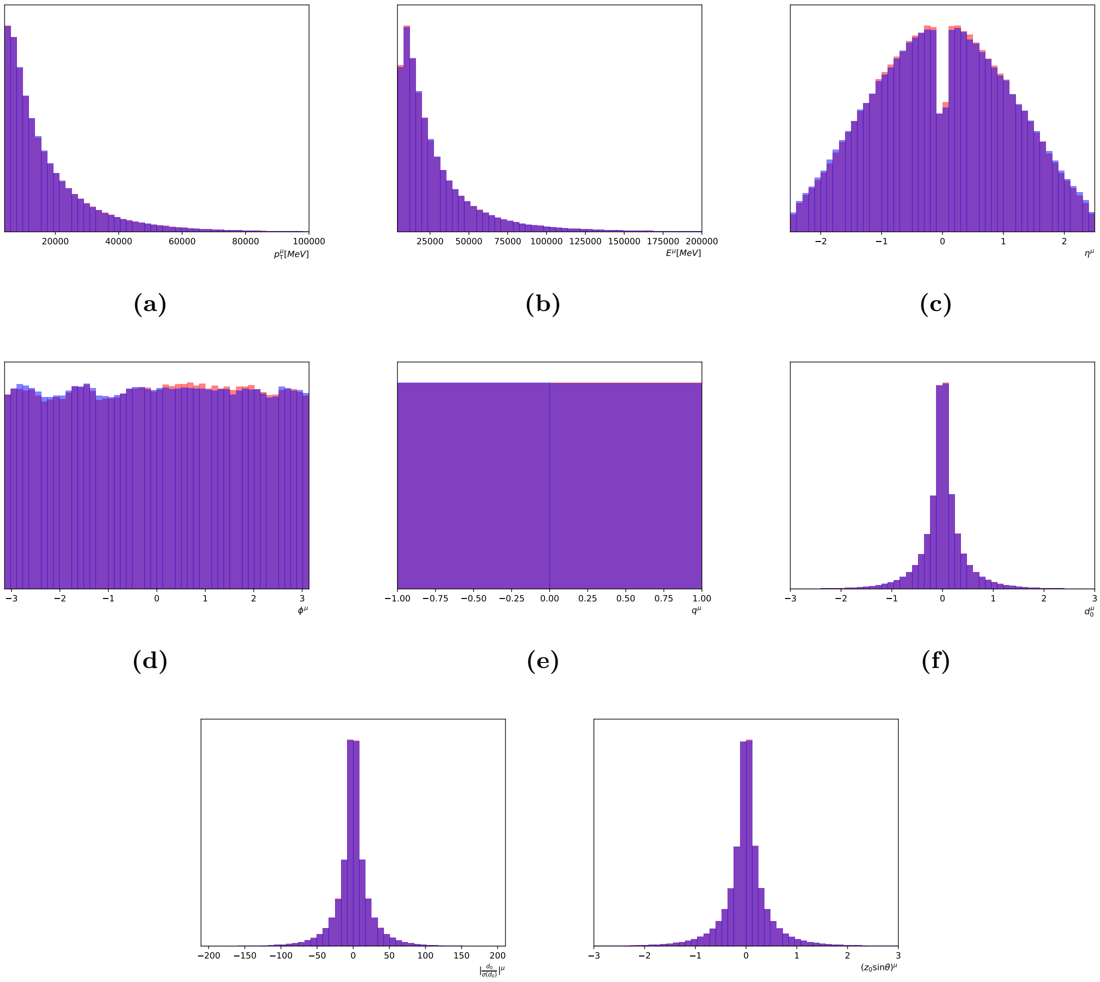

(a) **(b)** **(c)**

(d) **(e)** **(f)**

(g) **(h)**

Figure 10.10 The normalised distributions of the soft muon input features on the training dataset, with the true same-top events shown in red and the true different-top events shown in blue, comprising: **(a)** p_{T}^{μ}; **(b)** E^{μ}; **(c)** η^{μ}; **(d)** ϕ^{μ}; **(e)** q^{μ}; **(f)** d_0^{μ}; **(g)** $|\frac{d_0}{\sigma(d_0)}|^{\mu}$; **(h)** $(z_0 \sin\theta)^{\mu}$.

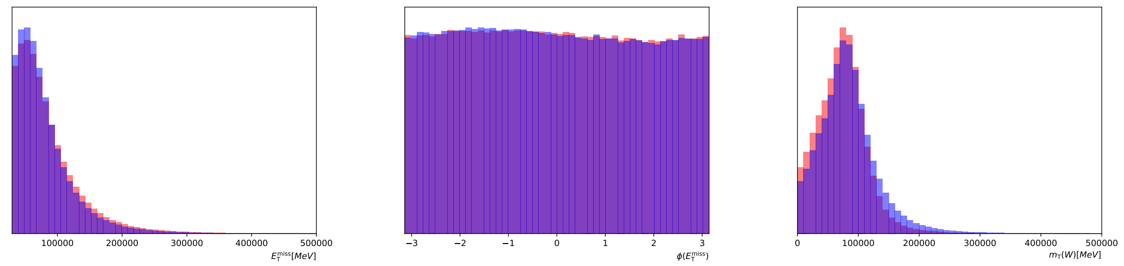

(a) **(b)** **(c)**

Figure 10.11 The normalised distributions of the neutrino-related input features on the training dataset, with the true same-top events shown in red and the true different-top events shown in blue, comprising: **(a)** $E_{\mathrm{T}}^{\mathrm{miss}}$; **(b)** $\phi(E_{\mathrm{T}}^{\mathrm{miss}})$; **(c)** $m_{\mathrm{T}}(W)$.

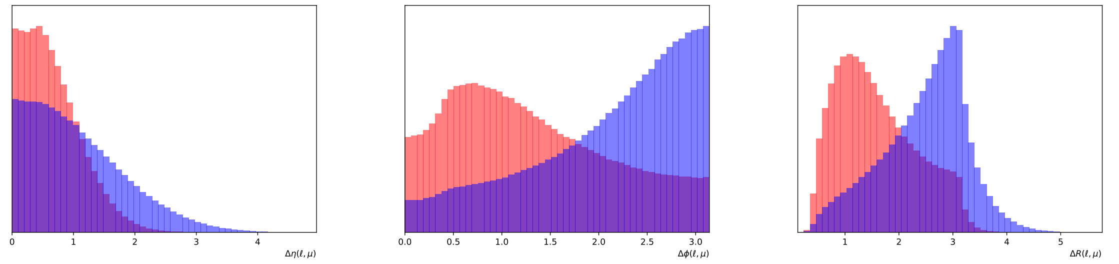

(a) **(b)** **(c)**

Figure 10.12 The normalised distributions of the angular separation input features on the training dataset, with the true same-top events shown in red and the true different-top events shown in blue, comprising: **(a)** $\Delta\eta(\ell,\mu)$; **(b)** $\Delta\phi(\ell,\mu)$; **(c)** $\Delta R(\ell,\mu)$.

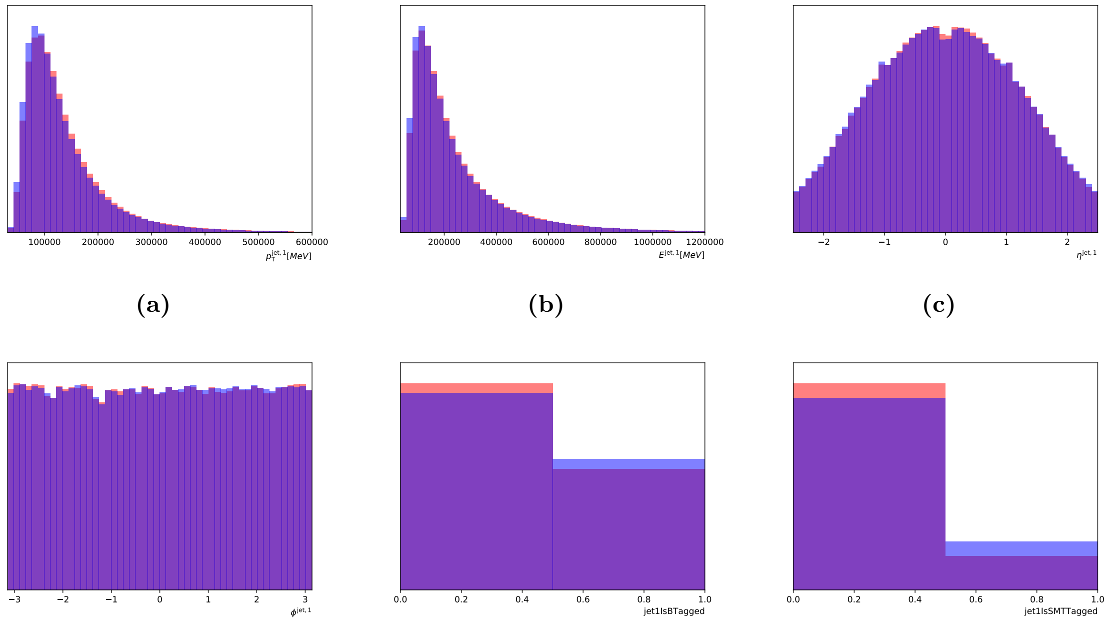

(a) **(b)** **(c)**

(d) **(e)** **(f)**

Figure 10.13 The normalised distributions of the kinematic input features for the highest-p_{T} jet on the training dataset, with the true same-top events shown in red and the true different-top events shown in blue, comprising: **(a)** $p_{\mathrm{T}}^{\mathrm{jet},1}$; **(b)** $E^{\mathrm{jet},1}$; **(c)** $\eta^{\mathrm{jet},1}$; **(d)** $\phi^{\mathrm{jet},1}$; **(e)** `jet1IsBTagged`; **(f)** `jet1IsSMTTagged`.

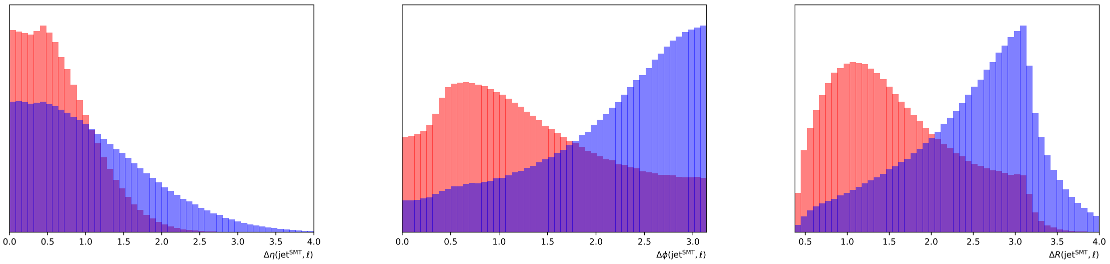

(a) **(b)** **(c)**

Figure 10.14 The normalised distributions of the angular separation input features for the SMT-tagged jet and the prompt lepton on the training dataset, with the true same-top events shown in red and the true different-top events shown in blue, comprising: **(a)** $\Delta\eta(\mathrm{jet}^{\mathrm{SMT}}, \ell)$; **(b)** $\Delta\phi(\mathrm{jet}^{\mathrm{SMT}}, \ell)$; **(c)** $\Delta R(\mathrm{jet}^{\mathrm{SMT}}, \ell)$.

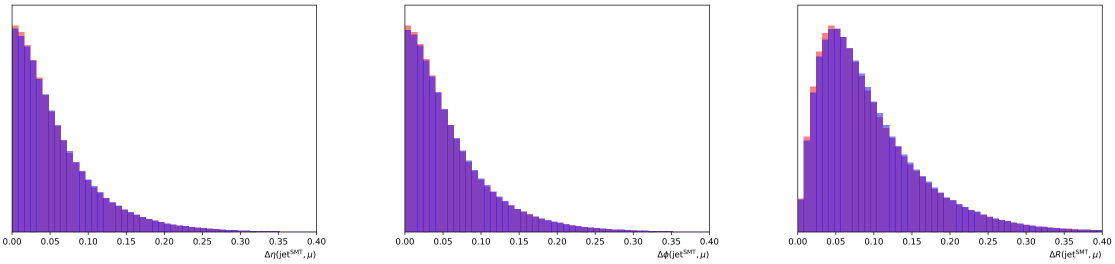

(a) **(b)** **(c)**

Figure 10.15 The normalised distributions of the angular separation input features for the SMT-tagged jet and the soft muon on the training dataset, with the true same-top events shown in red and the true different-top events shown in blue, comprising: **(a)** $\Delta\eta(\mathrm{jet}^{\mathrm{SMT}}, \mu)$; **(b)** $\Delta\phi(\mathrm{jet}^{\mathrm{SMT}}, \mu)$; **(c)** $\Delta R(\mathrm{jet}^{\mathrm{SMT}}, \mu)$.

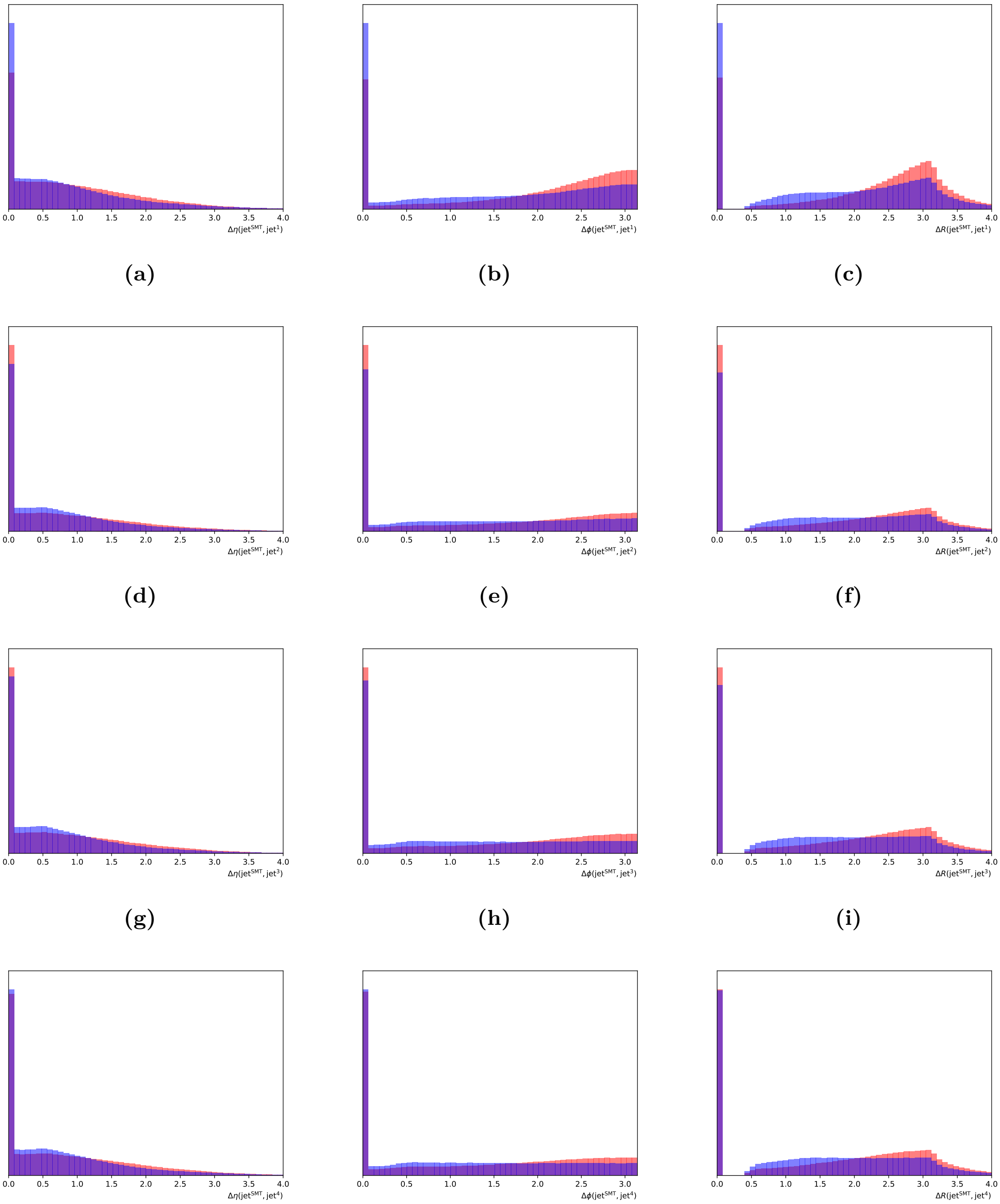

(a) **(b)** **(c)**

(d) **(e)** **(f)**

(g) **(h)** **(i)**

(j) **(k)** **(l)**

Figure 10.16 The normalised distributions of the angular separation input features for the SMT-tagged jet and the four highest-p_{T} jets on the training dataset, with the true same-top events shown in red and the true different-top events shown in blue, comprising: **(a)** $\Delta\eta(\mathrm{jet}^{\mathrm{SMT}}, \mathrm{jet}^{1})$; **(b)** $\Delta\phi(\mathrm{jet}^{\mathrm{SMT}}, \mathrm{jet}^{1})$; **(c)** $\Delta R(\mathrm{jet}^{\mathrm{SMT}}, \mathrm{jet}^{1})$; **(d)** $\Delta\eta(\mathrm{jet}^{\mathrm{SMT}}, \mathrm{jet}^{2})$; **(e)** $\Delta\phi(\mathrm{jet}^{\mathrm{SMT}}, \mathrm{jet}^{2})$; **(f)** $\Delta R(\mathrm{jet}^{\mathrm{SMT}}, \mathrm{jet}^{2})$; **(g)** $\Delta\eta(\mathrm{jet}^{\mathrm{SMT}}, \mathrm{jet}^{3})$; **(h)** $\Delta\phi(\mathrm{jet}^{\mathrm{SMT}}, \mathrm{jet}^{3})$; **(i)** $\Delta R(\mathrm{jet}^{\mathrm{SMT}}, \mathrm{jet}^{3})$; **(j)** $\Delta\eta(\mathrm{jet}^{\mathrm{SMT}}, \mathrm{jet}^{4})$; **(k)** $\Delta\phi(\mathrm{jet}^{\mathrm{SMT}}, \mathrm{jet}^{4})$; **(l)** $\Delta R(\mathrm{jet}^{\mathrm{SMT}}, \mathrm{jet}^{4})$.

10.4.2 BDT Algorithms

The type of algorithm considered for the ST/DT-assignment is a BDT. A BDT is an example of an ensemble method, where the predictions of many weak learners (which as individual classifiers may only be slightly better than a random guess) are combined in order to construct a strong classifier with a good level of performance [196].

The concept of decision trees as classifiers was developed in the 1970s and 1980s. An early algorithm, introduced in 1986, was the `Iterative Dichotomiser 3 (ID3)` algorithm [197]. The successor to `ID3` was the `C4.5` algorithm, expanding the options for configuring a decision tree and allowing for the handling of numerical features, as `ID3` was only able to handle categorical features [198]. Roughly parallel to the development of `ID3` and `C4.5`, the first versions of the `Classification and Regression Trees (CART)` algorithm were developed [199]. As the name suggests, `CART` is designed to be usable as both a classifier (as in the case of ST/DT-assignment) and a regressor (to predict a value of a continuous numerical target variable). The decision tree classifiers used in this thesis make use of an updated version of `CART`, accessed through the `scikit-learn` package [200]. This package is designed to provide a simple, efficient, and accessible interface to many popular machine learning algorithms and data preparation techniques [201].

A decision tree is made up of decision nodes, at which a dataset is split according to a cut on one or more of the data features. The feature(s) and value(s) used are determined by minimising a specified quantity, with the general aim of a binary classification tree being to increase the separation between the two classes. Each decision node splits the data into two subsets, and each subset can then be passed to another decision node for further splitting. This leads to the algorithm's eponymous tree-like structure. The number of times the data is split is known as the depth of the tree, and the final subsets of data that are used to determine the target variable are known as leaf nodes. An example of a simple decision tree is shown in Fig. 10.17.

The boosting process involves training a large quantity of low-depth decision trees. The first such tree is trained on the original dataset. For the training of the next tree, also known

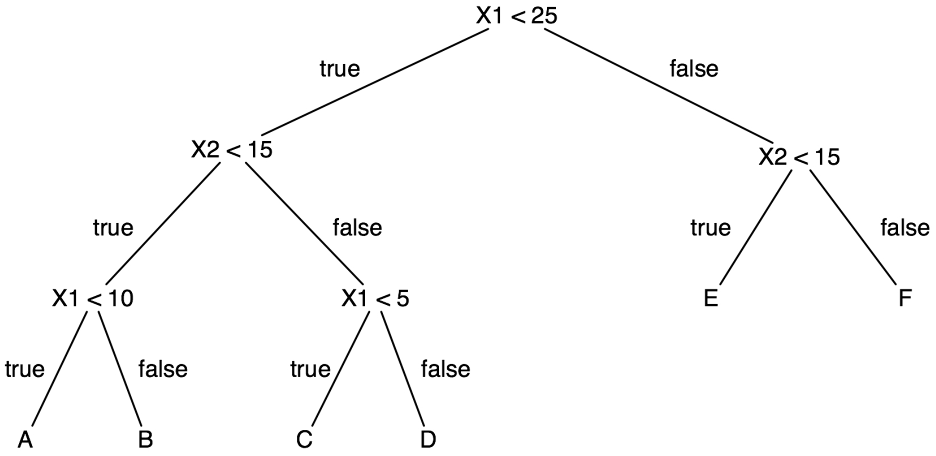

Figure 10.17 An example of a `CART` decision tree of depth three, which splits data into six leaf nodes by making decisions on two example features, $X1$ and $X2$ [202].

as the next boosting iteration, the dataset is reweighted so that previously misclassified events are given a higher weight, while events that were previously classified correctly are given a lower weight. This process is repeated for a large number of iterations, with the final classifier being a weighted sum of the decision trees from each iteration. A conceptual illustration of the boosting process is shown in Fig. 10.18. Different BDT algorithms provide different schemes for the reweighting procedure with each boosting iteration, along with the multipliers used to come up with the final ensemble classifier.

The specific algorithm implemented for performing the ST/DT-assignment is `Adaptive Boosting (AdaBoost)`, developed by Freund and Schapire [204–207]. As with the base decision trees, `AdaBoost` is accessed through the `scikit-learn` package. The `AdaBoost` algorithm uses an exponential error formula to update the weights and combine the individual decision trees with each boosting iteration. The algorithm is shown in full in Fig. 10.19.

10.4.3 Optimisation

The `AdaBoost` classifier possesses a number of freely adjustable model hyperparameters. These are in contrast to the model parameters, which are the parameters that are algorithmically adjusted in the training process, such as weights and multipliers. Despite not being adjusted

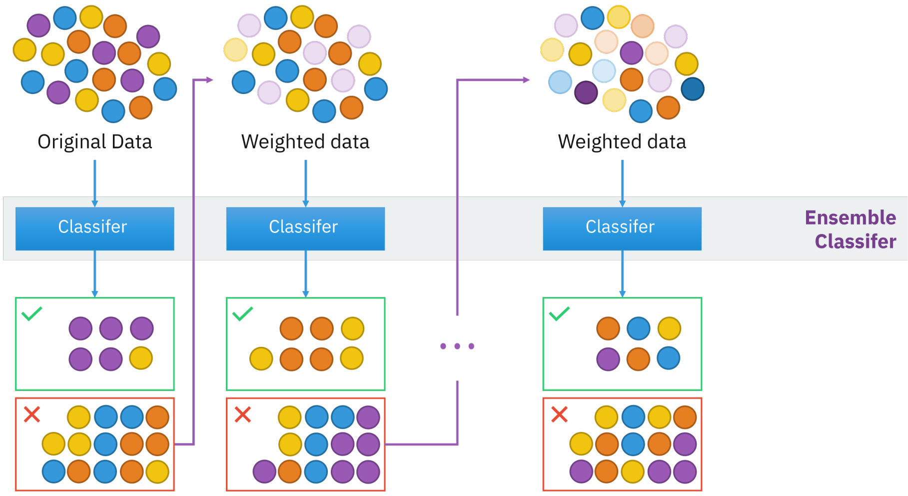

Figure 10.18 A conceptual illustration of the boosting process for combining individual weak classifiers into a strong ensemble classifier. The final decision of each classifier is used to reweight the input data for the next classifier. The translucent datapoints are given a reduced weight as they were previously classified correctly, while the opaque datapoints are given an increased weight as they were previously misclassified [203].

Take a training dataset of n events, with input feature set $X = \{X^1, \ldots, X^n\}$, labels $\mathbf{y} = \{y^1, \ldots, y^n\}$ with $y^i \in \{-1, 1\}$, and initialised event weights $\mathbf{w_0} = \{w_0^1, \ldots, w_0^n\}$ with $w_0^i = \frac{1}{n}$, where $i = 1, ..., n$. Define $h(X)$ as a weak classifier, and $f(X)$ as the ensemble classifier.

For $t = 1, ..., T$, with T the number of boosting iterations:
· Select the best weak classifier $h_t(\mathbf{w_t}, X)$ that minimises a weighted error function, $\epsilon_t(\mathbf{w_{t-1}}, X, \mathbf{y})$.
· Set a multiplier $\alpha_t = \frac{1}{2}\ln(\frac{1-\epsilon_t}{\epsilon_t})$.
· Add weak classifier to ensemble hypothesis: $f_t = f_{t-1}(X) + \alpha_t h_t(X)$.
· Update weights: $w_t^i = w_{t-1}^i e^{-y^i \alpha_t h_t(X^i)}$.
· Renormalise weights so that $\sum_i w_t^i = 1$.

Output final hypothesis $f_T(X) = \sum_t \alpha_t h_t(X)$.

Figure 10.19 The `AdaBoost` algorithm [204–207].

algorithmically, these hyperparameters can nonetheless affect the performance of a trained classifier. As such, they need to be optimised to ensure that the best performance is achieved. This optimisation is done by way of an exhaustive grid search of all possible combinations of hyperparameters, with the performance being assessed for each combination. After all hyperparameter combinations have been tested, the most performant combination is selected to be used for the final classifier.

To try and ensure that the selected best hyperparameter combination will generalise well beyond the training dataset, the search makes use of a statistical technique called k-fold cross-validation, with $k = 5$. This means that the training dataset is split into five folds (subsets). Five classifiers are then trained for each possible combination of hyperparameters. For each of these five classifiers, four of the folds are used in the training, with the fifth being used to assess the results. The performance of the hyperparameter combination is then taken as the average performance of these five classifiers. The concept of the data splitting for k-fold cross-validation is illustrated in Fig. 10.20.

For `AdaBoost`, the hyperparameters to be optimised are:

- The quantity H to be minimised by a base decision tree to determine the best split of the data S at a given decision node m, comprising n_S datapoints. Two options are considered: the entropy, $H(S) = -\sum_k p_{mk} \log p_{mk}$, and the Gini impurity, $H(S) = \sum_k p_{mk}(1 - p_{mk})$, where p_{mk} is the proportion of S at node m with target value $y = k$.
- The maximum depth of a base decision tree. Depths between one and five are considered.
- The number of boosting iterations, or equivalently the number of weak classifiers that contribute to the final ensemble. Values of 10, 20, 50, 100, and 200 are considered.
- The learning rate, which is an additional multiplier added to each weak classifier to reduce the effect it has on the final ensemble. Values of 0.1, 0.2, 0.3, 0.5, and 1.0 are considered.

This results in a total of 250 hyperparameter combinations to be checked, and the final combination of hyperparameters is chosen to maximise the overall efficiency (and equivalently purity).

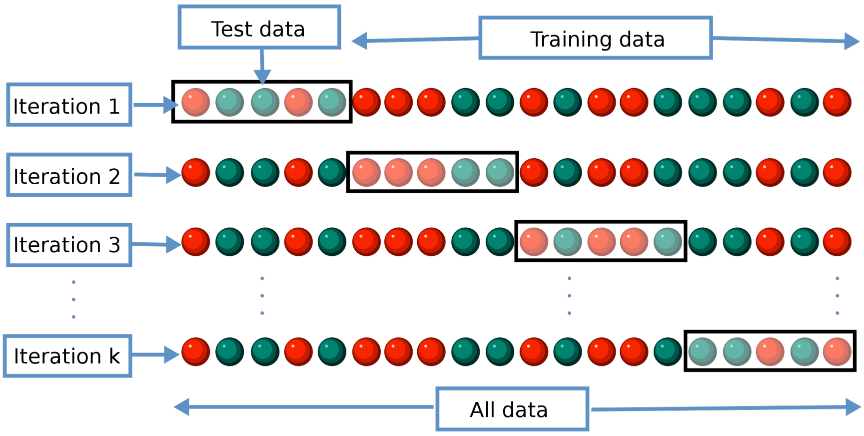

Figure 10.20 A conceptual illustration of the method known as k-fold cross-validation, by which the performance is assessed as an average across k iterations. The data is split into k subsets known as folds, and for each iteration one of these folds is held back to assess the performance, while the other $k-1$ folds are used for training [208].

The final hyperparameters selected for feature set X_ℓ are as follows:

- The final quantity H to be minimised by a base decision tree is entropy.
- The final maximum depth of a base decision tree is five.
- The final number of boosting iterations is 200.
- The final learning rate is 0.5.

The final hyperparameters selected for feature set X_f are as follows:

- The final quantity H to be minimised by a base decision tree is Gini impurity.
- The final maximum depth of a base decision tree is five.
- The final number of boosting iterations is 200.
- The final learning rate is 1.0.

While the selected value for the number of boosting iterations is at the maximum of the range tested, the efficiency was monitored per iteration up to this point and found to be essentially flat by 200 iterations, so higher numbers of iterations were not considered.

For both feature sets, while these final hyperparameters were chosen to maximise the overall efficiency, the same combination also results in the maximum ROC AUC.

10.4.4 Performance

The trained and optimised `AdaBoost` classifier maps the input features to an output known as a BDT score. The distribution of this BDT score is shown in Fig. 10.21.

The ST/DT-assignment is performed by making a cut on the BDT score distribution, above which events are assigned to be same-top and below which events are assigned to be different-top. In order to determine the optimal cut point, a range of cuts are tested (from the minimum BDT score to the maximum BDT score in increments of 0.001), with the efficiency and purity being calculated for each cut. The results for the same-top, different-top, and overall efficiency (purity) can be seen in Fig. 10.22 (Fig. 10.23), and the ROC curve can be seen in Fig. 10.24. Comparison of Fig. 10.21(a) with Fig. 10.21(b) and Fig. 10.24(a) with Fig. 10.24(b) shows good agreement between the training and testing datasets for both feature sets, demonstrating robustness to overfitting to statistical fluctuations and, consequently, good expected generalisability to new data (although the agreement between the training and testing datasets can be seen to be marginally better for X_ℓ than for X_f). As is to be expected by virtue of introducing more input features, the classifier trained on X_f outperforms the classifier trained on X_ℓ across all baseline metrics, with the latter achieving an overall efficiency and purity of $76.9 \pm 0.1\%$ and ROC AUC of 0.858 ± 0.002 and the former achieving an overall efficiency and purity of $82.8 \pm 0.1\%$ and ROC AUC of 0.912 ± 0.002, where all numbers are quoted with the associated statistical uncertainty.

It is instructive to attempt to understand the physical motivations behind the performances of these classifiers, rather than simply treating them as black-box solutions. The final BDT score is a prediction from an ensemble of individual decision trees. Each of these trees is highly

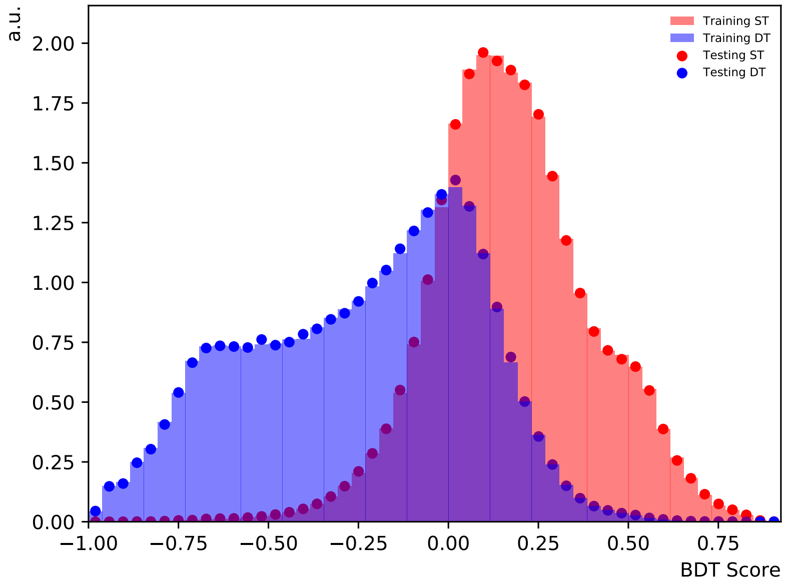

(a)

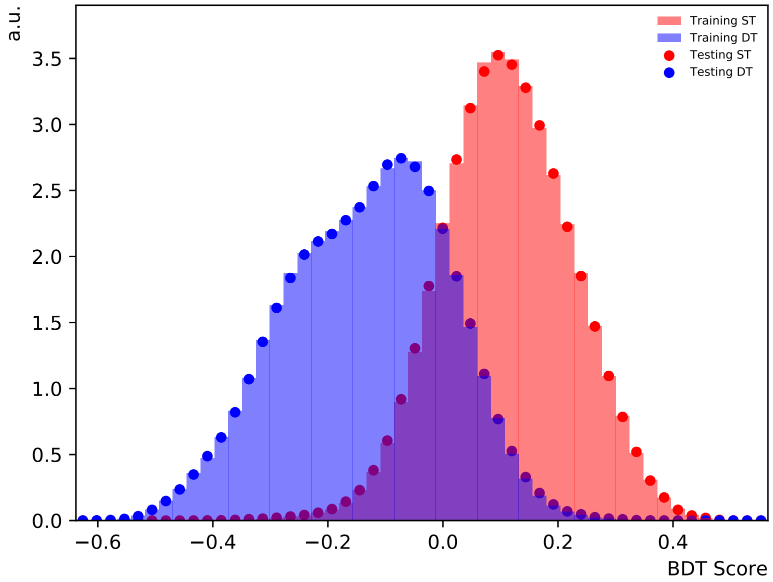

(b)

Figure 10.21 The BDT score for the optimised `AdaBoost` classifiers trained in MC simulation scaled to an integrated luminosity of 139 fb^{-1}, with true same-top events in red and true different-top events in blue. The histograms represent the training dataset, and the dotted markers represent the testing dataset. The distributions of the BDT score are normalised to have unit area in order to accurately compare distribution shape, which means that the height of each bin is in arbitrary units (a.u.). The BDT score distribution is shown separately for the classifier trained on: **(a)** the purely leptonic feature set, X_ℓ; **(b)** the full feature set, X_f.

interpretable. For example, if a decision tree of depth one splits on a particular feature, it can be inferred that the feature in question has good predictive power, and quantify to what extent. This interpretability is reduced when examining the overall ensemble prediction. However, the `sklearn` package implements a method to compute the importance of a feature. This was originally introduced for an alternative ensemble technique known as random forests, it is equally applicable to a boosting ensemble technique such as `AdaBoost` [209]. This importance is obtained by calculating the mean reduction in the quantity to be minimised (also known as the impurity) across all instances where the feature is selected for splitting. Features appearing at higher levels in the decision trees (and therefore being used to split a larger fraction of the data, i.e. giving a large reduction in impurity) will be given more importance than those appearing at lower levels (and therefore being used to split a relatively small fraction of the data, i.e. giving a small reduction in impurity). Usage of this impurity-based feature importance metric must be caveated with the fact that the method has been found to be biased towards continuous or high-cardinality features, so may not give an accurate reflection of the importance of categorical features with a small number of potential values [210]. However, as the majority of features used in the `AdaBoost` classifiers described above are continuous in nature, the impurity-based feature importance is still informative.

The 15 features with the highest impurity-based importance from X_ℓ and X_f are shown in Figs. 10.25(a) and 10.25(b) respectively. Examining Fig. 10.25(a), it can be seen that the feature from X_ℓ with the highest importance is $\Delta R(\ell, \mu)$, followed by the p_T of the soft muon and prompt lepton. This aligns with the physical justification of $\Delta R(\ell, \mu)$ as a feature of interest expected to have high discriminating power, as explored in Section 10.2, and fits with the separations seen in the single-feature distributions presented in Section 10.4.1. Examining Fig. 10.25(b), it can be seen that the feature from X_f with the highest importance is $\Delta R(\mathrm{jet}^\mathrm{SMT}, \ell)$. Again, this makes sense from a physical perspective, as $\Delta R(\mathrm{jet}^\mathrm{SMT}, \ell)$ would be expected to give a better measure of the angular separation between the parton-level W-boson and b-quark than $\Delta R(\ell, \mu)$, which is a combination of $\Delta R(\mathrm{jet}^\mathrm{SMT}, \ell)$ and $\Delta R(\mathrm{jet}^\mathrm{SMT}, \mu)$, and thus contains a small contribution from the diverging trajectory of the soft muon from the b-jet (although this is constrained to $\Delta R(\mathrm{jet}^\mathrm{SMT}, \mu) < 0.4$ by the selection cuts). The angular separations and transverse momenta of the jets make up a large proportion of the top 15 features from X_f, which again lines up with the trends seen in the single-feature distributions presented in Section 10.4.1, and motivates the higher level of separative performance seen for this feature set when compared to X_ℓ.

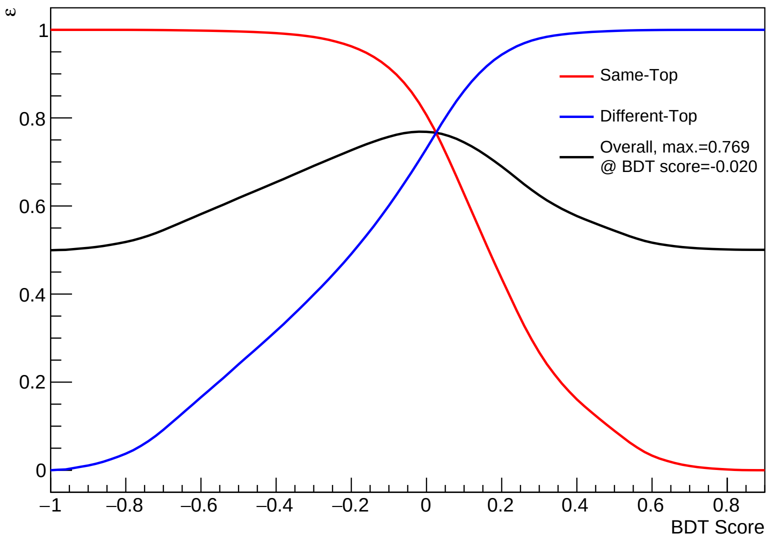

(a)

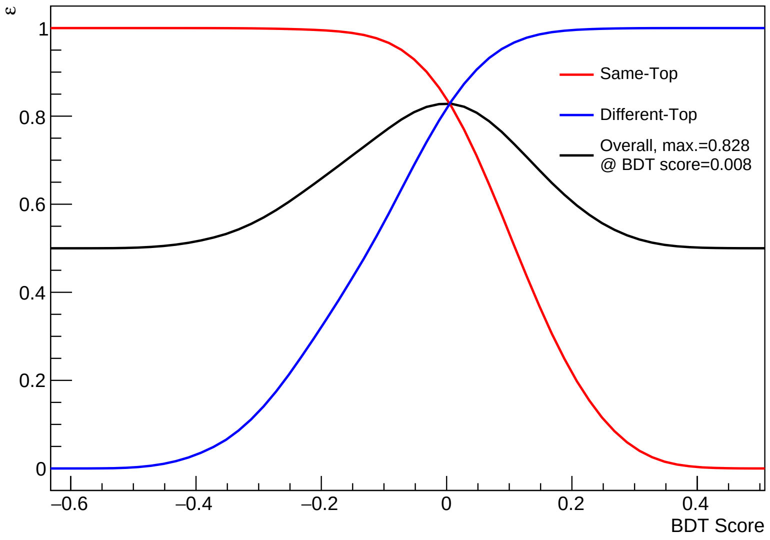

(b)

Figure 10.22 The efficiency, ε, for a range of cuts on the BDT score distribution of `AdaBoost` classifiers trained in MC simulation scaled to an integrated luminosity of $139\,\mathrm{fb}^{-1}$. The results are shown separately for the classifier trained on: **(a)** the purely leptonic feature set, X_ℓ; **(b)** the full feature set, X_f.

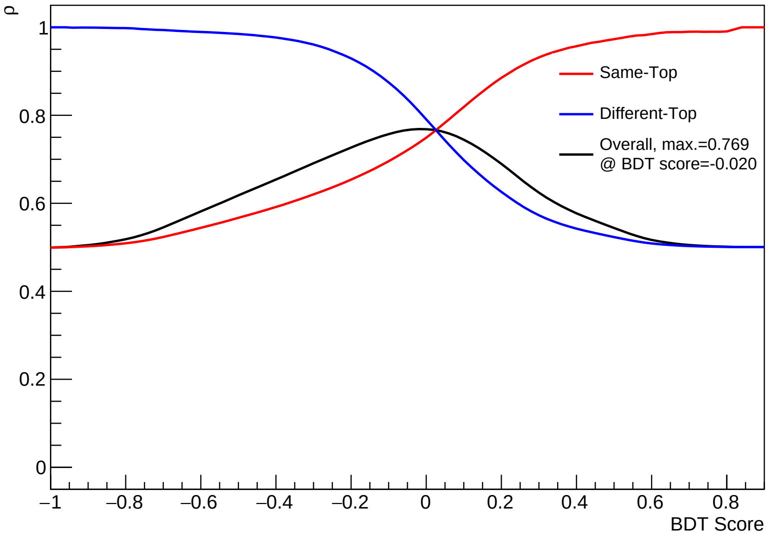

(a)

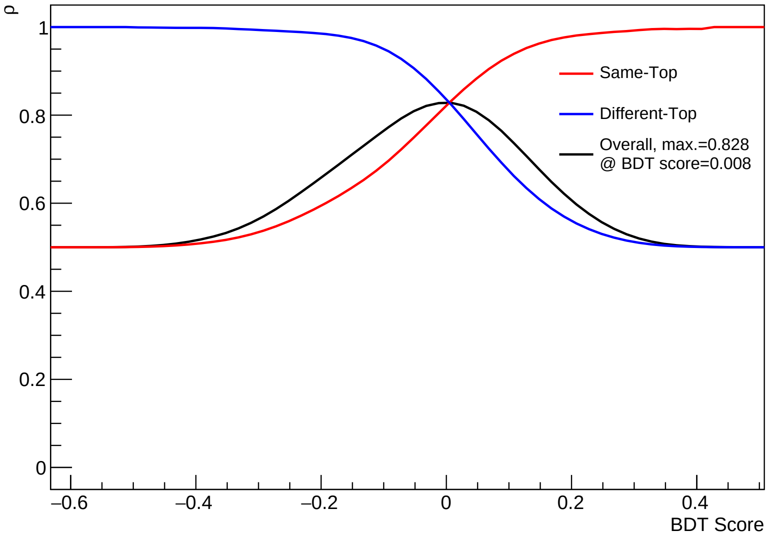

(b)

Figure 10.23 The purity, ρ, for a range of cuts on the BDT score distribution of `AdaBoost` classifiers trained in MC simulation scaled to an integrated luminosity of $139\,\text{fb}^{-1}$. The results are shown separately for the classifier trained on: **(a)** the purely leptonic feature set, X_ℓ; **(b)** the full feature set, X_f.

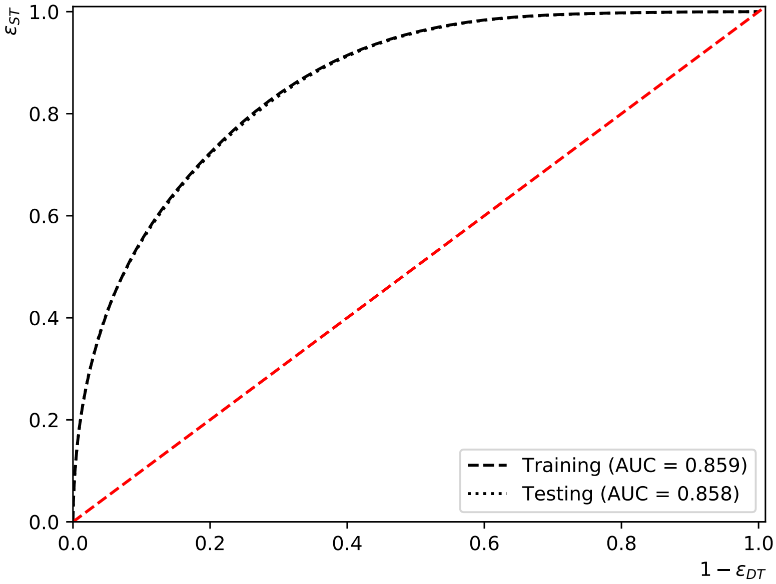

(a)

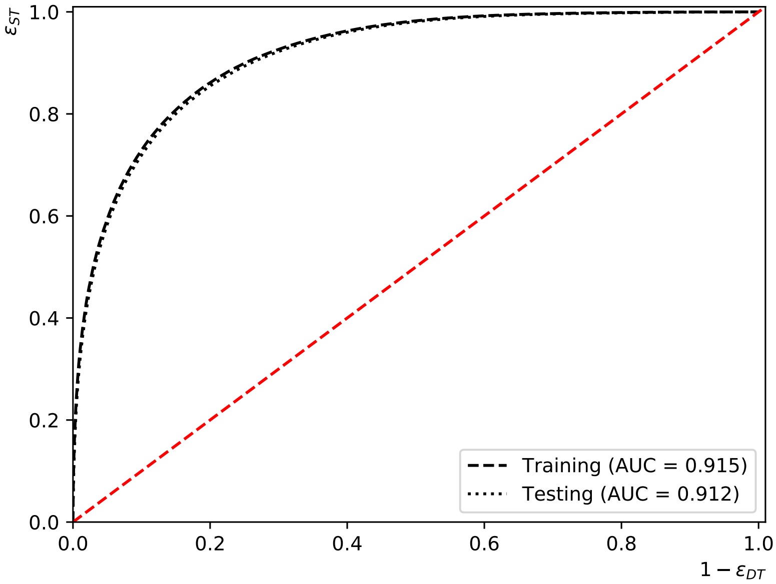

(b)

Figure 10.24 The ROC curves of `AdaBoost` classifiers trained in MC simulation scaled to an integrated luminosity of $139\,\mathrm{fb}^{-1}$, showing the effect of placing a cut on the BDT score on the same-top and different-top efficiencies, $\varepsilon_{\mathrm{ST}}$ and $\varepsilon_{\mathrm{DT}}$. The training dataset is represented by the dashed line and the testing dataset is represented by the dotted line. The ROC AUC metric is also shown for both, and the dotted red line represents the expected performance of a random classifier. The ROC curve is shown separately for the classifier trained on: **(a)** the purely leptonic feature set, X_ℓ; **(b)** the full feature set, X_f.

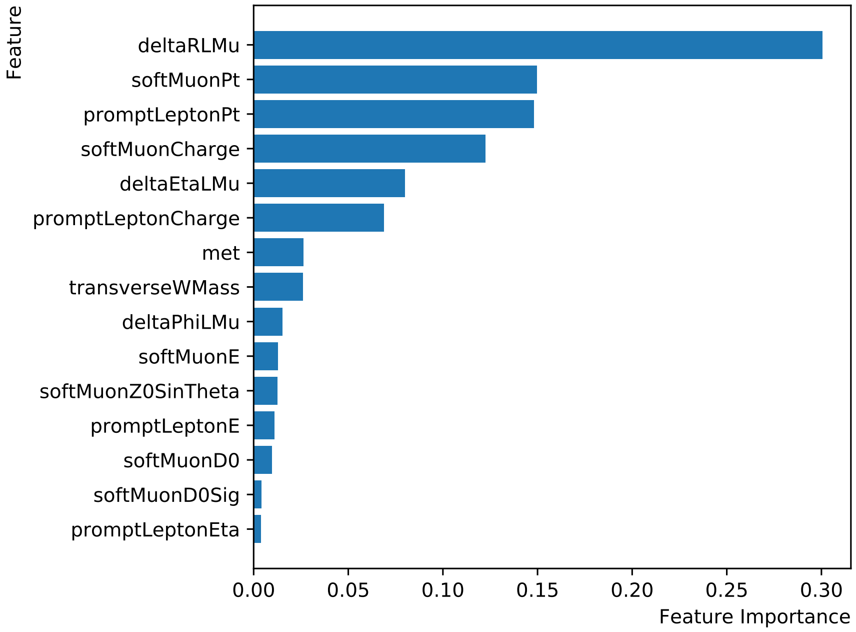

(a)

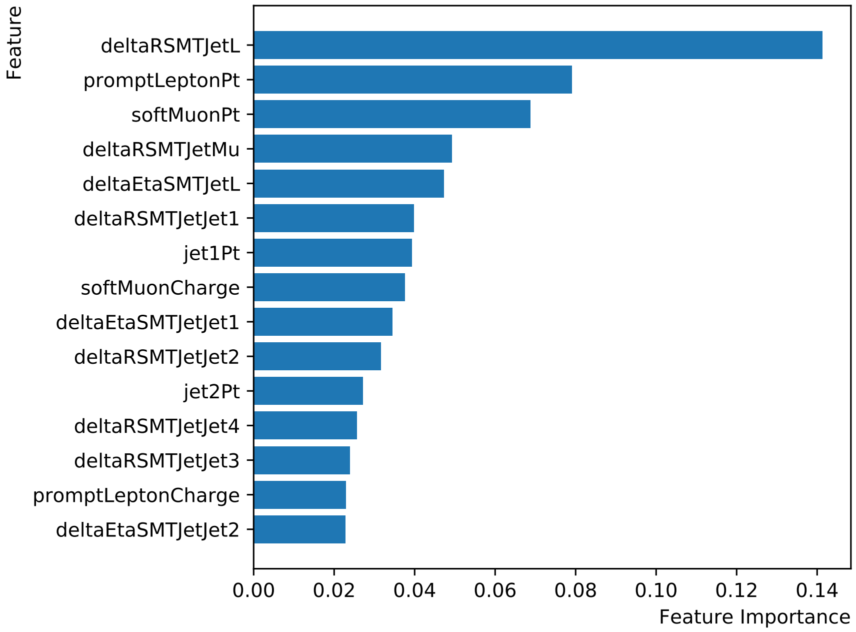

(b)

Figure 10.25 The impurity-based feature importances for the top fifteen features utilised by the `AdaBoost` classifiers trained in MC simulation scaled to an integrated luminosity of 139 fb^{-1}. The feature importances are shown separately for the classifier trained on: **(a)** the purely leptonic feature set, X_ℓ; **(b)** the full feature set, X_f.

Chapter 11

Unfolding

The process referred to in particle physics as unfolding, or alternatively in other fields as deconvolution, is the process of recovering the true distribution of a quantity from an observed distribution that has been changed or smeared in some way. A simple example to help conceptualise the technique is taking a blurry, pixelated image (the observed distribution) and transforming it (unfolding) to recover the original, clear image (true distribution). Observed distributions in particle physics settings can diverge from the observed distribution for a variety of reasons, such as limited detector resolutions, efficiency and acceptance effects, contributions from background processes, and errors in reconstruction such as getting the ST/DT-assignment, described in Chapter 10, incorrect. Unfolding the observed distributions corrects for these smearing effects. An unfolded result can be easily preserved for comparison with future experiments and theoretical predictions without having to re-simulate detector conditions and preserve all the individual details of the reconstruction process.

This chapter details the unfolding procedure that is used for the measurement described in this thesis. It begins in Section 11.1 with the mathematical formulation of the unfolding problem, following references [211, 212]. Section 11.2 details the implementation of unfolding for this measurement, which is performed using the software package `RooUnfold` [213, 214]. The validation of the unfolding is explored in Section 11.3, followed by Section 11.4, which explains how the uncertainties detailed in Chapter 9, both statistical and systematic, are propagated through the unfolding procedure. The chapter ends in Section 11.5 with a full comparison of the unfolding ingredients for each of the ST/DT-assignment methods introduced in Chapter 10, which affect the selection of the final method that is described in Section 13.2. The unfolding ingredients for one of these methods, `KLFitter`, is used throughout the preceding sections of the chapter to illustrate the various steps of the unfolding process.

11.1 The Unfolding Problem

To formalise the unfolding problem, consider the process of interest as a random variable for which the true value is denoted y, and the observed value x, which may in general be different to y. The aim is to construct a statistical estimator for the probability density function of y, $f_{\text{true}}(y)$.

In the case of experiments such as the one described in this thesis, where a number of events are counted, $f_{\text{true}}(y)$ can be discretised as the true histogram $\boldsymbol{\mu} = (\mu_1, \ldots, \mu_M)$, where μ_j is the expected number of events in bin j of the histogram, for $j \in \{1, \ldots, M\}$. The relation between $f_{\text{true}}(y)$ and $\boldsymbol{\mu}$, obtained by integrating across the width of the bin, is

$$\mu_j = \mu_{\text{tot}} \int_{\text{bin } j} f_{\text{true}}(y) \, dy, \tag{11.1}$$

where μ_{tot} is the expectation value for the total number of events. An observed histogram $\boldsymbol{n} = (n_1, \ldots, n_N)$ is also constructed, where n_i is the observed number of events in bin i of the histogram, for $i \in \{1, \ldots, N\}$. As introduced in Section 9.1, such an observed count of number of events can be treated as a Poisson variable with expectation ν_i. Some of the events in the observed histogram are considered to be coming from a background process with expectation $\boldsymbol{\beta} = (\beta_1, \ldots, \beta_N)$. $\boldsymbol{\beta}$ is assumed to have a known, fixed value from this point on.

Using the law of total probability, the expected observed number of events can be written as

$$\nu_i = \mu_{\text{tot}} \int_{\text{bin } i} \int r(x|y) f_{\text{true}}(y) \, dy \, dx + \beta_i, \tag{11.2}$$

where $r(x|y)$ is called the response function. It can be broken down into components such that

$$r(x|y) = \frac{\varepsilon(y) m(x|y)}{f_{\text{acc}}(x)}, \tag{11.3}$$

where the migration function, $m(x|y)$, is the conditional probability density function for the measured value x given that the true value was y, normalised so that $\int m(x|y)dx = 1$. $\epsilon(y)$ is the efficiency, which is the probability that an event with true value y will be observed somewhere, and is introduced to account for the possibility that some events may not be observed at all. Similarly, $f^{\text{acc}}(x)$ is the acceptance, which is the probability that an event with observed value x comes from the process of interest somewhere, and is introduced to account for the possibility that some events may be observed due to other measurement effects (not including events coming from the known background processes responsible for the expected events $\boldsymbol{\beta}$).

Discretising the integral into a sum over bins transforms Eq. 11.2 into

$$\nu_i = \sum_{j=1}^{M} R_{ij} \mu_j + \beta_i, \tag{11.4}$$

and it can be seen that the response function, $r(x|y)$, becomes the $N \times M$ response matrix, R_{ij}. Eq. 11.3 becomes

$$R_{ij} = \frac{\varepsilon^j \mathcal{M}_{ij}}{f^i_{\text{acc}}}, \tag{11.5}$$

and the migration function, $m(x|y)$, becomes the $N \times M$ migration matrix, $\mathcal{M}_{ij} = P(\text{observed in bin } i|\text{truly in bin } j)$, normalised so that $\sum_i \mathcal{M}_{ij} = 1$.

Generalising Eq. 11.4 for the expected number of events in bin i to a matrix equation for the entire histogram gives

$$\boldsymbol{\nu} = R\boldsymbol{\mu} + \boldsymbol{\beta}. \tag{11.6}$$

This equation now fully encapsulates how the true histogram is smeared. The original aim of constructing a statistical estimator for $f_{\text{true}}(y)$ becomes equivalent to constructing an estimator, which is denoted $\hat{\boldsymbol{\mu}}$, for the true histogram, $\boldsymbol{\mu}$.

For the case where $N = M$ and the response matrix is square, the simplest solution, which can also be shown to be both the maximum likelihood and least squares solution, is to invert Eq. 11.6 to obtain

$$\boldsymbol{\mu} = R^{-1}(\boldsymbol{\nu} - \boldsymbol{\beta}). \tag{11.7}$$

Taking the observed counts as the estimators of $\boldsymbol{\nu}$ means that the solution for the estimators of $\boldsymbol{\mu}$ is simply

$$\hat{\boldsymbol{\mu}} = R^{-1}(\boldsymbol{n} - \boldsymbol{\beta}). \tag{11.8}$$

This solution can be shown to give a set of estimators $\hat{\boldsymbol{\mu}}$ that are both unbiased and efficient, i.e. they have the smallest possible variance that can be achieved for zero-bias estimators. Despite this, this approach can lead to small statistical fluctuations in $\boldsymbol{n}$ being amplified to produce very large variances in the estimators, and spurious strong negative correlations between neighbouring bins. These problems are emphasised when R_{ij} has large off-diagonal elements that smear any original fine-structure in the true distribution, and for distributions with many bins. In many situations, it is therefore prudent to initiate a trade-off, reducing the variance by introducing a bias, through a process called regularisation. Many such methods of regularised unfolding exist. However, the issues leading to the large variances are not expected to cause a problem for the distributions to be unfolded for this measurement, so it is beneficial to use the zero-bias solution of unregularised matrix inversion.

11.2 Implementing Unfolding

Adapting the general prescription of Eq. 11.8 for application to the measurement in this thesis results in an equation that can be used to unfold observed $N^{\ell\mu}$ distributions to the full fiducial phase-space volume defined by the full list of selection cuts from Sections 7.1 and 7.2 applied at particle-level. This equation is

$$N^{j}_{\text{unfolded}} = \frac{1}{\varepsilon^{j}} \cdot \sum_{i} \mathcal{M}^{-1}_{ij} \cdot f^{i}_{\text{acc}} \cdot (N^{i}_{\text{data}} - N^{i}_{\text{bkg}});\, i, j \in \{--, ++, -+, +-\}, \tag{11.9}$$

where N^{j}_{unfolded} are the four bins of the unfolded particle-level truth $N^{\ell\mu}$ distribution, and N^{i}_{data} and N^{i}_{bkg} are respectively the four bins of the $N^{\ell\mu}$ distribution for the reconstruction-level data and the total contribution of non-$t\bar{t}$ backgrounds, as described in Section 8.2.

The 16 elements of the 4×4 migration matrix, $\mathcal{M}^{ij}$, four particle-level truth efficiencies, ε^{j}, and four reconstruction-level acceptances, f^{i}_{acc}, are all extracted by performing an event-matching process between the particle-level truth and reconstruction-level in MC simulation scaled to an integrated luminosity of 139 fb^{-1}. These ingredients, as derived using the `KLFitter` method of ST/DT-assignment, are shown in Fig. 11.1.

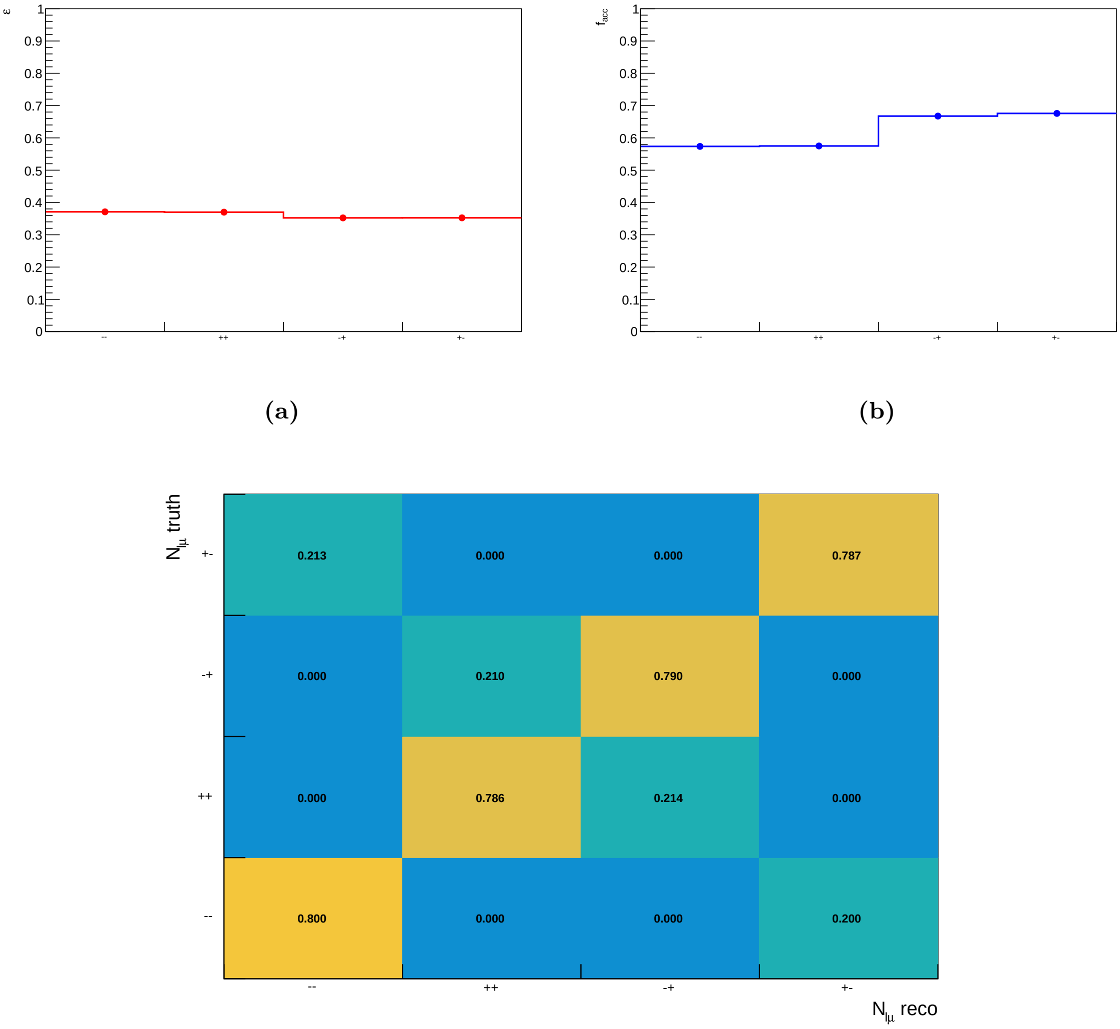

(a) **(b)**

(c)

Figure 11.1 The unfolding ingredients extracted from MC simulation scaled to an integrated luminosity of 139 fb^{-1}, derived using the `KLFitter` method of ST/DT-assignment. These ingredients are: **(a)** the efficiency, ε; **(b)** the acceptance, f_{acc}; **(c)** the migration matrix, $\mathcal{M}$. The associated statistical uncertainties are 0.001 for ε, 0.002 for f_{acc}, 0.002 for the elements on the leading diagonal of $\mathcal{M}$, and 0.001 for all other elements. The elements of $\mathcal{M}$ labelled with 0.000 have contributions from charge-misidentification at a level < 0.001.

The migrations between bins are captured in the migration matrix, $\mathcal{M}$, which is populated with events present at both the particle-level and reconstruction-level of the simulation. These migrations are expected to be dominated by the performance of the ST/DT-assignment, with correctly-assigned events appearing along the leading diagonal from the bottom left to the top right of the matrix. Incorrectly-assigned events have the wrong sign for the prompt lepton charge (e.g. an incorrectly-assigned true $--$ event would be reconstructed in the $+-$ bin) and therefore appear on the subleading diagonal from the top left to the bottom right of the matrix. All other possible migrations in the migration matrix are due to lepton charge-misidentification, which occurs with an extremely low frequency. Inspecting Fig. 11.1(c) confirms that these expectations match with what is seen for the migration matrix derived using the `KLFitter` method of ST/DT-assignment.

The four particle-level truth efficiencies, ε^{j}, account for events present in the fiducial volume at particle-level but not present at reconstruction-level, for example because they pass the particle-level selection cuts but due to a detector smearing effect one or more of these selection cuts is failed at reconstruction-level. The efficiencies are calculated as

$$\varepsilon^{j} = (\frac{n(\text{reco-level} \cap \text{particle-level})}{n(\text{particle-level})})^{j}, \tag{11.10}$$

where $n(C)$ denotes the number of events in the sample satisfying condition C. The efficiencies derived using the `KLFitter` method of ST/DT-assignment are

$$\varepsilon^{--} = 0.371 \pm 0.001\ (\text{Stat.}), \tag{11.11}$$

$$\varepsilon^{++} = 0.370 \pm 0.001\ (\text{Stat.}), \tag{11.12}$$

$$\varepsilon^{-+} = 0.352 \pm 0.001\ \text{(Stat.)}, \tag{11.13}$$

$$\varepsilon^{+-} = 0.352 \pm 0.001\ \text{(Stat.)}. \tag{11.14}$$

These efficiencies are also presented in Fig. 11.1(a).

Conversely to the efficiencies, the four reconstruction-level acceptances, f^i_{acc}, account for events present at reconstruction-level which have no corresponding event in the fiducial volume at particle-level. This could be due to smearing effects (in the reverse manner to those described for the efficiency), where a selection cut is failed at particle-level, but after smearing of the relevant value the cut is passed at reconstruction-level. It also includes contributions from the backgrounds coming from within the $t\bar{t}$ sample, as discussed in Section 8.1. The acceptances are calculated as

$$f^i_{\text{acc}} = (\frac{n(\text{reco-level} \cap \text{particle-level})}{n(\text{reco-level})})^i. \tag{11.15}$$

The acceptances derived using the `KLFitter` method of ST/DT-assignment are

$$f^{--}_{\text{acc}} = 0.574 \pm 0.002\ \text{(Stat.)}, \tag{11.16}$$

$$f^{++}_{\text{acc}} = 0.575 \pm 0.002\ \text{(Stat.)}, \tag{11.17}$$

$$f^{-+}_{\text{acc}} = 0.667 \pm 0.002\ \text{(Stat.)}, \tag{11.18}$$

$$f_{\text{acc}}^{+-} = 0.676 \pm 0.002\ (\text{Stat.}). \tag{11.19}$$

These acceptances are also presented in Fig. 11.1(b).

With $\mathcal{M}^{ij}$, ε^{j}, and f_{acc}^{i} obtained, Eq. 11.9 can be used to unfold an observed $N^{\ell\mu}$ distribution to obtain an unfolded $N^{\ell\mu}$ distribution in the full fiducial phase-space. This can then be used to construct the final quantities of interest for the measurement, which are the observed charge and underlying CP-violation asymmetries as introduced in Sections 7.3 and 7.4.

11.3 Validation

In order to validate that the extracted unfolding ingredients $\mathcal{M}^{ij}$, ε^{j}, and f_{acc}^{i} are correct, a technical closure test is performed. This means taking the reconstruction-level $N^{\ell\mu}$ distribution from the sample used to extract the ingredients, unfolding it in accordance with Eq. 11.9, and comparing it to the particle-level truth $\mathrm{N}^{\ell\mu}$ distribution from the sample used to extract the ingredients. If the unfolded distribution matches the particle-level truth distribution exactly, the unfolding is said to close. This closure test is intended primarily as a sanity check and is performed whenever such unfolding ingredients are extracted.

The observed reconstruction-level, unfolded reconstruction-level, and particle-level truth $\mathrm{N}^{\ell\mu}$ distribution derived using the `KLFitter` method of ST/DT-assignment are shown in Fig. 11.2. Comparison of the observed reconstruction-level distribution shown in Fig. 11.2(a) with the unfolded distribution shown in Fig. 11.2(b) demonstrates the significant change in the shape of the distribution as a result of the unfolding. Additionally, comparison of the unfolded distribution shown in Fig. 11.2(b) with the particle-level truth distribution shown in Fig. 11.2(c) confirms that these two distributions are identical and that therefore the unfolding closes as expected. The unfolding is also confirmed to close as expected for all the other unfolding ingredients presented in this thesis.

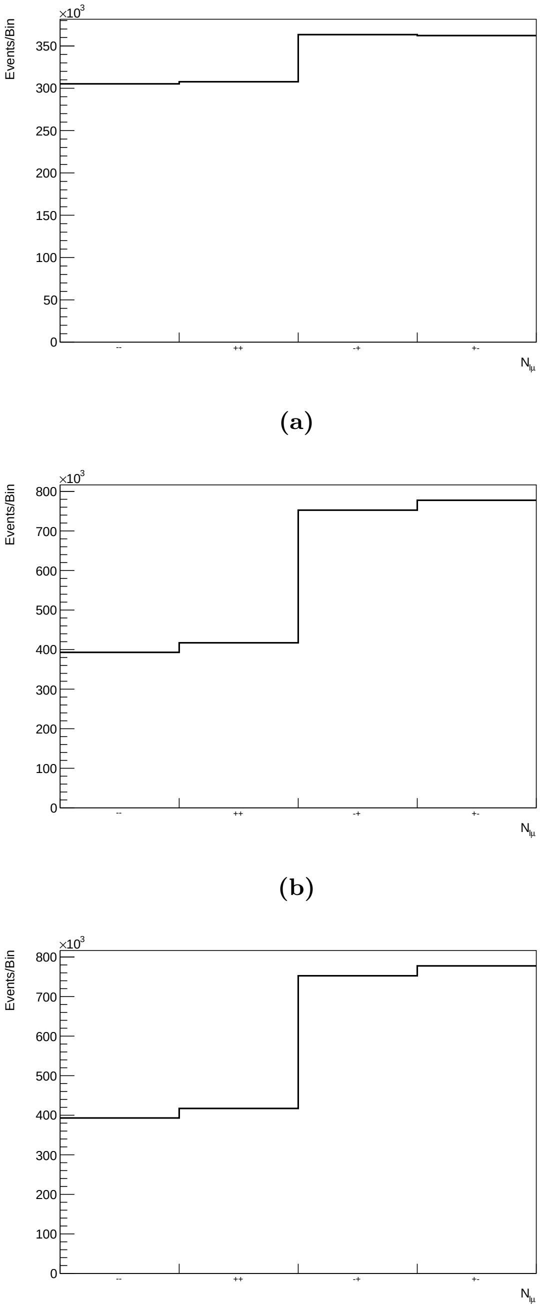

(a)

(b)

(c)

Figure 11.2 The distribution of $N^{\ell\mu}$ taken from MC simulation scaled to an integrated luminosity of $139\,\mathrm{fb}^{-1}$, derived using the `KLFitter` method of ST/DT-assignment, and shown for: **(a)** the observed reconstruction-level; **(b)** the unfolded reconstruction-level; **(c)** the particle-level truth. The identicalness of **(b)** and **(c)** confirms the closure of the unfolding.

11.4 Uncertainty Propagation

To obtain the final unfolded result, it is necessary to propagate the uncertainties that apply to the observed $N^{\ell\mu}$ distribution through the unfolding process to the unfolded $N^{\ell\mu}$ distribution. As presented in Chapter 9, the sources of uncertainty considered for this measurement can be subdivided into three categories. These three categories are the statistical uncertainties, the detector systematics, and the modelling systematics. The method used to propagate each of these through the unfolding process is considered in turn below.

11.4.1 Statistical Uncertainties

As derived in Section 9.1, the statistical uncertainties on the bins N^i_{data} of an observed $N^{\ell\mu}$ distribution are $\pm\sqrt{N^i_{\text{data}}}$. The simplest way to propagate these statistical uncertainties to the bins N^j_{unfolded} of the unfolded $N^{\ell\mu}$ distribution is to pass them to `RooUnfold` alongside N^i_{data}, with the package then returning a covariance matrix for N^j_{unfolded}. The diagonal elements of this covariance matrix can be taken as the statistical uncertainties on N^j_{unfolded}, and the uncertainties on the observable charge asymmetries, A^{SS} and A^{OS} (calculated from N^j_{unfolded} according to Eqs. 7.1 and 7.2), can be obtained using error propagation. Further error propagation can then be used to obtain the statistical uncertainties on the underlying CP-violation asymmetries. However, this would not take into account any of the correlations present between N^j_{unfolded} bins, which as a result would be expected to lead to a major over-estimation of the statistical uncertainties on the charge and CP-violation asymmetries. Therefore, this method is deemed unsuitable and an alternative approach must be taken.

This alternative approach involves performing a series of statistical pseudoexperiments. For each bin N^i_{data} of the observed distribution, a random variable p^i is constructed which follows a Poisson distribution with mean N^i_{data}, $p^i \sim \text{Pois}(N^i_{\text{data}})$. For each pseudoexperiment, also known as a toy, values are sampled from the distributions of p^i. The values of N^i_{data} are replaced with these sampled values, $N^i_{\text{data,toy}}$, and the data is unfolded to get $N^j_{\text{unfolded,toy}}$. These $N^j_{\text{unfolded,toy}}$ are in turn used to calculate values of $A^{\text{SS}}_{\text{toy}}$, $A^{\text{OS}}_{\text{toy}}$, and the CP-violation asymmetries. The ensemble distributions (across all pseudoexperiments) for all of these quantities are expected to follow a Gaussian distribution centred on the true value (e.g. centred on N^{j}_{unfolded} for the bins of the unfolded $N^{\ell\mu}$ distribution, or centred on A^{SS} and A^{OS} for the charge asymmetries), and the width of the ensemble distributions is taken to be the statistical uncertainty. Verification of the validity of this approach is performed by constructing variables known as pulls, defined for a general true value x_{true}, toy value x_{toy}, and assigned uncertainty σ_x as

$$\text{pull}(x) = \frac{x_{\text{toy}} - x_{\text{true}}}{\sigma_x}. \tag{11.20}$$

Fitting a Gaussian function to the ensemble distribution should return a pull mean of zero, $\mu_{\text{pull}}(x) = 0$, and a pull width of one, $\sigma_{\text{pull}}(x) = 1$.

The pseudoexperiment procedure is tested with the unfolding ingredients derived using the `KLFitter` method of ST/DT-assignment for ensembles containing differing numbers of toys, between $n_{\text{toys}} = 1,000$ and $n_{\text{toys}} = 10,000$. The pull mean, pull width, and resulting statistical uncertainty for the unfolded charge asymmetries, A^{SS} and A^{OS}, and the unfolded count N^{--} are shown in Table 11.1. It can be seen that for a low number of toys, the pull means and pull widths are relatively unstable, but they settle down to the expected values $\mu_{\text{pull}} = 0$ and $\sigma_{\text{pull}} = 1$ for $n_{\text{toys}} > 5,000$. As the resulting statistical uncertainty can also be seen to be stable by this value, it is concluded that $n_{\text{toys}} = 5,000$ is sufficient, and this is selected as the number of toys to be used to derive all the statistical uncertainties on all the unfolded results presented in this thesis. The pull distributions and fitted Gaussian functions for A^{SS}, A^{OS}, and unfolded event count N^{--} with $n_{\text{toys}} = 5,000$ are shown in Fig. 11.3, and look to be fully in line with expectations.

n_{toys}	$\mu_{\text{pull}}(A^{\text{SS}})$	$\sigma_{\text{pull}}(A^{\text{SS}})$	$\sigma_{\text{stat.}}(A^{\text{SS}})$	$\mu_{\text{pull}}(A^{\text{OS}})$	$\sigma_{\text{pull}}(A^{\text{OS}})$	$\sigma_{\text{stat.}}(A^{\text{OS}})$	$\mu_{\text{pull}}(N^{--})$	$\sigma_{\text{pull}}(N^{--})$	$\sigma_{\text{stat.}}(N^{--})$
100	-0.01 ± 0.30	1.63 ± 0.42	17.9%	0.03 ± 0.14	1.12 ± 0.13	17.9%	0.09 ± 0.23	1.40 ± 0.36	0.36%
200	-0.15 ± 0.10	1.05 ± 0.12	18.2%	0.05 ± 0.08	0.98 ± 0.08	18.2%	0.05 ± 0.12	1.15 ± 0.15	0.41%
500	0.08 ± 0.05	0.95 ± 0.05	18.9%	-0.09 ± 0.05	1.02 ± 0.04	18.9%	-0.03 ± 0.05	1.04 ± 0.04	0.40%
1000	-0.04 ± 0.03	0.95 ± 0.03	18.7%	0.03 ± 0.03	0.97 ± 0.03	18.7%	0.02 ± 0.03	0.96 ± 0.03	0.40%
2000	0.02 ± 0.02	0.99 ± 0.02	18.6%	-0.01 ± 0.02	0.99 ± 0.02	18.4%	0.03 ± 0.02	0.99 ± 0.02	0.40%
3000	0.01 ± 0.02	0.99 ± 0.01	18.7%	0.00 ± 0.02	1.00 ± 0.01	18.6%	-0.00 ± 0.02	1.00 ± 0.01	0.41%
4000	0.02 ± 0.02	0.99 ± 0.01	18.2%	-0.02 ± 0.02	1.00 ± 0.01	18.2%	-0.01 ± 0.02	0.98 ± 0.01	0.41%
5000	0.00 ± 0.01	1.00 ± 0.01	18.3%	-0.01 ± 0.01	1.00 ± 0.01	18.3%	0.00 ± 0.01	1.00 ± 0.01	0.41%
6000	0.00 ± 0.01	0.99 ± 0.01	18.3%	-0.01 ± 0.01	1.00 ± 0.01	18.3%	-0.01 ± 0.01	0.99 ± 0.01	0.41%
7000	-0.01 ± 0.01	1.00 ± 0.01	18.3%	0.00 ± 0.01	1.00 ± 0.01	18.3%	0.01 ± 0.01	1.00 ± 0.01	0.40%
8000	-0.01 ± 0.01	1.00 ± 0.01	18.4%	0.01 ± 0.01	1.00 ± 0.01	18.4%	0.00 ± 0.01	0.99 ± 0.01	0.41%
9000	0.00 ± 0.01	1.00 ± 0.01	18.4%	0.01 ± 0.01	1.00 ± 0.01	18.4%	0.00 ± 0.01	1.00 ± 0.01	0.41%
10000	0.00 ± 0.01	0.99 ± 0.01	18.3%	0.01 ± 0.01	1.00 ± 0.01	18.3%	0.00 ± 0.01	1.00 ± 0.01	0.40%

Table 11.1 The results of performing n_{toys} statistical pseudoexperiments in MC simulation scaled to an integrated luminosity of $139\,\text{fb}^{-1}$ for the unfolding ingredients derived using the `KLFitter` method of ST/DT-assignment. The results comprise the pull mean, μ_{pull}, pull width, σ_{pull}, and resulting percentage statistical uncertainty, $\sigma_{\text{stat.}}$, for the unfolded charge asymmetries A^{SS}, A^{OS} and unfolded count N^{--}. Green shading indicates where the conditions $\mu_{\text{pull}}(x) = 0$ and $\sigma_{\text{pull}}(x) = 1$ are satisfied, while red shading indicates where these conditions are not satisfied.

11.4.2 Detector Systematics

The detector systematic variations listed in Table 9.1 are assessed in MC simulation, by re-performing the MC simulation with the variation applied in order to obtain an observed reconstruction-level $N^{\ell\mu}$ distribution, with bins $N^{i}_{\text{syst.}}$. This is unfolded according to Eq. 11.9 with the unfolding ingredients derived from the nominal (non-varied) MC, in order to obtain $N^{j}_{\text{unfolded,syst.}}$, and in turn $A^{\text{SS}}_{\text{syst.}}$, $A^{\text{OS}}_{\text{syst.}}$. The variation is then assessed as the difference between the unfolded value from the varied MC and the unfolded value from the nominal MC. To put this in equation form yields

$$\sigma_{\text{syst.}}(A^{\text{SS}}) = A^{\text{SS}}_{\text{syst.}} - A^{\text{SS}}, \tag{11.21}$$

$$\sigma_{\text{syst.}}(A^{\text{OS}}) = A^{\text{OS}}_{\text{syst.}} - A^{\text{OS}}. \tag{11.22}$$

Similar equations are used to assess the detector systematic variations on the CP-violation asymmetries.

11.4.3 Modelling Systematics

The procedure for modelling systematic variations listed in Table 9.2 depends on whether the variation comes from comparing the nominal MC simulation to a re-performed MC simulation, which is the case for the detector systematics, or whether it comes from comparing the nominal MC simulation to an alternative MC simulation sample, which is the case for most of the modelling systematics. In the former case, the variations are assessed in the same way as the detector systematics as the difference between the unfolded value from the varied MC and the unfolded value from the nominal MC. This is equivalent to comparing the varied valued to the particle-level truth of the MC sample. In the latter case, the variation comes from an

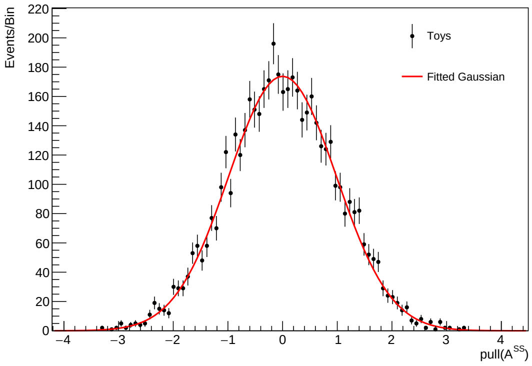

(a)

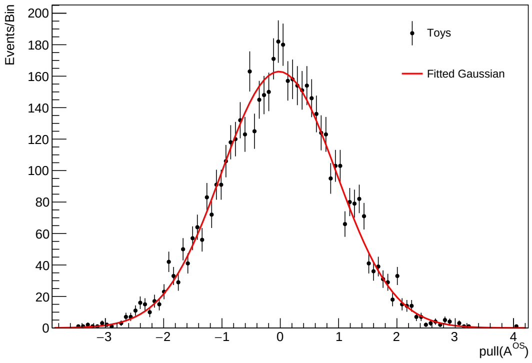

(b)

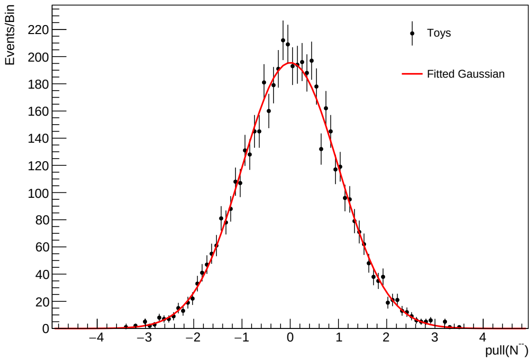

(c)

Figure 11.3 The pull distributions and fitted Gaussian functions from performing $n_{\text{toys}} = 5,000$ statistical pseudoexperiments in MC simulation scaled to an integrated luminosity of $139\,\text{fb}^{-1}$ for the unfolding ingredients derived using the `KLFitter` method of ST/DT-assignment, for: **(a)** the same-sign observable charge asymmetry, A^{SS}; **(b)** the opposite-sign observable charge asymmetry, A^{OS}; **(c)** the unfolded event count N^{--}.

alternative MC simulation sample which does not share the same particle-level truth as the nominal MC simulation. Therefore it is instead necessary to obtain $N^{i}_{\text{syst.}}$ from the alternative MC sample, unfold it according to Eq. 11.9 with the unfolding ingredients derived from the nominal MC sample to get $N^{j}_{\text{unfolded,syst.}}$, $A^{\text{SS}}_{\text{syst.}}$, and $A^{\text{OS}}_{\text{syst.}}$, and then compare these to the particle-level truth of the alternative MC sample. Labelling Eqs. 11.21 and 11.22 more explicitly with the sample from which everything derives, the equations for the former case become

$$\sigma_{\text{syst.}}(A^{\text{SS}}) = A^{\text{SS}}_{\text{syst.,nom.}} - A^{\text{SS}}_{\text{true,nom.}}, \tag{11.23}$$

$$\sigma_{\text{syst.}}(A^{\text{OS}}) = A^{\text{OS}}_{\text{syst.,nom.}} - A^{\text{OS}}_{\text{true,nom.}}, \tag{11.24}$$

while the equations for the latter case are

$$\sigma_{\text{syst.}}(A^{\text{SS}}) = A^{\text{SS}}_{\text{syst.,alt.}} - A^{\text{SS}}_{\text{true,alt.}}, \tag{11.25}$$

$$\sigma_{\text{syst.}}(A^{\text{OS}}) = A^{\text{OS}}_{\text{syst.,alt.}} - A^{\text{OS}}_{\text{true,alt.}}. \tag{11.26}$$

As with the detector systematics, similar equations are also used to assess the modelling systematic variations on the CP-violation asymmetries.

11.5 Comparison of Unfolding Ingredients

The unfolding ingredients $\mathcal{M}^{ij}$, ε^{j}, and f^{i}_{acc} are obtained, from the same MC simulation scaled to an integrated luminosity of $139\,\text{fb}^{-1}$, for all of the candidate methods that are considered for performing the final ST/DT-assignment, as introduced in Chapter 10. The ingredients for the $\Delta R(\ell, \mu)$ cut (see Section 10.2) are shown in Fig. 11.4. The ingredients for `KLFitter` (see Section 10.3), used in the preceding sections to demonstrate how the unfolding procedure works, are shown in Fig. 11.1. Two sets of ingredients are obtained for the BDTs (see Section 10.4), based on the feature sets used to train the algorithm (see Section 10.4.1). The ingredients for the BDT trained on the purely leptonic feature set are shown in Fig. 11.5, while the ingredients for the BDT trained on the full feature set are shown in Fig. 11.6.

Additionally to the plots described above, the acceptances and efficiencies for all of the candidate methods are listed in Table 11.2.

Comparing the migration matrices presented in Figs. 11.1(c), 11.4(c), 11.5(c), and 11.6(c) with the performance numbers presented in Chapter 10 shows the direct link between the diagonal elements of the migration matrices and the efficiencies of the method of ST/DT-assignment. Larger diagonal elements are seen for `KLFitter` and the BDT trained on the full feature set, and smaller diagonal elements are seen for the $\Delta R(\ell, \mu)$ cut and the BDT trained on the purely leptonic feature set. It is also of interest to note the disparity in the diagonal elements between the opposite-sign bins ($-+$ and $+-$) and the same-sign bins ($++$ and $--$) which is seen for both BDT migration matrices.

Examining Table 11.2, it can be seen that the acceptances and efficiencies are broadly similar across all methods of ST/DT-assignment. It is of interest to note that the acceptances show a difference between same-sign and opposite-sign bins. This is due to the $t\bar{t}$ background, and more specifically the $W \to c \to \mu$ background, contributing more significantly to the same-sign bins, resulting in a lower acceptance. For example, in events where the prompt lepton comes from the top quark, the decay chain is $t \to W^{+} \to \mu^{+}$. The full decay chain for the $W \to c \to \mu$ background is $\bar{t} \to W^{-} \to \bar{c}s \to \mu^{-}$. As this is always a true different-top event, most of the time the ST/DT-assignment will result in the event being placed in the $--$ bin.

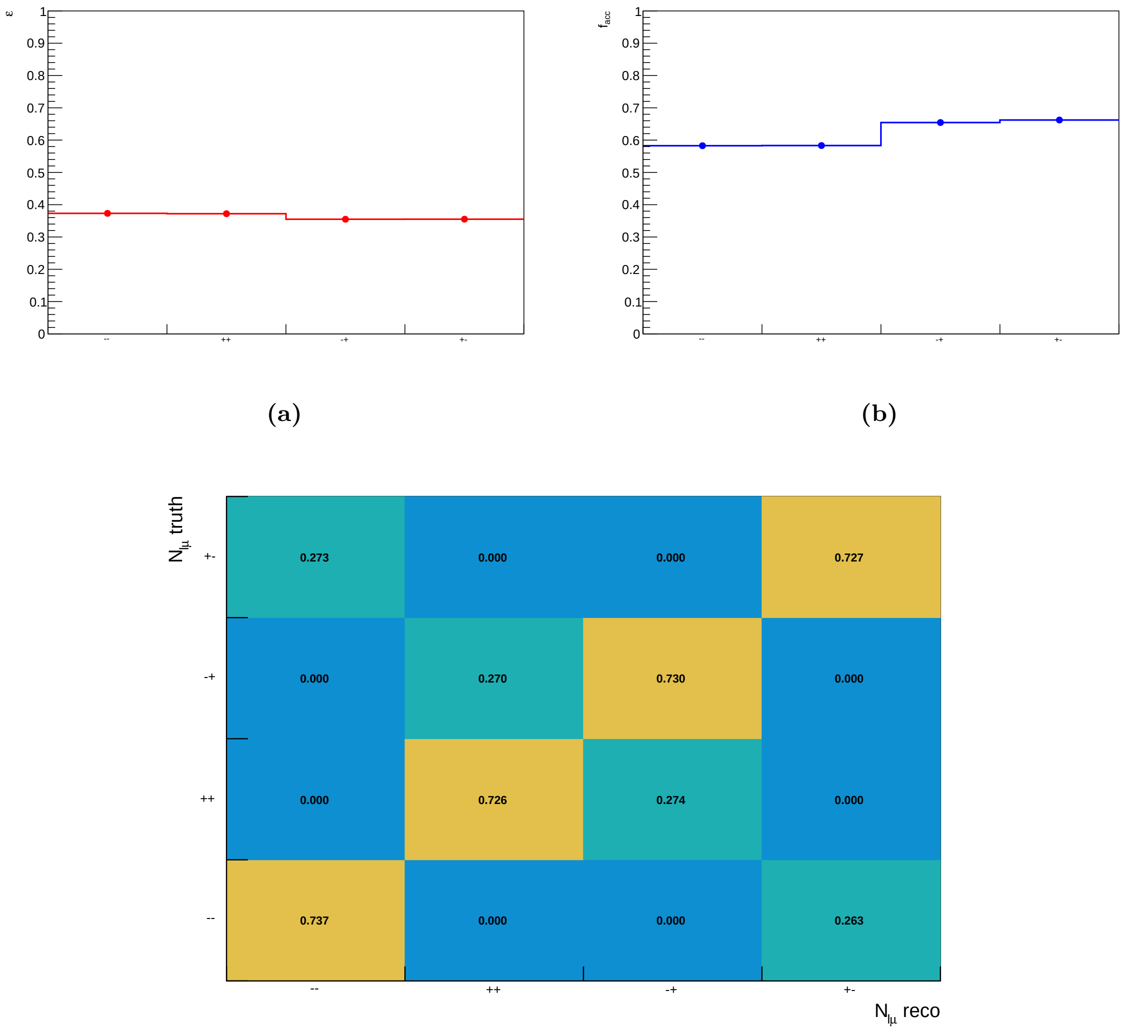

	--	++	-+	+-
+-	0.273	0.000	0.000	0.727
-+	0.000	0.270	0.730	0.000
++	0.000	0.726	0.274	0.000
--	0.737	0.000	0.000	0.263

(a) **(b)**

(c)

Figure 11.4 The unfolding ingredients extracted from MC simulation scaled to an integrated luminosity of 139 fb^{-1}, derived using the angular separation method of ST/DT-assignment. These ingredients are: **(a)** the efficiency, ε; **(b)** the acceptance, f_{acc}; **(c)** the migration matrix, $\mathcal{M}$. The associated statistical uncertainties are 0.001 for ε, 0.002 for f_{acc}, 0.002 for the elements on the leading diagonal of $\mathcal{M}$, and 0.001 for all other elements. The elements of $\mathcal{M}$ labelled with 0.000 have contributions from charge-misidentification at a level < 0.001.

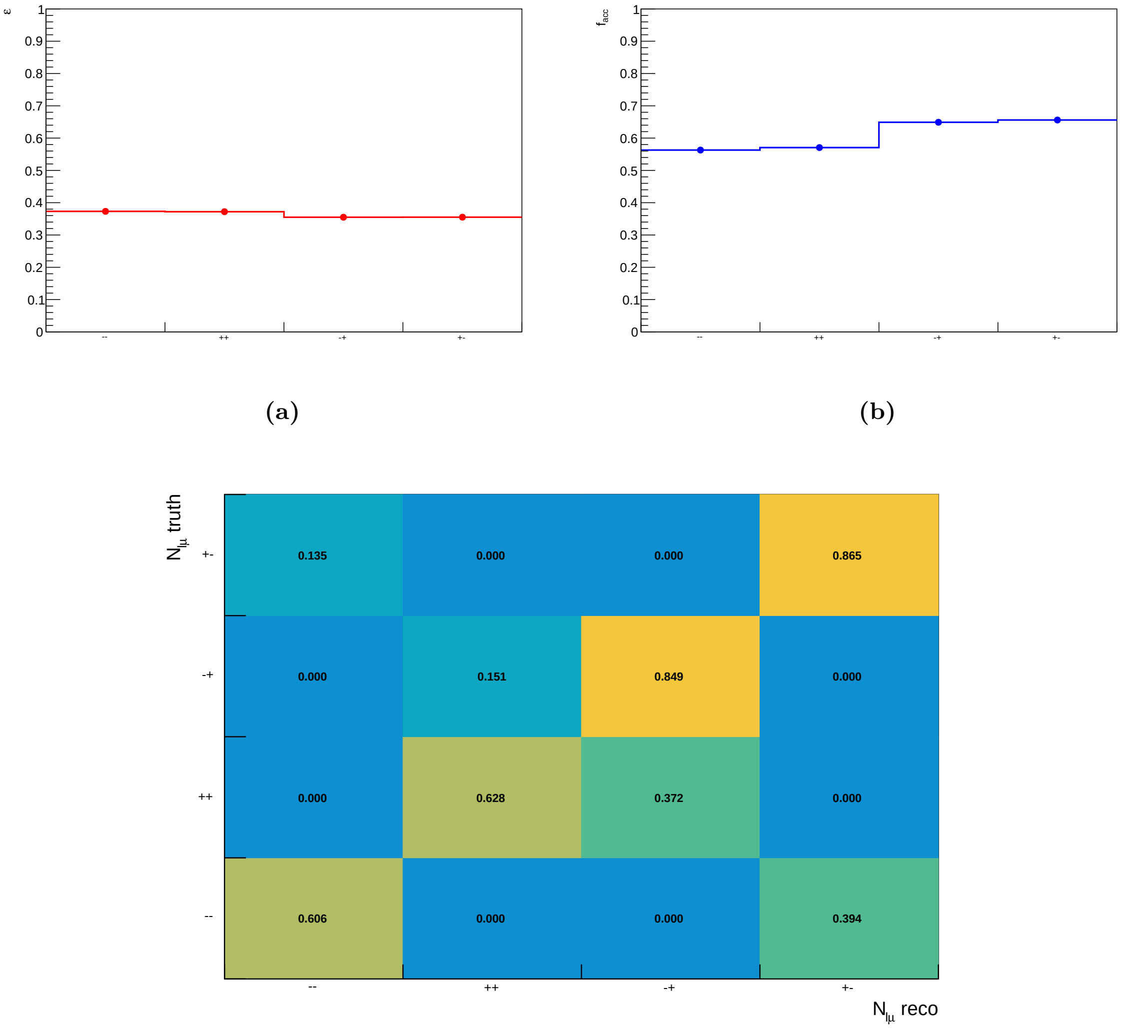

$N_{l\mu}$ truth \ $N_{l\mu}$ reco	--	++	-+	+-
+-	0.135	0.000	0.000	0.865
-+	0.000	0.151	0.849	0.000
++	0.000	0.628	0.372	0.000
--	0.606	0.000	0.000	0.394

(a) **(b)**

(c)

Figure 11.5 The unfolding ingredients extracted from MC simulation scaled to an integrated luminosity of 139 fb^{-1}, derived using a boosted decision tree trained on a purely leptonic feature set to perform the ST/DT-assignment. These ingredients are: **(a)** the efficiency, ε; **(b)** the acceptance, f_{acc}; **(c)** the migration matrix, $\mathcal{M}$. The associated statistical uncertainties are 0.001 for ε, 0.002 for f_{acc}, 0.002 for the elements on the leading diagonal of $\mathcal{M}$, and 0.001 for all other elements. The elements of $\mathcal{M}$ labelled with 0.000 have contributions from charge-misidentification at a level < 0.001.

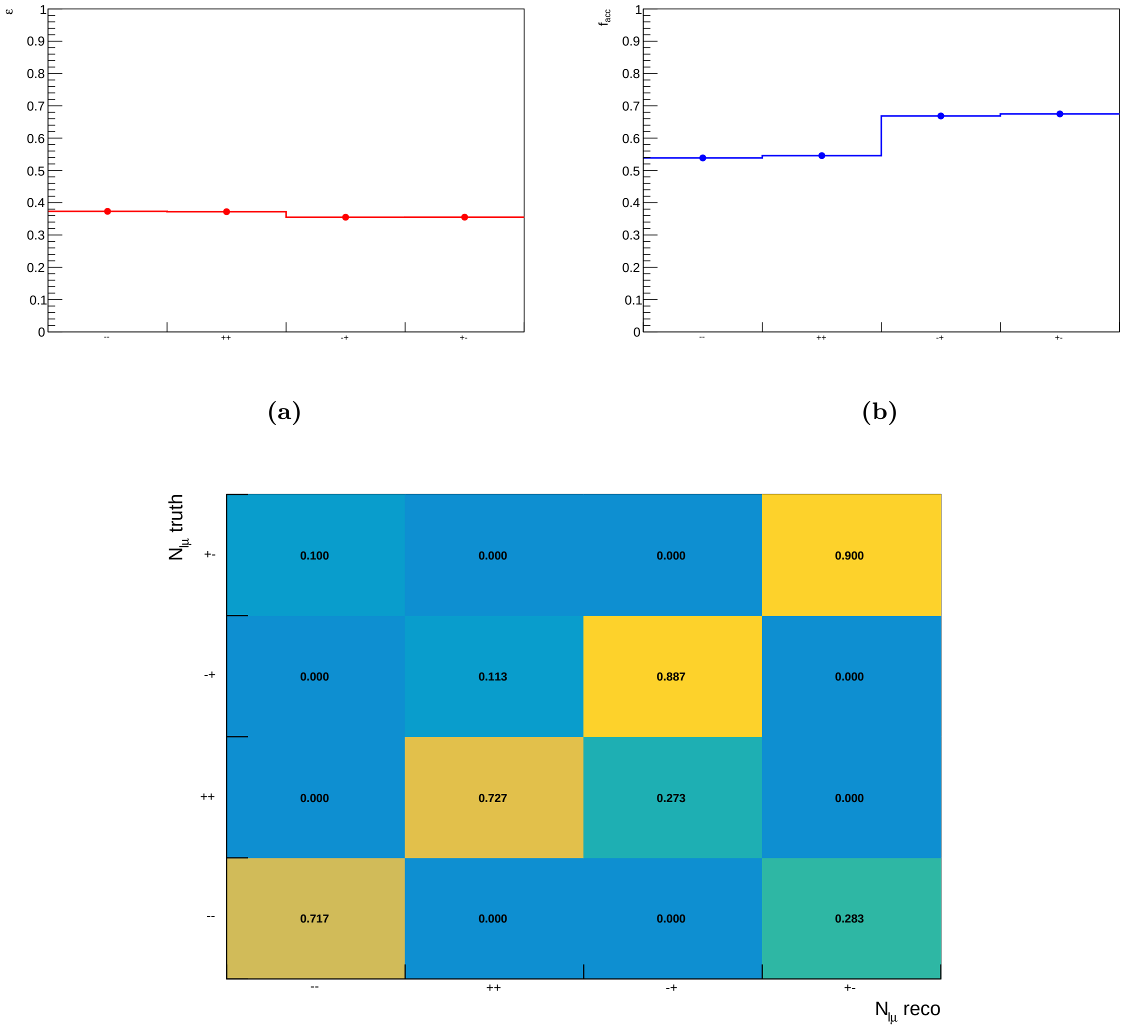

(a) **(b)**

(c)

Figure 11.6 The unfolding ingredients extracted from MC simulation scaled to an integrated luminosity of 139 fb^{-1}, derived using a boosted decision tree trained on a full feature set to perform the ST/DT-assignment. These ingredients are: **(a)** the efficiency, ε; **(b)** the acceptance, f_{acc}; **(c)** the migration matrix, $\mathcal{M}$. The associated statistical uncertainties are 0.001 for ε, 0.002 for f_{acc}, 0.002 for the elements on the leading diagonal of $\mathcal{M}$, and 0.001 for all other elements. The elements of $\mathcal{M}$ labelled with 0.000 have contributions from charge-misidentification at a level < 0.001.

Method	Charge Combination			
	$--$	$++$	$-+$	$+-$
`KLFitter`				
ε	0.371	0.370	0.352	0.352
f_{acc}	0.574	0.575	0.667	0.675
$\Delta R(\ell, \mu)$				
ε	0.373	0.372	0.355	0.355
f_{acc}	0.583	0.583	0.655	0.662
BDT, X_ℓ				
ε	0.373	0.372	0.355	0.355
f_{acc}	0.563	0.571	0.649	0.656
BDT, X_f				
ε	0.373	0.372	0.355	0.355
f_{acc}	0.539	0.546	0.669	0.675

Table 11.2 The unfolding efficiencies, ε, and acceptances, f_{acc}, for the different candidate methods for performing the ST/DT-assignment, as measured in MC simulation scaled to an integrated luminosity of $139\,\mathrm{fb}^{-1}$. All efficiencies listed in the table have an associated statistical uncertainty of 0.001, and all acceptances listed in the table have an associated statistical uncertainty of 0.002.

Chapter 12

Feasibility of a Time-Dependent Measurement

This chapter presents the studies performed on the feasibility of extending the time-integrated measurement introduced in Chapter 7 with a supplementary time-dependent measurement. This extension was originally posited alongside the prescription for the time-integrated measurement as a way to obtain a similar setup to B-factory experiments [90]. Such an extension would use the same object and event selection described in Sections 7.1 and 7.2. The idea was not explored in the previous ATLAS measurement at 8 TeV due to insufficient statistics, but the high volume of statistics provided by the full Run 2 ATLAS dataset opens the door to it being statistically viable [93].

The core of the time-dependent measurement is a time-dependent equivalent of the observable charge asymmetries introduced in Section 7.3, and Section 12.1 introduces this time-dependent asymmetry and explores how it can be related to underlying physical quantities in the b-physics sector that may be of interest for measurement. Section 12.2 explores the distribution of this asymmetry in MC simulation scaled to the full Run 2 luminosity to see what measurements could be extracted from the full Run 2 ATLAS data, making use of the particle-level truth of the simulation to establish the hadron decay time, i.e. how long after the initial hard collision the semileptonic decay that produced the soft muon occurred. However, obtaining an accurate and precise reconstruction of this hadron decay time from the ATLAS detector presents several challenges, which are explored in Section 12.3. The chapter ends in Section 12.4 with a discussion of the prospects for carrying out the time-dependent measurement in the near future.

12.1 Time-Dependent Formalism

The time-dependent charge asymmetry, $A(t)$, is of the form

$$A(t) = \frac{N^{\mathrm{OS}}(t) - N^{\mathrm{SS}}(t)}{N^{\mathrm{OS}}(t) + N^{\mathrm{SS}}(t)} = \frac{(N^{+-}(t) + N^{-+}(t)) - (N^{++}(t) + N^{--}(t))}{(N^{+-}(t) + N^{-+}(t)) + (N^{++}(t) + N^{--}(t))}, \tag{12.1}$$

where $N^{\ell\mu}(t)$ are the event counts for the combined prompt lepton and soft muon charge as introduced in Section 7.3, N^{OS} is the number of opposite-sign events (events where the prompt lepton and soft muon charges are different), and N^{SS} is the number of same-sign events (events where the prompt lepton and soft muon charges are the same) [215]. The difference from Section 7.3 is that these are all time-dependent quantities, with t being the hadron proper decay time. This means that the $N^{\ell\mu}(t)$ counts, considered separately for each bin of t, are related to the $N^{\ell\mu}$ of the time-integrated measurement by

$$N^{\ell\mu} = \sum_t N^{\ell\mu}(t). \tag{12.2}$$

Treating $N^{\mathrm{OS}}(t)$ and $N^{\mathrm{SS}}(t)$ as independently distributed Poisson variables gives the expression for the statistical uncertainty on each bin of $A(t)$, $\sigma_{A(t)}$, as

$$\sigma_{A(t)} = \frac{2}{N^{\mathrm{OS}}(t) + N^{\mathrm{SS}}(t)} \sqrt{\frac{N^{\mathrm{OS}}(t) N^{\mathrm{SS}}(t)}{N^{\mathrm{OS}}(t) + N^{\mathrm{SS}}(t)}}. \tag{12.3}$$

The manner in which the asymmetry $A(t)$ is expected to change is influenced by the different decay chains that contribute to it. For the analysis described in this thesis, the soft muon decay chains are of the general form $t \to Wb \to \ell\mu X$, and there are contributions to $A(t)$ from the various species of b-hadron and c-hadron. Specifically,

$$A(t) = [b - \text{hadron terms} + c - \text{hadron terms}] = \sum_q f_q \cos(\Delta m_q t) + [c - \text{hadron terms}], \tag{12.4}$$

where the sum over q runs over the possible hadronic states with which the leading order b-quark forms a b-hadron. Explicitly, $q \in \{d, u, s, q_1q_2\}$, where q_1q_2 denotes any pair of quarks forming a baryon with the b-quark. The symbols f_q and Δm_q represent respectively the production fraction and the mixing oscillation frequency (also known as the mass difference, hence the Δm notation) of the corresponding b-hadron (with all antiparticle equivalents inferred from here on), as summarised in Table 3.1. The c-hadron terms are neglected going forward in this chapter as the focus is on making measurements in the b-physics sector, but these terms would need to be treated as a background to any measurement that progressed beyond a feasibility study. This could potentially be suppressed through additional selection cuts that enriched the fraction of events coming from direct b-hadron decays, such as tighter p_{T} or impact parameter cuts.

Referring back to Section 3.2, it can be seen that the B^0 meson (with $q = d$) and B_s^0 meson (with $q = s$) are subject to mixing interactions via the process shown in Fig. 3.5. The B^+ meson (with $q = u$) and b-baryons (with $q = q_1q_2$) do not mix, and therefore have zero mixing oscillation frequencies, $\Delta m_u = \Delta m_{q_1q_2} = 0$. Expanding the sum from Eq. 12.4 while taking this into consideration, the asymmetry becomes

$$A(t) = f_d \cos(\Delta m_d t) + f_s \cos(\Delta m_s t) + (f_u + f_{q_1q_2}) + [c - \text{hadron terms}]. \tag{12.5}$$

It can thus be seen that the distribution of this asymmetry is expected to have a slow oscillatory component (from B^0), a fast oscillatory component (from B_s^0), and a constant component (from B^+ and b-baryons).

To ascertain what quantities of interest can be extracted from $A(t)$, similar time-dependent measurements performed at the B-factories (the BaBar experiment located in Stanford, California, USA, and the Belle experiment located in Tsukuba, Japan) and the LHCb experiment were reviewed [216, 217]. This showed that similar asymmetries to $A(t)$ have been used to make measurements of the mixing oscillation frequencies Δm_d and Δm_s [61, 62]. Δm_d is one of the inputs used to calculate the magnitude of the CKM matrix element $|V_{td}|$, while Δm_d and Δm_s are used jointly to calculate $|\frac{V_{td}}{V_{ts}}|$. These calculations are used to help overconstrain the unitarity triangle shown in Fig. 4.1, in an attempt to highlight any deviation from the Standard Model. The possibilities of extracting measurements of Δm_d and Δm_s in a similar fashion are considered in Section 12.2. In addition to oscillation frequency measurements, time-dependent asymmetries have been used at the B-factories and LHCb to make measurements of parameters relating to CP-violation in interference between decays to a common final state with and without mixing (the third type of CP-violation introduced in Section 4.5), utilising exclusive final states such as the so-called golden modes that proceed via a J/Ψ meson [218–222]. This is in contrast to the inclusive approach of the ATLAS time-integrated measurement, and further work is required to understand whether the inclusive asymmetry of Eq. 12.1 may provide sensitivity to an interference-related CP-violation asymmetry, A_{int}, in a similar manner to these measurements.

12.2 Expectations for Full Run 2

To examine what could be extracted from the full Run 2 ATLAS data, a reconstruction-level MC simulation sample is used, scaled to the full Run 2 luminosity of $139\,\text{fb}^{-1}$, with the decay time taken from the particle-level truth of the simulation. The events in the sample are first divided into 20 bins of hadron proper decay time over a range of 0 ps to 15 ps, encompassing more than 99.9% of all events in the sample. The majority of events are concentrated in the first few bins, with exponentially less in each bin. This is to be expected, as the b-hadrons have mean lifetimes ranging from 0.5 ps to 1.6 ps [7, 8]. For each of these bins, the $N^{\ell\mu}(t)$ counts are constructed and used to calculate the time-dependent asymmetry and its associated full Run 2 statistical uncertainty, as per Eq. 12.1 and Eq. 12.3. As well as being calculated for the events in each bin as a whole, $A(t)$ and $\sigma_{A(t)}$ are also calculated separately for each species of b-hadron, in order to examine each component individually.

The distribution of the asymmetry is shown in Fig. 12.1. The statistical uncertainties on the asymmetry reflect the overall exponential decay trend in the time, with small statistical uncertainties in the bins at lower values of the hadron proper decay time and higher uncertainties in the bins at higher values of the hadron proper decay time. Referring back to Eq. 12.5, the slow oscillatory component that is expected from B^0 mesons can clearly be identified (shown in blue), and indeed this dominates the shape of the overall distribution (shown in black) - although the clarity of the oscillation is obscured in the low statistics region of the higher time bins. The constant components expected from B^+ mesons (shown in red) and b-baryons (shown in green) can also be seen. The fast oscillatory component expected from B_s^0 mesons (shown in yellow) is not visible, due to the oscillation frequency for B_s^0, Δm_s, being significantly higher than the oscillation frequency for B^0, Δm_d (over the range of one bin, 0.75 ps, two full mixing oscillations would be expected for this component). The relatively small production fraction (8.4%) for B_s^0 makes a binning that is fine enough to be sensitive to this oscillation unfeasible without significantly more data, due to the magnitude of the resulting statistical uncertainties.

To investigate how a measurement of Δm_d could be extracted from the asymmetry distribution, a least-squares fitting method is employed. Two approaches are considered, both making use of the Levenberg-Marquandt algorithm to iteratively minimise the sum of squared residuals between a fitting function and the datapoints divided by the statistical uncertainties on the datapoints, implemented through the Python package `lmfit` [223][224][225]. The fitting function can be written $f(t;\boldsymbol{\alpha})$, where $\boldsymbol{\alpha}$ is the vector of parameters to be fitted.

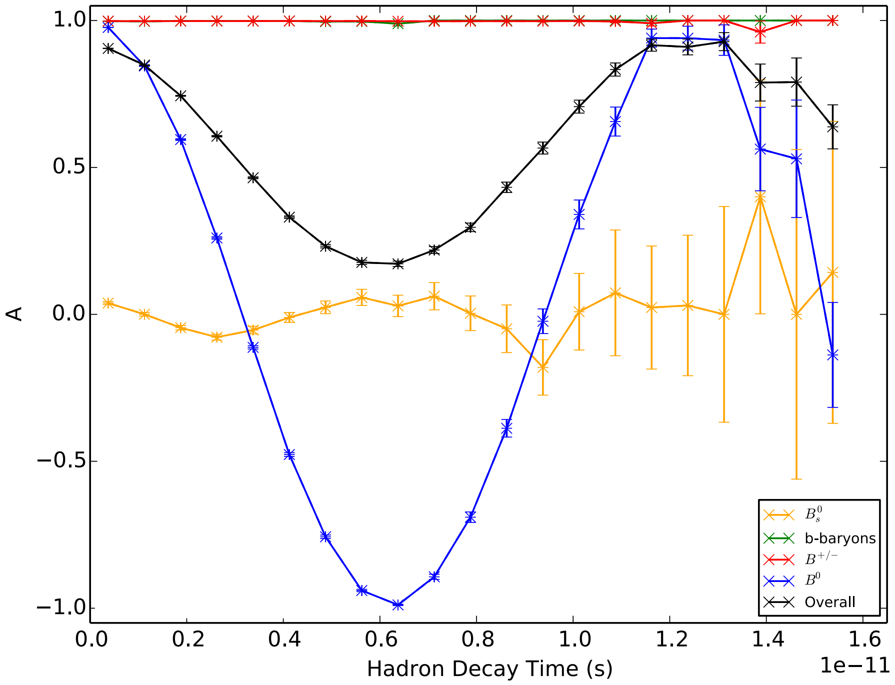

Figure 12.1 The time-dependent asymmetry, $A(t)$, as a function of the decay time of the b-hadron, in MC simulation scaled to an integrated luminosity of 139 fb^{-1}. The black line shows the overall distribution, and the coloured lines show the breakdown of this distribution for the different species of b-hadron.

The first approach is to fit directly to the B^0 component (shown in blue in Fig. 12.1), although this would not be possible when analysing a data sample as the information on the b-hadron species is only available at truth-level. The fitting function is chosen to be

$$f(t;\alpha) = \cos(\alpha t). \tag{12.6}$$

The second approach is to fit a more complicated function to the overall asymmetry distribution (shown in black in Fig. 12.1). Two fitting functions are considered,

$$f(t;\alpha,\beta,\gamma) = \beta + \gamma\cos(\alpha t), \tag{12.7}$$

$$f(t;\alpha,\beta,\gamma,\delta) = \beta + \gamma\cos(\alpha t) + \delta\cos(\Delta m_s t). \tag{12.8}$$

Both of these functions are comparable to Eq. 12.5, with the first being a simplification based on the assumption that the B_s^0 component can be approximated by a constant component with a value of zero, which seems like a reasonable approximation based on Fig. 12.1. The latter models the B_s^0 component as an oscillation with its frequency set to the PDG value as given in Table 3.1.

Equating Eq. 12.8 and Eq. 12.5 yields a set of relationships between the fit parameters and the physical quantities governing the asymmetry,

$$\alpha = \Delta m_d; \beta = f_u + f_{q_1 q_2}; \gamma = f_d; \delta = f_s. \tag{12.9}$$

No attempt is made to introduce a fit parameter to extract a value for Δm_s, due to the previously discussed insensitivity to this oscillation.

The goodness-of-fit is assessed using a chi-squared statistic [226]. This is defined as

$$\chi^2 = \sum_i (f(t_i; \boldsymbol{\alpha}) - y(t_i))^2, \tag{12.10}$$

where the sum is over the time values of the datapoints, and $f(t_i; \boldsymbol{\alpha})$ and $y(t_i)$ are respectively the value of the fitted function and the value of the datapoint at time t_i.

This is quoted with the number of degrees of freedom in the fit, given by

$$DoF = n_{\text{datapoints}} - n_{\text{fit parameters}}. \tag{12.11}$$

In general, a value of $\frac{\chi^2}{DoF} \approx 1$ indicates a good fit.

The fitting algorithm returns a covariance matrix for the fitted parameters. By taking the diagonal elements of this matrix, it is possible to obtain a standard error on each fitted parameter. This incorporates the errors on the data and the errors introduced by the performance of the fit.

A comparison of all the fitted functions and the datapoints can be seen in Fig. 12.2. The fit to the B^0 component results in a value of $\Delta m_d = 0.5018 \pm 0.0015\,\text{ps}^{-1}$ and a goodness-of-fit of $\frac{\chi^2}{DoF} = \frac{176.54}{19} = 9.29$. The full results of the fits to the overall data are summarised in Table 12.1, and only the headline results of the fitted value for Δm_d and the goodness-of-fit are discussed here. Using the simplified fitting function (Eq. 12.7) results in a value of $\Delta m_d = 0.5043 \pm 0.0032\,\text{ps}^{-1}$ and a goodness-of-fit of $\frac{\chi^2}{DoF} = \frac{50.65}{17} = 2.98$. Using the expanded fitting function (Eq. 12.8) results in a value of $\Delta m_d = 0.5043 \pm 0.0033\,\text{ps}^{-1}$ and a goodness-of-fit of $\frac{\chi^2}{DoF} = \frac{22.48}{16} = 1.41$.

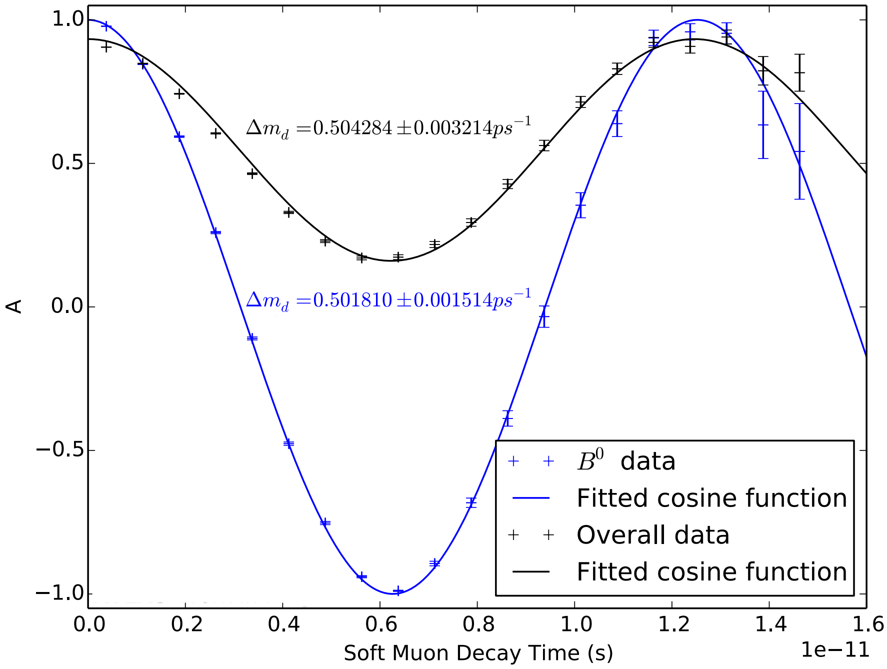

(a)

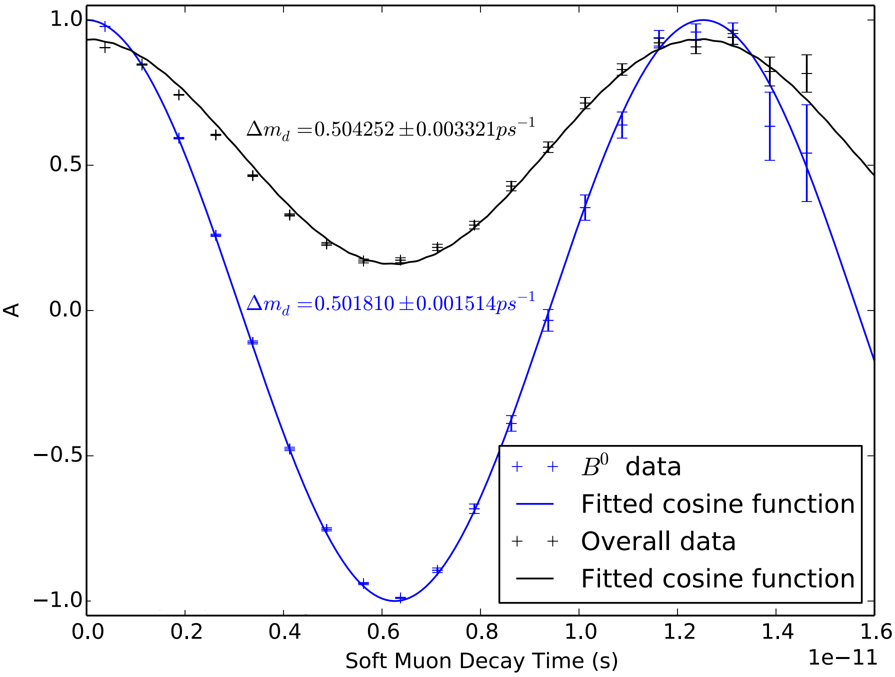

(b)

Figure 12.2 The results of the least-squares fits to the time-dependent asymmetry, $A(t)$ in MC simulation scaled to an integrated luminosity of $139\,\text{fb}^{-1}$. The blue line shows the function fitted to the B^0 component of the asymmetry (see Eq. 12.6), and the black line shows the function fitted to the overall distribution. The fits are shown for two different functions fitted to the overall distribution: **(a)** a function assuming that the B_s^0 component is zero (see Eq. 12.7); **(b)** a function modelling the B_s^0 component as an oscillation (see Eq. 12.8), with its frequency set to the PDG value as given in Table 3.1.

Fit Param.	Value
Δm_d	$0.5043 \pm 0.0032\,\mathrm{ps}^{-1}$
$f_u + f_{q_1 q_2}$	0.5318 ± 0.0025
f_d	0.3797 ± 0.0026
$\frac{\chi^2}{DoF}$	$\frac{50.65}{17} = 2.98$

(a)

Fit Param.	Value
Δm_d	$0.5043 \pm 0.0033\,\mathrm{ps}^{-1}$
$f_u + f_{q_1 q_2}$	0.5308 ± 0.0018
f_d	0.3749 ± 0.0021
f_s	0.0070 ± 0.0016
$\frac{\chi^2}{DoF}$	$\frac{22.48}{16} = 1.41$

(b)

Table 12.1 The results of the least-squares fits to the overall distribution of the time-dependent asymmetry in MC simulation scaled to an integrated luminosity of $139\,\mathrm{fb}^{-1}$. The fits are shown for two different functions fitted to the overall distribution: **(a)** a function assuming that the B_s^0 component is zero (see Eq. 12.7); **(b)** a function modelling the B_s^0 component as an oscillation (see Eq. 12.8), with its frequency set to the PDG value as given in Table 3.1.

The comparatively poor goodness-of-fit achieved for the fit to the B^0 component can be explained by the larger statistical uncertainties on this data in comparison to the overall data. For the fits to the overall data, it can be seen that the expanded fitting function results in a better $\frac{\chi^2}{DoF}$, but both fitting functions result in values of Δm_d that are compatible with the PDG value of $0.5065 \pm 0.0019\,\mathrm{ps}^{-1}$, which is the value of Δm_d used within the MC simulation [8]. The level of statistical uncertainty on the final value is of the same order of magnitude as the uncertainty on the existing best measurement from the LHCb experiment of $0.5050 \pm 0.0021 \pm 0.0010\,\mathrm{ps}^{-1}$, suggesting it may be possible to extract a statistically competitive measurement of Δm_d from the full Run 2 ATLAS dataset [61]. While this initial study seems promising, the fits are intended only to function as a proof-of-concept that the extraction of Δm_d is possible, and a more sophisticated and rigorous fitting method, such as a template fit, should be investigated if such a measurement proceeds beyond the stage of a feasibility study.

12.3 Reconstructing the Decay Time

The studies performed above in Section 12.2 make use of the particle-level truth of the simulation to obtain the hadron decay time, t. To perform a measurement on data, t needs to be determined from the information recorded by the ATLAS detector. There is no explicit timing instrumentation within the detector, so t has to be reconstructed from the spatial and kinematic information that is recorded.

The tracks of all final-state particles in an event can be traced back to establish the vertex from which they originated. The majority of tracks in an event will be associated with the primary vertex, where the initial proton-proton collision occurred. Top quarks and W-bosons are short-lived, so all the particle tracks originating from their decays, including the prompt lepton track, are expected to point directly to this vertex. However, b-hadrons have a sufficiently long lifetime to travel a few millimetres through the detector before they decay, so the tracks of soft muons and other b-hadron decay products will originate from a displaced location known as the secondary vertex. This is illustrated in Fig. 12.3.

Denoting the Cartesian coordinates of the primary vertex x_p, y_p, and z_p, and the Cartesian coordinates of the secondary vertex x_s, y_s, and z_s, the distance, d between the two vertices is given by

$$d = \sqrt{(x_s - x_p)^2 + (y_s - y_p)^2 + (z_s - z_p)^2}. \tag{12.12}$$

To go from this distance to the elapsed time requires factoring in a measure of the velocity of the b-hadron. Accounting for the effects of special relativity, the formula for the decay time is

$$t = \frac{d}{\gamma\beta c} = \frac{d m_B}{p_B} = \frac{d m_B}{\sqrt{\frac{E_B^2}{c^2} - m_B^2 c^2}}, \tag{12.13}$$

where $\beta = \frac{v}{c}$ is the ratio of velocity, v, to the speed of light, c, and γ is the relativistic Lorentz factor, $\gamma = \sqrt{1 - \beta^2}$. m_B, p_B, and E_B are respectively the mass, momentum, and energy of the b-hadron. The final equality follows from the relativistic energy-momentum

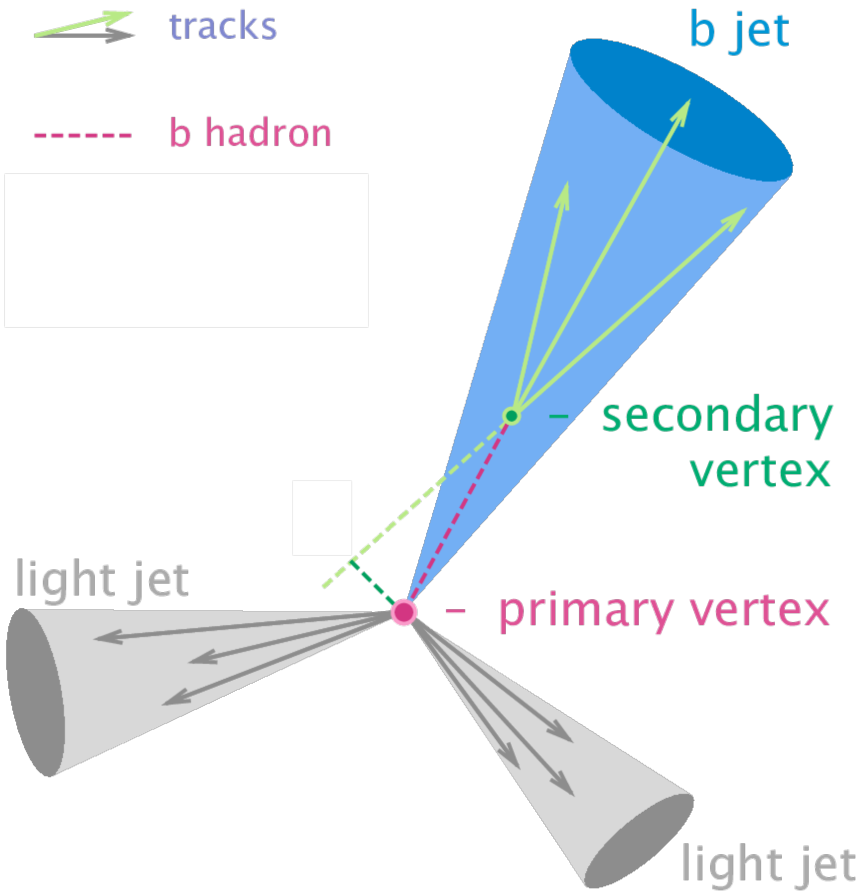

Figure 12.3 A diagram showing the concept of a primary and secondary vertex. At the primary vertex, light jet particles and a *b*-hadron are produced, and their tracks lead back to this point. The *b*-hadron propagates through the detector before decaying at the secondary vertex, and the tracks of the decay products lead back to this point [227].

relation, and shows that it is equivalent to consider either the mass and momentum, or mass and energy, when calculating the time. Henceforth, the mass and energy are used.

Eq. 12.13 shows that there are two facets to how well t can be reconstructed. The first of these is how well the primary and secondary vertices can be reconstructed, addressed in Section 12.3.1, and the second is how well the mass and energy of the hadron can be reconstructed, addressed in Section 12.3.2.

12.3.1 Vertex Reconstruction

Vertex reconstruction in the ATLAS detector proceeds via different methods for primary vertices and secondary vertices. Primary vertex reconstruction starts by applying track selection criteria to suppress fake tracks and tracks from secondary vertices, which is followed by a fit to determine the vertex position from the tracks passing these criteria [228]. The reconstruction is calibrated with MC simulations to account for the effects of pileup on reconstruction, and is found to achieve a reconstruction efficiency for hard-scatter interactions of $> 99\%$. The primary vertex resolution is $\sim 10\,\mu\text{m}$ for the transverse plane (so $\sigma_{x_p} = \sigma_{y_p} \approx 10\,\mu\text{m}$) and $\sim 50\,\mu\text{m}$ for the longitudinal axis (so $\sigma_{z_p} \approx 50\,\mu\text{m}$) [229].

Secondary vertex reconstruction is run for all candidate heavy-flavour jets, and is performed with an algorithm that takes as input the primary vertex information, the direction of the jet, and the list of tracks associated with the jet, and uses these inputs to fit for the secondary vertices within the jet [230, 231]. Additional cleaning procedures are applied to suppress vertices from interactions of light hadrons in the jet with the detector material. Secondary vertices are reconstructed with an efficiency of $\sim 80\%$. The secondary vertex resolution is $\sim 220\,\mu\text{m}$ for the transverse plane (so $\sigma_{x_s} = \sigma_{y_s} \approx 220\,\mu\text{m}$) and $\sim 250\,\mu\text{m}$ for the longitudinal axis (so $\sigma_{z_s} \approx 250\,\mu\text{m}$) [232].

The above values for the primary and secondary vertices can be propagated through Eq. 12.12 to get an idea of the overall resolution on the distance, σ_d. It can be shown that the typical distance travelled by a B-meson is $d \approx \gamma\beta c\tau_B \approx \gamma\beta \cdot 470\,\mu\text{m}$, where τ_B is the lifetime of the B-meson [233]. The mean value of $\gamma\beta$ observed in MC simulation is $\gamma\beta = 21.5$, which gives a typical distance of $d \approx 10\,\mathrm{mm}$. For this distance, $220\,\mu\mathrm{m} \leq \sigma_d \leq 255\,\mu\mathrm{m}$, varying depending on how much of the distance travelled is in the transverse plane or along the longitudinal axis.

The total uncertainty on t is given by

$$\sigma^2(t) = \sigma^2\left(\frac{d}{\gamma\beta c}\right) = t^2\left[\frac{\sigma^2(d)}{d^2} + \frac{\sigma^2(\gamma\beta)}{\gamma^2\beta^2c^2}\right], \tag{12.14}$$

which shows that the relative uncertainty on the time is given by the sum in quadrature of the relative uncertainty on the distance and the relative uncertainty on the energy-momentum term. This is expected to be dominated by the energy-momentum term (a lower bound on the uncertainty of the b-hadron energy would be the JER, which ranges from $6\% - 25\%$ depending on the jet p_{T}), with a distance resolution of the order calculated above (2.5%) not expected to contribute significantly [182, 233]. Therefore, the performance of vertex reconstruction is not expected to present an obstacle to the feasibility of performing a time-dependent measurement.

12.3.2 Hadron Mass and Energy Reconstruction

The strategy for reconstruction of the b-hadron mass and energy, m_B and E_B, for the time-dependent measurements made at b-physics focused experiments such as LHCb make use of dedicated particle identification detector systems to reconstruct all of the hadronic particles that make up a b-jet [119]. For example, a specific final state containing a reconstructed charged D or D^* meson can be required, which gives a sample that is dominated by B^0, in which case m_B is known to be m_{B^0} for all events [61]. The particle identification detectors are also used to perform a partial reconstruction of all the decay products of the b-hadron (corrected for the undetected neutrino), which is used to estimate the energy, E_B.

The ATLAS detector has no such particle identification system, so it is not well-suited to requiring specific final-state particles or performing partial decay product reconstruction. It is instead necessary to attempt to infer m_B and E_B to the best extent possible, and attempts to do this are detailed below. Anything less than perfect reconstruction will introduce a smearing to the asymmetry distribution, causing it to differ from its true distribution. However, if this level of smearing can be well understood in simulation, it can be corrected for during the unfolding process (see Chapter 11) and the underlying true distribution can be recovered. As discussed for the ST/DT-assignment in Section 10.1, the effectiveness of the reconstruction technique will therefore not affect the central value of any measurement made, but will instead affect the level of uncertainty on the measurement.

Starting with the mass and referring back to Table 3.1, it can be seen that the B^0 and B^+ masses differ by only 0.31 MeV, or less than one part in 10,000. Together, these b-hadrons comprise 82% of the sample. The next biggest fraction of the sample comes from B_s^0, for which the mass differs from the mass of the B^0 by 87.54 MeV, or $< 2\%$. The only significant mass difference is for the baryonic component, which makes up the smallest fraction of the sample. Therefore, the approximation $m_B = m_{B^0}$ is made for all particles.

The effect of this mass smearing is assessed by plotting the distribution of $A(t)$ with t recalculated using this approximation. The results are shown in Fig. 12.4. No significant change is seen for the B^0 and B^+ components. There is a noticeable smearing in the B_s^0 component due to the migration of events between bins introduced by the approximation. An even more pronounced migration between bins is observed for the b-baryon component, although this is not visible in the distribution due to the constant nature of this component. As expected from the low production fractions for B_s^0 and b-baryons, these changes have a negligible effect on the overall distribution, and the approximation $m_B = m_{B^0}$ is deemed to be a good one.

Attention is now turned to the reconstruction of E_B. Due to the continuous nature of the true energy distribution, the strategy employed for the mass of assuming a single value is not appropriate, and an estimate of the energy must be found on an event-by-event basis using the information that is reconstructed in the detector.

The avenue through which the estimate for E_B proceeds is via the reconstructed energy of the b-jet, $E_{b-\mathrm{jet}}$. However, the reconstructed b-jet energy is not equal to the original b-jet energy for the case of b-jets that have produced a soft muon, because the jet energy definition does not include the energy carried away by the soft muon and associated neutrino. To overcome

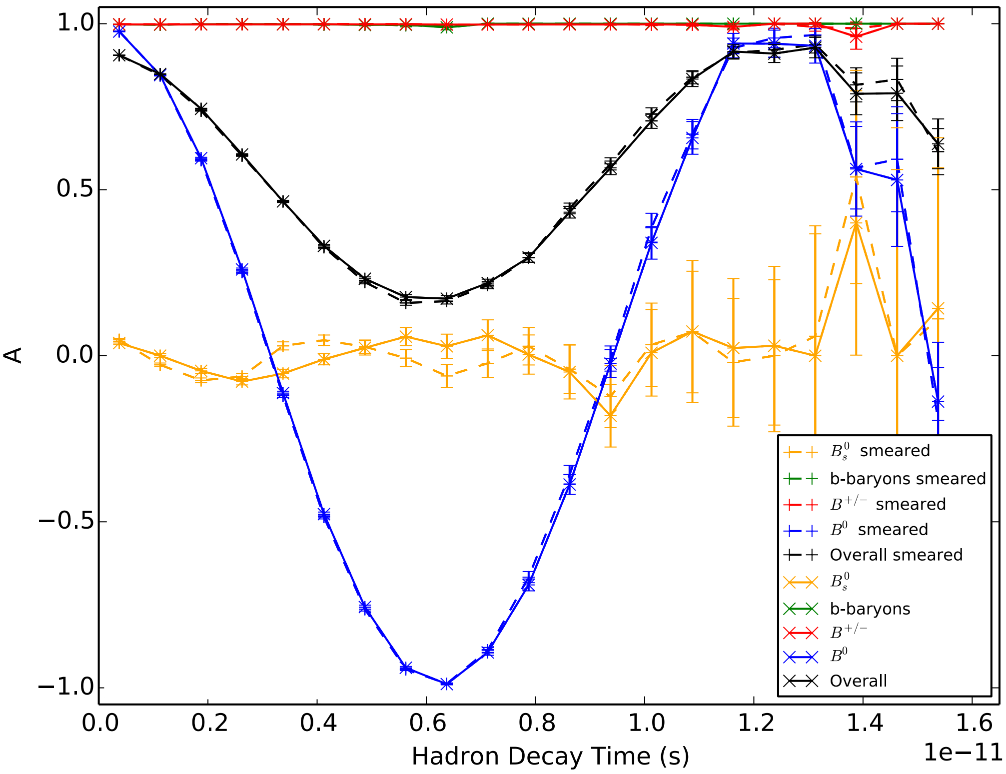

Figure 12.4 A comparison of the distributions of the time-dependent asymmetry, $A(t)$, in MC simulation scaled to an integrated luminosity of 139 fb^{-1}, with and without the smearing introduced by the assumption $m_B = m_{B^0}$. The black line shows the overall distribution, and the coloured lines show the breakdown of this distribution by the species of b-hadron. The solid lines show the original distributions, and the dotted lines show the smeared distributions.

this, an SLC similar to the one described in Section 10.3.2 is applied, and the original b-jet energy is estimated to be

$$E^0_{b-\text{jet}} = E_{b-\text{jet}} + E_\mu + E_\nu \approx E_{b-\text{jet}} + 2E_\mu. \tag{12.15}$$

Fig. 12.5 shows the comparison of both $E_{b-\text{jet}}$ and $E^0_{b-\text{jet}}$ to the true b-quark ($\bar{b}$-quark) energy (after ISR of gluons), which is the energy that is available at the formation of the b-jet. It confirms that $E_{b-\text{jet}}$ is underestimating the true energy, while showing that $E^0_{b-\text{jet}}$ then appears to over-correct for this effect. This shows that this is a fairly crude approximation to the original b-jet energy.

The final step is to go from an estimate of the b-quark energy to an estimate of the b-hadron energy. The b-hadron is formed from the initial b-quark during the hadronisation process as described in Section 3.2, with some fraction of the initial b-quark energy transferred to the b-hadron. This fraction of the energy is denoted x_B. Explicitly, this is defined at truth-level as

$$x_B = \frac{E_B}{E_{b-\text{quark}}}. \tag{12.16}$$

A similar quantity, the effective x_B, denoted x_B^{eff}, is introduced as the reco-level analogue to this truth-level quantity with the true b-quark energy replaced by its reco-level estimation

$$x_B^{\text{eff}} = \frac{E_B}{E^0_{b-\text{jet}}}. \tag{12.17}$$

Both x_B and x_B^{eff} are constructed for the sample, and are compared in Fig. 12.6, which shows that the true and effective distributions have broadly similar shapes. The average value of the true distribution is $< x_B >= 0.771$, while the average value of the effective distribution is lower, at $< x_B^{\text{eff}} >= 0.714$. This is due to the fact that $E_{b-\text{jet}}^0$ overestimates $E_{b-\text{quark}}$, as previously seen in Fig. 12.5.

Applying the average of the effective distribution allows the final estimate of the true b-hadron energy, E_B, to be constructed as

$$E_B \approx < x_B^{\text{eff}} > E_{b-jet}^0. \tag{12.18}$$

A comparison of the true energy distribution and the estimate is shown in Fig. 12.7. This shows a good level of agreement for the overall distribution. However, examining the resolution, defined as

$$\text{resolution} = \frac{< x_B^{\text{eff}} > E_{b-\text{jet}}^0 - E_B}{E_B}, \tag{12.19}$$

and shown in Fig. 12.8, reveals that this agreement is not as good on an event-by-event basis. The resolution distribution has a long tail to the right, showing that $< x_B^{\text{eff}} > E_{b-\text{jet}}^0$ overestimates E_B for a significant number of events.

This energy estimate is assessed on top of the mass approximation, by plotting the distribution of $A(t)$ with t recalculated using $m_B = m_B^0$ and $E_B =< x_B^{\text{eff}} > E_{b-\text{jet}}^0$. The result is shown in Fig. 12.9. The effect can be seen similarly in both the B^0 distribution (shown in blue) and the overall distribution (shown in black). The estimate seems reasonable in the high statistics region of the bins at low values of time, but breaks down at higher values of time. An improved estimate of E_B that made use of an event-by-event determination of x_B^{eff} would be expected to be much better than the estimation that makes use of the average of the distribution, $< x_B^{\text{eff}} >$. If the time-dependent measurement were to proceed beyond a feasibility study, the additional information that would have to be obtained to reconstruct the secondary vertex (as discussed above in Section 12.3.1) may also allow for such an event-by-event determination of x_B^{eff} by

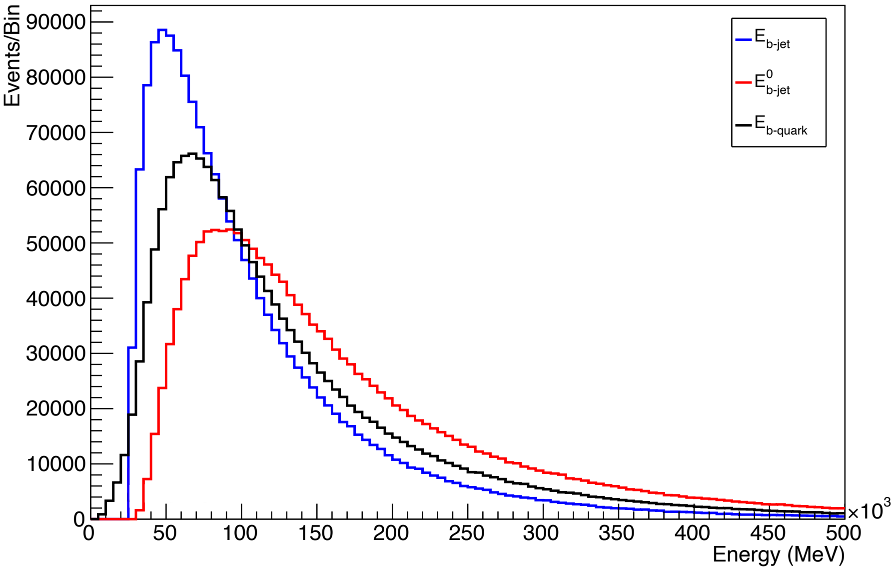

Figure 12.5 A comparison of the reco-level quantities $E_{b-\text{jet}}$ and $E^0_{b-\text{jet}}$ to the true b-quark energy, $E_{b-\text{quark}}$, in MC simulation scaled to an integrated luminosity of 139 fb^{-1}.

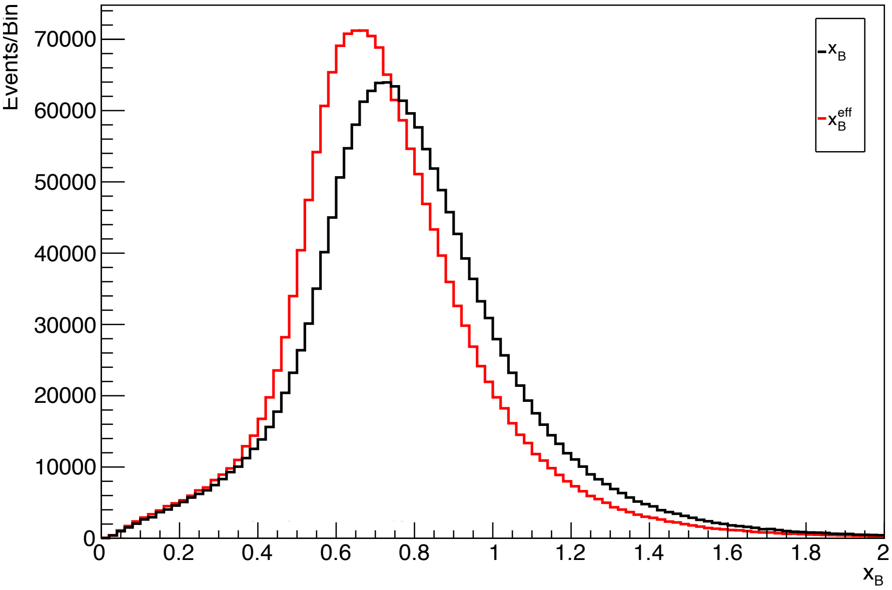

Figure 12.6 A comparison of the truth-level quantity x_B and the effective reco-level quantity x_B^{eff}, which represent the fraction of the b-quark energy that is transferred to the b-hadron, as measured in MC simulation scaled to an integrated luminosity of 139 fb^{-1}.

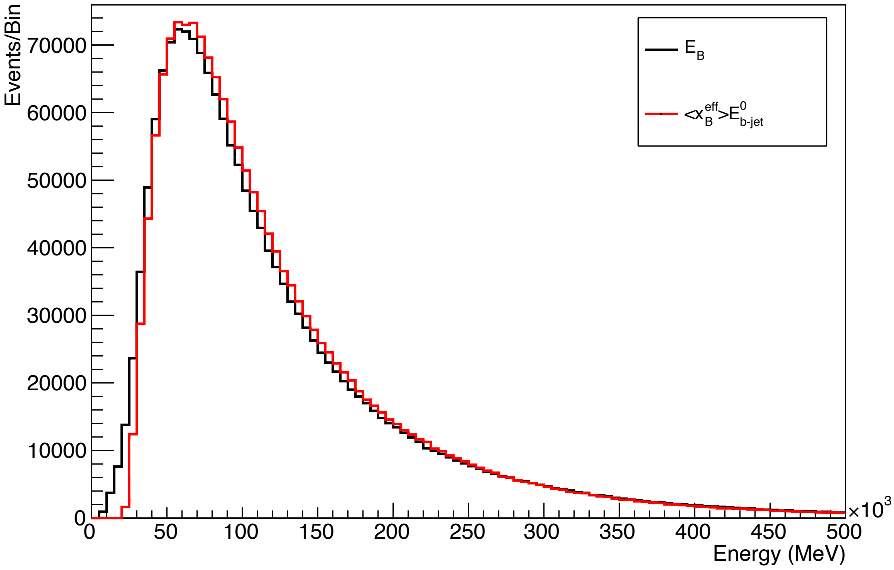

Figure 12.7 A comparison of the distribution of the estimate $< x_B^{\text{eff}} > E^0_{b-\text{jet}}$ with the true b-hadron energy, E_B, as measured in MC simulation scaled to an integrated luminosity of 139 fb^{-1}.

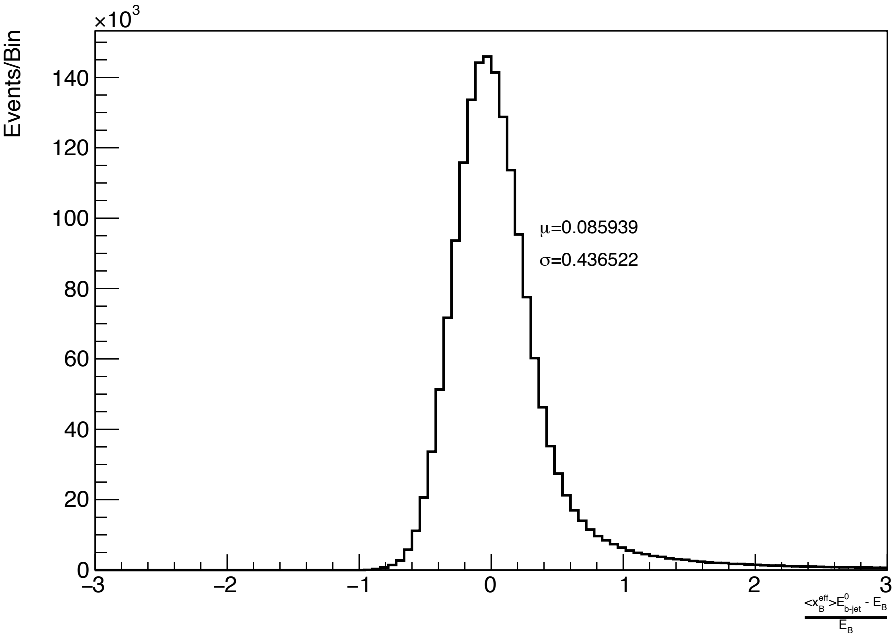

Figure 12.8 The resolution for the estimate $< x_B^{\text{eff}} > E^0_{b-jet}$ of the true b-hadron energy, E_B, as measured in MC simulation scaled to an integrated luminosity of 139 fb^{-1}.

employing a technique such as a machine learning regression algorithm. This can be motivated from a physics perspective as, for example, a b-jet where x_B is high might be expected to contain only a small number of additional fragmentation tracks with comparatively low momentum, as most of the momentum has been transferred to the leading b-hadron. Conversely, a b-jet where x_B is low might be expected to contain a large number of additional fragmentation tracks with comparatively high momentum, as only a small fraction of the momentum has been transferred to the leading b-hadron.

12.4 Prospects

The full Run 2 ATLAS dataset makes it statistically viable for the first time to consider extending the existing time-integrated analysis with a time-integrated measurement. This would open the door to several quantities of interest, as discussed in Section 12.1, namely a potential additional CP-violation asymmetry, A_{int}, and the B^0 mixing oscillation frequency, Δm_d. A measurement of Δm_d could help to constrain possible new sources of CP-violation by contributing to calculations of $|V_{td}|$ and $|\frac{V_{td}}{V_{ts}}|$, which are used to overconstrain the unitarity triangles of the CKM matrix. The proof-of-concept studies presented in Section 12.2 suggest that such a measurement of Δm_d would be statistically competitive with recent LHCb measurements.

Section 12.3 shows that reconstructing the hadron decay time, t, in the ATLAS detector is not without its challenges, but that it should be possible to make a good enough reconstruction to allow a time-dependent measurement to proceed.

Overall, the prospects for the time-dependent measurement to progress from a feasibility study to a full measurement of Δm_d (and potentially A_{int}) that complements the time-integrated analysis are considered to be highly promising.

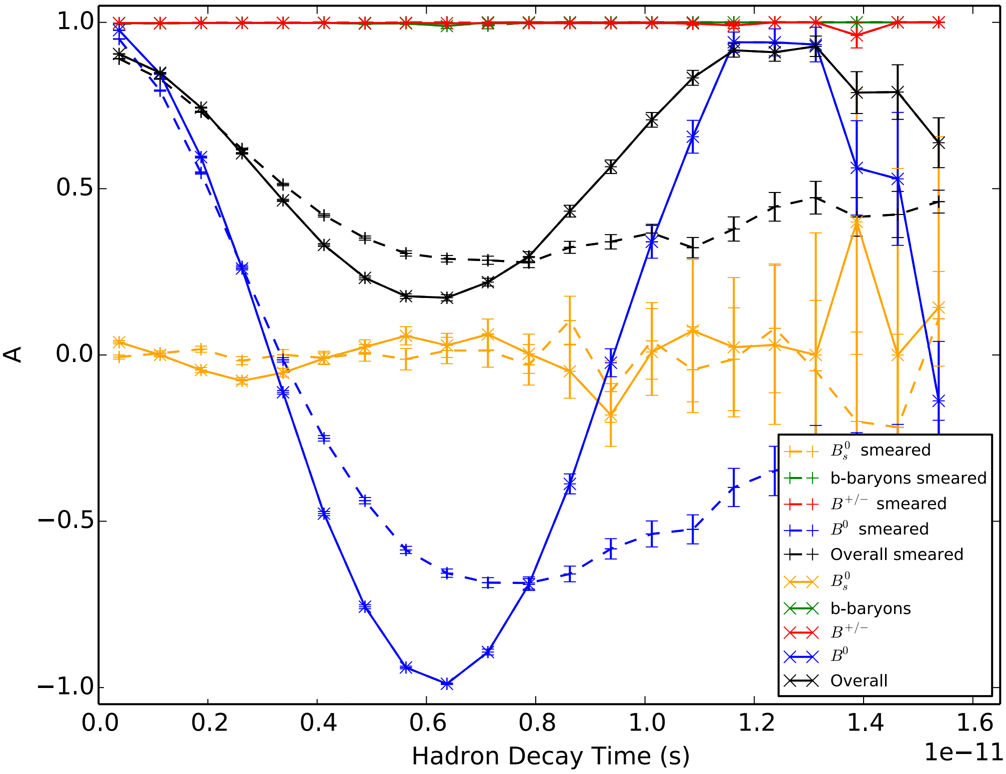

Figure 12.9 A comparison of the time-dependent asymmetry, $A(t)$, as a function of the decay time of the b-hadron, in MC simulation scaled to an integrated luminosity of 139 fb^{-1}, with and without the smearing introduced by setting $m_B = m_{B^0}$ and $E_B =< x_B^{\mathrm{eff}} > E^0_{b-\mathrm{jet}}$. The black line shows the overall distribution, and the coloured lines show the breakdown of this distribution by the species of b-hadron. The solid lines show the original distribution, and the dotted lines show the smeared distribution.

Chapter 13

Results

This chapter presents the results of the time-integrated measurement detailed over the course of this thesis. It begins in Section 13.1 with presentation of a selection of distributions (kinematics and $N^{\ell\mu}$) as measured for both the signal MC simulation and the experimental data corresponding to an integrated luminosity of $139\,\mathrm{fb}^{-1}$ and a centre-of-mass energy of $\sqrt{s} = 13\,\mathrm{TeV}$. No attempt is made in the experimental data to unfold and extract the observed charge asymmetries or CP-violation asymmetries, due to a desire to keep these results blinded until the full and final analysis pipeline is in place. However, the full asymmetry results are presented for MC simulation, beginning with the extraction of the observed charge asymmetries from the $N^{\ell\mu}$ distribution in Section 13.2. This is followed by Section 13.3, which presents the decay chain fractions and the values extracted for the underlying CP-violation asymmetries by following the procedure detailed in Section 7.4 to consider each asymmetry in turn while setting the remaining asymmetries to zero.

13.1 Data vs. MC Plots

The distributions of various kinematic quantities in both MC simulation and experimental data are presented below.

Firstly, Fig. 13.1 presents a selection of the prompt lepton kinematics, with Fig. 13.1(a) showing the p_T distribution and Fig. 13.1(b) showing the η distribution. This is followed by the soft muon kinematics in Fig. 13.2, with Fig. 13.2(a) showing the p_T distribution, Fig. 13.2(b) showing the η distribution, and Fig. 13.2(c) showing the d_0 distribution.

The missing transverse momentum kinematics are presented in Fig. 13.3, with Fig. 13.3(a) showing the $E_\mathrm{T}^\mathrm{miss}$ distribution and Fig. 13.3(b) showing the $m_\mathrm{T}(W)$ distribution.

The kinematics for the highest-p_T jet are presented in Fig. 13.4, with Fig. 13.4(a) showing the p_T distribution and Fig. 13.4(b) showing the η distribution. This is followed by the transverse momenta of the flavour-tagged jets in Fig. 13.5, with Fig. 13.5(a) showing the p_T distribution for the b-tagged jet and Fig. 13.5(b) showing the p_T distribution for the SMT-tagged jet.

Finally, the distribution of the total angular separation, $\Delta R(\ell, \mu)$, is shown in Fig. 13.6 and the combined charge count $N^{\ell\mu}$ is shown in Fig. 13.7.

For all the distributions, a similar shape is seen across both the experimental data and the MC simulation, with a larger number of events present across all bins for the experimental data, as is to be expected given that the MC simulation is for the signal process only, and has not yet been stacked with finalised background estimates.

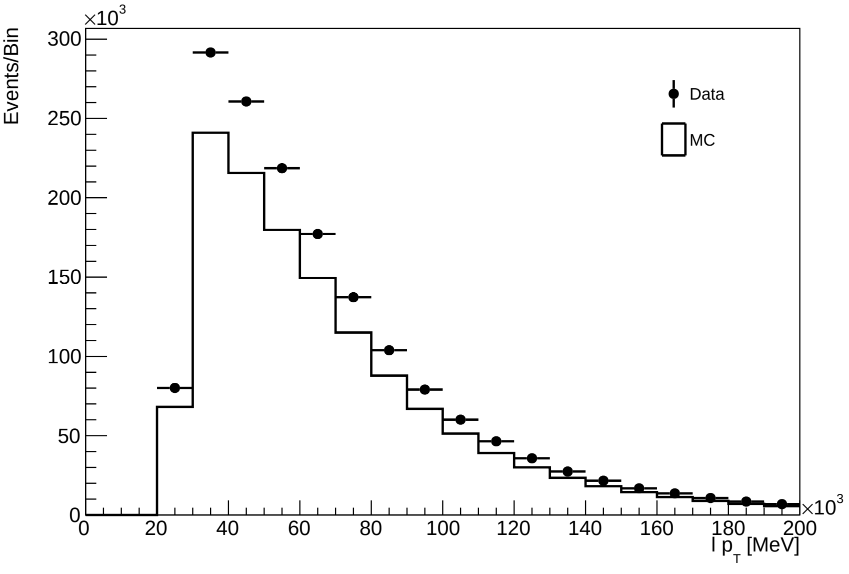

(a)

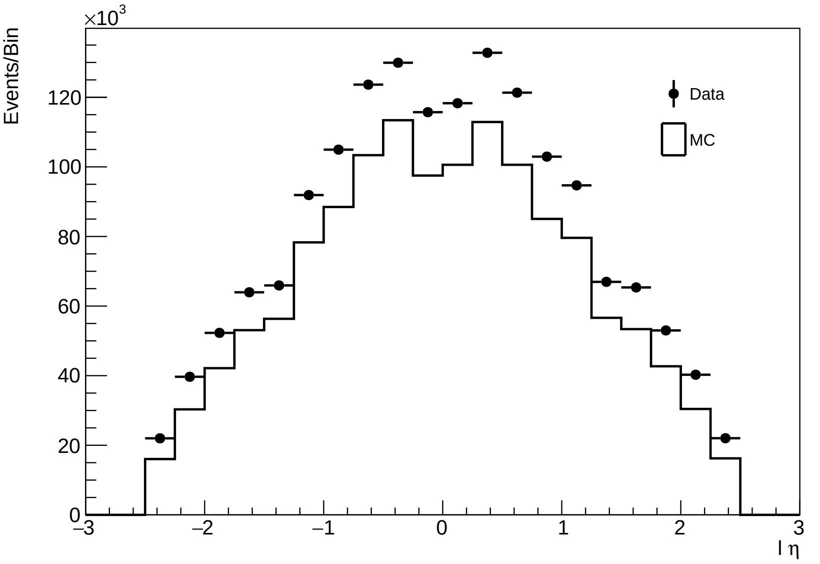

(b)

Figure 13.1 The distributions of the prompt lepton kinematics, as measured in signal MC simulation scaled to an integrated luminosity of $139\,\mathrm{fb}^{-1}$ (solid line) and in $139\,\mathrm{fb}^{-1}$ of experimental data (markers), comprising: **(a)** the transverse momentum, p_T; **(b)** the pseudorapidity, η.

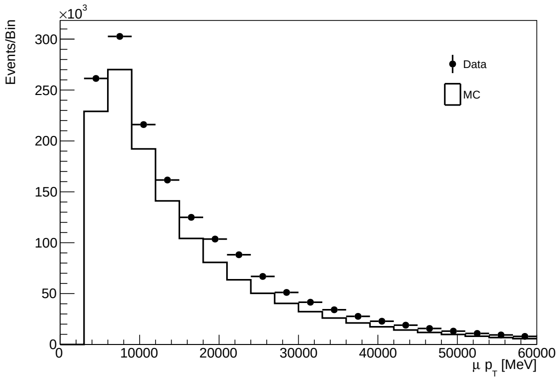

(a)

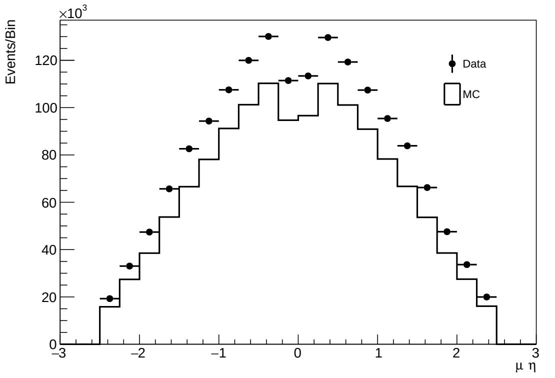

(b)

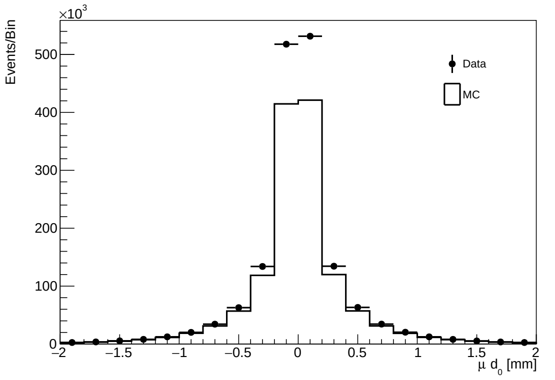

(c)

Figure 13.2 The distributions of the soft muon kinematics, as measured in signal MC simulation scaled to an integrated luminosity of $139\,\text{fb}^{-1}$ (solid line) and in $139\,\text{fb}^{-1}$ of experimental data (markers), comprising: **(a)** the transverse momentum, p_T; **(b)** the pseudorapidity, η; **(c)** the transverse impact parameter, d_0.

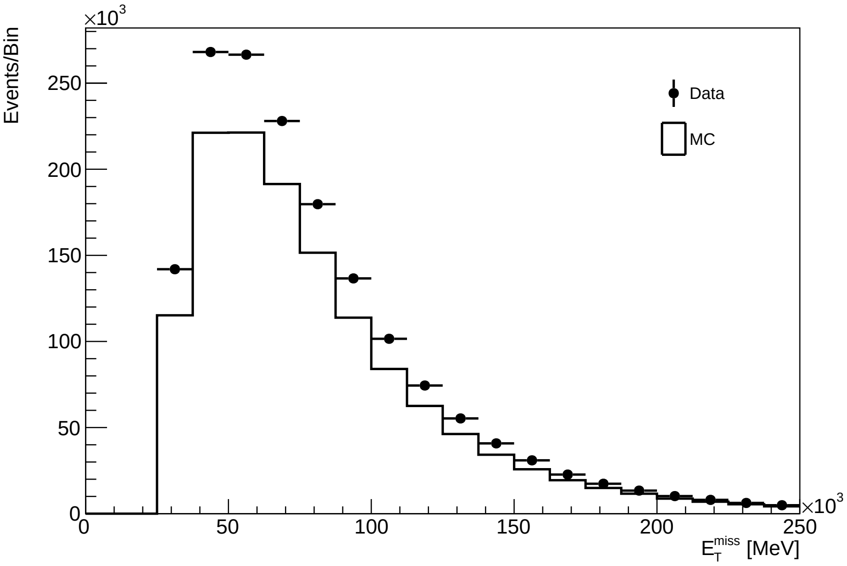

(a)

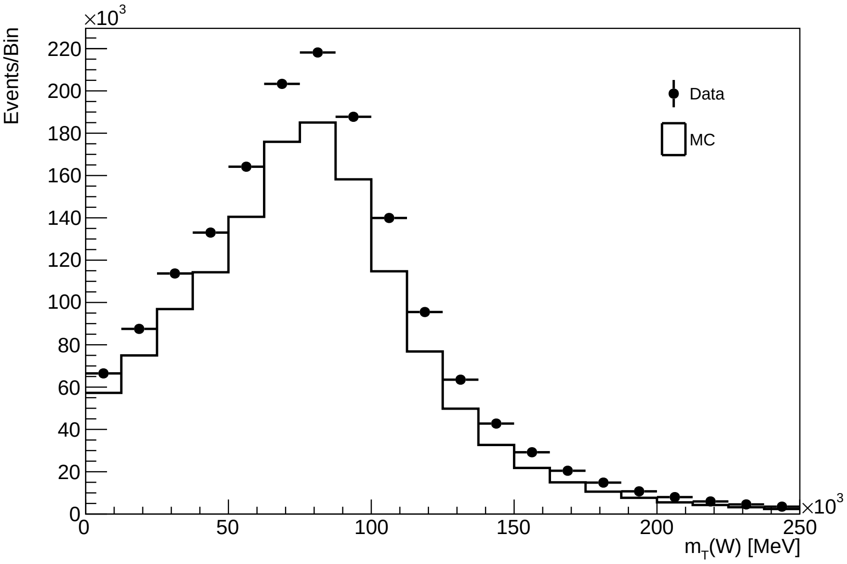

(b)

Figure 13.3 The distributions of the missing transverse momentum kinematics, as measured in signal MC simulation scaled to an integrated luminosity of $139\,\mathrm{fb}^{-1}$ (solid line) and in $139\,\mathrm{fb}^{-1}$ of experimental data (markers), comprising: **(a)** the missing transverse momentum, $E_{\mathrm{T}}^{\mathrm{miss}}$; **(b)** the transverse W-boson mass, $m_{\mathrm{T}}(W)$.

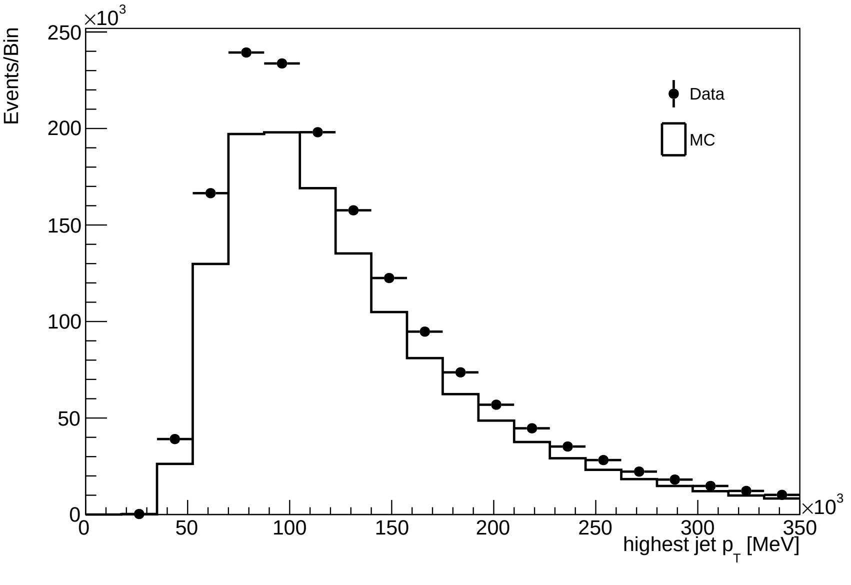

(a)

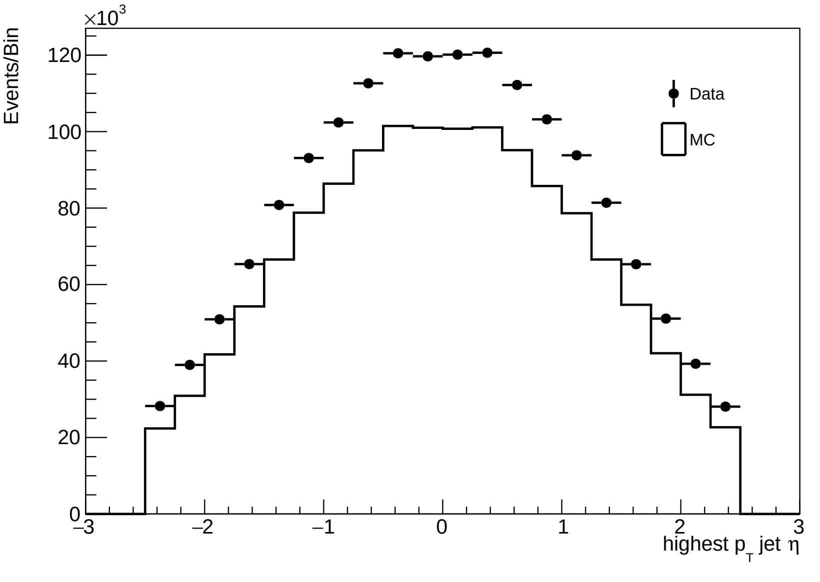

(b)

Figure 13.4 The distributions of the kinematics for the highest-p_{T} jet, as measured in signal MC simulation scaled to an integrated luminosity of $139\,\mathrm{fb}^{-1}$ (solid line) and in $139\,\mathrm{fb}^{-1}$ of experimental data (markers), comprising: **(a)** the transverse momentum, p_{T}; **(b)** the pseudorapidity, η.

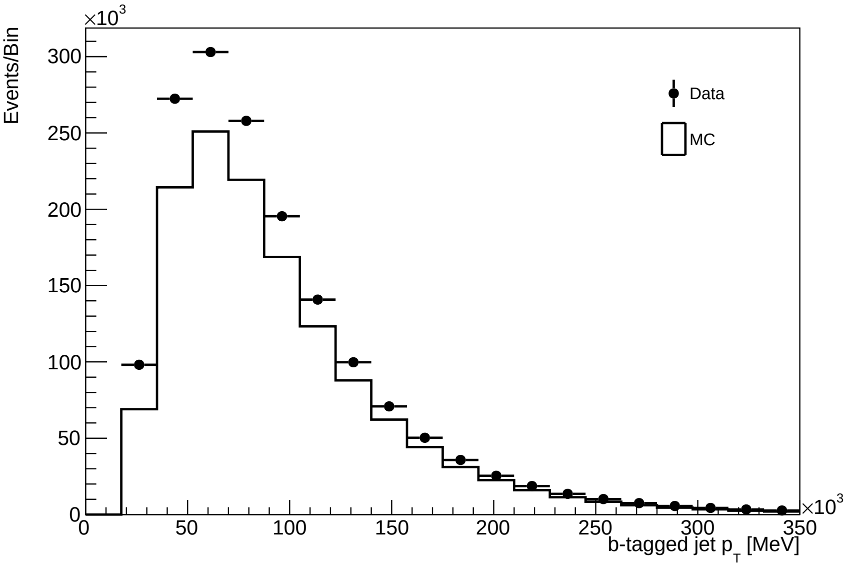

(a)

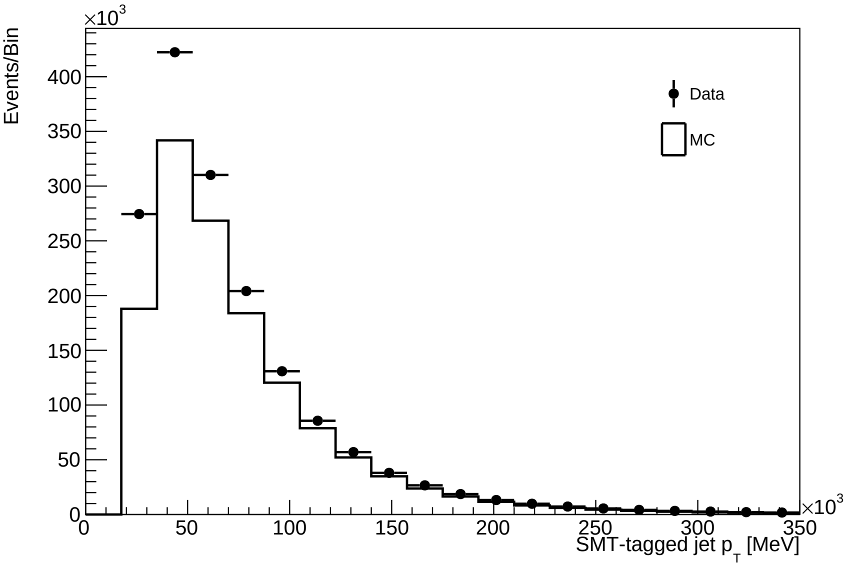

(b)

Figure 13.5 The distributions of the flavour-tagged jet momentum, as measured in signal MC simulation scaled to an integrated luminosity of 139 fb^{-1} (solid line) and in 139 fb^{-1} of experimental data (markers), comprising: **(a)** the transverse momentum, p_{T}, of the b-tagged jet; **(b)** the transverse momentum, p_{T}, of the SMT-tagged jet.

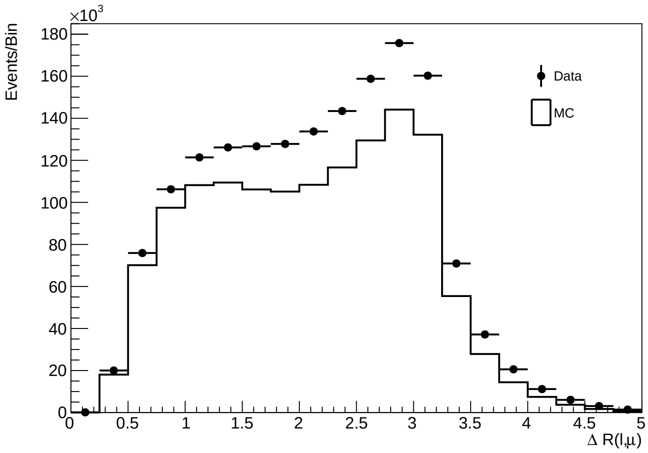

Figure 13.6 The distribution of the total angular separation between the prompt lepton and the soft muon, $\Delta R(\ell, \mu)$, as measured in signal MC simulation scaled to an integrated luminosity of $139\,\text{fb}^{-1}$ (solid line) and in $139\,\text{fb}^{-1}$ of experimental data (markers).

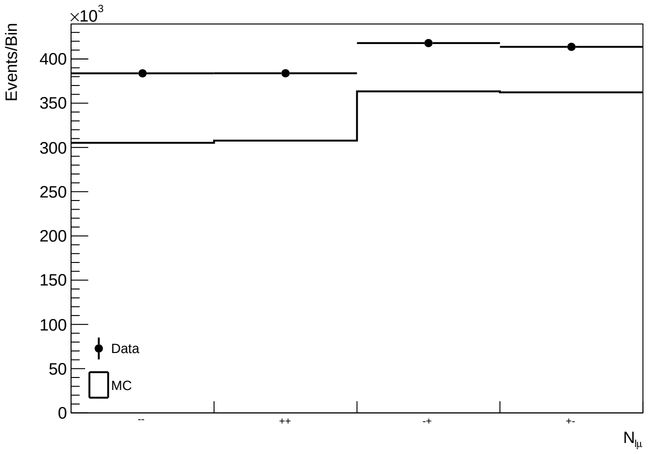

Figure 13.7 The distribution of the combined charge count $N^{\ell\mu}$, as measured in signal MC simulation scaled to an integrated luminosity of $139\,\text{fb}^{-1}$ (solid line) and in $139\,\text{fb}^{-1}$ of experimental data (markers), using the `KLFitter` method of ST/DT-assignment.

13.2 Charge Asymmetries

Unfolding the distribution from MC simulation and extracting the observable charge asymmetries gives results $A^{\mathrm{SS}}(\mathrm{MC})$ and $A^{\mathrm{OS}}(\mathrm{MC})$ for each of the four methods of ST/DT-assignment as

$$\begin{aligned} A^{\mathrm{SS}}_{\Delta R(\ell,\mu)}(\mathrm{MC}) &= +0.878 \pm 0.180\ (\mathrm{Stat.}) \pm 0.507\ (\mathrm{Syst.}) = +0.878^{+0.537}_{-0.538}\ (\mathrm{Total}), \\ A^{\mathrm{OS}}_{\Delta R(\ell,\mu)}(\mathrm{MC}) &= -0.465 \pm 0.095\ (\mathrm{Stat.}) \pm 0.867\ (\mathrm{Syst.}) = -0.465 \pm 0.873\ (\mathrm{Total}); \end{aligned} \tag{13.1}$$

$$\begin{aligned} A^{\mathrm{SS}}_{\mathrm{BDT},X_\ell}(\mathrm{MC}) &= +0.878 \pm 0.178\ (\mathrm{Stat.})^{+0.491}_{-0.490}\ (\mathrm{Syst.}) \quad = +0.878^{+0.523}_{-0.521}\ (\mathrm{Total}), \\ A^{\mathrm{OS}}_{\mathrm{BDT},X_\ell}(\mathrm{MC}) &= -0.465 \pm 0.094\ (\mathrm{Stat.}) \pm 0.839\ (\mathrm{Syst.}) = -0.465 \pm 0.884\ (\mathrm{Total}); \end{aligned} \tag{13.2}$$

$$\begin{aligned} A^{\mathrm{SS}}_{\mathrm{BDT},X_f}(\mathrm{MC}) &= +0.878 \pm 0.167\ (\mathrm{Stat.})^{+0.528}_{-0.525}\ (\mathrm{Syst.}) = +0.878^{+0.553}_{-0.551}\ (\mathrm{Total}), \\ A^{\mathrm{OS}}_{\mathrm{BDT},X_f}(\mathrm{MC}) &= -0.465 \pm 0.084\ (\mathrm{Stat.})^{+0.827}_{-0.828}\ (\mathrm{Syst.}) = -0.465 \pm 0.832\ (\mathrm{Total}); \end{aligned} \tag{13.3}$$

$$\begin{aligned} A^{\mathrm{SS}}_{\mathrm{KLFitter}}(\mathrm{MC}) &= +0.878 \pm 0.172\ (\mathrm{Stat.})^{+0.512}_{-0.511}\ (\mathrm{Syst.}) \quad = +0.878^{+0.540}_{-0.539}\ (\mathrm{Total}), \\ A^{\mathrm{OS}}_{\mathrm{KLFitter}}(\mathrm{MC}) &= -0.465 \pm 0.091\ (\mathrm{Stat.}) \pm 0.820\ (\mathrm{Syst.}) = -0.465 \pm 0.825\ (\mathrm{Total}). \end{aligned} \tag{13.4}$$

As explained in Section 10.1, the results for each of the different methods have the same central value but differing uncertainties. A comparison of the uncertainties across the four methods is presented in Table 13.1 for $A^{\mathrm{SS}}(\mathrm{MC})$ and Table 13.2 for $A^{\mathrm{OS}}(\mathrm{MC})$.

A^{SS}(MC)[10^{-2}]	$\Delta R(\ell, \mu)$		BDT, X_ℓ		BDT, X_f		KLFitter	
Measured Value	**+0.878**							
Statistical Uncertainty	**±0.180 (20.5%)**		**±0.178 (20.3%)**		**±0.167 (19.0%)**		**±0.172 (19.6%)**	
Detector Systematics								
Electron Energy Scale, Resolution	+0.002 (0.2%)	−0.005 (0.6%)	+0.004 (0.5%)	−0.006 (0.7%)	+0.002 (0.2%)	−0.006 (0.7%)	+0.003 (0.4%)	−0.006 (0.7%)
Muon Energy Scale, Resolution	+0.012 (1.4%)	−0.009 (1.0%)	+0.017 (1.9%)	−0.014 (1.6%)	+0.012 (1.4%)	−0.009 (1.0%)	+0.014 (1.6%)	−0.021 (2.4%)
Prompt Lepton Isolation, Reconstruction, Trigger	+0.060 (6.8%)	−0.060 (6.8%)	+0.057 (6.5%)	−0.057 (6.5%)	+0.057 (6.5%)	−0.057 (6.5%)	+0.030 (3.4%)	−0.030 (3.4%)
Soft Muon Isolation, Reconstruction	+0.027 (3.1%)	−0.035 (4.0%)	+0.026 (3.0%)	−0.034 (3.9%)	+0.025 (2.8%)	−0.035 (4.0%)	+0.015 (1.7%)	−0.017 (1.9%)
JES	+0.054 (6.2%)	−0.059 (6.7%)	+0.083 (9.5%)	−0.080 (9.1%)	+0.074 (8.4%)	−0.064 (7.3%)	+0.071 (8.1%)	−0.069 (7.9%)
JER	+0.053 (6.0%)	−0.053 (6.0%)	+0.122 (13.9%)	−0.119 (13.6%)	+0.118 (13.4%)	−0.117 (13.3%)	+0.084 (9.6%)	−0.078 (8.9%)
JVT	+0.014 (1.6%)	−0.015 (1.7%)	+0.011 (1.3%)	−0.017 (1.9%)	+0.012 (1.4%)	−0.015 (1.7%)	+0.007 (0.8%)	−0.007 (0.8%)
Pileup	+0.016 (1.8%)	−0.011 (1.3%)	+0.008 (0.9%)	−0.001 (0.1%)	+0.019 (2.2%)	−0.009 (1.0%)	+0.003 (0.4%)	−0.008 (0.9%)
Flavour-Tagging	+0.064 (7.3%)	−0.063 (7.2%)	+0.063 (7.2%)	−0.058 (6.6%)	+0.063 (7.2%)	−0.058 (6.6%)	+0.033 (3.8%)	−0.030 (3.4%)
$E_{\text{T}}^{\text{miss}}$	+0.017 (1.9%)	−0.010 (1.1%)	+0.011 (1.3%)	−0.011 (1.3%)	+0.018 (2.1%)	−0.014 (1.6%)	+0.016 (1.8%)	−0.006 (0.7%)
Electron Charge Misidentification	+0.002 (0.2%)	−0.002 (0.2%)	+0.002 (0.2%)	+0.002 (0.2%)	+0.002 (0.2%)	+0.002 (0.2%)	+0.002 (0.2%)	+0.002 (0.2%)
SMT Mistag rate	+0.010 (1.1%)	−0.009 (1.0%)	+0.010 (1.1%)	−0.009 (1.0%)	+0.010 (1.1%)	−0.009 (1.0%)	+0.010 (1.1%)	−0.009 (1.0%)
Fake Lepton Estimation	+0.050 (5.7%)	−0.050 (5.7%)	+0.050 (5.7%)	−0.050 (5.7%)	+0.050 (5.7%)	−0.050 (5.7%)	+0.050 (5.7%)	−0.050 (5.7%)
Background Estimation	+0.016 (1.8%)	−0.004 (0.5%)	+0.016 (1.8%)	−0.004 (0.5%)	+0.016 (1.8%)	−0.004 (0.5%)	+0.016 (1.8%)	−0.004 (0.5%)
Total	**+0.134 (15.0%)**	**−0.135 (15.4%)**	**+0.182 (20.7%)**	**−0.178 (20.3%)**	**+0.177 (20.2%)**	**−0.170 (19.3%)**	**+0.133 (15.1%)**	**−0.127 (14.5%)**
Modelling Systematics								
ISR μ_R, μ_F, and α_S	±0.029 (3.3%)		±0.023 (2.6%)		±0.027 (3.1%)		±0.014 (1.6%)	
FSR α_S	±0.419 (47.7%)		±0.369 (42.0%)		±0.385 (43.8%)		±0.377 (42.9%)	
h_{damp} Variation	±0.009 (1.0%)		±0.060 (6.8%)		±0.046 (5.2%)		±0.069 (7.9%)	
NLO Generator	±0.106 (12.1%)		±0.137 (15.6%)		±0.181 (20.6%)		±0.175 (19.9%)	
Parton Shower	±0.219 (24.9%)		±0.211 (24.0%)		±0.244 (27.8%)		±0.253 (28.8%)	
PDF	±0.028 (3.2%)		±0.045 (5.1%)		±0.038 (4.3%)		±0.012 (1.4%)	
b/c-Hadron Production Fraction	±0.013 (1.5%)		±0.013 (1.5%)		±0.013 (1.5%)		±0.013 (1.5%)	
Hadron-to-Muon Branching Ratio	±0.050 (5.7%)		±0.050 (5.7%)		±0.050 (5.7%)		±0.050 (5.7%)	
Total	**±0.489 (55.7%)**		**±0.456 (51.9%)**		**±0.497 (56.6%)**		**±0.495 (56.4%)**	
Total Systematic Uncertainty	**+0.507 (57.7%)**	**−0.507 (57.7%)**	**+0.491 (55.9%)**	**−0.490 (55.8%)**	**+0.528 (60.1%)**	**−0.525 (59.8%)**	**+0.512 (58.3%)**	**−0.511 (58.2%)**
Total Uncertainty (Stat. + Syst.)	**+0.537 (61.2%)**	**−0.538 (61.3%)**	**+0.523 (59.6%)**	**−0.521 (59.3%)**	**+0.553 (63.0%)**	**−0.551 (62.8%)**	**+0.540 (61.5%)**	**−0.539 (61.4%)**

Table 13.1 The set of uncertainties that impact the same-sign observable charge asymmetry, A^{SS}, assessed in MC simulation scaled to an integrated luminosity of 139 fb^{-1}. Uncertainties are presented in absolute terms ($\times 10^{-2}$) and as a percentage of the central value. A full breakdown of the detector and modelling systematics is provided. Systematics listed in italics have been estimated from the previous ATLAS measurement [93].

A^{OS}(MC)[10^{-2}]	$\Delta R(\ell,\mu)$		BDT, X_ℓ		BDT, X_f		KLFitter	
Measured Value	**−0.465**							
Statistical Uncertainty	**±0.095 (20.4%)**		**±0.094 (20.2%)**		**±0.084 (18.1%)**		**±0.091 (19.6%)**	
Detector Systematics								
Electron Energy Scale, Resolution	+0.002 (0.4%)	−0.001 (0.2%)	+0.003 (0.6%)	−0.002 (0.4%)	+0.003 (0.6%)	−0.001 (0.2%)	+0.003 (0.6%)	−0.001 (0.2%)
Muon Energy Scale, Resolution	+0.005 (1.1%)	−0.007 (1.5%)	+0.008 (1.7%)	−0.009 (1.9%)	+0.005 (1.1%)	−0.007 (1.5%)	+0.011 (2.4%)	−0.007 (1.5%)
Prompt Lepton Isolation, Reconstruction, Trigger	+0.032 (6.9%)	−0.032 (6.9%)	+0.031 (6.7%)	−0.031 (6.7%)	+0.030 (6.5%)	−0.030 (6.5%)	+0.016 (3.4%)	−0.015 (3.2%)
Soft Muon Isolation, Reconstruction	+0.016 (3.4%)	−0.016 (3.4%)	+0.014 (3.0%)	−0.016 (3.4%)	+0.0015 (3.2%)	−0.015 (3.2%)	+0.007 (1.5%)	−0.009 (1.9%)
JES	+0.031 (6.7%)	−0.030 (6.5%)	+0.043 (9.2%)	−0.044 (9.5%)	+0.034 (7.3%)	−0.039 (8.4%)	+0.037 (8.0%)	−0.038 (8.2%)
JER	+0.028 (6.0%)	−0.028 (6.0%)	+0.061 (13.1%)	−0.062 (13.2%)	+0.059 (12.7%)	−0.060 (12.9%)	+0.040 (8.6%)	−0.043 (9.2%)
JVT	+0.008 (1.7%)	−0.008 (1.7%)	+0.009 (1.9%)	−0.006 (1.3%)	+0.008 (1.7%)	−0.007 (1.5%)	+0.004 (0.9%)	−0.004 (0.9%)
Pileup	+0.006 (1.3%)	−0.009 (1.9%)	+0.001 (0.2%)	−0.005 (1.1%)	+0.005 (1.1%)	−0.010 (2.2%)	+0.004 (0.9%)	−0.001 (0.2%)
Flavour-Tagging	+0.034 (7.3%)	−0.034 (7.3%)	+0.032 (6.9%)	−0.034 (7.3%)	+0.031 (6.7%)	−0.033 (7.1%)	+0.016 (3.4%)	−0.017 (3.6%)
$E_{\mathrm{T}}^{\mathrm{miss}}$	+0.005 (1.1%)	−0.009 (1.9%)	+0.006 (1.3%)	−0.007 (1.5%)	+0.007 (1.5%)	−0.010 (2.2%)	+0.003 (0.6%)	−0.009 (1.9%)
Electron Charge Misidentification	+0.001 (0.2%)	−0.001 (0.2%)	+0.001 (0.2%)	+0.001 (0.2%)	+0.001 (0.2%)	+0.001 (0.2%)	+0.001 (0.2%)	+0.001 (0.2%)
SMT Mistag rate	+0.005 (1.1%)	−0.005 (1.1%)	+0.005 (1.1%)	−0.005 (1.1%)	+0.005 (1.1%)	−0.005 (1.1%)	+0.005 (1.1%)	−0.005 (1.1%)
Fake Lepton Estimation	+0.025 (5.4%)	−0.025 (5.4%)	+0.025 (5.4%)	−0.025 (5.4%)	+0.025 (5.4%)	−0.025 (5.4%)	+0.025 (5.4%)	−0.025 (5.4%)
Background Estimation	+0.002 (0.4%)	−0.009 (1.9%)	+0.002 (0.4%)	−0.009 (1.9%)	+0.002 (0.4%)	−0.009 (1.9%)	+0.002 (0.4%)	−0.009 (1.9%)
Total	**+0.071 (15.3%)**	**−0.072 (15.5%)**	**+0.092 (19.8%)**	**−0.096 (20.6%)**	**+0.087 (18.7%)**	**−0.092 (19.8%)**	**+0.066 (14.2%)**	**−0.069 (14.8%)**
Modelling Systematics								
ISR μ_R, μ_F, and α_S	±0.016 (3.4%)		±0.012 (2.6%)		±0.014 (3.0%)		±0.008 (1.7%)	
FSR α_S	±0.219 (47.1%)		±0.206 (44.3%)		±0.199 (42.8%)		±0.194 (41.7%)	
h_{damp} Variation	±0.581 (124.9%)		±0.554 (119.1%)		±0.561 (120.6%)		±0.550 (118.3%)	
NLO Generator	±0.578 (124.3%)		±0.564 (121.3%)		±0.540 (116.1%)		±0.543 (116.7%)	
Parton Shower	±0.162 (34.8%)		±0.161 (34.6%)		±0.173 (37.2%)		±0.181 (38.9%)	
PDF	±0.016 (3.4%)		±0.023 (4.9%)		±0.019 (4.1%)		±0.007 (1.5%)	
b/c-Hadron Production Fraction	±0.008 (1.7%)		±0.008 (1.7%)		±0.008 (1.7%)		±0.008 (1.7%)	
Hadron-to-Muon Branching Ratio	±0.026 (5.6%)		±0.026 (5.6%)		±0.026 (5.6%)		±0.026 (5.6%)	
Total	**±0.865 (186.0%)**		**±0.834 (179.4%)**		**±0.822 (176.8%)**		**±0.817 (176.7%)**	
Total Systematic Uncertainty	**+0.867 (186.4%)**	**−0.867 (186.4%)**	**+0.839 (180.4%)**	**−0.839 (180.4%)**	**+0.827 (177.8%)**	**−0.828 (178.0%)**	**+0.820 (176.3%)**	**−0.820 (176.3%)**
Total Uncertainty (Stat. + Syst.)	**+0.873 (187.7%)**	**−0.873 (187.7%)**	**+0.844 (181.5%)**	**−0.844 (181.5%)**	**+0.832 (178.9%)**	**−0.832 (178.9%)**	**+0.825 (177.4%)**	**−0.825 (177.4%)**

Table 13.2 The set of uncertainties that impact the opposite-sign observable charge asymmetry, A^{OS}, assessed in MC simulation scaled to an integrated luminosity of 139 fb^{-1}. Uncertainties are presented in absolute terms ($\times 10^{-2}$) and as a percentage of the central value. A full breakdown of the detector and modelling systematics is provided. Systematics listed in italics have been estimated from the previous ATLAS measurement [93].

Examining Table 13.1 and Table 13.2, the statistical uncertainties are seen to be directly correlated to the efficiency of the ST/DT-assignment used, with the highest uncertainty coming from the lowest-efficiency method ($\Delta R(\ell, \mu)$) and the lowest uncertainty coming from the highest-efficiency method (the BDT trained on X_f).

For the detector systematics, some naively intuitive trends are shown to play out, such as the fact that the lepton-focused $\Delta R(\ell, \mu)$ method has larger errors associated with the prompt lepton and soft muon isolation, reconstruction, and trigger compared to the jet-focused `KLFitter` method, but smaller errors associated with the JES and JER. However, not all such naive expectations are met, as the largest JES and JER uncertainties are in fact seen for the BDT trained on X_ℓ, despite the feature set not making explicit use of any of the jet kinematic variables.

In percentage terms, the detector systematics are seen to be consistent for each method across both A^{SS} and A^{OS}. Comparison with the previous ATLAS measurement for the `KLFitter` method (the only method for which a like-for-like comparison can be made) shows reductions in the absolute value of the total detector systematics of $\sim 36\%$ for A^{SS} and $\sim 42\%$ for A^{OS} [93].

Turning attention to the modelling systematics for A^{SS}, it is interesting to note that the ISR and FSR uncertainties are largest for the $\Delta R(\ell, \mu)$ method, when the hypothesis that drove the development of this method was that by using less jet information, it would therefore be less sensitive to these uncertainties.

Comparing the total modelling uncertainties in percentage terms between A^{SS} and A^{OS} shows a large difference, with the uncertainties being more than a factor of three greater for A^{OS}, driven primarily by the h_{damp} variation and NLO generator uncertainty. Additionally, contrasting the modelling uncertainties with the previous ATLAS measurement shows that the total modelling uncertainty is of a similar size for A^{SS}, but greatly increased for A^{OS} [93]. The stark difference in these A^{OS} modelling uncertainties when compared to both the A^{SS} uncertainties and the uncertainties from the previous measurements suggests that further detailed investigation is necessary to establish an explanation for such a difference.

The results presented in Tables 13.1 and 13.2 allow for conclusions to be drawn about which of the four methods of ST/DT-assignment should be selected as the final method. It is clear that despite there being a relatively large range of performance when assessed in terms of efficiencies and purities, there is little to separate the four methods when assessed by the total uncertainty, as motivated by the discussion in Section 10.1. If only the total uncertainty on A^{SS} is considered, the BDT trained on X_ℓ performs best, with $\Delta R(\ell, \mu)$ second, `KLFitter` third, and the BDT trained on X_f worst. If instead the total uncertainty on A^{OS} is considered, this ordering changes, with `KLFitter` performing best, the BDT trained on X_f second, the BDT trained on X_ℓ third, and $\Delta R(\ell, \mu)$ worst. Summing the total uncertainty on A^{SS} and A^{OS} suggests `KLFitter` performs best on the whole, and therefore this is the method that is used to derive the results presented below in Section 13.3. However, it should be reiterated that the total uncertainty resulting from all four methods is close enough that the best method could feasibly change as a result of the full implementation of the remaining systematic uncertainties and the further investigation of the modelling uncertainties for A^{OS}.

13.3 CP-Violation Asymmetries

The decay chain fractions introduced in Section 7.4 and defined by Eqs. 7.9 to 7.14 are measured in MC simulation, and found to be

$$r_b = 0.254 \pm 0.008 \text{ (Syst.)}, \tag{13.5}$$

$$r_c = 0.721 \pm 0.020 \text{ (Syst.)}, \tag{13.6}$$

$$r_{c\bar{c}} = 0.024 \pm 0.002 \text{ (Syst.)}, \tag{13.7}$$

$$\tilde{r}_b = 0.860 \pm 0.014 \text{ (Syst.)}, \tag{13.8}$$

$$\tilde{r}_c = 0.060 \pm 0.004 \text{ (Syst.)}, \tag{13.9}$$

$$\tilde{r}_{c\bar{c}} = 0.080 \pm 0.013 \text{ (Syst.)}. \tag{13.10}$$

Each decay chain fraction has an associated MC statistical uncertainty at a level < 0.001. The systematic uncertainties come wholly from modelling (they are measured in the particle-level truth of the MC simulation, so there are no detector systematics), and are presented in Table 13.3.

Decay Chain Fractions	$\boldsymbol{r_b}$	$\boldsymbol{r_c}$	$\boldsymbol{r_{c\bar{c}}}$	$\boldsymbol{\tilde{r}_b}$	$\boldsymbol{\tilde{r}_c}$	$\boldsymbol{\tilde{r}_{c\bar{c}}}$
Measured Value	0.254	0.721	0.024	0.860	0.060	0.080
Modelling Systematics						
ISR μ_R, μ_F, and α_S	±0.00111 (0.436%)	±0.000985 (0.758%)	±0.000114 (0.469%)	±0.00445 (0.517%)	±0.000119 (0.200%)	±0.000794 (0.994%)
FSR α_S	±0.0000397 (0.0156%)	±0.00546 (0.758%)	±0.000182 (0.751%)	±0.00164 (0.191%)	±0.000143 (0.240%)	±0.000118 (0.148%)
h_{damp} Variation	±0.0000413 (0.0162%)	±0.000144 (0.0199%)	±0.000102 (0.422%)	±0.000186 (0.0216%)	±0.000202 (0.338%)	±0.0000157 (0.0196%)
NLO Generator	±0.00109 (0.428%)	±0.00111 (0.154%)	±0.0000191 (0.0788%)	±0.00112 (0.130%)	±0.000451 (0.755%)	±0.000668 (0.835%)
Parton Shower	±0.000376 (0.148%)	±0.0000492 (0.00682%)	±0.000425 (1.753%)	±0.00418 (0.486%)	±0.00262 (4.38%)	±0.00156 (1.95%)
PDF	±0.000820 (0.322%)	±0.00340 (0.471%)	0.0000124 ± (0.0512%)	±0.00124 (0.144%)	±0.000234 (0.392%)	±0.000306 (0.383%)
b/c-Hadron Production Fraction	±0.00697 (2.74%)	±0.0186 (2.58%)	±0.00224 (9.33%)	±0.0125 (1.45%)	±0.00228 (3.8%)	±0.0131 (16.4%)
Hadron-to-Muon Branching Ratio	±0.00354 (1.39%)	±0.00333 (0.46%)	±0.0002423 (1.01%)	±0.00137 (0.159%)	±0.00127 (2.12%)	±0.000100 (0.125%)
Total	**±0.00802 (3.16%)**	**±0.0200 (2.77%)**	**±0.00231 (9.63%)**	**±0.0142 (1.65%)**	**±0.00374 (6.23%)**	**±0.0132 (16.5%)**

Table 13.3 The breakdown of the systematic uncertainties from modelling that impact the decay chain fractions, assessed in MC simulation. Uncertainties are presented in absolute terms and as a percentage of the central value. Systematics listed in italics have been estimated from the previous ATLAS measurement [93].

Following the procedure described in Section 7.4, using the measured decay chain fractions in conjunction with Eqs. 7.17 to 7.20, values are extracted for the underlying CP-violation asymmetries from MC simulation scaled to an integrated luminosity of $139\,\mathrm{fb}^{-1}$, giving

$$\begin{aligned}
A^{b}_{\mathrm{mix}}(\mathrm{MC}) &= +0.032 \pm 0.006\ (\mathrm{Stat.}) \pm 0.018\ (\mathrm{Syst.})\ = +0.032 \pm 0.019\ (\mathrm{Total.}), && (13.11)\\
A^{b\ell}_{\mathrm{dir}}(\mathrm{MC}) &= -0.005 \pm 0.001\ (\mathrm{Stat.}) \pm 0.009;(\mathrm{Syst.}) = -0.005 \pm 0.009\ (\mathrm{Total.}), && (13.12)\\
A^{c\ell}_{\mathrm{dir}}(\mathrm{MC}) &= -0.012 \pm 0.002\ (\mathrm{Stat.}) \pm 0.007\ (\mathrm{Syst.})\ = -0.012 \pm 0.007\ (\mathrm{Total.}), && (13.13)\\
A^{bc}_{\mathrm{dir}}(\mathrm{MC}) &= +0.012 \pm 0.002\ (\mathrm{Stat.}) \pm 0.007\ (\mathrm{Syst.})\ = +0.012 \pm 0.007\ (\mathrm{Total.}). && (13.14)
\end{aligned}$$

As they have been extracted from MC simulation in which CP-violation is not present, all of the CP-violation asymmetries (and by extension, the observable charge asymmetries) are expected to be compatible with zero within the statistical uncertainties, and it can be seen from Eqs. 13.11 to 13.14 that this is not the case. Detailed examinations of the truth origin information of the soft muons in each event have been performed, in order to try and ascertain what is causing the central values of the asymmetries to become non-zero.

The only fruitful lead arising from these studies is that there is an excess of soft muons originating from the top quark over soft muons originating from the antitop quark, when it would be expected that equal numbers of top and antitop quarks should be present, and examining the parton-level truth of the simulation confirms this to be the case. The excess of soft muons originating from the top quark is visible in the particle-level truth of the simulation, and so it is concluded that the selection cuts that define the fiducial volume must somehow introduce this excess (although experimentation with relaxing selection cuts such as the soft muon p_{T} and η did not remove the excess). Despite the clear presence of this unexpected excess, a definitive link between said excess and the non-zero central values has not been established. Attempts to artificially reweight events to remove the excess does not significantly change the central value of the asymmetries, and in any case any effect on the asymmetries introduced by the definition of the fiducial volume would be expected to cancel out upon application of the decay chain fractions that take the measurements from the fiducial volume to the full phase-space.

The statistical and systematic uncertainties assessed on the observable charge asymmetries and decay chain fractions are propagated to the CP-violation asymmetries. Despite the fact that the central values for the asymmetries are only assessed in MC simulation at this stage, the total uncertainty will also be applicable to the values extracted from experimental data. Therefore, examining the total uncertainty allows us to assess the projected sensitivity of the measurement.

Specifically, it is of key interest to see whether a measurement found to be in agreement with the Standard Model (and therefore compatible with an asymmetry value ~ 0) would have small enough uncertainties to refute the 3.2σ measurement made at D∅ [83]. As discussed in Section 4.5, LHCb measurements of a_{sl}^{d} and a_{sl}^{s} refuted the possibility that the D∅ result could be explained in terms of CP-violation in mixing [84, 85]. However, a possible explanation in terms of direct CP-violation is yet to be refuted, and would require either $|A_{\mathrm{dir}}^{b\ell}| \approx 0.003$ or $|A_{\mathrm{dir}}^{c\ell}| \approx 0.010$ [87, 88]. The previous ATLAS measurement was found to be compatible with both the Standard Model and the D∅ result, due to a total uncertainty on $A_{\mathrm{dir}}^{b\ell}$, which is labelled σ_{dir}^{b}, of $\sigma_{dir}^{b} = 0.005$; the corresponding total uncertainty on $A_{\mathrm{dir}}^{c\ell}$, which is labelled σ_{dir}^{c}, was $\sigma_{dir}^{c} = 0.010$ [93].

Given the required values of $|A_{\mathrm{dir}}^{b\ell}| \approx 0.003$ and $|A_{\mathrm{dir}}^{c\ell}| \approx 0.010$, it can be seen that there are two thresholds of note. The first of these is at $\sigma_{dir}^{b} = 0.003$ and $\sigma_{dir}^{c} = 0.010$. Measurements with uncertainties at or above these levels, such as the previous ATLAS measurement, cannot be found to have central values at the level of the Standard Model (~ 0) without also being found to be compatible with the D∅ result. The second threshold is at $\sigma_{dir}^{b} = 0.0015$ and $\sigma_{dir}^{c} = 0.005$. Measurements with uncertainties at or below these levels can only be found to be compatible with either the Standard Model or the D∅ result, i.e. the uncertainty band cannot possibly overlap both, and agreement with the Standard Model guarantees refutation of the D∅ result. Measurements with uncertainties between the two thresholds have the sensitivity to potentially agree with the Standard Model while refuting the D∅ measurement, although there is the possibility for the uncertainty band to overlap both.

Examining Eq. 13.13, it can be seen that $\sigma^{c}_{dir} = 0.007$, which falls between the two thresholds. Turning attention to Eq. 13.12, it can be seen that $\sigma^{b}_{dir} = 0.009$, which is well above the first threshold. However, if it turns out to be the case that the surprisingly high modelling uncertainties on A^{OS} are due to an error and the final percentage modelling uncertainties on A^{OS} end up being at a similar level to the modelling uncertainties on A^{SS}, the expected uncertainty becomes $\sigma^{b}_{dir} = 0.003$, reaching the first threshold.

Therefore, it can be concluded that while refutation is not guaranteed, the important step has been taken of achieving a small enough total uncertainty (on $A^{c\ell}_{\mathrm{dir}}$, and potentially also $A^{b\ell}_{\mathrm{dir}}$) to open up the possibility of refuting the D∅ result in terms of direct CP-violation, which has stood in conflict with the Standard Model for several years. This will be the first such measurement for which this is the case. Conversely to this, the door is also opened to the possibility of confirming the conflict between the D∅ result and the Standard Model prediction for direct CP-violation, which may indicate the presence of potential sources of BSM physics.

Chapter 14

Conclusions

This thesis has presented the process used to make a measurement of CP-violation by tagging soft muons from the semileptonic decays of b-hadrons and c-hadrons in lepton+jets $t\bar{t}$ events, using data from the ATLAS experiment at the LHC corresponding to an integrated luminosity of $139\,\mathrm{fb}^{-1}$ and a centre-of-mass energy of $\sqrt{s} = 13\,\mathrm{TeV}$. The measurement builds upon a theoretical prescription and previous ATLAS measurement, with the aim of making use of novel techniques and the wealth of data collected by ATLAS, in order to improve the sensitivity of the measurement to potential sources of new physics and attempt to refute or confirm the possible explanation of the $D\varnothing$ anomalous dimuon asymmetry arising from a BSM source of direct CP-violation [83, 90, 93].

A fiducial volume is defined with a range of object and event selection cuts, foremost among them the requirement that lepton+jets $t\bar{t}$ events contain exactly one prompt lepton, from the decay of a W, and a soft muon, from the decay of a b-hadron or c-hadron. The charges of the prompt lepton and soft muon are measured, with the former being used to tag the flavour of the b-quark at the time it is produced and the latter being used to tag the flavour of the b-quark at the time it decays. This opens up sensitivity to CP-violation effects, and this is quantified through the construction of a distribution of the combined charges of the prompt lepton and soft muon, $N^{\ell\mu}$. This distribution is then unfolded to the fiducial volume, and used to extract a pair of observable charge asymmetries, A^{SS} and A^{OS}. These observable charge asymmetries, combined with decay chain fractions measured in MC simulation, are used in turn to extract a set of four underlying CP-violation asymmetries, A^{b}_{mix}, $A^{b\ell}_{dir}$, $A^{c\ell}_{dir}$, A^{bc}_{dir}. These CP-violation asymmetries are not specific to the fiducial volume, and can be readily compared with theoretical predictions and other previous and future experimental results.

One of the key parts of the analysis is the ST/DT-assignment, which needs to be applied to ensure that the constructed $N^{\ell\mu}$ distribution is accurate. Four separate methods for performing the ST/DT-assignment have been detailed and assessed. The first of these is a cut on the total angular separation $\Delta R(\ell, \mu)$. Two machine learning algorithms in the form of BDT are trained on separate feature sets, with the first using a restricted feature set containing purely leptonic features, and the second using a full feature set containing all the features of the first plus additional features pertaining to jets. The final method is a kinematic likelihood fitting approach using the `KLFitter` algorithm. The final decision on which of the four methods to use is to be made by considering which method results in the smallest total (statistical + systematic) uncertainty.

The composition of the background processes that contribute to the $N^{\ell\mu}$ distribution has been presented, accompanied by a breakdown of the various sources of statistical and systematic uncertainties that must be considered when performing the analysis, and details of how these uncertainties are estimated. The unfolding process has been detailed, and the efficiency terms, acceptance terms, and migration matrices required to unfold have been presented for each of the four methods of ST/DT-assignment.

In addition to the two observable charge asymmetries and four underlying CP-violation asymmetries described above, a feasibility study has been presented for the possibility of complementing these time-integrated asymmetries with an additional time-dependent measurement, given that it is now statistically viable. A time-dependent measurement increases the complexity of the analysis, and poses challenges relating to constructing the position of secondary vertices and accurately estimating the fraction of the b-quark energy transferred to the leading hadron on an event-by-event-basis. The conclusions of the feasibility study are that these challenges can be overcome, and the results coming from a time-integrated measurement of Δm_d are expected to be competitive with measurements from other experiments such as LHCb, and could potentially also be used to extract a new CP-violation asymmetry, A_{int}.

The $N^{\ell\mu}$ distribution has been presented for both signal MC simulation and the experimental data. At this time, no attempt has been made to extract the observable charged asymmetries and underlying CP-violation asymmetries for the experimental data, due to a desire to keep these results appropriately blinded until the full and final analysis pipeline is in place. However, the observable charge asymmetries have been extracted in MC simulation and presented, accompanied by the statistical uncertainty and systematic uncertainty numbers for each of the four candidate ST/DT-assignment methods. While there is very little to separate the four methods, it is concluded that the `KLFitter` method of ST/DT-assignment results in the lowest total uncertainty across the combination of both A^{SS} and A^{OS}.

The decay chain fractions have been measured in MC simulation and presented with their associated modelling uncertainties. In conjunction with the observable charge asymmetries, these decay chain fractions have been used to extract the underlying CP-violation asymmetries in MC simulation. All sources of uncertainty from the observable charge asymmetries and decay chain fractions have been propagated and presented alongside the results for A^{b}_{mix}, $A^{b\ell}_{dir}$, $A^{c\ell}_{dir}$, A^{bc}_{dir}. Comparison of the uncertainties on these MC CP-violation asymmetries to the previous ATLAS measurement and the asymmetry values required to explain the $D\varnothing$ result has been presented and used to conclude that the measurement opens up the possibility of refuting or confirming for the first time the hypothesis that the $D\varnothing$ result can be explained in terms of a BSM source of direct CP-violation.

14.1 Remaining Work

Whilst the majority of the required work to unblind the experimental data and extract the final values of the underlying CP-violation asymmetries is accomplished by the work presented in this thesis, some additional work remains. Primary among these is the estimation of the contributions of the various sources of background to the measured $N^{\ell\mu}$ distribution, so that these contributions can be subtracted during the unfolding process. The handful of systematic uncertainties that have currently been presented as estimates based on the previous ATLAS measurement also need to be fully implemented, but the majority are fully implemented. Additional work is required to understand why the measured asymmetry values in the MC simulation are non-zero and adjust the analysis pipeline to correct for this. Finally, a study should be undertaken to establish whether the surprisingly high modelling uncertainties seen for A_{OS} are correct or due to an error, and if the former is true, then an effort should be made to motivate these values.

As discussed above, the feasibility of extending the existing time-integrated analysis with a time-dependent measurement is found to be good, and future work dedicated to fully implementing such a time-dependent measurement is expected to produce new and exciting results for Δm_d (and potentially A_{int}). Such a measurement could either be carried out in time to publish alongside the time-integrated results, or form a separate publication.

14.2 Future Improvements

Looking ahead to Run 3 of the LHC, there is scope to iterate further on the analysis strategy detailed in this thesis in order to perform another measurement, and a discussion for improvements that could be incorporated into such a measurement follows below.

A key area deserving additional attention can be seen by examining the uncertainties presented alongside the MC CP-violation asymmetries. These show clearly that the measurement of these asymmetries is limited by the modelling systematic uncertainties, and not the detector systematics or the statistical uncertainties. The biggest return on investment for future work would therefore come from finding a way to reduce the impact of these modelling uncertainties on the ST/DT-assignment process, which are currently seen to be large across all four methods.

There are three potential ways to reduce the modelling uncertainties. The first possibility is to explore additional ST/DT-assignment methods. More sophisticated machine learning methods are one option of interest here, with deep learning methods a notable omission from the possible methods that have been explored so far. However, as the goal is primarily to reduce the systematic uncertainties, more focus should be put on examining the response of methods to the key modelling variations than on increasing performance in terms of efficiency or purity. As such, exploring options for incorporating regularisation and ideas from the domain of multi-task learning may prove useful, i.e. explicitly exposing a machine learning algorithm to the modelling systematic samples during training may allow it to learn and develop resilience to the differences introduced by these modelling systematics.

The second possibility is to leverage the fact that multiple ST/DT-assignment methods have been developed. For some events, these methods will produce the same prediction for the ST/DT-status as each other, while for other events the different methods will produce different predictions. By introducing a requirement that multiple, or even all, of the methods produce the same prediction in order for events to be retained, it is hoped that a trade-off could be established whereby the statistical uncertainty could be allowed to increase if such a requirement produces a reduction in the systematic uncertainties, which would be beneficial if the total uncertainty was to reduce. A similar line of reasoning can be used to justify examining how the various selection cuts are affected by the modelling systematics, and seeing if it is possible to modify them to make a similar trade-off of increasing the statistical uncertainty to reduce the systematic uncertainty.

The third and final possibility for reducing the modelling uncertainties is to investigate the possibility of performing the measurement with the dilepton $t\bar{t}$ channel rather than the lepton+jets $t\bar{t}$ channel. While the branching ratio results in lower statistics for the dilepton channel, it produces a cleaner experimental signature, and the presence of two prompt leptons would in theory make the process of ST/DT-assignment more robust by requiring each event to have one of the prompt leptons identified as same-top and the other prompt lepton identified as different-top. This would be expected to lead to lower sensitivity to modelling systematic uncertainties, as well as potentially further reducing the detector systematics related to jets due to the cleaner experimental signature of the dilepton channel, which will contain significantly fewer jets than the lepton+jets channel. If the current statistics lead to the dilepton $t\bar{t}$ channel producing a statistically-dominated result, this idea could be revisited down the line, following the collection of additional data as part of Run 3 of the LHC and beyond.

References

[1] P. Langacker, *The Standard Model and Beyond*. CRC Press, Boca Raton, FL, USA, second ed., 2017.

[2] L. Canetti et al., *Matter and Antimatter in the Universe*. New Journal of Physics **14**(9) (2012) pp. 095012–1–095012–21.

[3] M. Thomson, *Modern Particle Physics*. Cambridge University Press, Cambridge, UK, 2013.

[4] D. Griffiths, *Introduction to Elementary Particles*. Wiley-VCH, Weinheim, Germany, second ed., 2008.

[5] A. Liddle, *An Introduction to Modern Cosmology*. Wiley, Chichester, UK, third ed., 2015. `https://www.wiley.com/en-us/An+Introduction+to+Modern+Cosmology%2C+3rd+Edition-p-9781118502143` (accessed on 21/12/2022).

[6] Wikimedia Commons, *Standard Model of Elementary Particles*, 2019. `https://commons.wikimedia.org/wiki/File:Standard_Model_of_Elementar_Particles.svg` (accessed on 10/01/2022).

[7] Particle Data Group, P. A. Zyla et al., *Review of Particle Physics: Baryon Summary Table*. Progress of Theoretical and Experimental Physics **2020**(8) (2020) pp. 92–110.

[8] Particle Data Group, P. A. Zyla et al., *Review of Particle Physics: Meson Summary Table*. Progress of Theoretical and Experimental Physics **2020**(8) (2020) pp. 38–91.

[9] Super-Kamiokande Collaboration, Y. Fukuda et al., *Evidence for Oscillation of Atmospheric Neutrinos*. Physical Review Letters **81**(8) (1998) pp. 1562–1567.

[10] Particle Data Group, P. A. Zyla et al., *Review of Particle Physics: Gauge and Higgs Boson Summary Table*. Progress of Theoretical and Experimental Physics **2020**(8) (2020) pp. 31–33.

[11] M. Planck, *The Theory of Heat Radiation*. P. Blakiston's Son & Co., Philadelphia, PA, USA, 1914. `https://www.gutenberg.org/ebooks/40030` (accessed on 21/12/2022).

[12] A. Einstein, *Über einen die Erzeugung und Verwandlung des Lichtes betreffenden heuristischen Gesichtspunkt (On a Heuristic Point of View Concerning the Production and Transformation of Light)*. Annalen der Physik **17** (1905) pp. 132–148.

[13] E. Schrödinger, *An Undulatory Theory of the Mechanics of Atoms and Molecules*. Physical Review **28**(6) (1926) pp. 1049–1070.

[14] M. Born, W. Heisenberg, and P. Jordan, *Zur Quantenmechanik II (On Quantum Mechanics II)*. Zeitschrift für Physik **35** (1926) pp. 557–615.

[15] P. A. M. Dirac, *The Quantum Theory of the Electron*. Proceedings of the Royal Society A **117**(778) (1928) pp. 610–624.

[16] C. D. Anderson, *The Positive Electron*. Physical Review **43**(6) (1933) pp. 491–494.

[17] F. J. Dyson, *The Radiation Theories of Tomonaga, Schwinger, and Feynman*. Physical Review **75**(3) (1949) pp. 486–502.

[18] C. N. Yang and R. L. Mills, *Conservation of Isotopic Spin and Isotopic Gauge Invariance*. Physical Review **96**(1) (1954) pp. 191–195.

[19] E. Fermi, *Versuch einer Theorie der Beta-Strahlen I (Attempt at a Theory of Beta-Radiation I)*. Zeitschrift für Physik **88** (1934) pp. 161–177.

[20] S. L. Glashow, *The Renormalizability of Vector Meson Interactions*. Nuclear Physics **10** (1959) pp. 107–117.

[21] S. Weinberg, *A Model of Leptons*. Physical Review Letters **19**(21) (1967) pp. 1264–1266.

[22] A. Salam and J. C. Ward, *Weak and Electromagnetic Interactions*. Il Nuovo Cimento **11**(4) (1959) pp. 568–577.

[23] F. Englert and R. Brout, *Broken Symmetry and the Mass of Gauge Vector Mesons*. Physical Review Letters **13**(9) (1964) pp. 321–323.

[24] P. W. Higgs, *Broken Symmetries and the Masses of Gauge Bosons*. Physical Review Letters **13**(16) (1964) pp. 508–509.

[25] G. S. Guralnik, C. R. Hagen, and T. W. B. Kibble, *Global Conservation Laws and Massless Particles*. Physical Review Letters **13**(20) (1964) pp. 585–587.

[26] UA1 Collaboration, G. Arnison et al., *Experimental Observation of Isolated Large Transverse Energy Electrons with Associated Missing Energy at* $\sqrt{s} = 540\,GeV$. Physics Letters B **122**(1) (1983) pp. 103–116.

[27] UA2 Collaboration, M. Banner et al., *Observation of Single Isolated Electrons of High Transverse Momentum in Events with Missing Transverse Energy at the CERN pp Collider*. Physics Letters B **122**(5-6) (1983) pp. 476–485.

[28] UA1 Collaboration, G. Arnison et al., *Experimental Observation of Lepton Pairs of Invariant Mass Around 95 GeV/c^2 at the CERN SPS Collider*. Physics Letters B **126**(5) (1983) pp. 398–410.

[29] UA2 Collaboration, P. Bagnaia et al., *Evidence for* $Z \to e^+e^-$ *at the CERN pp Collider*. Physics Letters B **129**(1-2) (1983) pp. 130–140.

[30] ATLAS Collaboration, G. Aad et al., *Observation of a new particle in the search for the Standard Model Higgs boson with the ATLAS detector at the LHC*. Physics Letters B **716**(1) (2012) pp. 1–29.

[31] CMS Collaboration, S. Chatrchyan et al., *Observation of a new boson at a mass of 125 GeV with the CMS experiment at the LHC*. Physics Letters B **716**(1) (2012) pp. 30–61.

[32] S. H. Neddermeyer and C. D. Anderson, *Note on the Nature of Cosmic-Ray Particles*. Physical Review **51**(10) (1937) pp. 884–886.

[33] M. L. Perl et al., *Evidence for Anomalous Lepton Production in* e^+e^- *Annihilation*. Physical Review Letters **35**(22) (1975) pp. 1489–1492.

[34] M. Gell-Mann, *A Schematic Model of Baryons and Mesons*. Physics Letters **8**(3) (1964) pp. 214–215.

[35] G. Zweig, *An SU(3) model for strong interaction symmetry and its breaking*. CERN-TH-401, 1964. `http://cds.cern.ch/record/352337` (accessed on 21/12/2022).

[36] D. J. Gross and F. Wilczek, *Ultraviolet Behavior of Non-Abelian Gauge Theories*. Physical Review Letters **30**(26) (1973) pp. 1343–1346.

[37] H. D. Politzer, *Reliable Perturbative Results for Strong Interactions?* Physical Review Letters **30**(26) (1973) pp. 1346–1349.

[38] PLUTO Collaboration, C. Berger et al., *Evidence for Gluon Bremsstrahlung in* e^+e^- *Annihilations at High Energies*. Physics Letters B **86**(3-4) (1979) pp. 418–425.

[39] S. L. Glashow, J. Iliopoulos, and L. Maiani, *Weak Interactions with Lepton-Hadron Symmetry*. Physical Review D **2**(7) (1970) pp. 1285–1292.

[40] M. Kobayashi and T. Maskawa, *CP-Violation in the Renormalizable Theory of Weak Interaction*. Progress of Theoretical Physics **49**(2) (1973) pp. 652–657.

[41] J. E. Augustin et al., *Discovery of a Narrow Resonance in e^+e^- Annihilation*. Physical Review Letters **33**(23) (1974) pp. 1406–1408.

[42] J. J. Aubert et al., *Experimental Observation of a Heavy Particle J*. Physical Review Letters **33**(23) (1974) pp. 1404–1406.

[43] S. W. Herb et al., *Observation of a Dimuon Resonance at 9.5 GeV in 400 GeV Proton-Nucleus Collisions*. Physical Review Letters **39**(5) (1977) pp. 252–255.

[44] CDF Collaboration, F. Abe et al., *Observation of Top Quark Production in pp Collisions with the Collider Detector at Fermilab*. Physical Review Letters **74**(14) (1995) pp. 2626–2631.

[45] D0 Collaboration, S. Abachi et al., *Observation of the Top Quark*. Physical Review Letters **74**(14) (1995) pp. 2632–2637.

[46] E. Noether, *Invariante Variationsprobleme (Invariant Variations Problems)*. Transport Theory and Statistical Physics **1**(3) (Original - 1918, Translation - 1971) pp. 186–207.

[47] J. Goldstone, *Field Theories with 'Superconductor' Solutions*. Il Nuovo Cimento **19**(1) (1961) pp. 154–164.

[48] Wikimedia Commons, *Mexican Hat Potential Polar*, 2009. `https://commons.wikimedia.org/wiki/File:Mexican_hat_potential_polar.svg` (accessed on 12/01/2022).

[49] H. Yukawa, *On the Interaction of Elementary Particles*. Progress of Theoretical Physics Supplement **1** (1955) pp. 1–71.

[50] R. P. Feynman, *Space-Time Approach to Quantum Electrodynamics*. Physical Review **76**(6) (1949) pp. 769–789.

[51] N. Cabibbo, *Unitary Symmetry and Leptonic Decays*. Physical Review Letters **10**(12) (1963) pp. 531–533.

[52] Particle Data Group, P. A. Zyla et al., *Review of Particle Physics: CKM Quark-Mixing Matrix*. Progress of Theoretical and Experimental Physics **2020**(8) (2020) pp. 261–271.

[53] Particle Data Group, P. A. Zyla et al., *Review of Particle Physics: Quark Summary Table*. Progress of Theoretical and Experimental Physics **2020**(8) (2020) p. 37.

[54] ATLAS Collaboration, *Top Quark Mass Summary Plots Spring 2021*. ATL-PHYS-PUB-2021-015, 2021. `http://cds.cern.ch/record/2767052` (accessed on 21/12/2022).

[55] T. J. Humanic, *Extracting the Hadronization Timescale in $\sqrt{s} = 7$ TeV Proton–Proton Collisions From Pion and Kaon Femtoscopy*. Journal of Physics G: Nuclear and Particle Physics **41**(7) (2014) .

[56] J. Gao, L. Harland-Yang, and J. Rojo, *The Structure of the Proton in the LHC Precision Era*. Physics Reports **742** (2018) pp. 1–122.

[57] ATLAS Collaboration, *Top Working Group Cross-Section Summary Plots - Spring 2021*. ATL-PHYS-PUB-2021-014, 2021. `http://cds.cern.ch/record/2767049` (accessed on 21/12/2022).

[58] Particle Data Group, P. A. Zyla et al., *Review of Particle Physics: Top Quark (Rev.)*. Progress of Theoretical and Experimental Physics **2020**(8) (2020) pp. 741–761.

[59] LHCb Collaboration, R. Aaij et al., *Measurement of b-hadron Fractions in 13 TeV pp Collisions*. Physical Review D **100**(3) (2019) pp. 031102–1 – 031102–11.

[60] LHCb Collaboration, R. Aaij et al., *Measurement of b-hadron Masses*. Physics Letters B **708**(3) (2012) pp. 241 – 248.

[61] LHCb Collaboration, R. Aaij et al., *A Precise Measurement of the B^0 Meson Oscillation Frequency*. The European Physical Journal C **76**(7) (2016) pp. 412–1 – 412–14.

[62] LHCb Collaboration, R. Aaij et al., *Precise Determination of the $B_s^0 - \bar{B}_s^0$ Oscillation Frequency*. Nature Physics **18**(1) (2022) pp. 54–65.

[63] Particle Data Group, P. A. Zyla et al., *Review of Particle Physics: Meson Particle Listings - $B^{\pm}/B^0/B_s^0$/b-baryon Admixture*. Progress of Theoretical and Experimental Physics **2020**(8) (2020) pp. 1625–1633.

[64] Particle Data Group, P. A. Zyla et al., *Review of Particle Physics: Meson Particle Listings - $B^{\pm}$*. Progress of Theoretical and Experimental Physics **2020**(8) (2020) pp. 1466–1529.

[65] Particle Data Group, P. A. Zyla et al., *Review of Particle Physics: Meson Particle Listings - B^0*. Progress of Theoretical and Experimental Physics **2020**(8) (2020) pp. 1529–1603.

[66] Particle Data Group, P. A. Zyla et al., *Review of Particle Physics: Meson Particle Listings - B_s^0*. Progress of Theoretical and Experimental Physics **2020**(8) (2020) pp. 1640–1661.

[67] T. D. Lee and C. N. Yang, *Question of Parity Conservation in Weak Interactions*. Physical Review **104**(1) (1956) pp. 254–258.

[68] C. S. Wu et al., *Experimental Test of Parity Conservation in Beta Decay*. Physical Review **105**(4) (1957) pp. 1413–1415.

[69] R. L. Garwin, L. M. Lederman, and M. Weinrich, *Observations of the Failure of Conservation of Parity and Charge Conjugation in Meson Decays: the Magnetic Moment of the Free Muon*. Physical Review **105**(4) (1957) pp. 1415–1417.

[70] M. Goldhaber, L. Grodzins, and A. W. Sunyar, *Helicity of Neutrinos*. Physical Review **105**(3) (1958) pp. 1015–1017.

[71] L. Landau, *On the conservation laws for weak interactions*. Nuclear Physics **3**(1) (1957) pp. 127–131.

[72] J. H. Christenson et al., *Evidence for the* 2π *Decay of the* K_2^0 *Meson*. Physical Review Letters **13**(4) (1964) pp. 138–140.

[73] KTeV Collaboration, A. Alavi-Harati et al., *Observation of Direct CP Violation in* $K_{S,L} \to \pi\pi$ *Decays*. Physical Review Letters **83**(1) (1999) pp. 22–27.

[74] NA48 Collaboration, V. Fanti et al., *A New Measurement of Direct CP Violation in Two Pion Decays of the Neutral Kaon*. Physics Letters B **465**(4) (1999) pp. 335–348.

[75] BABAR Collaboration, B. Aubert et al., *Measurement of CP-Violating Asymmetries in B0 Decays to CP Eigenstates*. Physical Review Letters **86**(12) (2001) pp. 2515–2522.

[76] Belle Collaboration, K. Abe et al., *Observation of Large CP Violation in the Neutral B Meson System*. Physical Review Letters **87**(9) (2001) pp. 091802–1–091802–7.

[77] BABAR Collaboration, B. Aubert et al., *Direct CP Violating Asymmetry in* $B^0 \to K^+$ *Decays*. Physical Review Letters **93**(13) (2004) pp. 131801–1–131801–7.

[78] LHCb Collaboration, R. Aaij et al., *First Observation of CP Violation in the Decays of* B_s^0 *Mesons*. Physical Review Letters **110**(22) (2013) pp. 221601–1–221601–9.

[79] LHCb Collaboration, R. Aaij et al., *Observation of CP Violation in Charm Decays*. Physical Review Letters **122**(21) (2019) pp. 211803–1–211803–12.

[80] L. Wolfenstein, *Parametrization of the Kobayashi-Maskawa Matrix*. Physical Review Letters **51**(21) (1983) pp. 1945–1947.

[81] CKMfitter Group, J. Charles et al., *CP Violation and the CKM Matrix: Assessing the Impact of the Asymmetric B Factories*. The European Physical Journal C **41**(1) (2005) pp. 1–131.

[82] CKMfitter Group, *The Global CKM Fit in the Large* $(\bar{\rho}, \bar{\eta})$ *Plane*, 2021. `http://ckmfitter.in2p3.fr/www/results/plots_spring21/png/rhoeta_large.png`

(accessed on 17/02/2022).

[83] D0 Collaboration, V. M. Abazov et al., *Evidence for an Anomalous Like-Sign Dimuon Charge Asymmetry*. Physical Review D **82**(3) (2010) pp. 032001–1–032001–30.

[84] LHCb Collaboration, R. Aaij et al., *Measurement of the Semileptonic CP Asymmetry in $B^0 - \bar{B}^0$ Mixing*. Physical Review Letters **114**(4) (2015) pp. 041601–1–041601–9.

[85] LHCb Collaboration, R. Aaij et al., *Measurement of the CP Asymmetry in $B_s^0 - \bar{B}_s^0$ Mixing*. Physical Review Letters **117**(6) (2016) pp. 061803–1–061803–9.

[86] LHCb Collaboration, *Overview of the Most Precise Measurements of a_{sl}^d and a_{sl}^s*, 2016. `https://lhcbproject.web.cern.ch/Publications/LHCbProjectPublic/LHCb-PAPER-2016-013.html` (accessed on 17/02/2022).

[87] S. Descotes-Genon and J. F. Kamenik, *A possible explanation of the D0 like-sign dimuon charge asymmetry*. Physical Review D **87**(7) (2013) pp. 074036–1–074036–7.

[88] S. Descotes-Genon and J. F. Kamenik, *Erratum: A possible explanation of the D0 like-sign dimuon charge asymmetry*. Physical Review D **92**(7) (2015) pp. 079903–1.

[89] CKMfitter Group, A. Lenz et al., *Anatomy of New Physics in B-$\bar{B}$ Mixing*. Physical Review D **83**(3) (2011) pp. 036004–37.

[90] O. Gedalia et al., *Top B Physics at the LHC*. Physical Review Letters **110**(23) (2013) pp. 232002–1–232002–5.

[91] Y. Grossman, Y. Nir, and G. Perez, *Testing New Indirect CP Violation*. Physical Review Letters **103**(7) (2009) pp. 071602–1–071602–4.

[92] A. L. Kagan and M. D. Sokoloff, *Indirect CP Violation and Implications for $D^0 - \bar{D}^0$ and $B_s - \bar{B}_s$ Mixing*. Physical Review D **80**(7) (2009) pp. 076008–1–16.

[93] ATLAS Collaboration, M. Aaboud et al., *Measurements of Charge and CP Asymmetries in b-hadron Decays Using Top-Quark Events Collected by the ATLAS Detector in pp Collisions at $\sqrt{s} = 8$ TeV*. Journal of High Energy Physics **2017**(2) (2017) pp. 071–1–071–48.

[94] S. Bar-Shalom et al., *Second-Order Direct CP Asymmetry in $B_s \to Xl\nu$*. Physics Letters B **694**(4-5) (2011) pp. 374 – 379.

[95] Heavy Flavour Averaging Group, Y. Amhis et al., *Averages of b-hadron, c-hadron, and -lepton properties as of summer 2018*. The European Physical Journal C **81**(3) (2021) pp. 226–1–226–326.

[96] M. Artuso, G. Borissov, and A. Lenz, *CP Violaton in the* B_s^0 *System*. Reviews of Modern Physics **88**(4) (2016) pp. 045002–1–045002–45.

[97] M. Artuso, G. Borissov, and A. Lenz, *Erratum: CP Violaton in the* B_s^0 *System*. Reviews of Modern Physics **91**(4) (2019) pp. 049901–1.

[98] G. Steigman, *Primordial Nucleosynthesis in the Precision Cosmology Era*. Annual Review of Nuclear and Particle Science **57**(1) (2007) pp. 463–491.

[99] E. Komatsu et al., *Seven-Year Wilkinson Microwave Anisotropy Probe (WMAP) Observations: Cosmological Interpretation*. The Astrophysical Journal Supplement Series **192**(2) (2011) pp. 18–1–18–47.

[100] A. H. Guth, *Inflationary Universe: A Possible solution to the Horizon and Flatness Problems*. Physical Review D **23**(2) (1981) pp. 347–356.

[101] A. A. Starobinsky, *A New Type of Isotropic Cosmological Models Without Singularity*. Physics Letters B **91**(1) (1980) pp. 99–102.

[102] A. D. Linde, *A New Inflationary Universe Scenario: A Possible Solution of the Horizon, Flatness, Homogeneity, Isotropy and Primordial Monopole Problems*. Physics Letters B **108**(6) (1982) pp. 389–393.

[103] A. D. Sakharov, *Violation of CP Invariance, C Asymmetry, and Baryon Asymmetry of the Universe*. Journal of Experimental and Theoretical Physics Letters **5**(1) (1967) pp. 24–25.

[104] T2K Collaboration, K. Abe et al., *Constraint on the Matter–Antimatter Symmetry-Violating Phase in Neutrino Oscillations*. Nature **580**(7803) (2020) pp. 339–348.

[105] C. Abel et al., *Measurement of the Permanent Electric Dipole Moment of the Neutron*. Physical Review Letters **124**(8) (2020) pp. 081803–1–081803–7.

[106] L. Evans and P. Bryant, *LHC Machine*. Journal of Instrumentation **3**(8) (2008) pp. S08001–1–S08001–158.

[107] Mobs, Esma, *The CERN Accelerator Complex - August 2018*, 2018. `https://cds.cern.ch/record/2636343` (accessed on 07/03/2022).

[108] Taking a Closer Look at LHC, *Proton Source*. `https://www.lhc-closer.es/taking_a_closer_look_at_lhc/0.proton_source` (accessed on 07/03/2022).

[109] Taking a Closer Look at LHC, *LINAC4*. `https://www.lhc-closer.es/taking_a_closer_look_at_lhc/0.linac4` (accessed on

07/03/2022).

[110] CERN, *Facts and Figures About the LHC.* `https://home.cern/resources/faqs/facts-and-figures-about-lhc` (accessed on 07/03/2022).

[111] CERN, *Accelerators.* `https://home.cern/science/accelerators` (accessed on 07/03/2022).

[112] CERN, *Experiments.* `https://home.cern/science/experiments` (accessed on 07/03/2022).

[113] ATLAS Collaboration, G. Aad et al., *The ATLAS Experiment at the CERN Large Hadron Collider.* Journal of Instrumentation **3**(8) (2008) pp. S08003–1–S08003–407.

[114] LHCf Collaboration, O. Adriani et al., *The LHCf Detector at the CERN Large Hadron Collider.* Journal of Instrumentation **3**(8) (2008) pp. S08006–1–S08006–36.

[115] J. L. Feng et al., *ForwArd Search ExpeRiment at the LHC.* Physical Review D **97**(3) (2018) pp. 035001–1–035001–23.

[116] ALICE Collaboration, K. Aamodt et al., *The ALICE Experiment at the CERN LHC.* Journal of Instrumentation **3**(8) (2008) pp. S08002–1–S08002–245.

[117] CMS Collaboration, S. Chatrchyan et al., *The CMS Experiment at the CERN LHC.* Journal of Instrumentation **3**(8) (2008) pp. S08004–1–S08004–334.

[118] TOTEM Collaboration, G. Anelli et al., *The TOTEM Experiment at the CERN Large Hadron Collider.* Journal of Instrumentation **3**(8) (2008) pp. S08007–1–S08007–107.

[119] LHCb Collaboration, A. Augusto Alves Jr. et al., *The LHCb Detector at the LHC.* Journal of Instrumentation **3**(8) (2008) pp. S08005–1–S08005–205.

[120] MoEDAL Collaboration, V. A. Mitsou et al., *The MoEDAL Experiment at the LHC: Status and Results.* Journal of Physics: Conference Series **873** (2017) pp. 012010–1–012010–15.

[121] W. Herr and B. Muratori, *Concept of Luminosity.* CERN Accelerator School: Intermediate Accelerator Physics (2006) p. 364.

[122] W. Herr and B. Muratori, *Concept of Luminosity.* CERN Accelerator School: Intermediate Accelerator Physics (2006) p. 365.

[123] ATLAS Collaboration, *Luminosity Public Results Run 2.* `https://twiki.cern.ch/twiki/bin/view/AtlasPublic/LuminosityPublicResultsRun2` (accessed on 07/03/2022).

[124] W. Herr and B. Muratori, *Concept of Luminosity*. CERN Accelerator School: Intermediate Accelerator Physics (2006) p. 371.

[125] ATLAS Collaboration, *Delivered Luminosity versus Time for 2011-2018 (p-p Data Only)*, 2018. `https://twiki.cern.ch/twiki/bin/view/AtlasPublic/LuminosityPublicResultsRun2` (accessed on 07/03/2022).

[126] ATLAS Collaboration, *Total Integrated Luminosity and Data Quality in 2015-2018*, 2018. `https://twiki.cern.ch/twiki/bin/view/AtlasPublic/LuminosityPublicResultsRun2` (accessed on 07/03/2022).

[127] ATLAS Outreach, *ATLAS Fact Sheet*. `https://cds.cern.ch/record/1457044` (accessed on 31/03/2022).

[128] ATLAS Collaboration, *Computer Generated Image of the Whole ATLAS Detector*, 2008. `https://cds.cern.ch/record/1095924` (accessed on 31/03/2022).

[129] ATLAS Collaboration, *ATLAS Magnet System: Technical Design Report*. CERN-LHCC-97-018; ATLAS-TDR-6, 1997. `https://cds.cern.ch/record/338080` (accessed on 21/12/2022).

[130] ATLAS Collaboration, *ATLAS Central Solenoid: Technical Design Report*. CERN-LHCC-97-021; ATLAS-TDR-9, 1997. `https://cds.cern.ch/record/331067` (accessed on 21/12/2022).

[131] ATLAS Collaboration, *ATLAS Barrel Toroid: Technical Design Report*. CERN-LHCC-97-019; ATLAS-TDR-7, 1997. `https://cds.cern.ch/record/331065` (accessed on 21/12/2022).

[132] ATLAS Collaboration, *ATLAS End-Cap Toroids: Technical Design Report*. CERN-LHCC-97-020; ATLAS-TDR-8, 1997. `https://cds.cern.ch/record/331066` (accessed on 21/12/2022).

[133] ATLAS Collaboration, *ATLAS Inner Detector: Technical Design Report*. CERN-LHCC-97-016; ATLAS-TDR-4, 1997. `https://cds.cern.ch/record/331063` (accessed on 21/12/2022).

[134] ATLAS Collaboration, *Computer Generated Image of the ATLAS Inner Detector*, 2008. `https://cds.cern.ch/record/1095926` (accessed on 31/03/2022).

[135] ATLAS Collaboration, *ATLAS Liquid-Argon Calorimeter: Technical Design Report*. CERN-LHCC-96-041; ATLAS-TDR-2, 1996. `https://cds.cern.ch/record/331061` (accessed on 21/12/2022).

[136] ATLAS Collaboration, *ATLAS Tile Calorimeter: Technical Design Report.* CERN-LHCC-96-042; ATLAS-TDR-3, 1996. `https://cds.cern.ch/record/331062` (accessed on 21/12/2022).

[137] ATLAS Collaboration, *Computer Generated Image of the ATLAS Calorimeter*, 2008. `https://cds.cern.ch/record/1095927` (accessed on 31/03/2022).

[138] ATLAS Collaboration, *ATLAS Muon Spectrometer: Technical Design Report.* CERN-LHCC-97-022; ATLAS-TDR-10, 1997. `https://cds.cern.ch/record/331068` (accessed on 21/12/2022).

[139] ATLAS Collaboration, *Computer Generated Image of the ATLAS Muons Subsystem*, 2008. `https://cds.cern.ch/record/1095927` (accessed on 31/03/2022).

[140] ATLAS Collaboration, *ATLAS Level-1 Trigger: Technical Design Report.* CERN-LHCC-98-014; ATLAS-TDR-12, 1998. `https://cds.cern.ch/record/381429` (accessed on 21/12/2022).

[141] ATLAS Collaboration, *ATLAS High-Level Trigger, Data-Acquisition and Controls: Technical Design Report.* CERN-LHCC-2003-022; ATLAS-TDR-16, 2003. `https://cds.cern.ch/record/616089` (accessed on 21/12/2022).

[142] A. Martyniuk et al., *The Database Driven ATLAS Trigger Configuration System.* Journal of Physics: Conference Series **664**(082030) (2015) pp. 082030–1 – 082030–8.

[143] ATLAS Collaboration, *Functional Diagram of the ATLAS Trigger and Data Acquisition System*, 2017. `https://twiki.cern.ch/twiki/pub/AtlasPublic/ApprovedPlotsDAQ/` (accessed on 01/04/2022).

[144] C. P. Robert and G. Casella, *Monte Carlo Statistical Methods.* Springer, New York, NY, USA, second ed., 2004.

[145] J. Gao, L. Harland-Lang, and J. Rojo, *The Structure of the Proton in the LHC Precision Era.* Physics Reports **742** (2018) pp. 1–121.

[146] J. J. Ethier and E. R. Nocera, *Parton Distributions in Nucleons and Nuclei.* Annual Review of Nuclear and Particle Science **70** (2020) pp. 43–76.

[147] Y. L. Dokshitzer, *Calculation of the Structure Functions for Deep Inelastic Scattering and e^+ e^- Annihilation by Perturbation Theory in Quantum Chromodynamics.* Journal of Experimental and Theoretical Physics **46** (1977) pp. 641–653. `https://www.semanticscholar.org/paper/Calculation-of-the-Structure-Functions-for-Deep-and-Dokshitzer/c96496a859a2cc104ef305bb8604871fbfa2971f` (accessed on 21/12/2022).

[148] V. N. Gribov and L. N. Lipatov, *Deep Inelastic e p Scattering in Perturbation Theory.* Journal of Experimental and Theoretical Physics **15** (1972) pp. 438–450. `https://inspirehep.net/literature/73449` (accessed on 21/12/2022).

[149] G. Altarelli and G. Parisi, *Asymptotic Freedom in Parton Language.* Nuclear Physics B **126** (1977) pp. 298–318.

[150] B. Andersson et al., *Parton Fragmentation and String Dynamics.* Physics Reports **97**(2) (1983) pp. 31–145.

[151] B. R. Webber, *A QCD Model for Jet fragmentation Including Soft Gluon Interference.* Nuclear Physics B **238**(3) (1984) pp. 492–528.

[152] S. Agostinelli et al., *Geant4 – a simulation toolkit.* Nuclear Instruments and Methods in Physics Research A **506** (2003) pp. 250–303.

[153] J. Allison et al., *Geant4 Developments and Applications.* IEEE Transactions on Nuclear Science **53**(1) (2006) pp. 270–278.

[154] J. Allison et al., *Recent developments in Geant4.* Nuclear Instruments and Methods in Physics Research A **835** (2016) pp. 186–225.

[155] ATLAS Collaboration, M. Aaboud et al., *Electron Reconstruction and Identification in the ATLAS Experiment Using the 2015 and 2016 LHC Proton-Proton Collision Data at sqrts =13 TeV.* The European Physical Journal C **79**(8) (2019) pp. 639–1–639–40.

[156] ATLAS Collaboration, G. Aad et al., *Electron and Photon Performance Measurements with the ATLAS Detector Using the 2015–2017 LHC Proton-Proton Collision Data.* Journal of Instrumentation **14**(12) (2019) pp. P12006–1–P12006–67.

[157] ATLAS Collaboration, G. Aad et al., *Muon Reconstruction and Identification Efficiency in ATLAS Using the Full Run 2 pp Collision Data Set at sqrts =13 TeV.* The European Physical Journal C **81**(7) (2021) pp. 578–1–578–44.

[158] J. Illingworth and J. Kittler, *A Survey of the Hough Transform.* Computer Vision, Graphics, and Image Processing **44**(1) (1988) pp. 87–116.

[159] ATLAS Collaboration, G. Aad et al, *Identification and Energy Calibration of Hadronically Decaying Tau Leptons with the ATLAS Experiment.* Nuclear and Particle Physics Proceedings **273-275** (2015) pp. 1141–1146.

[160] ATLAS Collaboration, M. Aaboud et al., *Performance of Missing Transverse Momentum Reconstruction with the ATLAS Detector Using Proton–Proton Collisions at sqrts =13 TeV.* The European Physical Journal C **78**(11) (2018) pp. 903–1–903–46.

[161] ATLAS Collaboration, G. Aad et al., *Topological Cell Clustering in the ATLAS Calorimeters and its Performance in LHC Run 1*. The European Physical Journal C **77**(7) (2017) pp. 490–1–490–100.

[162] M. Cacciari, G. P. Salam, and G. Soyez, *The Anti-k_t Jet Clustering Algorithm*. Journal of High Energy Physics **2008**(4) (2008) pp. 063–1–063–14.

[163] ATLAS Collaboration, G. Aad et al., *Jet Reconstruction and Performance Using Particle Flow with the ATLAS Detector*. The European Physical Journal C **77**(7) (2017) pp. 466–1–466–67.

[164] ATLAS Collaboration, *Tagging and Suppression of Pileup Jets with the ATLAS Detector*. ATLAS-CONF-2014-018, 2014. `https://cds.cern.ch/record/1700870` (accessed on 21/12/2022).

[165] ATLAS Collaboration, G. Aad et al., *ATLAS b-Jet Identification Performance and Efficiency Measurement with $t\bar{t}$ events in pp Collisions at sqrts =13 TeV*. The European Physical Journal C **79**(11) (2019) pp. 970–1–970–52.

[166] ATLAS Collaboration, *Optimisation and Performance Studies of the ATLAS b-Tagging Algorithms for the 2017-18 LHC Run*. ATL-PHYS-PUB-2017-013, 2017. `http://cds.cern.ch/record/2273281` (accessed on 21/12/2022).

[167] ATLAS Collaboration, *JetEtMiss Recommendations for Release 21 MC16 (2015-2018)*. `https://twiki.cern.ch/twiki/bin/view/AtlasProtected/JetEtmissRecommendationsR21` (accessed on 27/04/2022).

[168] ATLAS Collaboration, *Tagger Calibration Recommendations for Release 21*. `https://twiki.cern.ch/twiki/bin/view/AtlasProtected/BTagCalibrationRecommendationsRelease21` (accessed on 27/04/2022).

[169] ATLAS Collaboration, *Latest Run 2 Electron Recommendations*. `https://twiki.cern.ch/twiki/bin/view/AtlasProtected/LatestRecommendationsElectronIDRun2` (accessed on 27/04/2022).

[170] ATLAS Collaboration, *Muon Combined Performance Analysis Guidelines MC16*. `https://twiki.cern.ch/twiki/bin/view/AtlasProtected/MCPAnalysisGuidelinesMC16` (accessed on 27/04/2022).

[171] M. Czakon et al., *Top-Quark Charge Asymmetry at the LHC and Tevatron through NNLO QCD and NLO EW*. Physical Review D **98**(1) (2018) pp. 014003–1–014003–10.

[172] ATLAS Collaboration, *TopDerivations*. `https://twiki.cern.ch/twiki/bin/view/AtlasProtected/TopDerivations`

(accessed on 28/04/2022).

[173] P. Nason, *A New Method for Combining NLO QCD with Shower Monte Carlo Algorithms*. Journal of High Energy Physics **2004**(11) (2004) pp. 040–1–040–27.

[174] S. Frixione, P. Nason, and C. Oleari, *Matching NLO QCD Computations with Parton Shower Simulations: the POWHEG Method*. Journal of High Energy Physics **2007**(11) (2007) pp. 070–1–070–91.

[175] S. Alioli et al., *A General Framework for Implementing NLO Calculations in Shower Monte Carlo Programs: the POWHEG BOX*. Journal of High Energy Physics **2010**(6) (2010) pp. 043–1–043–56.

[176] S. Alioli, S.-O. Moch, and P. Uwer, *Hadronic Top-Quark Pair-Production with One Jet and Parton Showering*. Journal of High Energy Physics **2012**(1) (2012) pp. 137–1–137–36.

[177] C. Bierlich et al., *A Comprehensive Guide to the Physics and Usage of PYTHIA 8.3*. `https://arxiv.org/abs/2203.11601` (accessed on 28/04/22).

[178] C. H. Kom and W. J. Stirling, *Charge Asymmetry in W + Jets Production at the LHC*. The European Physical Journal C **69**(1-2) (2010) pp. 67–73.

[179] G. Cowan, *Statistical Data Analysis: Statistical Tests - The Significance of an Observed Signal*. Clarendon Press, Oxford, UK, first ed., 1998. `https://global.oup.com/academic/product/statistical-data-analysis-9780198501558` (accessed on 21/12/2022).

[180] ATLAS Collaboration, M. Aaboud et al., *Electron and Photon Energy Calibration with the ATLAS Detector Using 2015–2016 LHC Proton-Proton Collision Data*. Journal of Instrumentation **14**(3) (2019) pp. P03017–1–P03017–58.

[181] ATLAS Collaboration, G. Aaboud et al., *Determination of Jet Calibration and Energy Resolution in Proton–Proton Collisions at sqrts =8 TeV Using the ATLAS Detector*. The European Physical Journal C **80**(12) (2020) pp. 1104–1–1104–81.

[182] ATLAS Collaboration, *Jet Energy Scale and Jet Energy Resolution Uncertainties for Full Run 2 Analyses*. `https://twiki.cern.ch/twiki/bin/view/AtlasProtected/JetUncertaintiesRel21Summer2018SmallR#Jet_energy_scale_JES_uncertainti` (accessed on 04/07/2022).

[183] J. Butterworth et al., *PDF4LHC recommendations for LHC Run II*, 2015. `https://arxiv.org/abs/1510.03865v1` (accessed on 17/06/22).

[184] J. Alwall et al., *The Automated Computation of Tree-Level and Next-to-Leading Order Differential Cross Sections, and Their Matching to Parton Shower Simulations*. Journal of High Energy Physics **2014**(7) (2014) pp. 079–1–079–155.

[185] R. Frederix et al., *The Automation of Next-to-Leading Order Electroweak Calculations*. Journal of High Energy Physics **2018**(7) (2018) pp. 185–1–185–120.

[186] R. Frederix et al., *Erratum: The Automation of Next-to-Leading Order Electroweak Calculations*. Journal of High Energy Physics **2021**(11) (2021) pp. 085–1–085–2.

[187] M. Bähr et al., *Herwig++ Physics and Manual*. The European Physical Journal C **58**(4) (2008) pp. 639–707.

[188] J. Bellm et al., *Herwig 7.0/Herwig++ 3.0 Release Note*. The European Physical Journal C **76**(4) (2016) pp. 196–1–196–8.

[189] ATLAS Collaboration, *Improvements in $t\bar{t}$ Modelling Using NLO+PS Monte Carlo Generators for Run 2*. ATL-PHYS-PUB-2018-009, 2018. `https://cds.cern.ch/record/2630327` (accessed on 21/12/2022).

[190] Wikimedia Commons, *Receiver Operating Characteristic (ROC) Curve*, 2018. `https://commons.wikimedia.org/wiki/File:Roc_curve.svg` (accessed on 11/05/2022).

[191] J. Erdmann et al., *A Likelihood-Based Reconstruction Algorithm for Top-Quark Pairs and the KLFitter Framework*. Nuclear Instruments and Methods in Physics Research Section A **748** (2014) pp. 18–25.

[192] The KLFitter Team, *KLFitter - The Kinematic Likelihood Fitter*. `https://github.com/KLFitter/KLFitter` (accessed on 04/05/2022).

[193] ATLAS Collaboration, *KLFitter Transfer Functions*. `https://twiki.cern.ch/twiki/bin/view/AtlasProtected/KLFitterTF` (accessed on 04/05/2022).

[194] The KLFitter Team, *KLFitter - The Kinematic Likelihood Fitter: LikelihoodTopLeptonJets_Angular*. `https://github.com/KLFitter/KLFitter/blob/master/src/LikelihoodTopLeptonJets_Angular.cxx` (accessed on 04/05/2022).

[195] A. Czarnecki, J. G. Körner, and J. H. Piclum, *Helicity Fractions of W from Top Quark Decays at Next-to-Next-to-Leading Order in QCD*. Physical Review D **81**(11) (2010) pp. 111503–1–111503–5.

[196] C. Zhang and Y. Ma, *Ensemble Machine Learning: Methods and Applications*. Springer, New York, NY, USA, first ed., 2012.

[197] J. R. Quinlan, *Induction of Decision Trees*. Machine Learning **1** (1986) pp. 81–106.

[198] J. R. Quinlan, *C4.5: Programs for Machine Learning*. Morgan Kaufmann Publishers, San Mateo, CA, USA, 1993. `https://dl.acm.org/doi/10.5555/152181` (accessed on 21/12/2022).

[199] L. Breiman et al., *Classification and Regression Trees*. Routledge, New York, NY, USA, 1984.

[200] F. Pedregosa et al., *Scikit-learn: Machine Learning in Python*. Journal of Machine Learning Research **12** (2011) pp. 2825–2830.

[201] L. Buitinck et al., *API Design for Machine Learning Software: Experiences from the Scikit-learn Project*. European Conference on Machine Learning and Principles and Practices of Knowledge Discovery in Databases (2013) pp. 108–122.

[202] T. M. Mitchell, *Machine Learning*. McGraw-Hill, New York, NY, USA, first ed., 1997.

[203] Wikimedia Commons, *Illustration of a Boosting Method for Ensemble Learning*, 2020. `https://commons.wikimedia.org/wiki/File:Ensemble_Boosting.svg` (accessed on 06/05/2022).

[204] R. E. Schapire, *The Strength of Weak Learnability*. Machine Learning **5** (1990) pp. 197–227.

[205] Y. Freund and R. E. Schapire, *Experiments with a new Boosting Algorithm*. Proceedings of the Thirteenth International Conference on Machine Learning (1996) pp. 148–156. `https://dl.acm.org/doi/10.5555/3091696.3091715` (accessed on 21/12/2022).

[206] Y. Freund and R. E. Schapire, *A Decision-Theoretic Generalization of On-Line Learning and an Application to Boosting*. Journal of Computer and System Sciences **55**(1) (1997) pp. 119–139.

[207] R. E. Schapire and Y. Singer, *Improved Boosting Algorithms Using Confidence-rated Predictions*. Machine Learning **37** (1999) pp. 297–336.

[208] Wikimedia Commons, *Cross-Validation Visualized*, 2019. `https://commons.wikimedia.org/wiki/File:K-fold_cross_validation_EN.svg` (accessed on 11/05/2022).

[209] S. learn Developers, *Feature Importance Evaluation*. `https://scikit-learn.org/stable/modules/ensemble.html#random-forest-feature-importance` (accessed on 23/07/2022).

[210] G. Loupe, *Understanding Random Forests: From Theory to Practice*. `https://arxiv.org/abs/1407.7502` (accessed on 23/07/2022).

[211] G. Cowan, *Statistical Data Analysis: Unfolding - Formulation of the Unfolding Problem*. Clarendon Press, Oxford, UK, first ed., 1998. `https://global.oup.com/academic/product/statistical-data-analysis-9780198501558` (accessed on 21/12/2022).

[212] F. Spanò, *Unfolding in Particle Physics: A Window on Solving Inverse Problems*. European Physical Journal Web of Conferences **55** (2013) pp. 03002–1–03002–32.

[213] L. Brenner et al., *Comparison of Unfolding Methods Using RooFitUnfold*. International Journal of Modern Physics A **35**(24) (2020) pp. 2050145–1–2050145–17.

[214] The RooUnfold Team, *RooUnfold: ROOT Unfolding Framework*. `https://gitlab.cern.ch/RooUnfold/RooUnfold` (accessed on 25/07/2022).

[215] M. Thomson, *Modern Particle Physics*. Cambridge University Press, Cambridge, UK, 2013.

[216] A. J. Bevan et al., *The Physics of the B Factories*. The European Physical Journal C **74**(11) (2014) pp. 3026–1–3026–928.

[217] S. Chen et al., *Heavy Flavour Physics and CP Violation at LHCb: a Ten-Year Review*, 2021. `https://arxiv.org/abs/2111.14360` (accessed on 24/07/22).

[218] LHCb Collaboration, R. Aaij et al., *Measurement of CP Violation in $B^0 \to J/\Psi K^0_S$ Decays*. Physical Review Letters **115**(3) (2015) pp. 031601–1–031601–9.

[219] LHCb Collaboration, R. Aaij et al., *Measurement of CP Violation in $B^0 \to J/\Psi K^0_S$ and $B^0 \to \Psi(2S) K^0_S$ Decays*. Journal of High Energy Physics **2017**(11) (2017) pp. 170–1–170–17.

[220] LHCb Collaboration, R. Aaij et al., *Precision Measurement of CP Violation in $B^0_S \to J/\Psi K^+K^-$ Decays*. Physical Review Letters **114**(4) (2015) pp. 041801–1–041801–9.

[221] LHCb Collaboration, R. Aaij et al., *Updated Measurement of Time-Dependent CP-Violating Observables in $B^0_S \to J/\Psi K^+K^-$ Decays*. The European Physical Journal C **79**(8) (2019) pp. 706–1–706–26.

[222] LHCb Collaboration, R. Aaij et al., *Erratum to: Updated Measurement of Time-Dependent CP-Violating Observables in $B^0_S \to J/\Psi K^+K^-$ Decays*. The European Physical Journal C **80**(7) (2020) pp. 601–1–601–8.

[223] K. Levenberg, *A Method for the Solution of Certain Problems in Least Squares*. Quarterly of Applied Mathematics **2**(2) (1944) pp. 164–168. `https://www.jstor.org/stable/43633451` (accessed on 21/12/2022).

[224] D. W. Marquandt, *An Algorithm for Least-Squares Estimation of Nonlinear Parameters*. Journal of the Society for Industrial and Applied Mathematics **11**(2) (1963) pp. 431–441.

[225] The lMfit Team, *LMfit*. `https://github.com/lmfit/lmfit-py` (accessed on 24/07/2022).

[226] G. Cowan, *Statistical Data Analysis: Statistical Tests - Pearson's* χ^2 *Test*. Clarendon Press, Oxford, UK, first ed., 1998. `https://global.oup.com/academic/product/statistical-data-analysis-9780198501558` (accessed on 21/12/2022).

[227] Wikimedia Commons, *B-tagging Diagram*, 2016. `https://commons.wikimedia.org/wiki/File:B-tagging_diagram.png` (accessed on 24/07/2022).

[228] G. Piacquadio, K. Prokofiev, and A. Wildauer, *Primary Vertex Reconstruction in the ATLAS Experiment at LHC*. Journal of Physics: Conference Series **119**(3) (2008) pp. 032003–1–032003–8.

[229] S. Boutle et al., *Primary Vertex Reconstruction at the ATLAS Experiment*. Journal of Physics: Conference Series **898**(4) (2017) pp. 042056–1–042056–8.

[230] G. Piacquadio and C. Weiser, *A New Inclusive Secondary Vertex Algorithm for b-Jet Tagging in ATLAS*. Journal of Physics: Conference Series **119**(3) (2008) pp. 032032–1–032032–10.

[231] S. Heer, *The Secondary Vertex Finding Algorithm with the ATLAS Detector*. Proceedings of Science **314**(EPS-HEP2017) (2018) pp. 762–1–762–5.

[232] ATLAS Collaboration, M. Aaboud et al., *A Measurement of Material in the ATLAS Tracker using Secondary Hadronic Interactions in 7 TeV pp Collisions*. Journal of Instrumentation **11**(411) (2016) pp. P11020–1–P11020–40.

[233] C. Gay, *B Mixing: Anatomy of a Time-Dependent Oscillation Measurement*. Annual Review of Nuclear and Particle Science **50**(11) (2000) pp. 596–603.